*A glimpse into the 'core-cusp' problem in clusters of galaxies : a combination of Hubble Space Telescope imaging, VLT/MUSE spectroscopy, and strong gravitational lensing*

CATHERINE CERNY

**A glimpse into the 'core-cusp' problem in clusters of galaxies : a combination of *Hubble Space Telescope* imaging, VLT/MUSE spectroscopy, and strong gravitational lensing**

Catherine Cerny

## Abstract

Clusters of galaxies play a key role in studying the distribution of dark matter (DM) throughout the universe. As the most massive observable objects in the Universe, they represent the largest concentrations of DM one can study with current ground- and space-based telescopes. However, the shape of their DM density profiles in the inner region is currently a source of tension between observations and theory. While cold DM (CDM, the favored DM candidate today) cosmological simulations predict mass profiles that follow a steep power law, where the density increases in a 'cusp' in the center, observations suggest that instead it flattens out, forming an almost constant central density 'core'. From an observational perspective, resolving this core-cusp problem requires robust mass distribution models for many different galaxy clusters to examine the structure of their density profiles. In this thesis, I present precise mass models of eight different clusters, created using a combination of gravitational lensing and stellar kinematics thanks to imaging with the *Hubble Space Telescope* and spectroscopy with the Very Large Telescope. Strong lensing is one of the most powerful tools for obtaining clusters' total mass profiles, as it is purely geometric, independent of clusters' dynamical states, and relying principally on the identification of multiply lensed background galaxies to constrain the model. The inner DM profile can then be recovered from the total mass profile by subtracting the baryonic component, which I model using stellar kinematics of the brightest cluster galaxy (BCG) as a proxy for the total stellar mass in the cluster center. The slope of the cluster sample, on average, is core-like. I ultimately aim to statistically examine what physical processes might account for these core-like slopes to distinguish between potential DM candidates, such as self-interacting DM, warm DM, or even more exotic types of DM.

# A glimpse into the 'core-cusp' problem in clusters of galaxies : a combination of *Hubble Space Telescope* imaging, VLT/MUSE spectroscopy, and strong gravitational lensing

**Catherine Cerny**

A Thesis presented for the degree of
Doctor of Philosophy


Centre for Extragalactic Astronomy
Department of Physics
Durham University
United Kingdom
June 2024

# Contents

# List of Tables

# List of Figures

# Declaration

The work in this thesis was undertaken between October 2020 and June 2024 while the author was a research student under the supervision of Dr. Mathilde Jauzac and Dr. Richard Massey in the Centre for Extragalactic Astronomy, which is a part of the Department of Physics at the University of Durham. No part of this thesis has been submitted for any other degree or qualification at Durham University or any other University, and it is all my own work unless referenced to the contrary in the text. Chapter 3 has been submitted to as a paper to the Monthly Notices of the Royal Astronomical Society (MNRAS). All figures in this thesis have been produced by the author, or have been attributed in the figure caption. The copyright of this thesis rests with the author. No quotations from it should be published without the author's prior written consent and information derived from it should be acknowledged.

# Acknowledgements

I started this journey in the middle of the COVID-19 pandemic. It was, and still is, one of the hardest things I have ever done. I would never have reached this point were it not for everyone has supported and encouraged me over the last several years.

I am infinitely grateful to Keren for her unwavering support and advocacy. Words genuinely fail me here- without her, I wouldn't be writing this acknowledgement section at all. She is the person who first introduced me to wonder of working with the universe's natural cosmic telescopes, and I'm so so excited to come back and work with her again as a postdoc this coming fall.

I'm deeply grateful to Mathilde for being a phenomenal PhD advisor for the last several years. She has motivated me to become a better version of myself, and has been such an amazing presence in my life. I couldn't have done any of this without her wonderful mentorship and her constant support.

I want to thank David, who has been a really reassuring and helpful mentor for me as I've gone through this PhD. He was instrumental in putting together so much of my work, and I'm very grateful for his help and support. I'm super happy that we get to keep working together a little in the future.

Thank you as well to Guillaume and Anna, who made the initial journey from Michigan to Durham along with me. They have been wonderful mentors, and I feel privileged to have gotten to work with them over the last few years. I'm very grateful to both for all the conversations and discussions I've had with them in order to figure out fun things like Bayesian statistical analysis or putting together MUSE proposals.

I want to thank Alastair for acting as an additional supporter for my work, particularly while Mathilde was away. He has guided and inspired so much of my work. I'll also never forget the sincere kindness he showed when he took me around and introduced me to Durham the very first month I arrived in England, which was during the middle of the pandemic. I'm deeply grateful to have gotten to work with him over the last few years.

I want to extend thanks to Eric and Marceau for giving me the opportunity to travel to Marseille to work with them for a month. It was a very productive period of time for me, and I'm really happy I had the opportunity to have the experience. I am also grateful for all the close conversations and advice they have offered me over the last few years.

Thank you as well to Richard for reading over my paper several times and for providing helpful notes and commentary that helped me shape the structure of this thesis. I'm very grateful for the conversations we've had that have helped me understand how to direct my work.

I want to thank Johan for giving me the opportunity to participate in the dark matter group that has met for the last two years at ISSI in Bern. The conversations that we've had have been very helpful for my work.

I want to acknowledge Dr. Adi Zitrin for helping me make a LTM model for one of the clusters I present in this thesis. It was super useful to have, and I'm happy we had the opportunity to interact in this way.

I want to thank Dr. Pat Seitzer, who was my first mentor in astronomy and who gave me my first taste of the field. I will be forever grateful that he put an advertisement into the freshman undergraduate research program that caught my attention and, later, my heart.

Thank you as well to Dr. Dan Coe, who wrote me a recommendation letter for this program on extremely short notice. I'm deeply grateful for his willingness to help me continue to advance my career.

Finally, thank you to Nency for being a great fellow student in this group. It's been really nice to travel together and talk about science, and I'm so happy that we were able to meet and work together during this time.

Formally, I thank the University of Durham and the staff in the Department of Physics for all their help in managing my status as an international student. I acknowledge support from the UKRI FLF grant numbers MR/S017216/1 + NR/X006069/1, and from the Durham Doctoral Studentship (Faculty of Science), which was awarded to me in 2020.

On the personal side, I couldn't have done this without my mom, my aunt, and my grandparents, who have been my biggest supporters at every step of the way. I'm so thankful for everything that they've done for me, from driving me to the US consulate to get my visa for travel to the UK, to making sure I had enough food and furniture in my apartment, to helping me get through a month abroad on a low budget. The pictures that you've sent and the phone calls we've had have been so wonderful. It was a joy to see both my grandparents in Edinburgh, and I'm so grateful for the time that we took together to explore the Scottish highlands. Thank you to my mom for our weekly phone calls, and to my aunt for sending me all those cute pictures of her dogs. I'm beyond glad that I won't be an ocean away from you anymore in just a few short weeks. Love you Gaby!

Thank you to all my friends who been there for me throughout this whole process through online calls, chats, and movie nights. I literally would not have gotten through this without their support. To Mercedes, Alexi, Julie, Rui, Eva, Alek, Justin, Paul, Kai, Tony, Beatrix, and everyone I have met through Elira, thank you so much for being such wonderful people and keeping me sane.

Finally, thank you to my sister, my bro, for being the best supporter ever by sending me food and memes and calling me on FaceTime so her children could scream how much they love their auntie. Thanks for helping me get back home.

# Dedication

Dedicated to my cat, Princess, who will have traveled across the Atlantic Ocean twice for me by the time this is over, and who has kept me company all through this long, sometimes lonely journey.

# CHAPTER 1

# Introduction

Astronomy is, at its core, an attempt to comprehend the Universe, starting from the moment of its inception all the way to the present day. From the development of the first telescope in the early 17th century, which allowed us to gaze out at the vast expanse of the cosmos, to the creation and use of photographic plates in the late 19th century, which more easily enabled the study of astronomical objects that change over time, all the way to the creation of modern instruments and telescopes that we now use to trace back the history of the Universe to the primordial moments of its creation, astronomy has covered a great deal of ground in a relatively short period of time. We have discovered the structure of our solar system, created systems to classify and categorize stars and galaxies, and developed physics to explain the large-scale formation history of the Universe. Yet there is still more to do, and countless more discoveries left to make to fully understand the past, present, and future of the Universe. This thesis aims to contribute one small piece of knowledge toward this gargantuan task, but before we can begin, we must first establish the basis upon which all of the following work rests.

## 1.1 Cosmology

Cosmology lays the groundwork for our understanding of the origin of the universe and provides the methodology through which we can study its evolution. Modern cosmology rests on the assumption that we can describe the physics governing the universe with two key concepts: the Cosmological Principle, which states that the Universe is spatially homogeneous and isotropic at large scales, and General Relativity, which we assume correctly describes gravity.

### 1.1.1 The Cosmological Principle

Early in the 1900s, astronomers measured the radial velocities of nearby galaxies and observed that they were moving away from us. At around the same time, Henrietta Swan Leavitt, a 'computer' working at Harvard College Observatory, discovered something equally curious. Cepheid variable stars, which were first independently identified by both Edward Piggott and John Goodricke in 1784, are a type of star that regularly pulsates, such that its brightness increases and decreases over time. In 1912, Leavitt determined that there was a simple relationship between the period of these pulsations and the brightness of the stars, and showed that this relation could be used to measure distances across the Universe (Leavitt & Pickering 1912). This 'distance ladder' was of great importance in the later work of Edwin Hubble, who used Cepheids to measure the distance to 18 different galaxies (Hubble 1929). He combined the measurements of distance and radial velocities for these galaxies and discovered a proportional relationship between a galaxy's recessional velocity, $v$, and its distance from Earth, $d$, as shown in Figure 1.1. This relationship built off of earlier work by Alexander Friedmann (Friedmann 1922) and by Georges Lemaître (Lemaître 1927), and is now known as Hubble's law. This law takes the following form,

$$v = H_0 d. \tag{1.1}$$

Hubble's law allows the distance of any galaxy to be measured from its recessional velocity. The speed at which a galaxy moves away from us is directly correlated

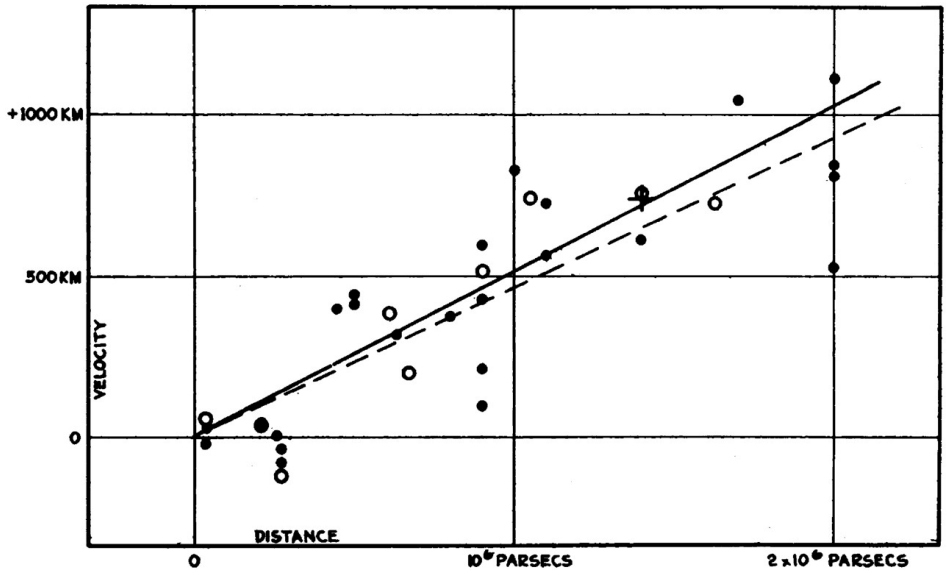


Figure 1.1: Diagram of Hubble's Law, as published in his 1929 paper (Hubble 1929). The x-axis shows the distance to extra-galactic nebulae as measured from Earth using Cepheid variable stars, and the y-axis shows the velocity of the nebulae as measured from spectroscopic observations. Two different solutions to the relationship between these quantities are shown using solid circles and solid line, and the open circles and dashed line. The cross shows the mean velocity-distance relationship for an additional group of 22 nebulae.

to a shift in the wavelength of its observed spectrum to redder wavelengths. This quantity is also known as the 'redshift' of a galaxy, and it is always measured relative to Earth, which is assumed to be at a redshift of 0. The linear relationship between distance and velocity implies that the Universe is expanding, and that this expansion can be measured by any observer at any position in the Universe. The rate of expansion at the present time ($t = t_0$) is thus represented by the value of $H_0$, which is known as the Hubble constant. The value of $H_0$ is presently measured to be around 70 km s$^{-1}$ Mpc$^{-}$1 (Di Valentino et al. 2021). However, there is some debate regarding the exact value of $H_0$. In theory, this measurement should be independent of the method used to obtain it. In practice, this is decidedly not the case. Measurements of this constant that are based on measurements of Cepheids made with space-based telescopes result in values of around $73 - 74$ km/s/Mpc, with minimal uncertainty ($\sim 1\%$) (Riess et al. 2022a, 2024). By contrast, measurements made by using the signal from the earliest parts of the Universe yield a value of around $67 - 68$ km/s/Mpc, also with minimal uncertainty ($< 1\%$) (Planck Collaboration

et al. 2020). This disagreement between these different measurements is also known as the Hubble tension, and it is currently one of the biggest challenges facing modern astronomy. I discuss this tension further in Section 1.2.1.

I will now describe what I mean by 'the signal from the earliest parts of the Universe'. Since the Universe is expanding, then logically, its present size must be larger than it was in the past, and since galaxies are moving away from each other at speeds linearly related to their distance from each other, then there must have been a moment where everything in the Universe converged at a single point of infinite temperature and density. Our description of modern physics begins at the instant after this hot, dense Universe begins to expand outward. This model is known as the Hot Big Bang theory, and it is further supported by the existence of the cosmic microwave background (CMB) (Gamow 1948; Alpher & Herman 1948; Penzias & Wilson 1965). The nature of the CMB is related to our description of the earliest moments in the Universe.

In the time directly following the Big Bang, the environment of the Universe was hot enough to effectively be in thermal equilibrium, which prevented the formation of neutral hydrogen atoms. Additionally, photons were efficiently scattered by interactions with electrons, which meant the Universe was opaque. As the Universe cooled, neutral hydrogen began to form from electrons and protons, and the mean free path for photons increased, which made the Universe transparent to radiation. This period is known as recombination, and it occurred roughly 400,000 years after the Big Bang. Leftover blackbody radiation from this period still suffuses the Universe, though its energy has decreased as the Universe has expanded and it has propagated outward. It was first detected in 1964 by Arno Penzias and Robert Wilson as microwaves, with a temperature of $\sim 3$ K. This radiation is the CMB, and it exists at the same temperature in every observable part of the Universe. The latest measurements from the Wilkinson Microwave Anisotropy Probe (WMAP) have measured the CMB temperature to be 2.725 K (Hinshaw et al. 2013), and further observations made using the Planck space telescope (Planck Collaboration et al. 2020) and with the South Pole Telescope (Balkenhol et al. 2023) have shown extremely small fluctuations of this temperature ($10^{-5}$), which supports the assump-

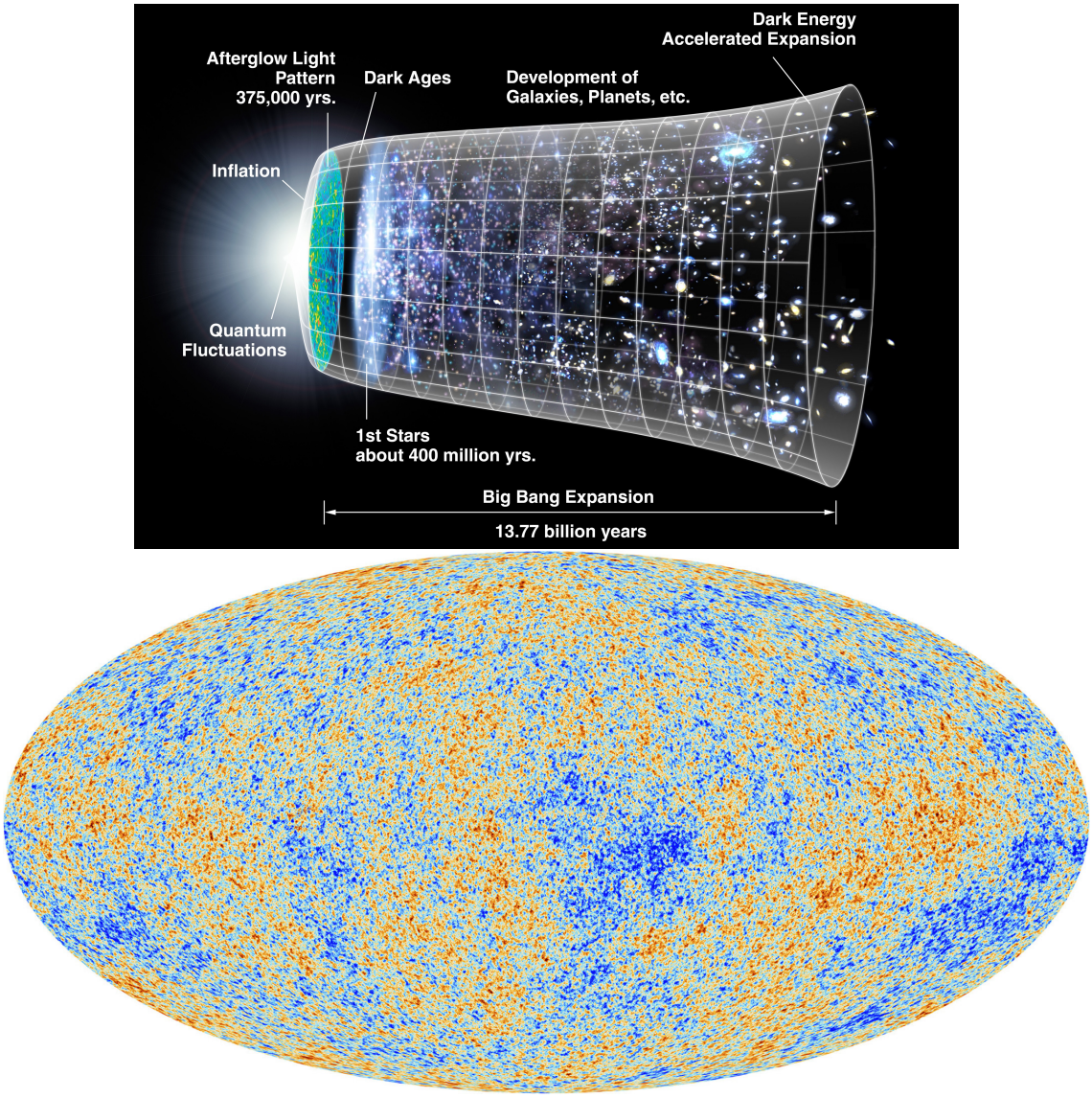


Figure 1.2: *Top:* Timeline of the evolution of the Universe over the past 13.77 billion years, beginning from the Big Bang on the left to the present day on the right. The CMB is represented by the 'Afterglow Light Pattern', and the era of recombination happens after the 'Dark Ages'. (Image credit: NASA / WMAP Science Team) *Bottom:* Clearer image of the CMB from the above figure. This map shows anisotropies, or temperature fluctuations, in the CMB. (Image credit: ESA / Planck Collaboration)

tion that the very early Universe was homogeneous. Figure 1.2 shows a timeline of the evolution of the Universe, as well as a map of these fluctuations in the CMB.

The cosmological principle is thus strongly tied to the Hot Big Bang theory, as the principles that we use to describe the expansion of the Universe in this way necessarily require the assumption of an isotropic and homogeneous Universe. Though this is obviously not true at small scales (as in the case of our own Solar System), all-sky radio observations show a fairly uniform distribution of objects, which suggests that the Universe is indeed homogeneous and isotropic at the largest distance scales. Therefore, with the assumption that the cosmological principle indeed applies, we can express the average evolution of the Universe at these large scales with the Friedmann-Lemaître-Robertson-Walker (FLRW) metric,

$$(ds)^2 = (cdt)^2 - a^2(t)\left[\left(\frac{d\varpi}{\sqrt{1-k\varpi^2}}\right)^2 + (\varpi d\omega)^2 + (\varpi \sin\theta d\phi)^2\right], \tag{1.2}$$

where $t$ is the proper time, $k$ describes the spatial curvature of the Universe, $\varpi$ expresses the proper distance $r$ in terms of the dimensionless scale factor $a(t)$ as $r(t) = a(t)\varpi$, and $\{\theta, \phi\}$, represent the spherical coordinates of the spatial part of the metric. $a(t)$ characterizes the size of the Universe at a time $t$ with respect to its size today, $(t_0)$, where $a(t_0) = 1$. This can be described with the Hubble parameter, $H(t) \equiv \frac{\dot{a}}{a}$, and at the present time $t_0$, we can calculate the Hubble constant as $H(t_0) \equiv H_0$. The parameter $k$ describes the spatial curvature of the Universe, and generally has three possible values: if the Universe is spatially flat, $k = 0$; if the Universe is spherical, or positively curved, then $k = 1$; and if the Universe is hyperbolic, or negatively curved, then $k = -1$. With this framework in mind, we can now discuss the physical equations that govern an isotropic, homogeneous Universe.

### 1.1.2 General Relativity

Einstein's theory of general relativity (Einstein 1915a,b; Wald 1984) was proposed in response to the failure of Newton's law of universal gravitation to accurately predict the shift of Mercury's angular position in orbit. It is, in essence, a re-

contextualization of 'gravity' from Newton's relationship between force, mass, and distance, to a geometric description of how mass and spacetime interact with each other. To this day, it remains the simplest theory consistent with observational data like gravitational redshifts, which describe the phenomenon of photons losing energy and acquiring a redder wave frequency (a redshift) as they travel out of a gravitational well; gravitational time dilation, which describes the difference in elapsed time between two events as measured by observers located some distance from a gravitational mass; and gravitational lensing, which describes the physical effect of curved spacetime on the path of light traveling from a distant source toward an observer. General relativity relies on the principle of equivalence: namely, that inertial and gravitational mass are observationally equivalent and indistinguishable from each other regardless of the observer's location. Einstein's field equations describe how the curvature of spacetime by matter, or energy, affects gravitational interactions, and are expressed as follows:

$$G_{\mu\nu} \equiv R_{\mu\nu} - \frac{1}{2} R g_{\mu\nu} = \frac{8\pi G}{c^4} T_{\mu\nu}, \tag{1.3}$$

where $G_{\mu\nu}$ is the Einstein tensor, which is symmetric and determined by the curvature of spacetime at a specific point in space and time; this is expressed by writing the Einstein tensor in terms of the Ricci curvature tensor, $R_{\mu\nu}$, the Ricci curvature scalar, $R$, and the metric tensor, $g_{\mu\nu}$, of which the Ricci tensor and scalar are functions, and which specifies the spacetime geometry. On the right-hand side, $T_{\mu\nu}$ is the energy-momentum tensor. The field equations thus relate the energy and momentum of a particle at a specific point in space and time to the curvature of space and time at that point.

The solutions to these equations are very complex and difficult to obtain unless some simplifying assumptions are made about the nature of spacetime. For example, if we solve the equations following the assumptions of the cosmological principle (an isotropic, homogeneous Universe), we obtain the first Friedmann equation, which is written in terms of the scale factor $a(t)$ as

$$\left(\frac{\dot{a}}{a}\right)^2 = \frac{8}{3}\pi G\rho + \frac{1}{3}\Lambda c^2 - \frac{c^2}{a^2}k \tag{1.4}$$

where $\rho$ is the volumetric mass density of the Universe and $\Lambda$ is the cosmological constant. This equation is a representation of the expansion history of the Universe. If we take the derivative of this equation, we can then obtain a representation of the acceleration (or deceleration, depending on the nature of the cosmological constant) of this expansion:

$$\frac{\ddot{a}}{a} = -\frac{4}{3}\pi G\left(\rho + \frac{3P}{c^2}\right) + \frac{1}{3}\Lambda c^2, \tag{1.5}$$

where $P$ is the pressure of the Universe.

We can now manipulate these equations to determine the overall geometry of the Universe. We begin by obtaining the critical density of the Universe, which is found by solving Equation 1.4 with the cosmological constant $\Lambda$ and the spatial curvature $k$ both set to zero, which is equivalent to a flat, matter-only universe:

$$\rho_c = \frac{3H^2}{8\pi G} = 2.7754 \text{ x } 10^{11} h^2 M_\odot Mpc^{-3}, \tag{1.6}$$

where $h = H_0/(100$ km/s/Mpc), and the Hubble parameter $H$ is equivalent to $\left(\frac{\dot{a}}{a}\right)^2$. We can then find the ratio between the observed density of the universe, $\rho$, and this critical density, and in so doing obtain the density parameter, $\Omega \equiv \frac{\rho}{\rho_c}$, which allows us to characterize the nature of the Universe. If $\Omega$ is greater than unity, then the Universe is closed, and will eventually stop expanding and collapse. If $\Omega$ is less than unity, then the Universe is open, and will expand into infinity. If $\Omega$ is equal to unity, then the Universe is flat, and expansion will slow down over time but will never cease completely.

We can be even more explicit in our determination of the geometry of the Universe by breaking up the density parameter into the different components of the total energy-density content of the Universe:

$$\Omega \equiv \Omega_M + \Omega_R + \Omega_k + \Omega_\Lambda, \tag{1.7}$$

where $\Omega_M$, $\Omega_R$, $\Omega_k$, and $\Omega_\Lambda$ represent matter, radiation, curvature, and the cosmological constant, respectively. We can measure these density ratios at the present time, $t = t_0$, and have done so: the most recent results from the Planck satellite (Planck Collaboration et al. 2020), which measures CMB anisotropies, give a matter density parameter of $\Omega_M = 0.315 \pm 0.007$, a constraint on the spatial curvature measurement that is consistent with a flat universe, $\Omega_k = 0.001 \pm 0.002$, and a radiation density $\Omega_R \approx 9.2 \text{ x } 10^{-5}$. Assuming the Universe is spatially flat, $\Omega_\Lambda$ is then measured as $0.6847 \pm 0.0073$. When summed together, these measurements are approximately equal to 1 (they will never be exactly 1 due to the uncertainties in the measurements). This indicates that we live in a flat Universe.

We now turn toward a discussion of the physical meaning of the cosmological constant. The cosmological constant is included in the preceding equations to account for an observed but unknown quantity in the Universe. It is presently associated with dark energy, which is a form of energy that affects the Universe on large scales, is currently the dominant energy component of the Universe, and is thought to be responsible for the accelerated expansion of the Universe. The exact characterization of dark energy depends on the cosmological model. In this thesis, I use the $\Lambda$-cold dark matter ($\Lambda$-CDM) model as the basis for all of my work, and I discuss this model and its implications in Section 1.2.

### 1.1.3 Cosmological Redshift

Before proceeding further, it is useful to connect the theory of general relativity that we have established in the preceding sections to the actual observables we can measure. Cosmological distance measurements are of particular interest since the Universe is expanding, and these can be most easily and directly obtained through the redshift. The scale factor $a(t)$, which characterizes the expansion, influences the time it takes for light to travel. If a photon is emitted at time $t_e$ and received at time $t_0$, and then a second photon is emitted at $t_e + \Delta t_e$ and received at $t_0 + \Delta t_0$, if we assume that $\Delta t_e \ll t_o - t_e$, then we can treat $a(t)$ as a constant with respect to time integration. Then, using $a(t_0) = 1$, we can show that the relationship between the time intervals can be expressed as follows:

$$\Delta t_0 = \frac{\Delta t_e}{a(t_e)}. \tag{1.8}$$

We can then relate these time intervals to the wavelengths of the emitted and received light through the expression $\lambda = c\Delta t$. If we define the redshift, z, as

$$z = \frac{\lambda_0 - \lambda_e}{\lambda_e}, \tag{1.9}$$

where $\lambda_e$ and $\lambda_o$ are the emitted and observed wavelengths, respectively, then we can obtain the expression for the cosmological redshift,

$$\frac{1}{a(t_e)} = \frac{\lambda_0}{\lambda_e} = 1 + z. \tag{1.10}$$

The redshift thus serves as a way to measure the distance to an object. As long as stellar light can be detected from some physical process corresponding to a known wavelength, we can determine its redshift. For example, in this thesis we observe the spectra of galaxies and identify emission lines corresponding to, among other processes, [OII] and Ly-$\alpha$ emissions. We can then associate the wavelengths of these observed lines, $\lambda_0$, with the known wavelengths of these processes in a laboratory environment, $\lambda_e$, and in so doing, calculate the redshift, or distance, of the galaxy.

### 1.1.4 Luminosity Distance

Another quantity that we can measure from observables is the stellar flux of an object. If we know the luminosity $L$ of an object, and observe its flux $F$, then we can measure the distance of the object from its observed flux as

$$F = \frac{L}{4\pi D_L^2}, \tag{1.11}$$

where $D_L$ is the luminosity distance. We define the luminosity distance in relationship to the absolute magnitude, $M$, and the apparent magnitude, $m$, of the object, as follows:

$$D_L = 10^{\frac{(m-M)}{5}+1}, \tag{1.12}$$

where $m$ is related to $M$ through the relationship between the redshift and magnitude of an object, which is defined as:

$$M = m - 5(\log D_L - 1). \tag{1.13}$$

The redshift-magnitude relation thus shows that the apparent magnitude of an object increases with distance, such that more distant sources appear fainter. The luminosity distance is most useful for observations of nearby objects (e.g. within the Milky Way). Beyond this regime, factors like the redshift, the curvature of spacetime, and time dilation can all affect the apparent magnitude of an object and must necessarily be taken into account.

## 1.2 The Λ-CDM Model

Λ-CDM is currently the standard model of cosmology because it is the simplest model capable of explaining the structure of the Universe. It assumes that general relativity is the correct description of gravity, and on large scales, it follows the cosmological principle. It characterizes the Universe as being primarily 'dark', a term that refers to quantities that we have not yet directly detected but whose presence and effects are consistent with observations. Figure 1.3 shows our current understanding of the energy distribution of the Universe based on observations from the Planck space observatory, which mapped the CMB with high sensitivity. The results from Planck show that the Universe is mostly comprised of dark energy and dark matter, where dark energy (described by the cosmological constant $\Lambda$) drives the expansion of the Universe, and dark matter comprises most of the matter. However, direct detections of dark matter have not yet been successful, and so the exact nature of these particles are still in question. The Λ-CDM model represents them as 'cold' dark matter, or a non-relativistic fluid of massive collisionless particles that only interact through gravity.

The model also incorporates the concept of cosmological inflation to explain the expansion history of the Universe (Achúcarro et al. 2022). Inflation describes a period of exponential accelerated expansion within $10^{-29}$ s of the Big Bang, which

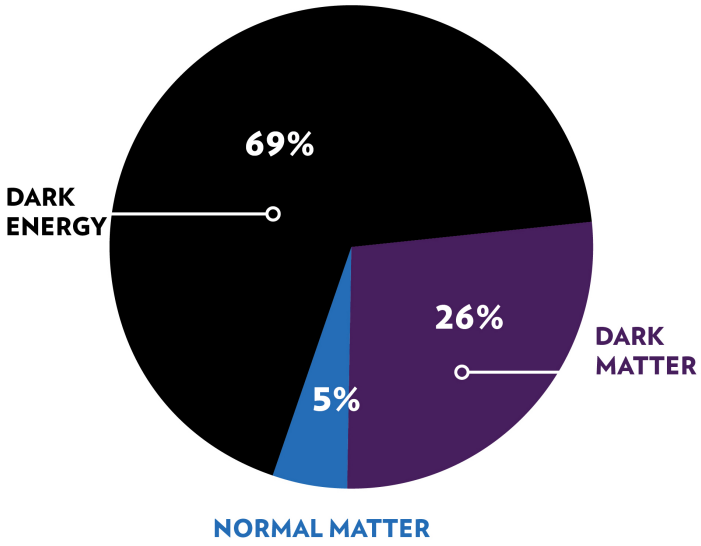


Figure 1.3: The latest results from the Planck 2016 survey (Planck Collaboration et al. 2016) estimate the energy distribution of the Universe. Most of the Universe is made up of dark energy and dark matter; baryonic matter represents only a small fraction of the total distribution. (Image credit: NASA/CXC/K.Divona)

rapidly stretched out space in a manner that smoothed out any initial inhomogeneities over very large length scales, which allows for the Universe to achieve spatial flatness and for disconnected regions of space to be homogeneous. This theory also explains the evolution of large scale structure, as these small initial density fluctuations were spread across the observable length of the Universe by this rapid expansion and grew in magnitude concurrently with the Universe's evolution. However, even though it can compellingly explain the physical structure of the Universe and is supported by observations of small anisotropies in the CMB, inflation has yet to be experimentally confirmed and is thus another assumption rolled into the $\Lambda$-CDM model.

$\Lambda$-CDM successfully predicts a number of cosmological and astrophysical observations, including the accelerating expansion of the Universe, the baryon acoustic oscillation feature, the polarization and anisotropies of the CMB, and the observed abundances of different elements (Weinberg et al. 2013; Planck Collaboration et al. 2016; Abbott et al. 2018). It is thus the present basis for a great deal of work, including this thesis. However, it is not without flaws, and we discuss some of the challenges facing this model in the following section.

### 1.2.1 Cosmological Challenges

Though Λ-CDM is a robust model capable of making many successful predictions, some major issues remain unsolved. One fundamental problem rests with the value of the cosmological constant, Λ: observations of the CMB have been used to measure a value that is in extreme tension with theoretical expectations (at least 60 orders of magnitude; see Copeland et al. 2006). Other major observational issues include the Hubble tension, while on smaller scales (i.e. hundreds of kpc and below), several discrepancies appear that clash with observations. The complete list of challenges facing Λ-CDM is extensive, and for a full review we refer the reader to Perivolaropoulos & Skara (2022). We discuss a few of the more compelling criticisms below.

#### The Hubble Tension

We have shown in previous sections that the Universe is expanding, and that the rate of the expansion can be related to the distance of objects relative to an observer with the Hubble constant $H_0$ (see Equation 1.1). The Hubble constant thus determines the rate of the expansion. However, the exact value of the Hubble constant is currently under debate, as different measurements of independent astronomical sources yield conflicting values.

The way to obtain the Hubble constant has for a number of years been through observations of Cepheid variable stars, a type of bright star whose luminosity changes on a regular period. Recent measurements of $H_0$ using observations of Cepheids with the Hubble Space Telescope (*HST*) made by the SH0ES collaboration have returned a value of $\approx 73\ km\ s^{-1}\ Mpc^{-1}$ (Riess et al. 2022b). Another way is to indirectly infer $H_0$ from measurements of the angular scale of fluctuations of the CMB, which are calculated using the Λ-CDM model. Recent results from Planck put this value at $H_0 \approx 67\ km\ s^{-1}\ Mpc^{-1}$ (Aghanim et al. 2020). The difference between these values constitutes a tension of about $5\sigma$, which is concerning when CMB measurements should be consistent with local observations according to the predictions of the Λ-CDM model. This tension is currently being investigated to rule out potential sources of error, such as systematic error in the *HST* photometry

of Cepheids that might arise from observations in the near-infrared, as *HST* does not perform well in this region of the spectrum. However, recent results from the James Webb Space Telescope (*JWST*), which excels at probing the infrared, agree with (*HST*) measurements, ruling out this specific systematic error as a source of this tension (Riess et al. 2023).

The failure of Λ-CDM to resolve the Hubble tension has led to the need for new physics to be proposed, including alternative descriptions of gravity (e.g. Famaey & McGaugh 2012) and physics that changes between the early and late epochs of the Universe (e.g. Poulin et al. 2019). However, none of these proposals have yet to explain as many observations as Λ-CDM, and so it is still considered the standard for cosmology despite the significance of the Hubble Tension.

### The Missing Satellites Problem

The missing satellites problem describes the discrepancy between the number of predicted halo substructures in collisionless N-body simulations, which are designed to reproduce the Universe according to the physics of the Λ-CDM model and are thus a primary way to evaluate the predictions of the model, and the number of observed dwarf galaxies in the Local Group. This problem originated from the Λ-CDM prediction that we should see around 500 satellite galaxies (Mateo 1998), but we only observe around 50 (Moore et al. 1999). Recent simulation studies (Sales et al. 2022; Jung et al. 2024) seem to suggest that CDM models that include accurate baryonic feedback processes solve this problem at the scale of the Local Group and Milky Way. However, there is still some disagreement about the universality of this resolution, as the problem may still remain in galaxy cluster environments (Hashimoto et al. 2022), and another recent study claims that there are actually too *many* dwarf galaxies in M83 (Müller et al. 2024). These differing results suggest that more theoretical work on this problem is needed to reach an accurate resolution.

### The "Too Big To Fail" Problem

A potentially related issue is the Too Big To Fail problem, which is the inconsistency between the observed central mass of bright satellite dwarf galaxies and the Λ-CDM

predictions of their dark matter subhalo masses. This mismatch between the mass inferred from the kinematics of the galaxies and the predicted mass from Λ-CDM depends on subhalo structure, and could potentially change depending on the central shapes of the density profiles of these satellite galaxies (Garrison-Kimmel et al. 2014). Possible solutions to this problem include alternative models of dark matter, including self-interacting dark matter, which assumes that dark matter particles have strong interactions with other particles, and fuzzy dark matter, which treats dark matter particles as ultralight scalar particles. I discuss these alternative models of dark matter in more detail in Section 1.3.1.

### The "Core-Cusp" Problem

The core-cusp problem refers to the tension between collisionless N-body simulations of dark matter (DM) halo profiles and their observed values. Simulations have generally predicted DM distributions that increase toward the center following the shape of the Navarro-Frenk-White (NFW) profile (Navarro et al., 1996), where the DM density, $\rho_{\rm DM}$, increases as $\sim r^{-\gamma}$, where the inner slope, $\gamma$, is equal to 1. However, this cusp-like increase is not always seen observationally, where a core-like profile tends to be favored. A visual example of this discrepancy can be seen in Figure 1.4. This tension exists across all scales, from dwarf galaxies to galaxy clusters, and does not seem to have an easy solution as observational measurements have been made that both disagree and agree with simulations. For example, recent work in Cooke et al. (2022) measured cuspy DM density profiles in six massive dwarf galaxies that were in agreement with predictions from the FIRE (Hopkins et al. 2014) and NIHAO (Wang et al. 2015) simulations, which are cosmological simulations designed to study galaxy formation. FIRE focuses on including stellar feedback processes and 'an explicit treatment of the multiphase interstellar medium', and models galaxies with halo masses $\sim 10^8 - 10^{13} M_\odot$. NIHAO is also a hydrodynamical simulation concentrating on galaxy formation, and uses halo masses between $\sim 10^9 - 10^{12} M_\odot$. Oh et al. (2015), on the other hand, measured 26 low mass dwarf galaxies ($\sim 10^8 - 10^9 M_\odot$) and found much more core-like values ($\gamma \sim 0.3$). These discrepancies may point to the need for a range of profiles to describe DM halos,

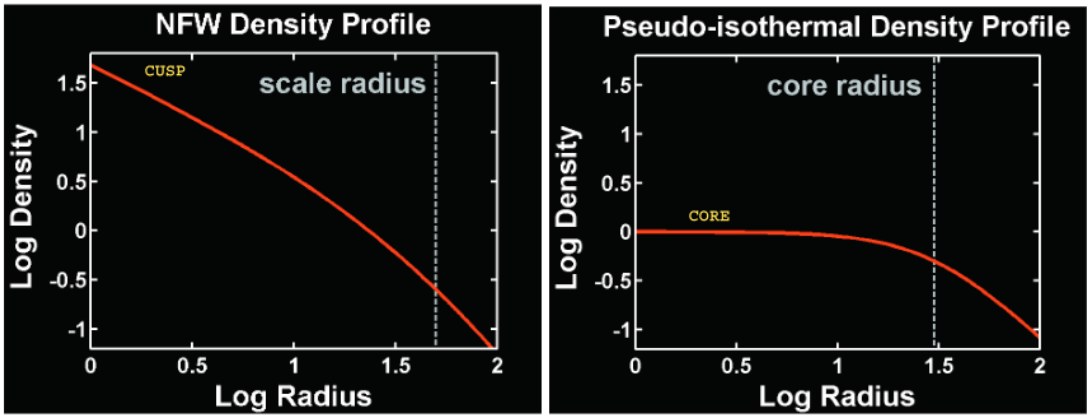


Figure 1.4: Visual example of the core-cusp problem. The NFW profile on the left, which corresponds to simulation measurements, is cuspy. The dotted vertical line corresponds to the profile's scale radius. The right profile, which corresponds to observational measurements, is cored. The vertical dotted line denotes the profile's core radius. Figure reproduced from Del Popolo & Le Delliou (2022).

rather than the 'one-size-fits-all' approach currently used in Λ-CDM (Del Popolo & Le Delliou 2022). Alternative forms of dark matter may also be a possible solution.

## 1.3 Dark Matter

In Λ-CDM, dark matter accounts for 85% of the total mass of the Universe. Quantifying the nature of its existence is thus of great importance, though this is made difficult by our inability to directly detect it. Current theories speculate that dark matter is composed of subatomic particles, and experimental searches for DM have largely concentrated on weakly-interacting massive particles (WIMPS), which are heavy, electromagnetically neutral, and slow moving particles, and axions, which are also slow moving and electromagnetically neutral, but are different from WIMPS because they are lightweight. Particle colliders like the Large Hadron Collider (LHC) at the European Organization for Nuclear Research (CERN) are used to run these experiments by colliding protons together and analyzing the composition of the resulting impact to search for dark matter subatomic particle candidates (Aad et al. 2024). From an astrophysical perspective, though we have failed to detect dark matter directly so far, we can make numerous observations that offer (indirect) evidence for its existence, and in so doing can place constraints on how it has shaped the

structure of the observable Universe.

### 1.3.1 Dark Matter Candidates

There are currently several theories regarding the characteristics of dark matter. They are separated based on their interactions with other particles, and by their velocities relative to the speed of light, where 'cold' dark matter moves slowly, and 'hot' dark matter moves close to the speed of light, and 'warm' dark matter is somewhere in between. These velocities affect the characteristic distance over which DM particles free-stream before gravitational collapse occurs, and consequently determine how large-scale structures are formed. Comparing the predictions from these models to the observations of the Universe today can thus help to determine the most likely model(s). I discuss three proposed forms for DM below.

#### Cold Dark Matter

CDM is the simplest model that can explain the most astrophysical observations, which is why it is incorporated into Λ-CDM. The theory of CDM casts dark matter as a weakly interacting particle moving at speeds which are generally insufficient to smooth out the formation of structure. As a result, the formation history of the Universe allows for matter to clump together, and structure formation occurs hierarchically as small groups of matter merge together to form the large structures we can observe today, like galaxy clusters and the 'cosmic web', which is the largest structure in the Universe and is composed of interconnected filaments comprised mostly of dark matter. These filaments are traced by clustered galaxies and gases and stretch across the breadth of the Universe. A visual example of the cosmic web can be seen in Figure 1.5. While CDM does remarkably well at explaining current observations of the Universe, the tensions discussed in the previous sections highlight some of its more prominent issues, demonstrating that more work is needed before we arrive at an accurate description of the physics of our Universe.

Since we have not directly detected any dark matter particles, the description of CDM is still open to alternative formulations. One such model is 'fuzzy' cold dark matter (FDM), which was proposed to solve the core-cusp problem (Hu et al. 2000).


Figure 1.5: Image of the cosmic web, as taken from the Illustris Collaboration simulation suite (Vogelsberger et al. 2014). The filamentery structures represent the distribution of dark matter, galaxies, and gas, which are strung together in these structures rather than being uniformly scattered throughout space. The regions in between the filaments are mostly devoid of matter, and as such are called cosmic voids. Regions where filaments intersect, such as in the center of the image, produce large concentrations of matter that can form massive galaxy clusters.

FDM retains most of the properties of CDM, with the addition that the particles are characterized as ultralight scalar particles whose wave behavior would stabilize gravitational collapse and prevent the formation of cuspy halos. FDM halos are instead composed of a central core and are surrounded by an outer envelope that is similar in structure to a CDM halo. FDM also produces galaxy formation at a later time in the Universe than CDM, but still creates high-redshift galaxies and late reionization at a time consistent with Planck observations (Hui et al. 2017).

### Warm Dark Matter

Warm dark matter (WDM) is another potential DM candidate, theorized to be a weakly interacting particle moving at faster speeds than CDM, such that while structure formation in the Universe still occurs hierarchically, the formation of low mass haloes is suppressed and occurs at a more delayed rate compared to CDM (Dodelson & Widrow 1994; Moore et al. 1999). WDM largely agrees with CDM on concepts like hierarchical structure formation, temperature fluctuations in the CMB, and the clustering of galaxies (Cole et al. 2005; Komatsu et al. 2011). However, WDM provides a potential solution small-scale tensions like the 'too big to fail' problem (see discussion in Section 1.2.1) because it forms structures at a later time than CDM, which changes the central densities of halo masses to values lower than CDM that are more consistent with observational mass measurements (Avila-Reese et al. 2001; Lovell et al. 2012). These later structure formations are, however, still consistent with high-redshift galaxy formation and observational CMB fluctuations as measured with Planck (Lovell et al. 2014. WDM also offers an alternative solution to the Missing Satellites problem (see discussion in Section 1.2.1) for the same reasons, as the later collapse of the halos in the evolution history of the Universe results in fewer subhalos than predicted by CDM, at a number that is more consistent with observations (Kim et al. 2018). However, more theoretical work and observations of dwarf galaxies are needed to test this model and unify simulation results with observational information.

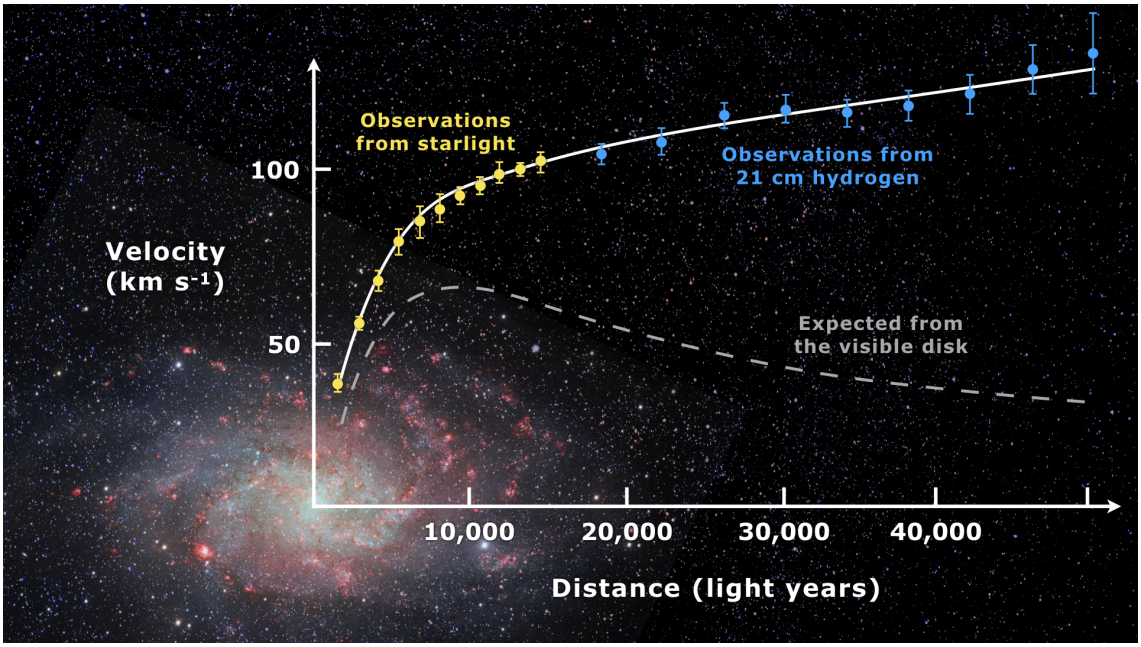


Figure 1.6: Rotation curve of M33, which clearly shows the effect that dark matter has on the observed measurements of the galaxy. The gap between the curve expected from the disk of visible matter and the observations made with stellar mass measurements (yellow points) and gas measurements (blue points) can be filled by adding a dark matter halo to the galaxy. (Image credit: Mario De Leo, Wikimedia Commons)

### Self-Interacting Dark Matter

Where the previous two types of dark matter are characterized by weak interactions with themselves and with other matter, self-interacting dark matter (SIDM) has strong interactions with other DM particles. It was proposed in 2000 as a potential solution to the core-cusp problem (Spergel & Steinhardt 2000), which it can resolve due to the larger self-scattering length of SIDM particles, which scatters DM particles outside of halo centers and makes the central density profile more cored, in line with observations (Tulin & Yu 2018). It can also explain the too big to fail problem through these reduced central density profiles (Vogelsberger et al. 2012). The self-scattering effect also suppresses the subhalo mass function on the galaxy scale, which solves the missing satellites problem. It also tends to work well with observations made using gravitational lensing, and is one of the more popular alternatives to CDM currently being researched (Robertson et al. 2019; Dutta & Mahapatra 2024).

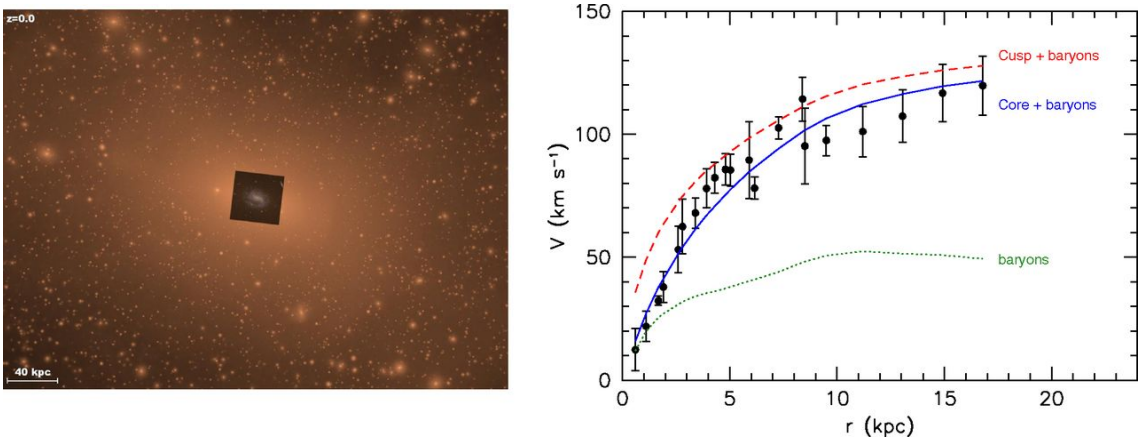


Figure 1.7: Left: Optical image of the galaxy F568-3, from the Sloan Digital Sky Survey, superimposed on the dark matter density distribution from the "Via Lactea" cosmological simulation of a CDM halo with a similar mass. Right: Measured rotation curve of F568-3 (points) plotted against the predicted fits assuming a cored halo (blue line) and a cuspy halo (red dashed line), assuming Λ-CDM cosmology for both. The discrepancy illustrates how the core-cusp problem appears within observational data. Figure reproduced from Weinberg et al. (2015).

### 1.3.2 Dark Matter Probes

The most accurate dark matter model is one that can reproduce the most pieces of observational evidence. The core-cusp problem, which has led to the introduction of two separate dark matter candidates, is a particularly tantalizing observable case to solve. We can study this tension by measuring the density profile of DM within massive objects and comparing that to predicted results from simulated Universes. One way to do this is by examining the rotation curves of galaxies, which flatten out as distance from the center increases. If dark matter did not exist, then these curves would not flatten out in this way and would decrease more rapidly with distance, but since we see flat curves, we must assume that a non-negligible (invisible) mass is distributed around the galaxies, as the amount of observable stars and gas would not be enough to account for this behavior. This behavior was first observationally characterized by the astronomer Vera Rubin (Rubin et al. 1980), and an example of her findings is represented visually in Figure 1.6. One specific way rotation curves are used today to study dark matter is shown in Figure 1.7, which illustrates how the core-cusp problem can be visibly identified by measuring rotation curves in galaxies. The separation between the cored and cuspy models and their match to

the observational data is distinct, demonstrating how we use observables to constrain our theoretical cosmological models.

We can also use the large-scale structure of the Universe to study different dark matter models. The ability of simulations to reproduce the large filaments of matter we observe in the Universe (the 'cosmic web') can be tested through simulations like the MillenniumTNG project (Pakmor et al. 2023b), a large-scale cosmological hydrodynamical simulation suite. Figure 1.8 shows an example of how large-scale structure can be modeled using simulations. MillenniumTNG is a recent effort to study dark matter and structure formation at scales comparable to large observational surveys like the Dark Energy Survey (DES; Dark Energy Survey Collaboration et al. 2016), which was designed to characterize dark energy and dark matter through observations of large-scale structure, cluster counts, weak gravitational lensing, and supernovae; the Dark Energy Spectroscopic Instrument (DESI) Legacy Imaging Surveys (Dey et al. 2019), which were designed to image 14,000 square degrees of the extragalactic sky; and Euclid, a space-based survey mission from the European Space Agency designed to examine dark energy and dark matter through observations of weak gravitational lensing and baryonic acoustic oscillations (Laureijs et al. 2011). MillenniumTNG is also capable of being used to study the full expanse of galaxy clusters, which is useful because clusters are some of the best places in the Universe to observe dark matter.

## 1.4 Galaxy Clusters

Galaxy clusters, with masses above $10^{14} M_{\odot}$ and sizes on the order of several Mpc, are the largest observable gravitationally-bound objects in the Universe, which means they constitute a kind of endpoint for hierarchical structure formation. They are thus ideal cosmic laboratories for studying the properties of baryonic and dark matter, and can serve as constraints on our cosmological model of the Universe (see Allen et al. 2011 for a full review). For instance, the number density of galaxy clusters is sensitive to the rate of the Universe's expansion and can thus be used as a tracer to probe different cosmological models. This number density, which depends on redshift

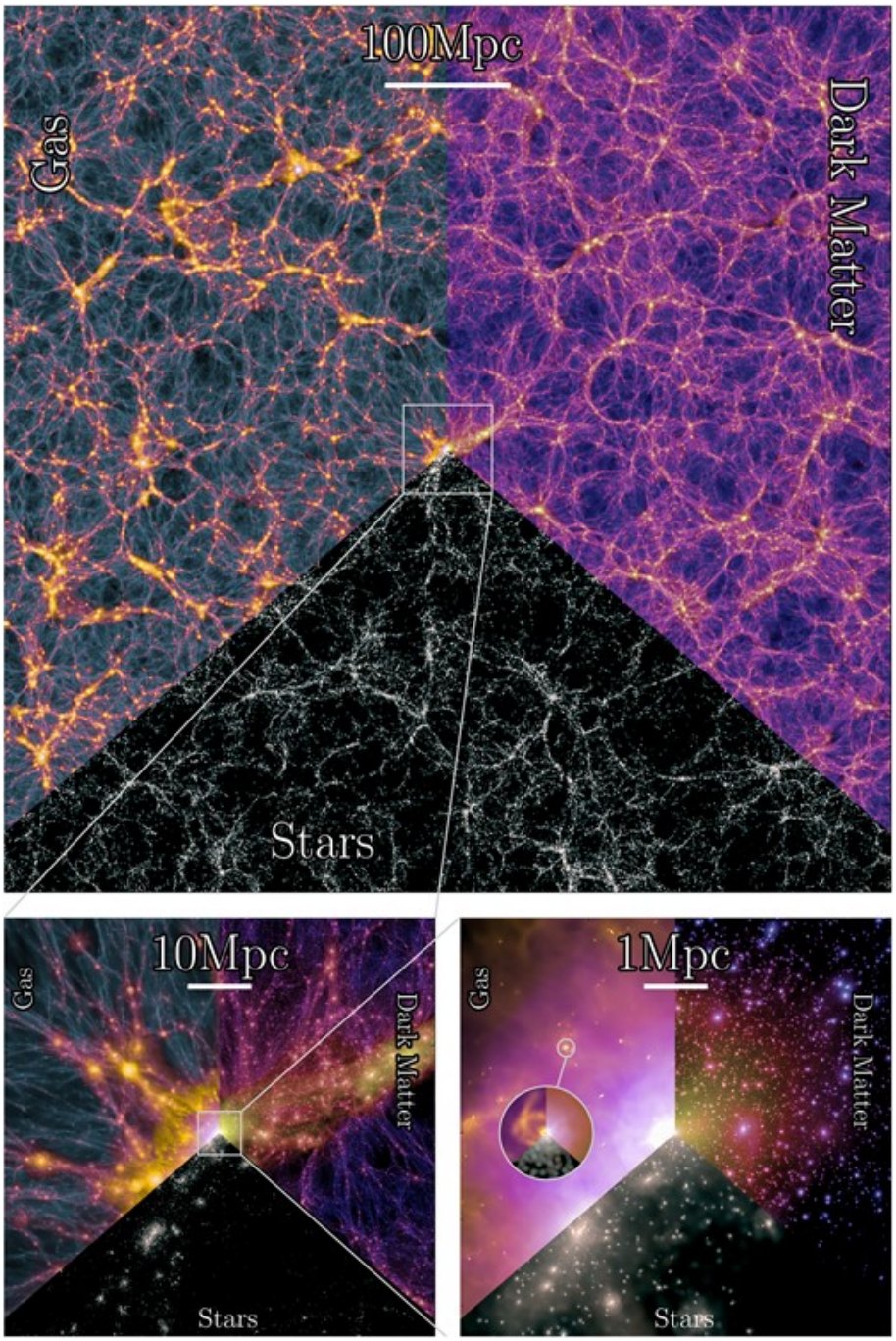


Figure 1.8: Large-scale structure of the Universe as shown with the MillenniumTNG simulations project. The center image shows projections of gas (top left), dark matter (top right), and stellar light (bottom center) at a depth of 10 Mpc (i.e. at the scale of a galaxy cluster) at $z = 0$. The left inset shows the range of scales of the simulation, from a 740 Mpc box on the bottom left to an individual spiral galaxy on the bottom right. Reproduced from Pakmor et al. (2023a).

as $n(M, z)$, effectively shows how matter in the Universe has evolved over time, and relies on how we describe the evolution of the density perturbations responsible for the formation of clusters. Observationally constraining the number density of clusters, and thereby constraining the cosmological parameters of the Universe, thus relies on the measurement of cluster masses at different redshifts. This is not so straightforward a task, however.

Cluster masses are generally described using a Navarro-Frenk-White (NFW) profile, which is a universal profile of dark-matter haloes derived from high-resolution N-body simulations (Navarro et al. 1996). The NFW profile describes the radial density as follows:

$$\rho_{NFW}(r) = \frac{\rho_0}{(r/r_s)(1 + r/r_s)^2}, \tag{1.14}$$

where $\rho_0$ is a characteristic scale density defined at a corresponding scale radius, $r_s$. $\rho_0$ can be related to the critical density of the Universe, $\rho_c = \frac{3H(z)^2}{8\pi G}$, through the scale factor $\delta_c$, which varies per halo. The scale radius is defined as $r_s \equiv r_{200}/c$, where $r_{200}$ is defined as the radius at which the spherically-averaged mass density reaches 200 times the critical mass density. The scale radius describes the characteristic radius where $\rho_{NFW}(r) \propto r^{-2}$. $c$ is a dimensionless number known as the concentration parameter, which varies based on the halo mass and is defined in relation to the scale radius for some radius $r$ as $c = r/r_s$.

Fitting the observed density profile of the cluster to this form allows for the derivation of the cluster's mass, which is calculated for a sphere of radius $R$ as:

$$\begin{aligned} M_{NFW}(r) &= 4\pi \int_0^R \rho_{NFW}(r)\ r^2\, dr \\ &= 4\pi\rho_0 r_s^3 \left[ ln(1 + \frac{R}{r_s} - \frac{R/r_s}{1 + R/r_s} \right]. \end{aligned} \tag{1.15}$$

This mass is divergent, so the edge of the halo is usually set to be the equivalent to the virial radius $R_{vir}$, which can be related to the scale radius $r_s$ as $R_{vir} = cr_s$. Integrating over these bounds thus gives the mass of the halo as

$$M = 4\pi\rho_0 r_s^3 \left[ ln(1+c) - \frac{c}{1+c} \right]. \tag{1.16}$$

The general shape of the NFW profile is plotted in the left-hand box of Figure 1.4. The mathematical form of the profile shows that the central mass density and total mass are infinite, though the mass of the cluster can still be measured within the virial radius.

Numerical simulations use the NFW profile to construct mass haloes for dark matter because it can be fitted to a variety of different mass distributions, from $10^9 - 10^{15} M_\odot$, with no apparent discontinuities. However, the assumed universality of the NFW profile is based on its performance in simulations, where quantities like the scale radius and the concentration of the halo can be definitively measured. In practice, these parameters can be challenging to measure with accuracy due to the inherent difficulty of constraining complicated mass distributions based on observational data. The usual (and easiest) way to obtain the parameters for an NFW fit is by using gravitational lensing.

## 1.5 Gravitational Lensing

Gravitational lensing occurs as a consequence of the theory of general relativity. According to the theory, an object of sufficient mass will interact with its local volume of spacetime, creating distortions in the otherwise regular spacetime lattice structure. As light rays emitted from a more distant source travel close to the object, they experience these distortions, altering their initial (straight line) trajectory to follow a curved path known as a geodesic. As a result, the light will appear visibly distorted in the vicinity of the massive object, according to the perspective of an observer along the line of sight. Quantifying the shape of these distortions provides information about the mass distribution responsible for their creation. Lensing is thus a powerful tool for tracing mass distributions, and it is independent of dynamical interactions and other processes since it is purely geometric. The strength of the distortions defines two types of lensing, which I discuss below.

### 1.5.1 Strong Gravitational Lensing

A light ray passing by a body of mass $M$ will be deflected by this mass according to the principles of general relativity. Solving for the form of the deflection can be done by using the Schwarzschild metric, and yields a description of the path traveled by the light ray. The deflection angle of the mass is given by the 'Einstein angle',

$$\alpha = \frac{4GM}{c^2 b}, \tag{1.17}$$

where $b$ is the impact parameter. This equation is valid when $b$ is much larger than the Schwarzschild radius $R_s = 2GM/c^2$. A light ray that passes by the mass $M$ at a distance $b$ is thus deflected by an angle $\alpha$. As the observer, our ability to see this deflection is given by the relative geometry of our position, the position of the mass $M$, and the starting position of the light ray.

In observational astrophysics, we are typically concerned with very small deflection angles (for example, angles that are visible in the field of view of a telescope). We can thus make use of the optical principle known as the thin lens approximation, which assumes an instantaneous deflection of light when it encounters the lens, and also assumes that the distances between the observer and the lens and source are much larger than the size of the lens itself. This latter assumption is always valid for galaxy clusters. With this approximation, we can flatten into planes the three regions of interest in this geometry: the source plane, or the origin of the light rays; the lens plane, or the mass $M$ that causes the deflection; and the observer plane, which describes our present location on Earth or in space, depending on the telescope used to make the observations. We also assume that the lens plane is transparent, which means that light from background sources always has some way to reach us as the observer, as there are theoretically an infinite number of paths for the light to travel if the lens plane is transparent.

This geometry is illustrated in Figure 1.9, and can be described with the lens equation,

$$\beta = \theta - \frac{D_{LS}}{D_s}\hat{\alpha}(b), \tag{1.18}$$

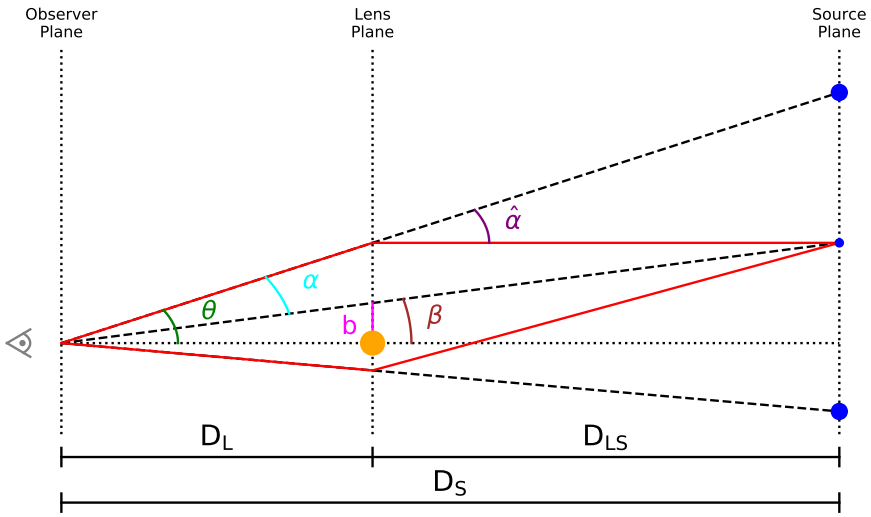


Figure 1.9: Visual representation of the lensing equation, demonstrating the geometry of how multiple images appear to an observer on the left-hand side of the image. The variables correspond to those presented in Equations 1.17, 1.18, and 1.19. Image reproduced from Johnson (2018).

where $\beta$ is the position of the source in the source plane, $\theta$ is the position of the image in the image plane, $D_s$ describes the angular diameter distance between the observer and the source, $D_{LS}$ is the angular diameter distance of the source from the lens, and $D_L$ is the angular diameter distance between the observer and the lens. $\hat{\alpha}(b)$ corresponds to the reduced deflection angle, which is defined as

$$\hat{\alpha}(\theta) = \frac{D_{LS}}{D_S}\alpha(\theta). \tag{1.19}$$

The alignment of the matter distribution of the lens and the position of the source relative to the observer plane may result in more than one possible distance $b$. This will result in multiple images of the source appearing at several positions in the field of view, a phenomenon known as strong gravitational lensing.

The strength of the lens can be characterized by the Einstein radius, which is calculated for $\beta = 0$, i.e. for a source that is perfectly aligned with the center of the lens, as

$$\theta_E = \frac{D_{LS}}{D_s}\hat{\alpha}(b). \tag{1.20}$$

If we substitute Equation 1.17 for $\hat{\alpha}$, we can rewrite the Einstein radius purely in terms of the relative distances and the mass of the lens as

$$\theta_E = \sqrt{\frac{4GM(\theta_E)}{c^2}\frac{D_{LS}}{D_s D_L}}, \tag{1.21}$$

which describes the angular deflection of a lens. This equation shows that the probability of a background source being lensed is only dependent on the *total* mass of the lens and that a larger mass will result in a larger Einstein radius. Additionally, in the case of a circularly symmetric lens, the probability of a source being lensed is not affected by the specific mass distribution.

We can make one more modification to the lensing equation to directly relate the deflection angle to the mass of the lens. The path that light travels is described by the gravitational potential of the local area it passes through, and in the case of lensing, we call this the lensing potential, $\varphi$, which is a lensing-normalized version of the local Newtonian gravitational potential and is defined as

$$\varphi = \frac{2D_L D_{LS}}{c^2 D_S}\nabla_\phi(\theta), \tag{1.22}$$

where $\phi$ is the projected 3D Newtonian potential, $\Phi_{3D}$:

$$\phi(\theta) = \int \Phi_{3D} dz. \tag{1.23}$$

We can thus rewrite the lens equation in terms of the lens potential $\varphi$ at the image position $\theta$ as

$$\beta = \theta - \nabla_\theta \varphi(\theta). \tag{1.24}$$

I have said already that there can be multiple solutions to the lensing equation, which results in the production of multiple images of the same background source. The images of this source undergo a mathematical transformation due to the effects of lensing, which can be thought of as a change in the shape of the image in the

source plane to the observed shape in the image plane. One side effect of this transformation is that the ratio of the surface of the lensed image increases relative to its source, and since lensing conserves surface brightness, this results in a net increase in flux of the lensed image, which can be described by the magnification, $\mu$, of the source. The value of $\mu$ can be computed from the magnification matrix, $A$, which is conventionally written as

$$A^{-1} = \begin{pmatrix} 1-\kappa-\gamma_1 & -\gamma_2 \\ -\gamma_2 & 1-\kappa+\gamma_1 \end{pmatrix}, \tag{1.25}$$

where $\kappa$ is the convergence, and the term $1-\kappa$ describes the isotropic deformation, while $\overrightarrow{\gamma} = (\gamma_1, \gamma_2)$ is the shear vector, which describes the anisotropic deformation. The two $\gamma$ components are mathematically defined in relation to the center of mass. We can write $\gamma$ and $\kappa$ as

$$\begin{aligned} \gamma_1 &= \frac{1}{2}\left(\frac{\partial\alpha_1}{\partial\theta_1} - \frac{\partial\alpha_2}{\partial\theta_2}\right) = \frac{\partial_{yy}\varphi - \partial_{xx}\varphi}{2} \\ \gamma_2 &= \frac{\partial\alpha_1}{\partial\theta_2} = \frac{\partial\alpha_2}{\partial\theta_1} = \partial_{xy}\varphi \end{aligned} \tag{1.26}$$

and

$$\kappa = \frac{1}{2}\nabla_{ij}\alpha_{ij} = \frac{\nabla\varphi}{2} = \frac{\Sigma}{\Sigma_{crit}}, \tag{1.27}$$

where $\Sigma$ is the projected surface mass density and $\Sigma_{crit}$ is the critical surface mass density, which is defined in relation the relative distances as

$$\Sigma_{crit} = \frac{c^2}{4\pi G}\frac{D_S}{D_L D_{LS}}. \tag{1.28}$$

An observed region where the surface mass density is equal to or exceeds this critical value is more likely to produce multiple images of background galaxies; when multiple images are observed, the lens is called a *strong* lens. When the surface mass density is much smaller than the critical density, multiple images cannot be produced, but lensing still occurs; in these cases, the lens is called a *weak* lens. The

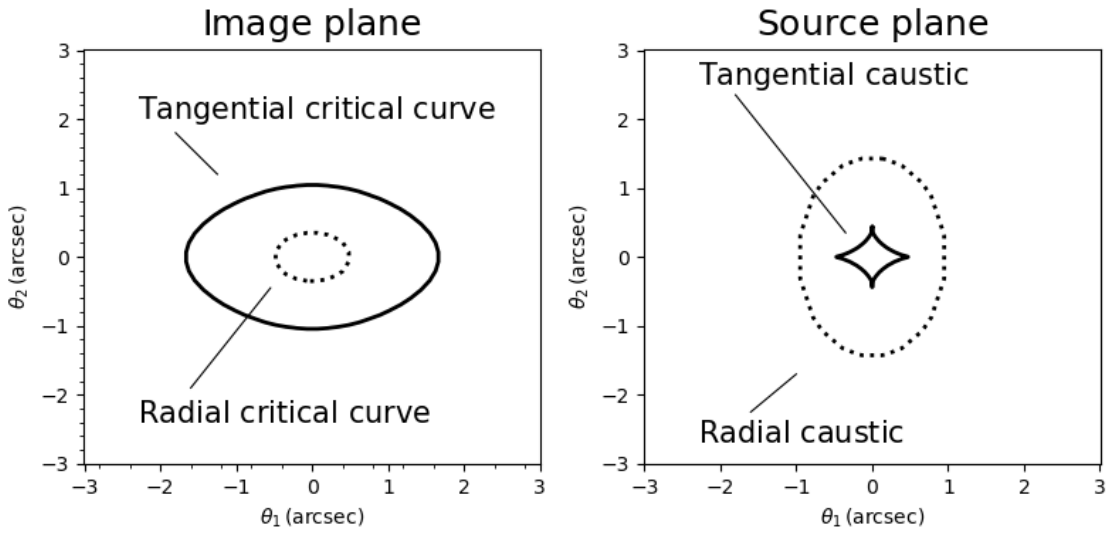


Figure 1.10: Diagram illustrating the positions of the tangential critical curve and radial critical curve in the image plane. The tangential and radial caustic lines swap positions in the source plane relative to the tangential and radial critical lines in the image plane. Image reproduced from Bovy 2023 (in prep.).

lensing effect will vary depending on where the source is in relation to the lens, such that the most effective lenses will be placed at a distance that is roughly less than half the source redshift.

The magnification $\mu$ of a multiple image is then computed as the determinant of $A$ and written in terms of $\kappa$ and $\gamma$ as

$$\mu^{-1} = det(A^{-1}) = (1-\kappa)^2 - \gamma^2. \tag{1.29}$$

The two locations in the image plane where $\mu^{-1} = 0$ have infinite magnification and are called 'critical lines', referring to two closed non-intersecting lines. The same locations in the source plane are called 'caustic lines', and are similar to their image plane counterparts save for the fact that they can intersect. The two critical lines are distinguished from each other by their positions relative to the center of the mass distribution: the external critical line produces tangential deformations and is thus called a 'tangential critical line', while the internal critical line produces radial lines and is referred to as the 'radial critical line'. This geometry is visualized in Figure 1.10.

The critical lines are the method we use to understand the mass distribution

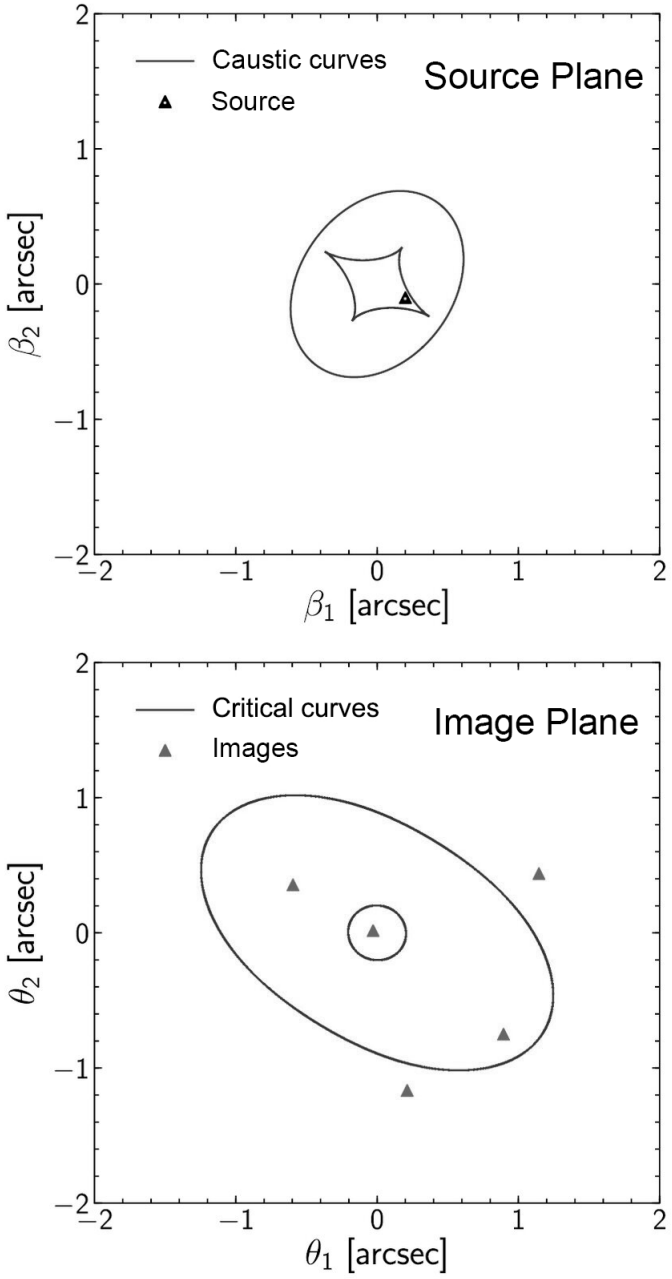


Figure 1.11: An example of the configuration of multiple images. The top panel shows the source plane and plots both caustic lines and the location of the source as the triangle with a black square at the center. The bottom panel shows the image plane and plots both critical curves, as well as the locations of the multiple images, which are shown as light gray triangles. Five images are produced in this configuration. Figure reproduced from Oguri (2019).

responsible for lensing. In the simplest case of a circularly symmetric mass distribution, the projected mass enclosed within a radius $r$ can be written as

$$M(r) = \frac{c^2}{4\pi G}\frac{D_S D_L}{D_L S} r\partial_r\varphi(r) = \pi\Sigma_{crit} r\partial_r\varphi(r). \tag{1.30}$$

The tangential critical radius, which is also called the Einstein radius $\theta_E$, can be described with the equation $r_E = \partial_r\varphi(r_E)$. The mass within the Einstein radius is thus given by

$$M(r_E) = \pi\Sigma_{crit} r_E^2. \tag{1.31}$$

The mass concentration of the lens will thus affect the Einstein radius, where larger mass concentrations will increase the size of $r_E$. We can also see that the relative redshifts of the lens and the source will affect $r_E$. Perhaps the most important takeaway message, however, is that the total projected mass enclosed within a circular aperture can be precisely measured from the location of the tangential critical curve. The radial critical curve offers information about the slope of the mass profile near the cluster center, as can be seen from its definition:

$$\partial_{rr}\varphi(r) = \partial_r\left(\frac{M(r)}{\pi\Sigma_{crit} r}\right) = 1. \tag{1.32}$$

Accurate redshifts for the source and the lens can thus allow us to derive the shape of the mass distribution in the lens.

Of course, mass distributions are very rarely circularly symmetric. In more complex cases, we cannot analytically determine the position of the critical lines, and must instead rely on numerical methods to solve for the shape of the mass distribution, which are dependent on the type of mass profile one uses during the modeling. I discuss the specific techniques used in this thesis in Section 2.2.

Regardless of the choice of mass profile, multiple images are used to determine the position of the critical lines. This is due to the geometry of their production, such that images of background sources will always appear in predictable configurations around the critical lines for a given lens mass distribution. An example configuration is shown in Figure 1.11. Determining the locations of multiple images is thus the

first step to determining the mass of the lens by mapping out the critical lines. The second step is to determine the redshift of the source and the lens. These two components are crucial to numerically modeling the correct position of the critical lines in the lens. Finally, I note that some images are less likely to be magnified, which makes them difficult to observe. Radial images located around the brightest central galaxy in clusters are particularly difficult to detect due to the light from this galaxy obscuring their presence. I discuss these radial images in Section 3.1.

### 1.5.2 Weak Gravitational Lensing

We have demonstrated how a lens with a sufficient surface mass density and deflection angle can generate multiple images. However, lines of sight where this happens are rare. It is far more common for the deflection angle to be small enough that no multiple images are produced. Additionally, when multiple images are produced, they only appear in the central parts of galaxy clusters and can thus only constrain their central mass. However, every background galaxy in the field of view is still affected by lensing: we call this weak gravitational lensing. In this regime, the shapes of galaxies are distorted; for example, a circular galaxy is distorted to appear as though it has an elliptical light distribution, as shown in Figure 1.12. By measuring how the galaxies in the field of view have been distorted, it is possible to statistically characterize the mass distribution responsible for their creation and extend our ability to map the shape of this distribution out to larger radii.

Weak lensing maps the shape transformation of galaxies from the source plane to the image plane by using the observed shapes of galaxies on a physical detector, such as a Charge Coupled Device (CCD), which counts photons collected from a telescope mirror. This transformation is supported by the fact that surface brightness is conserved by gravitational lensing, such that the surface brightness in the image plane, $I(\theta_I)$, is equivalent to the one in the source plane, $I(\theta_S)$. With this property in mind, weak lensing uses the moments of the light distribution of galaxies to define the shape parameters that describe the lensing distortion. The first moment is used to define the center of the image, $\theta_c$, as

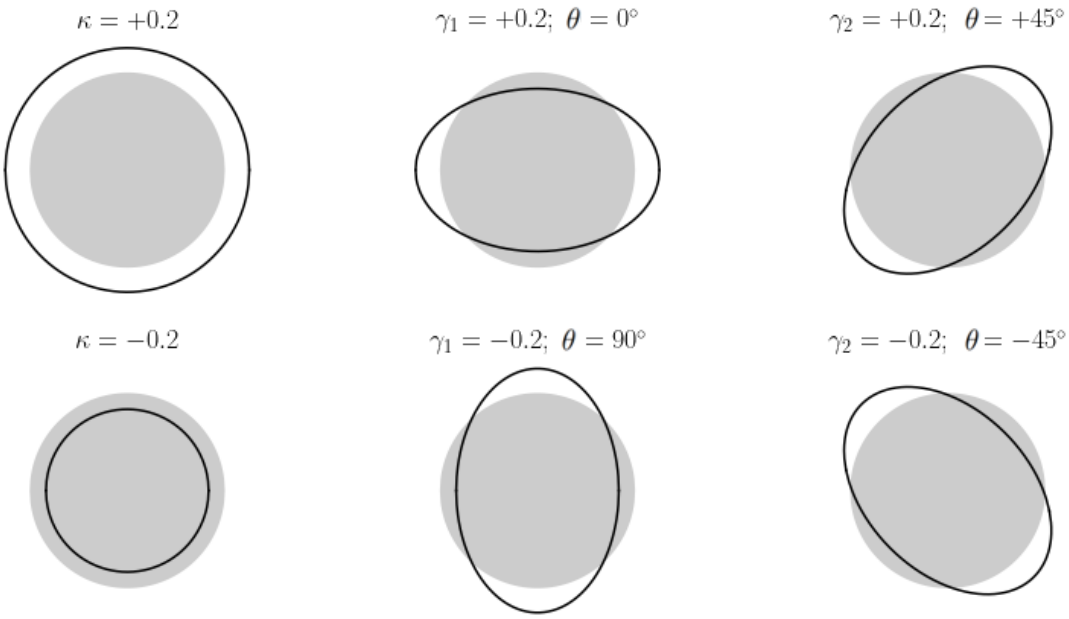


Figure 1.12: Diagram illustrating how convergence ($\kappa$) and shear ($\gamma$) can distort the shape of a circular galaxy into elliptical shapes, depending on the value of the parameters. The position angle of the ellipse is represented as $\theta$. Image reproduced from Bovy 2023 (in prep.).

$$\theta_c = \frac{\int W(I(\theta))\theta d\theta}{\int W(I\theta))d\theta}, \tag{1.33}$$

where $W(I)$ is a weight/window function chosen to make the integrals finite in the case of noisy data. The second moment contains information about the galaxy's size, ellipticity, and orientation, and can be written in its principal axes as:

$$M_{ij} = R_\theta \begin{pmatrix} a^2 & 0 \\ 0 & b^2 \end{pmatrix} R_{-\theta}, \tag{1.34}$$

where $a$ is the semi-major axis, $b$ is the semi-minor axis, $\theta$ is the position angle of the ellipse, and $R_\theta$ is the rotation matrix of $\theta$. This form of the second moment is referred to as the moment matrix. The shape parameter and orientation of the galaxy can be expressed through the complex ellipticity $\varepsilon = 2\epsilon/(1 + |\epsilon|^2)$, where $\varepsilon$ and $\epsilon$ are given as

$$\begin{aligned} |\varepsilon| &= \frac{a^2 - b^2}{a^2 + b^2} \\ |\epsilon| &= \frac{a - b}{a + b} \end{aligned} . \tag{1.35}$$

The lensing effect for weak lensing both magnifies and extends the light distribution of the galaxy along the shear direction, and it can be expressed mathematically in terms of the moment matrix relative to the source plane ($M^S$) and the image plane ($M^I$) as

$$M^S = A^{-1} M^I A^{\intercal -1}, \tag{1.36}$$

where $A^\intercal$ is the transpose of matrix $A$. When $A^{-1}$ is not singular, this equation becomes

$$M^I = A M^S A^\intercal. \tag{1.37}$$

The size of the background galaxy in the source plane, $\sigma_S$, can be described in terms of the magnification factor $\mu$ and the size of the galaxy in the image plane, $\sigma_I$, such that the galaxy is enlarged as

$$\sigma_S = \mathrm{det} M^S = \mathrm{det} M^I \cdot (\mathrm{det} A^- 1)^2 = \sigma_I^2 \cdot \mu^{-2}. \tag{1.38}$$

The lensing transformation of the ellipticity can be mathematically expressed in terms of the reduced shear, $g$, which is given as: $g = \gamma/(1-\kappa)$. In the weak lensing regime, lensing distortions are small (e.g. $|g| << 1$), and the ellipticity in the image plane, $\epsilon_I$, is related to the ellipticity in the source plane, $\epsilon_S$, as

$$\epsilon_I = \epsilon_S + g. \tag{1.39}$$

Measuring the ellipticity of a number of observed background galaxies and averaging over the results can thus yield a measurement of the reduced shear, which in turn allows for the calculation of the mass through the parameters $\kappa$ and $\gamma$ as shown in the preceding section. I refer the reader to Bartelmann & Schneider (2001) for a

full review of weak lensing.

Finally, I note that the lensing-based mass measurement of the full expanse of a galaxy cluster (i.e. a mass measurement that extends beyond $> 1000kpc$) is only possible with weak lensing. Ideally, strong lensing is used as well to better constrain the central mass distribution (i.e. within $\sim$ 200 kpc). From a lensing perspective, constraining the mass of the entire cluster by applying an NFW profile (Equation 1.14) is thus only possible through weak lensing. This is because the scale radius, $r_s$, is much larger than the region constrained by strong lensing, and a mass map built by strong lensing will thus be unable to account for the precise distribution of mass representing the scale radius. I discuss this more thoroughly in Chapter 2.

# CHAPTER 2

## Probing the Inner Density Profile of Galaxy Clusters

I have discussed the tensions that the Λ-CDM cosmological model is currently facing in the previous chapter. In this thesis, I am interested in examining one of these tensions on some of the largest cosmological scales by examining the core-cusp tension in the context of galaxy clusters. I am interested in this regime because I can probe the inner profile of galaxy clusters using strong gravitational lensing, and thereby obtain a mass measurement in the interior of clusters that is independent of everything but the mass distribution of the cluster itself. Precisely and accurately determining the distribution of dark matter in the inner part of several galaxy clusters is the goal of this thesis, and in the following sections I will discuss this tension in clusters, how I model it, and how I account for systematic errors in the measurement that can affect the value of the DM inner profile slope.

## 2.1 The Core-Cusp Tension in Galaxy Clusters

The core-cusp tension is often characterized as a problem with the dark matter haloes of dwarf galaxies. These objects are typically used as a point of reference because their low baryonic mass content means that their profiles are essentially dominated

by dark matter. As a result, measurements of their density expose the core-cusp tension more easily than other, bigger galaxies, where effects of mixing between dark matter and baryons becomes more pronounced. For example, Figure 2.1 shows how different measurements of the inner slope affect the shape of the inner profile in dwarf galaxies, such that measurements of the slope that are $< 1$ are cored, and measurements that are $\geq 1$ are cuspy. By the same logic, the core-cusp tension can be observed in galaxy clusters as well, as clusters are dominated by dark matter that determines their mass distribution. However, mass-modeling galaxy clusters is, on the whole, more challenging, due to the large number of individual components that make up their structure. These include the cluster galaxies themselves, which can range from between a few dozen and a few hundred, to the intracluster gas, which can have a complex distribution depending on the dynamical history of the cluster, and finally, the large-scale dark matter halos responsible for binding the entire structure together. Fortunately, by using gravitational lensing as the primary probe of the cluster's mass distribution, one can eliminate some of the complexity involved in the measurement. This is because lensing relies solely on spatial geometry and general relativity, making it one of the most direct ways of obtaining mass values. However, observational papers that have used lensing as a primary probe of the dark matter content of cluster cores have historically conflicted with simulations (Sand et al. 2004, 2008; Newman et al. 2013a; Annunziatella et al. 2017; Sartoris et al. 2020; He et al. 2020; Biviano et al. 2023), which I discuss in the following section.

### 2.1.1 Observational Measurements of the Inner Profile

Measurements of the inner slope for the density profiles of galaxy clusters usually rely on lensing, which excels at probing the gravitational potential at the center of the cluster (Zitrin et al. 2012). Yet, while lensing can accurately capture the total mass distribution in the center, it cannot distinguish between dark and baryonic matter. Precise measurements of the baryonic matter are thus needed to accurately quantify the dark matter inner slope as distinct from the total inner slope. Deblending a mass profile into its baryonic and dark matter components is most effectively done through stellar kinematics of the brightest cluster galaxy (BCG; see Section 2.3.3),

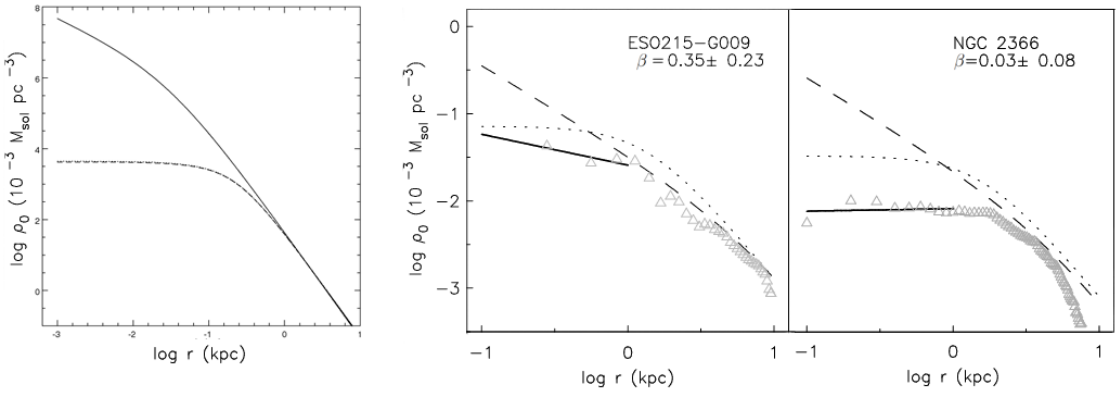


Figure 2.1: *Left:* Example of cored and cuspy density profiles. The cored profile corresponds to the dashed line, while the cuspy profile corresponds to the solid line. Reproduced from Del Popolo (2009). *Right:* The core-cusp problem as illustrated through observational data. The profiles shown are for dwarf galaxies, and the inner slope, $\beta$, changes the shape of the profile. The dashed line represents the NFW profile with a slope of $\beta = 1$, and the dotted line represents a pseudo-isothermal profile (ISO). Reproduced from van Eymeren et al. (2009).

since this is the dominant mass component within the inner <30 kpc of the cluster. This combination of lensing and kinematics has been carried out numerous times in the literature.

Early work by Sand et al. (2004) modeled a total of six galaxy clusters using a combination of strong lensing and long-slit spectroscopy, which was used to obtain measurements of the BCG velocity dispersion profile (see Section 2.4.1). After fitting the dark matter component of the cluster to an NFW profile, the average slope value for these six clusters was reported as being between 0.52-0.57. Sand et al. (2008) remodeled two of these clusters with an updated lensing method and found slope values of around 0.45 for the new models of these two clusters, with some significant statistical uncertainties in the latter model. Newman et al. (2013a) also used BCG kinematics and strong lensing to model a total of seven clusters, but also added weak lensing into the models as an additional constraint on the total mass profile. They also used an NFW profile to parameterize the cluster dark matter halo, and the paper reported an average dark matter slope of $0.50 \pm 0.13$. However, not all observational papers report the same shallow slope values. For instance, Annunziatella et al. (2017) found an inner slope value of $1.36 \pm 0.01$ for a single cluster, which they modeled using a combination of BCG kinematics, strong

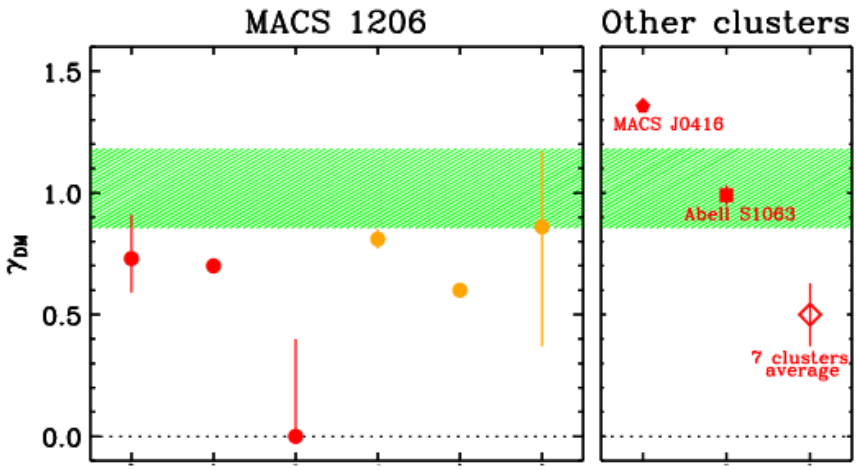


Figure 2.2: Summary of inner slope measurements for several different galaxy clusters. The left box shows disparate measurements for the cluster MACS 1206 made by six different papers, represented with the red and orange dots, where red dots are direct determinations of the inner slope and orange points indicate values obtained from the total slope. The green shaded region indicates the predicted slope value from simulations. The right box shows sample measurements from three other clusters from three different papers. Reproduced from Biviano et al. (2023).

lensing, and X-ray modeling.

Recent work with integral field unit spectroscopy (see Section 2.4.1) has also enabled a different, though related, technique to be used: dynamical modeling of cluster member kinematics and the BCG, which are used to constrain the total cluster mass profile. Sartoris et al. (2020) constrained the kinematics of the cluster members and the BCG in one cluster and found an inner slope of $0.99 \pm 0.04$, while Biviano et al. (2023) found an inner slope of $0.7^{+0.2}_{-0.1}$ for a different cluster using the same method.

Each of these papers fits the dark matter halo of their clusters with NFW profiles. The lensing papers all use different lensing modeling techniques and different instruments, while the dynamical modeling papers use the same techniques and the same instruments. The variance of the inner slope in the different papers, shown in Figure 2.2, despite different measurement techniques seems to indicate that measurement biases are not the sole cause of the core-cusp tension. We will now examine results from simulations.

### 2.1.2 Simulations of the Inner Profile

We previously introduced the NFW profile in Section 1.4 as a 'universal' profile capable of fitting a range of different mass distributions. However, observational papers found inconsistencies with the dark matter distributions predicted by this profile. While the NFW profile predicted an inner density that varied with radius $r$ as $\rho(r) \propto r^{-1}$, papers like Smith et al. (2001) found that the presence of radial multiple images required a cored inner profile to produce the gravitational lensing effects observed in the cluster Abell 383. Williams et al. (1999) found that lensing properties for the most massive clusters were consistent with the NFW profile, but required a large central mass to make these observations agree with measurements predicted by simulations. This prompted an evaluation of the NFW profile's universality, and led to the introduction of a modified form of the profile in Wyithe et al. (2001). This 'generalized' NFW profile takes the following form:

$$\rho(r) = \frac{\partial_c \rho_c}{(\frac{r}{r_s})^{\beta}(1+\frac{r}{r_s})^{3-\beta}} \tag{2.1}$$

where $\partial_c$ is the characteristic over-density and $\rho_c$ is the critical density; both act as scale parameters. The key difference between the generalized and original NFW profiles is in the introduction of the parameter $\beta$, which represents the slope of the inner dark matter density profile. This parameter is left free in the generalized profile, which allows for different measurements of the inner slope that are more consistent with the variety measured in observations.

The last twenty years have seen a massive increase in computational processing power, which has been accompanied by higher-resolution DM simulations and the advance of hydrodynamical simulations that more accurately reflect the physical environment of the Universe. The introduction of baryonic physics has allowed for the exploration of different models for dark matter, such as warm DM and self-interacting DM (as discussed in Section 1.3). One crucial metric to evaluate these models is testing $\beta$, which has conflicting observational measurements. We will discuss these observational values of $\beta$ in the following section, but first we will examine the results from two modern cluster-scale hydrodynamical simulations,

which all find $\beta$ values that are around or greater than 1: BAHAMAS (McCarthy et al. 2017) and Cluster-EAGLE (Barnes et al. 2017).

### BAHAMAS

The BAryons and HAloes of MAssive Systems (BAHAMAS) simulations were created as self-consistent hydrodynamical models aimed at exploring large-scale structure cosmology, and consist of periodic boxes that are 400 Mpc/$h$ on a side, containing 2x1024$^3$ particles. One of the main goals of the model was to properly incorporate baryonic feedback processes from stars and active galactic nuclei (AGN) to reproduce current observable metrics, like the galaxy stellar mass function and the hot gas mass fractions of groups and clusters (McCarthy et al. 2017). The model was specifically calibrated to recover these observables and succeeds over a variety of scales, including galaxy clusters. The X-ray and Sunyaev Zel'dovich scalings of local groups and clusters are also reproduced well.

Robertson et al. (2019) added self-interacting dark matter to the BAHAMAS simulations to test how SIDM behaved when reproducing the density profiles of galaxy clusters. Figure 2.3 shows the results for a simulated cluster at $z = 0$, and subsequently demonstrates that the BAHAMAS models constructed with CDM have a $\beta$ value of about 1, while the SIDM models are more cored ($\beta < 1$). This result also shows the precision required to distinguish between these different slope measurements in the inner $\sim$ 50 kpc of the cluster, particularly for lower mass clusters where the separation between the CDM and SIDM models is not as clear.

### Cluster-EAGLE

Cluster-Evolution and Assembly of Galaxies and their Environments (C-EAGLE/Hydrangea) (Barnes et al. 2017) is a set of hydrodynamical cosmological zoom simulations designed to model the formation of 30 different galaxy clusters with a mass range of $10^{14} < M_{200}/M_{\odot} < 10^{15.4}$, which incorporates the Hydrangea sample from Bahé et al. (2017). C-EAGLE provides a physical spatial resolution of 0.7 kpc and a mass resolution of 2x10$^6 M_{\odot}$, allowing for the resolution of cluster galaxy formation and explorations of intra-cluster medium (ICM) interactions. The high resolution of this

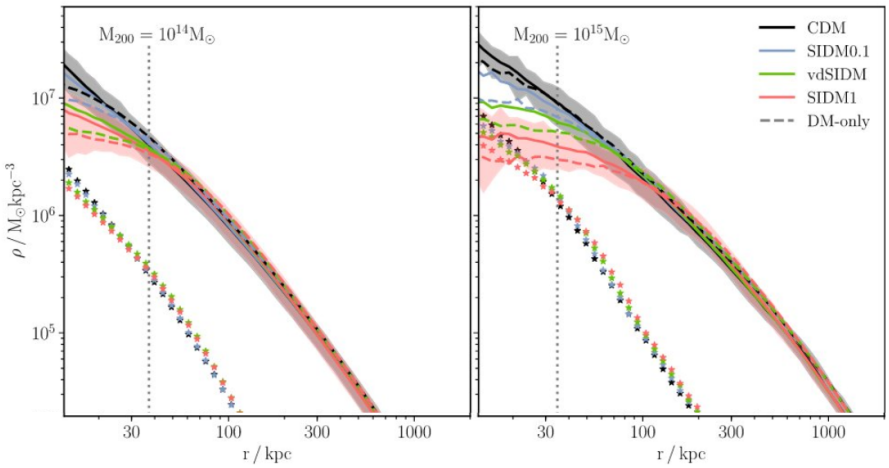


Figure 2.3: The density profiles for simulated galaxy clusters with different masses ($M_{200} = 10^{15} M_\odot$ on the left, $M_{200} = 10^{15} M_\odot$ on the right), calculated using different models of dark matter. The fiducial CDM model is represented in black, while different variations of self-interacting dark matter are plotted as the different colored lines. The dashed lines are dark-matter only models, while the solid lines represent the full hydrodynamical models. High accuracy measurements of the dark matter density profile constructed from observations can thus be used to distinguish between different DM models. Reproduced from Robertson et al. (2019).

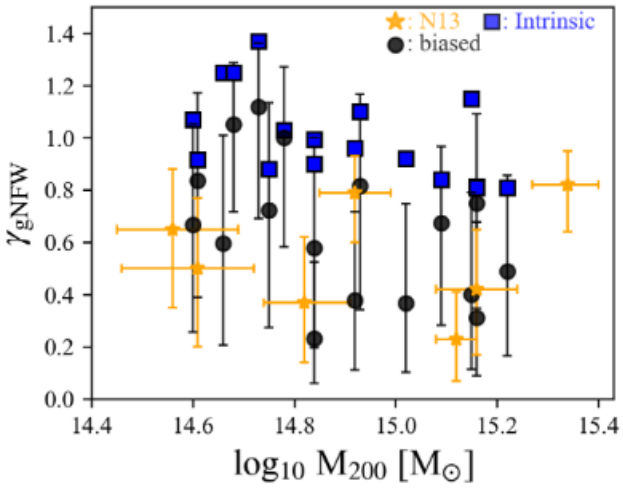


Figure 2.4: Comparison of the values for the inner slope as inferred from biased weak lensing measurements, which were specifically altered to decrease the scale radius to the values reported in N13, and are shown as black dots; the values from N13 shown as orange stars; and the true value of the slope from the C-EAGLE clusters, shown as blue squares. The plot indicates that biased weak lensing measurements can drastically affect the inner slope measurement, sometimes dropping it by more than half of its true value. Reproduced from He et al. (2020).

simulation suite makes it ideal for studying the inner regions of clusters, as was done in He et al. (2020).

The measurements from Newman et al. (2013a) (N13), which reported an inner slope value of $\sim 0.5$, were examined in more detail in this paper, which investigated the ability of the combination of lensing and kinematics to accurately measure the inner slope. The results of this paper suggested that there is a strong degeneracy between the asymptotic gNFW slope and the scale radius $r_s$, which meant that incorrectly estimating the scale radius, which was done using weak lensing in N13, could lead to much shallower measurements of the inner DM profile, as shown in Figure 2.4. However, using the mean inner slope of the dark matter density profile, rather than the asymptotic gNFW slope, was shown to be a better metric of comparison between the observational models and the simulated clusters. As a result, He et al. (2020) definitively showed that care must be taken when making modeling observations, and that weak lensing was particularly important to constrain, given its large impact on the NFW slope measurement. With this information in mind, we turn toward the methods used in this thesis to measure the inner slope.

## 2.2 Parametric Strong Lens Modeling

Modeling strong lensing requires a solution to the lens equation for the positions of the multiple images. This is typically done in two ways: through parametric solutions of the lens equation, and through non-parametric solutions to the lens equation. The difference between these solutions primarily lies in the computational cost, or the time it takes to run a complete model. Parametric models are overall more expensive to run, requiring large amounts of processing power to find solutions due to the large number of constraints involved in the models (Meneghetti et al. 2017). They subdivide the mass distribution into different mass clumps, which are described by haloes of some specific profile. The parameters for each halo are then optimized to find the model that best reproduces the data. As a result, parametric models perform better when they have more constraints, and completed models excel at reproducing observable constraints and provide high accuracy measurements (often

within $5-10\%$ of the true value; see Treu et al. (2016); Meneghetti et al. (2017)). Non-parametric models are typically much cheaper to compute, and as a result they are more flexible to iteration. They typically tessellate the mass distribution into a grid of small mass elements, which can be manipulated according to the specific technique used by the modeler. They can reproduce the overall light distribution of a galaxy cluster and predict multiple images with high accuracy, but they sometimes struggle to achieve the same precision of parametric models because their flexibility means that the specific contribution of different components to the total mass budget is not well-defined, which makes it harder to come up with an unambiguous physical interpretation of the model. For example, non-parametric models tend to not distinguish between galaxy mass scales, even though small-scale mass clumps can significantly affect the placement and location of multiple images. As a result, distinguishing between non-parametric mass models to find the 'best' model can be challenging. In this thesis, we require high accuracy mass models with concrete components to examine the core-cusp problem and so adopt a parametric approach to lens modeling, which we discuss below.

### 2.2.1 Lenstool

We use the parametric Markov chain Monte Carlo modeling software `Lenstool` to construct our mass models in this thesis (Kneib et al. 1996; Jullo et al. 2007a; Jullo & Kneib 2009). `Lenstool` uses the positions and redshifts of multiple images as constraints and parameterizes mass haloes for the different components of the model, optimizing over the parameter space until determining the best fit parameters that both reproduce the observed multiple images and maximize the likelihood. Markov chain Monte Carlo (MCMC) sampling is used to sample the posterior density of the model, which is expressed as a function of the likelihood of the model (as described in Jullo et al. 2007a). This function is minimized as

$$\chi^2_{SL} = \sum_i \chi^2_i \tag{2.2}$$

where the sum is performed over the different families of multiple images in the model, and $\chi_i^2$, the chi-square value for each multiply imaged source, is given as

$$\chi_i^2 = \sum_{j=1}^{n_i} \frac{\left(\theta_{\rm obs}^j - \theta^j(\mathbf{p})\right)^2}{\sigma_{ij}^2}. \tag{2.3}$$

$\theta_{\rm obs}^j$ is the vector position of the observed multiple image $j$, $\theta^j$ is the predicted vector position of the image $j$, $n_i$ is the number of images in system $i$, and $\sigma_{ij}$ is the error of the position of image $j$. The model with maximum likelihood thus minimizes the distance between the observed and predicted positions of the multiple images. This difference is the rms value, given as

$$\text{rms} = \sqrt{\frac{1}{N_{\rm tot}} \sum_{i=1}^{N_{\rm tot}} |\theta_{\rm obs}^j - \theta^j(\mathbf{p})|^2}, \tag{2.4}$$

where $N_{\rm tot}$ is the total number of multiple images. The optimized model is then used to solve for the best fit set of parameters of each halo. A smaller rms value corresponds to a better fit for the model.

## 2.3 Lensing Model Components

`Lenstool` can be used to break up the total mass distribution of a cluster into distinct components. In this thesis, we separate the mass distribution into one cluster-scale dark matter halo; multiple haloes for cluster member galaxies; and one halo for the BCG, which essentially describes its stellar mass (see Section 2.3.3). We show the specific methods and choices for the mass haloes in the following sections.

### 2.3.1 Cluster Dark Matter Halo

#### The Dual-Pseudo Isothermal Elliptical Mass Distribution

We have discussed the generalized NFW profile and how it was developed to match observations of dark matter haloes. However, we have also discussed how the work of He et al. (2020) shows the difficulty of properly constraining the scale radius

and concentration parameters from observable quantities alone. The significant effect that the scale radius can have on the shape of the dark matter halo in this profile is a good reason to test alternative profiles. In this thesis, we utilize the 'dual pseudo isothermal elliptical mass distribution' (dPIE), which is also sometimes called the truncated PIEMD, as implemented in `Lenstool` (Elíasdóttir et al. 2007). The reasons we use this profile are twofold: first, the dPIE has a finite mass and a finite central density, whereas the NFW profile assumes that both of these quantities are infinite; and second, the dPIE breaks up the mass distribution into two components that describe the core separately from the outskirts of the mass distribution, which allows for greater flexibility in determining the shape of the core. The boundary between these regions is described with a core radius $r_{\rm core}$ and a cut radius $r_{\rm cut}$, and the 3D density distribution of the dPIE is given as follows:

$$\rho_{\rm dPIE}(r) = \frac{\rho_0}{(1 + r^2/r_{\rm core}^2)(1 + r^2/r_{\rm cut}^2)}; r_{\rm cut} > r_{\rm core}, \tag{2.5}$$

where $\rho_0$ is the central density. The distribution is spherical, and the core is not strictly isothermal. In the transition region, where $r_{\rm core} \lesssim r \lesssim r_{\rm cut}$, the density scales as $\rho \sim r^{-2}$, while in the outer regions the density scales as $\rho \sim r^{-4}$; we note that this is because $r_{\rm cut}$ is a scale radius, rather than a truncation radius, with $\rho \sim r^{-4}$ for $r >> r_{\rm cut}$. The scale radius, in this case, is a distance that describes where the density profile begins to fall off exponentially, while the truncation radius describes the distance at which the density profile starts to behave like something else, i.e. the dPIE description of the density no longer applies to the profile (Limousin et al. 2022).

We do not fit observable data to the 3D form of the profile, however: instead, it is most useful for lensing to use the projected density, which is given as:

$$\Sigma_{\rm dPIE}(R) = \Sigma_0 \frac{r_{\rm cut} r_{\rm core}}{r_{\rm cut} - r_{\rm core}} \left( \frac{1}{\sqrt{r_{\rm core}^2 + R^2}} - \frac{1}{\sqrt{r_{\rm cut}^2 + R^2}} \right), \tag{2.6}$$

where $R$ is the 2D radius, and where the central projected density is given as

$$\Sigma_0 = \pi \rho_0 \frac{r_{\rm cut} r_{\rm core}}{r_{\rm cut} + r_{\rm core}}. \tag{2.7}$$

We can also recast the profile in terms of the central velocity dispersion, rather than the central density, which is a quantity that we can more easily constrain observationally (Limousin et al. 2005). In this instance, the profile becomes

$$\Sigma_{\rm dPIE}(R) = \frac{\sigma_0^2 r_{\rm cut}}{2G(r_{\rm cut} - r_{\rm core})}\left(\frac{1}{\sqrt{r_{\rm core}^2 + R^2}} - \frac{1}{\sqrt{r_{\rm cut}^2 + R^2}}\right), \tag{2.8}$$

where $\sigma_0$ is the velocity dispersion for a circular potential, which is related to $\rho_0$ as

$$\rho_0 = \frac{\sigma_0^2}{2\pi G}\left(\frac{r_{\rm cut} + r_{\rm core}}{r_{\rm core}^2 r_{\rm cut}}\right). \tag{2.9}$$

The mass inside the projected 2D radius $R$ is then given as

$$M_{2D}(R) = 2\pi\Sigma_0 \frac{r_{\rm cut} r_{\rm core}}{r_{\rm cut} - r_{\rm core}}\left(\sqrt{r_{\rm core}^2 + R^2} - r_{\rm core} - \sqrt{r_{\rm cut}^2 + R^2} + r_{\rm cut}\right), \tag{2.10}$$

and the total finite mass is then

$$M_{\rm TOT} = 2\pi^2 \rho_0 \frac{r_{\rm core}^2 r_{\rm cut}^2}{r_{\rm core} + r_{\rm cut}} = 2\pi\Sigma_0 r_{\rm cut} r_{\rm core} \tag{2.11}$$

For a vanishing core radius ($r_{\rm core} \to 0$), $r_{\rm cut}$ is equal to the half-mass radius, and the effective radius, which is defined as $M_{2D}(R_e) = M_{\rm TOT}/2$, goes as $R_e \approx (3/4) r_{\rm cut}$ under the same limit.

In `Lenstool`, the projected mass distribution is allowed to have ellipticity and position angle. The dPIE halo thus includes eight parameters: the redshift, $z$; the central position (R.A., Dec); the ellipticity and orientation $(e, \theta)$; $r_{\rm cut}$ and $r_{\rm core}$; and the central velocity dispersion $\sigma_0$. In the models presented in this thesis, we use the dPIE halo parameterization for the cluster-scale dark matter halo, the small-scale mass halos describing the cluster member galaxies, and the brightest cluster galaxy alone, the latter two of which we discuss in the next sections.

### 2.3.2 Cluster Member Galaxies

Cluster member galaxies are separately parameterized as small-scale mass clumps within `Lenstool`. In general, cluster members are all modeled to follow the same

scaling relations, which reduces the computational time needed for the model to converge. We follow the assumption that luminosity traces mass (refer to the discussion in Harvey et al. 2016) to model each cluster member with galaxy-scale PIEMD halos, where the positional parameters for each halo ($x$, $y$, $e$, $\theta$) are fixed to the properties of their light distribution as measured with `SExtractor` (Bertin & Arnouts, 1996a). The remaining PIEMD parameters ($\sigma$, $r_{\rm core}$, $r_{\rm cut}$) are then rescaled to match a reference galaxy with luminosity $L^*$ following the Faber & Jackson (1976) relation:

$$\begin{cases} \sigma = \sigma^* \left(\frac{L}{L^*}\right)^{1/4} \\ r_{\rm core} = r^*_{\rm core} \left(\frac{L}{L^*}\right)^{1/2} \\ r_{\rm cut} = r^*_{\rm cut} \left(\frac{L}{L^*}\right)^{1/2} \end{cases} \tag{2.12}$$

The mass of each halo is then derived with the following relation:

$$M = \frac{\pi}{G} (\sigma^*)^2 r^*_{\rm core} \left(\frac{L}{L^*}\right) \tag{2.13}$$

where $\sigma^*$, $r^*_{\rm core}$, and $r^*_{\rm cut}$ are the reference velocity dispersion, core radius, and truncation radius. Previous models have demonstrated that $r^*_{\rm core}$ is small in galaxy-scale halos and has a minimal effect on mass models (e.g. Covone et al. 2006; Limousin et al. 2007b; Elíasdóttir et al. 2007). $r^*_{\rm core}$ is thus fixed to 0.15 kpc for cluster galaxies (Brainerd & Specian 2003; Limousin et al. 2007b). The remaining two parameters, velocity dispersion and cut radius, are optimized by the model for a reference galaxy $L^*$. The velocity dispersion is allowed to vary between 27 and 250kms$^{-1}$, and the cut radius between 3 and 50 kpc. The cut radius is constrained to an upper limit in order to account for tidal stripping of galactic dark matter halos (e.g. Limousin et al. 2007a, 2009; Natarajan et al. 2009; Wetzel & White 2010; Niemiec et al. 2019). These parametric constraints do not allow any dark matter haloes to contain zero mass, which enables the model to reproduce observational constraints. We differentiate between models using $\chi^2$ and rms statistics, where a low rms generally indicates a better model.

Cluster member galaxies that are located in close proximity to multiple images may have an additional lensing effect responsible for producing the multiple images.

As a result, these specific galaxies can be parameterized separately as individual dPIE haloes in order to give the model greater freedom to find a better fit.

### 2.3.3 Brightest Cluster Galaxy

The brightest galaxy in a galaxy cluster is referred to, somewhat unimaginatively, as the brightest cluster galaxy (BCG). BCGs are among the most massive and the most luminous galaxies in the Universe, and they are generally located at the bottom of the potential well of galaxy clusters at a point that is often coincident with the peak of X-ray emission. They dominate the mass distribution of the inner regions of galaxy clusters ($< 30$ kpc), and can consequently necessitate more specialized treatment than a typical cluster galaxy to ensure that their mass distribution is properly described. In the case of this thesis, separately parameterizing the BCG allows for dynamical mass modeling to be added as a constraint that is independent of lensing. This modeling is carried out using the stellar kinematics of the BCG, which constrains the mass distribution in the central region of the cluster by probing the total gravitational potential well that causes the motion of the stars. In `Lenstool`, we can model the BCG with a separate dPIE halo to take advantage of this dynamical modeling. We can also add more specific constraints to the halo by using photometry, which reduces the model's ability to explore parameter space regions that are not physical. For example, the dPIE halo parameters of ellipticity and position angle can be measured from photometric shape fits, and $r_{\rm cut}$ and $r_{\rm core}$ can be obtained by fitting a mass profile to an observed surface brightness profile. We discuss these photometric methods in more detail in Chapter 3. In the following section, we describe how kinematics can be used to probe the mass distribution, and we introduce our practical application of kinematic modeling into `Lenstool` in Chapter 3.

## 2.4 Dynamical Mass Modeling

The rotation curve of a galaxy describes how the rotational velocity of stars changes as the distance is increased radially outward from the center. Generally, for galaxies,

this velocity increases and then eventually flattens off as the radius increases, even though the amount of stellar material in the galaxy visibly decreases with radius. This discrepancy is explained by the presence of dark matter, and rotation curves remain one of our strongest pieces of evidence for the existence of dark matter in the Universe. However, in early-type elliptical galaxies, dark matter only comprises a small fraction of the total mass within the half-light radius of the galaxy, $R_e$, or the radius in which half the light of the galaxy is contained (see Gerhard et al. 2001, Borriello et al. 2003, Thomas et al. 2007, Bolton et al. 2008). We can thus safely assume that these galaxies are, on the whole, dominated by their stellar mass component, which means that constraining the kinematics of the stars can be effectively used to describe the total mass distribution of the galaxy.

We describe the motions of stars within a gravitational potential by using the Jeans equations, which are derived by incorporating gravity into the collisionless Boltzmann equation. Following the derivations presented in Agnello et al. (2014), we can write the Jeans equation for an elliptical galaxy using the spherical formalism, where the aperture-averaged projected velocity dispersion $\sigma_{\rm ap}$ can be simply obtained through measurements of the surface brightness profile, which is a direct observable quantity. This approach avoids making assumptions about the orbital structure of the luminous component of the galaxy via projection and deprojection of the surface brightness profile. Instead, it associates the velocity dispersion profile directly with the observed surface brightness of the galaxy, which is valid for an observation where the kinematic information of a galaxy's unresolved stellar populations is obtained from, for example, an IFU spectrograph, which averages this information across a spatial aperture. This effect places more importance on the chosen physical model used to describe the galaxy, rather than on descriptions of the orbit-modelling for the luminous component.

The spherical Jeans equations, which diagonalize the velocity dispersion tensor in spherical coordinates $r, \theta, \phi$ and distinguish only between the radial and tangential motions of stars, begin with a description of the anisotropy, encoded in the parameter $\beta(r)$ as

$$\beta(r) = 1 - \frac{\langle v_\theta^2 + v_\phi^2 \rangle}{2\langle v_r^2 \rangle}. \tag{2.14}$$

The luminosity density $\nu$ in a gravitational potential $\Phi$ can then be described as

$$\frac{\partial(\nu \bar{v}_r^2)}{\partial r} + \frac{2\beta\nu\bar{v}_r^2}{r} = -\nu\frac{\partial\Phi}{\partial r}, \tag{2.15}$$

where $v_r$ is the radial velocity dispersion. Solving this equation for $v_r$ and rewriting the radial force in terms of the enclosed mass $M(r)$ gives

$$\bar{v}_r^2 = \frac{G}{\nu(R)} \int_r^\infty \frac{M(r)\nu(r)}{r^2} J_\beta(R, r) dr, \tag{2.16}$$

where $J_\beta$ is a correction term that can be adjusted depending on the internal physics of the object the equations are applied to (i.e. for stationary or non-stationary models). Here, we assume a stationary model ($\partial_t \nu = \partial_t \Phi = 0$), with no radial flow ($\langle v_r \rangle = 0$) and no Hubble flow.

We can then proceed to write the observational portion of the velocity dispersion, which is encoded in the projected second velocity moment, $\sigma_{\rm los}$, as

$$\sigma_{\rm los}^2(R) I(R) = 2 \int_R^\infty \left(1 - \beta(r)\frac{R^2}{r^2}\right) \frac{\nu(r)\bar{v}_r^2 r}{\sqrt{r^2 - R^2}} dr, \tag{2.17}$$

where $I(r)$ is the observed surface brightness profile. The luminosity density $\nu(r)$ is then classically obtained via Abell deprojection from the surface brightness profile by inserting the following equation,

$$\nu(r) = -\frac{1}{\pi} \int_r^\infty \frac{\partial_R(I(R))}{\sqrt{R^2 - r^2}} dR, \tag{2.18}$$

into Equation 2.17 and integrating. However, we choose to adopt the formalism presented in Agnello et al. (2014), which removes the need for explicit deprojection and projection to obtain the luminosity density, and instead rewrites the observed velocity dispersion profile directly in terms of the observed surface brightness profile.

This is accomplished by inserting Equation 2.16 into Equation 2.17 and exchanging the orders of integration, at which point an integration by parts can be done to

obtain

$$\sigma^2_{\rm los}(R)I(R) = 2G\int_R^\infty \frac{M(r)\nu(r)}{r^2}\left(\sqrt{r^2-R^2}+k_\beta(R,r)\right)dr, \tag{2.19}$$

where $k_\beta$ is a kernel that is related to the anisotropy profile, $\beta(r)$, as

$$k_\beta(R,x) = \int_R^x \frac{(2r^2-3R^2)\beta(r)J_\beta(r,x)}{r\sqrt{r^2-R^2}}dr, \tag{2.20}$$

and which can be expressed analytically depending on the choice of anisotropy profile (Mamon & Łokas 2005). This result can be rearranged to depend only on the observed stellar surfade brightness $I(R)$.

By inserting Equation 2.18 into Equation 2.19, we can write the line of sight velocity dispersion explicitly in terms of the observable surface brightness, the enclosed mass $M(R)$, and the kernel $k_\beta(R,r)$, which is intrinsically connected to the anisotropy profile $\beta(r)$, as

$$\begin{aligned}\sigma^2_{\rm los}(R)I(R) = &\frac{2G}{\pi}\int_R^\infty sI(s)\int_R^s \frac{\partial_r(M(r)\sqrt{r^2-R^2}/r^3)}{\sqrt{s^2-r^2}}drds \\ &+\frac{2G}{\pi}\int_R^\infty sI(s)\int_R^s \frac{\partial_r(M(r)k_\beta(R,r)/r^3}{\sqrt{s^2-r^2}}drds.\end{aligned} \tag{2.21}$$

This form of the equation is particularly useful because it explicitly splits the mass components into an isotropic part ($\beta = 0$) and an anisotropic part ($\beta \neq 0$). The total mass is thus proportional to the line of sight velocity as $\sigma_{\rm los} \propto GM/R$, and the scaling will vary depending on the choice of surface brightness profile and anisotropy profile. This also means that the density of stars is only weighted on the luminosity, and is therefore only dependent on the mass-to-light ratio measured for the galaxy. In this thesis, I assume a constant mass-to-light ratio across the radial extent of the BCG. I discuss the consequences of assuming a radially varying mass-to-light ratio for the BCGs analyzed in this thesis in Section 3.5.1.

The final step in the measurement of the line-of-sight velocity dispersion is to account for the fact that kinematics are measured within an aperture and are blurred by some kind of point-spread function. To account for these effects, we write the velocity dispersion as the radial average inside a circular aperture as

$$\sigma^2_{\rm ap}(R) = \frac{2\pi \int_0^R sI(s)\sigma_{\rm los}(s)ds}{L(R)}, \tag{2.22}$$

where the projected luminosity within R is given as

$$L(R) = 2\pi \int_0^R sI(s)ds. \tag{2.23}$$

This equation can again be decomposed into isotropic and anisotropic parts as

$$\begin{aligned}\sigma^2_{\rm ap}(R) = \frac{4G}{3L(R)} &\int_0^\infty sI(s) \int_0^s \frac{4\pi\rho_{\rm tot}(r)r^2}{\sqrt{s^2-r^2}}drds \\ &- \int_R^\infty \int_R^s \frac{\partial_r \left(M(r)(r^2-R^2)^{3/2}/r^3\right)}{\sqrt{s^2-r^2}}drds \\ &+ 3R^2 \int_R^\infty sI(s) \int_R^s \frac{\partial_r (M(r)Z_\beta(R,r)/r^3)}{\sqrt{s^2-r^2}}drds.\end{aligned} \tag{2.24}$$

The first line corresponds to the virial limit, the second line gives the aperture corrections for $\beta = 0$, and the third line describes the corrections for the anisotropic part ($\beta \neq 0$). Figure 2.5 shows how the shapes of the anisotropic and isotropic profiles differ.

It should now be clear that kinematic velocity dispersion measurements of an elliptical galaxy can be used as a method to determine the mass of that galaxy, and that the mass of a galaxy can be constrained from observational measurements alone without assuming any projections or deprojections. In this thesis, we apply this equation to the BCG in order to constrain its mass within our parameterization of the mass distribution. We discuss our profile choices and incorporation of the velocity dispersion as a constraint further in Chapter 3. In the next section, we turn toward the methods we use to obtain the velocity dispersion.

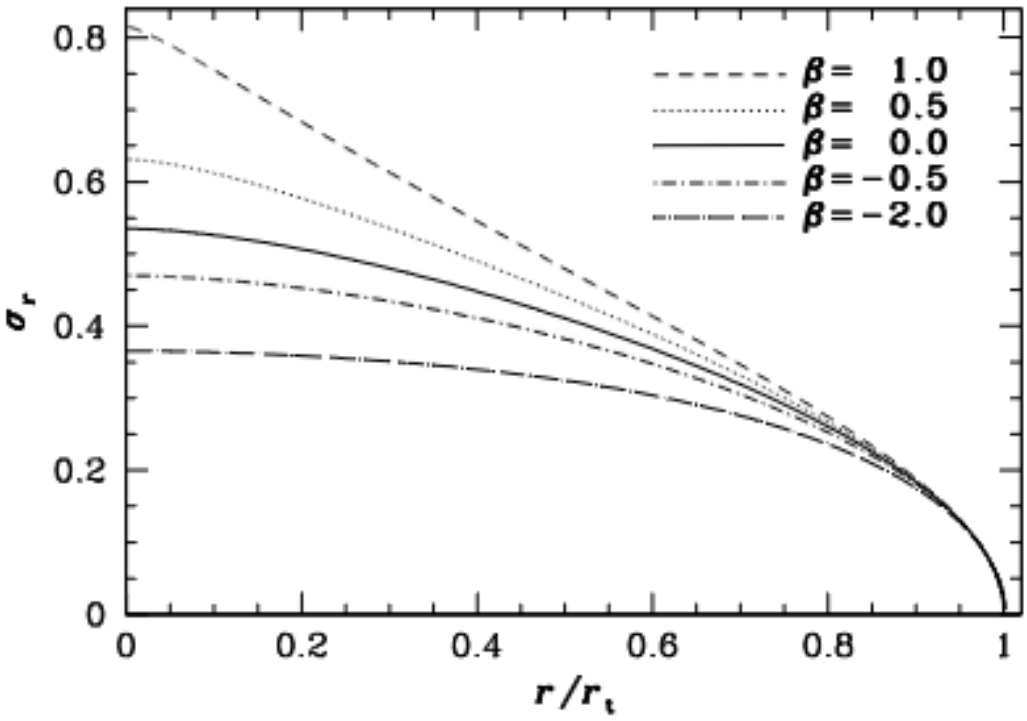


Figure 2.5: Example of how including anisotropy affects the resulting radial velocity dispersion profile. The isotropic model is plotted as the solid line for $\beta = 0$. $r_t$ corresponds to the truncation radius of the galaxy. Reproduced from Dehnen et al. (2006).

### 2.4.1 Velocity Dispersion Profile

A crucial component of constraining the mass of a galaxy is obtaining an accurate measurement of its velocity dispersion profile. This measurement describes the intrinsic broadening of spectral features caused by the varying directions in which a group of stars in a gravitational potential are moving. It is particularly obvious in elliptical galaxies, which do not rotate (i.e. most stars are orbiting in the same direction, as in the massive arms of spiral galaxies); instead, stars in ellipticals move randomly, and the spread between their velocities is described by the velocity dispersion. The most effective way to measure the velocity dispersion is through spectroscopic measurements of the galaxy's spectral features. There are various computational ways to do this, and we discuss our particular choice of program in Chapter 3. One important quantity to consider when measuring the profile is the aperture used in the spectrograph. For example, long-slit spectroscopy observes objects through a long, narrow slit, which allows for the measurement of the velocity dispersion along the spatial extent of a galaxy. An example of long-slit spectroscopy for a BCG is shown in Figure 2.6. The image shown is taken from the Low Resolution Imaging Spectrometer (LRIS), which is currently in operation on the Keck I telescope at the W.M. Keck Observatory on Mauna Kea in Hawaii. Another type of aperture is Integral Field Unit (IFU) spectroscopy, which acquires spatially resolved spectroscopic information over a 2D field of view. Specific IFU instruments differ in their optimal wavelength coverage and resolution. An example IFU observation of a BCG is shown in Figure 2.7. The image is taken from the Multi Unit Spectroscopic Explorer (MUSE), which is currently in operation on the Very Large Telescope on Cerro Paranal in Chile. We will discuss MUSE more thoroughly in Chapter 3.

I have now presented the core-cusp problem in galaxy clusters, discussed parametric strong lens modeling with `Lenstool`, and shown how the mass distribution of clusters can be broken down into three primary components: the cluster DM halo, the cluster member galaxies, and the BCG. I have also presented the equations that can be used to model the mass of a galaxy using stellar kinematics as a basis. I will now put all these concepts into practice in Chapters 3 and 4 to measure the inner DM density slope in a small sample of galaxy clusters.

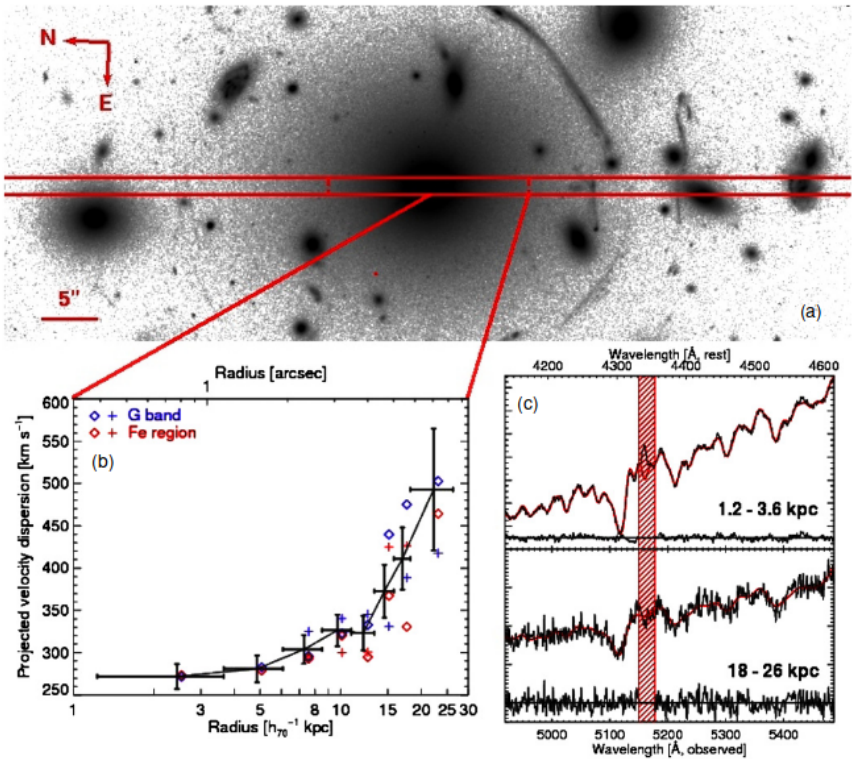


Figure 2.6: Example of long-slit spectroscopy from LRIS. The top image shows the slit configuration in red; the vertical line marks the boundary of the velocity dispersion derivation. The left bottom image shows the stellar velocity dispersion profile as determined from the Fraunhofer G band and Fe $\lambda$5270 absorption line regions. The right bottom image shows the spectra for the inner and outermost spatial bins around the G band, where the red curves show the fitted stellar template, with residuals plotted below. The red shaded region denotes the area that was excluded from the fit due to the presence of sky lines. Reproduced from Newman et al. (2011).

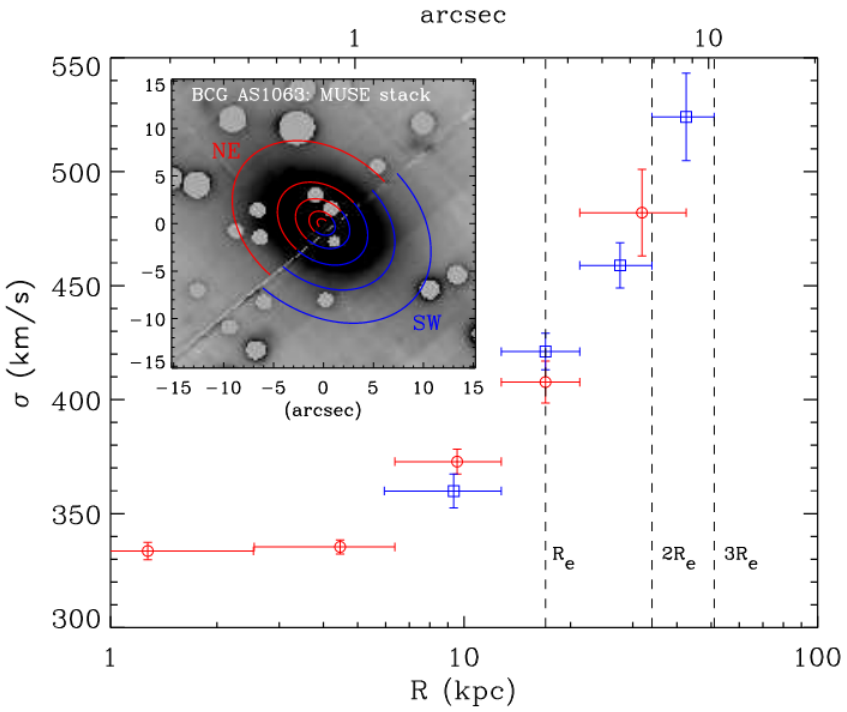


Figure 2.7: Example of IFU spectroscopy from VLT/MUSE. The inset image shows the full extent of the IFU cube, and the gray circles represent masks to cover projected faint cluster members. The main plot shows the velocity dispersion profile for the BCG of the cluster AS1063, with measurements from the SW side of the BCG shown in blue and measurements from the NE side shown in red. The vertical dashed lines indicate 1, 2, and 3 effective radii. Reproduced from Sartoris et al. (2020).

# CHAPTER 3

# The Inner Dark Matter Density Slope in Galaxy Clusters with Radial Arcs

The following chapter is adapted from a paper submitted to MNRAS on May 29, 2024, entitled "The Kaleidoscope Survey: Strong Gravitational Lensing in Galaxy Clusters with Radial Arcs".

I have established how measurements of the inner density slope of galaxy clusters are a direct test of the Λ-CDM cosmological model in the preceding chapters. I have also shown how the blend of strong gravitational lensing and BCG kinematics can be used to constrain this slope measurement. In this chapter, I measure the inner dark matter density slope for a group of galaxy clusters that all have a unique physical feature in common: radial arcs.

## 3.1 Radial Arcs

In Section 1.5, I discussed how the geometry of lensing produces two different critical and caustic lines that are differentiated based on their location relative to the center of the mass distribution. The same distinction can be applied to strongly lensed images, which I will call 'arcs' hereafter. Radial arcs, similarly to radial critical

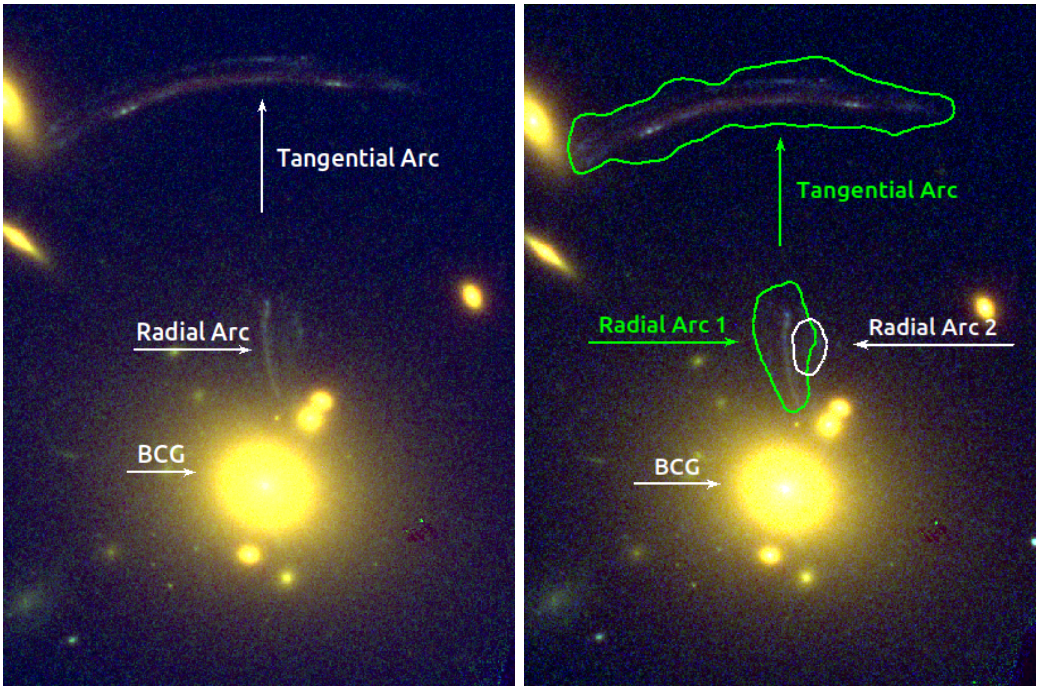


Figure 3.1: *Left:* An example of lensing geometry where both a radial arc and a tangential arc are produced. The image is a false-color image of the cluster MS 2137−23, made using a combination of *HST*/F160W, F814W, and F435W pass-bands. The radial arc is located within $\sim$ 10 kpc of the BCG, while the tangential arc is around $\sim$ 70 kpc away. *Right:* The same image with contours at 9300 Å ($z = 1.496$) from VLT/MUSE spectroscopy overplotted in green for the main arc system in the image. Inspection of the spectroscopic data reveals another radial system located to the right of the first radial arc, with contours at 8160 Å ($z = 1.19$) overplotted in white.

lines, are located in close proximity to the center of the mass distribution of the cluster. The BCG, as the brightest galaxy in the cluster, is generally coincident with the center of this mass potential (van den Bosch et al. 2004, Weinmann et al. 2006), and so radial arcs usually appear near the center (within $10 - 20$ kpc) of the BCG. This arrangement poses an obvious problem for the detection of radial arcs: multiple images are by nature less bright than cluster galaxies in most cases, and the relative positions of the BCG and the radial arc can prevent the detection of the radial arc, as the light from the BCG can easily obscure its presence (Bartelmann, 2010). In these cases, I rely on spectroscopic detections to confirm the presence of these arcs.

Figure 3.1 shows an example of both radial and tangential arcs in the galaxy cluster MS 2137−23. In this case, a radial arc is clearly visible in the *HST* photometry.

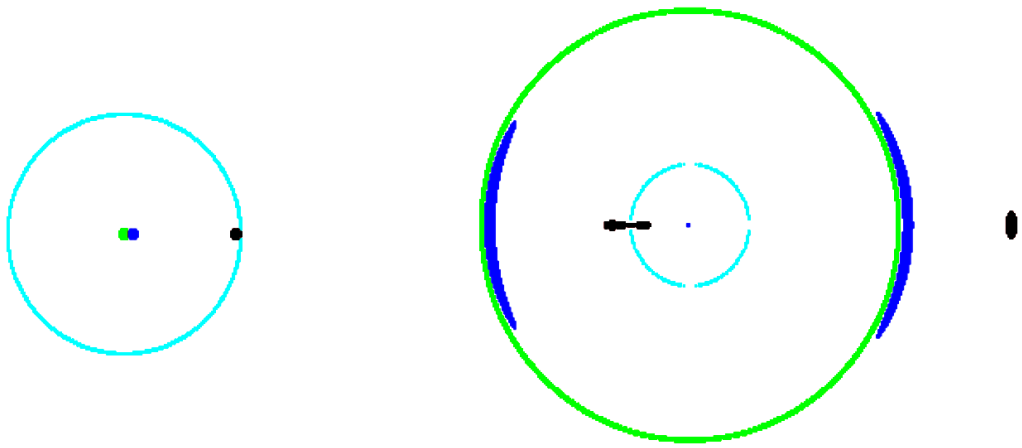

Figure 3.2: The caustics and critical lines for a circular lens with a finite core. The caustics are drawn as cyan lines, the critical lines are drawn as the yellow lines, and the lensed sources are shown as the red and blue dots. The leftmost panel shows the source plane, while the right panel shows the image plane. The lensed source that produces the radial arc is located directly on the caustic in the source plane, which produces two images in the image plane that appear to merge together across the radial caustic line, thus generating a radially stretched single image. Reproduced from Hattori et al. (1999) with modified colors for easier visual understanding.

However, this cluster actually hosts two radial arcs from two different background galaxies. The second system is too faint to unambiguously identify from *HST* photometry alone, but can be clearly detected in spectroscopic data. The right-most image of Figure 3.1 shows two separate contours taken from the Multi Unit Spectroscopic Explorer (MUSE) Integral Field Unit (IFU) spectrograph on the Very Large Telescope (VLT), plotted at 9300 Å for the obvious radial arc, and at 8160 Å for the second radial arc, located to the right of the first system. These detections help to demonstrate the necessity of spectroscopy for determining whether a radial arc is present or not, and particularly for IFU spectroscopy, as long-slit spectroscopy is subject to either correctly guessing the position of the radial arc *a priori* or a lucky alignment to detect a previously unknown radial arc.

Another crucial property of radial arcs is the geometry required for their appearance, an example of which is plotted in Figure 3.2 for a circularly symmetric mass potential. Under the assumption that the total density profile of a cluster can be

approximated by $\rho \propto r^{-\beta}$, radial arc detections implicitly constrain the shape of the central cluster mass potential because they cannot be generated if the profile is steeper than $\rho \propto r^{-2}$, or if $\beta \geq 2$ (Hattori et al., 1999). If this limit for the slope is exceeded, light rays that pass through the center of the cluster are unable to travel to the observer because the gravitational delay becomes infinite at the center, and so no radial image can be observed. This places a strict limit on the slope of the density profile for clusters that have radial arcs, since the slope *must* be flatter than $\rho \propto r^{-2}$. This serves as a useful limitation on the basic shape of the central mass profile. However, in Section 2.1.2, I discussed how modern simulations using NFW profiles found an inner dark matter density slope of $\beta \sim 1$, which is well within this limit. The presence of radial arcs is not a sufficient observable to distinguish between cored and cuspy mass profiles, but their appearance does place an upper limit on the steepness of the profile. I take advantage of this property to specifically examine the inner density profiles of clusters with radial arcs, which I discuss in the next sections.

## 3.2 Sample of Clusters

In Cerny+2024, I measure the inner density profiles of six galaxy clusters that are hosts to radial arcs. These clusters were chosen for their presence in the ESO Kaleidoscope Clusters survey (PID 0104.A-0801; PI A. Edge), a programme structured around the identification of bright strong-lensing features in galaxy clusters using new IFU spectroscopy from VLT/MUSE. As of May 2024, Kaleidoscope consists of observations of more than 200 clusters, which makes it a potentially lucrative sample for studying the core-cusp problem using the combination of strong lensing and kinematics that I have described in previous sections. However, the survey does have some limitations. Kaleidoscope is a large 'filler' programme and is designed on premise that all targets are able to be observed regardless of seeing or atmospheric conditions. As a result, the quality of the observations is often shallow or contaminated by sky noise. However, clusters targeted by this survey were chosen specifically to maximize the amount of observational information that can be

extracted in sub-optimal observing conditions. The spectral range of VLT/MUSE covers 4650-9300 Å, the field of view is 1x1 arcmin$^2$ in Wide Field Mode (WFM), and the spatial resolution ranges between 0.3-0.4 arcsec. All these properties make VLT/MUSE uniquely suited to observe crowded FOVs, such as strong lensing clusters. since it can easily detect spectral features from lensed galaxies across a wide range of redshifts. It also spatially covers almost the entire strong lensing region, which maximizes the chances of obtaining at least one spectroscopic redshift for a multiple image system. As an IFU instrument, VLT/MUSE is also extremely good at resolving the stellar kinematics of cluster members, which can be used to constrain the cluster mass profile (Bergamini et al. (2019), Sartoris et al. (2020), Biviano et al. (2023)).

In this chapter, I select six clusters from Kaleidoscope that are hosts to radial arcs. I note here that radial arcs are still relatively uncommon among cluster lenses. For example, the ratio of clusters with radial arcs vs clusters without these arcs in the Kaleidoscope sample is around 1%, which easily shows that radial arcs, while a powerful constraint on the inner DM profile, are a unique physical feature and cannot be relied upon to appear in lensing analyses of cluster mass profiles at scale. Of these six clusters, I present new strong lensing models for four: Abell 383 (A383 hereafter), MS 2137−23 (MS2137 hereafter), MACS J0326.8-0043 (MACS J0326 hereafter), and MACS J1427.6−2521 (MACS J1427 hereafter). I also include two additional clusters observed in the Kaleidoscope survey: MACS J0417.5-1154 (MACS J0417 hereafter), and MACS J0949.8+1708 (MACS J0949 hereafter). Existing strong lensing models are used for these latter two clusters because the Kaleidoscope observations did not offer new strong lensing constraints. Lensing models for these two clusters are presented in Jauzac et al. (2019) and Allingham et al. (2023), respectively, and I refer the reader to these papers for more details on the construction of the lens models. I add new measurements of the BCG kinematics to all six clusters in order to obtain the inner DM slope value.

In the following sections, I assume a standard ΛCDM cosmology with $\Omega_M$=0.3, $\Omega_\Lambda$=0.7, and $H_0$ =70 km s$^{-1}$ Mpc$^{-1}$. All magnitudes are measured in the AB system unless stated otherwise.

Table 3.1: Summary of *HST* observations used in this work to build lens models, create cluster member catalogues, and perform photometric extractions for A383, MS 2137, MACS J0326, and MACS J1427; and only to perform photometric extractions for MACS J0417 and MACS J0949. Column 1 is the name of the cluster. Column 2 and 3 are the Right Ascension and Declination, given in degrees (J2000). Column 4 is the pass-band. Column 5 is the PID. Column 6 is the P.I. of the observation. Column 7 is the exposure time. Column 8 is the observation date.

| Name | R.A. | Decl. | Band | PID | P.I. | Exp. time [s] | Obs. date |
|---|---|---|---|---|---|---|---|
| A383 | 42.0141667 | -3.5291389 | ACS/F435W | 12065 | Postman | 4250 | 2010-12-28 |
| | | | ACS/F606W | | | 4210 | 2011-01-18 |
| | | | ACS/F814W | | | 8486 | 2010-12-08 |
| | | | WFC3/F105W | | | 3620 | 2011-01-18 |
| | | | WFC3/F125W | | | 3320 | 2011-01-05 |
| | | | WFC3/F140W | | | 2411 | 2011-01-18 |
| | | | WFC3/F160W | | | 5935 | 2010-11-19 |
| MS 2137 | 325.0632083 | -23.6611667 | ACS/F435W | 12102 | Postman | 4026 | 2011-09-29 |
| | 325.0916667 | -23.6325000 | ACS/F606W | 10635 | Ziegler | 17920 | 2006-05-16 |
| | 325.0632083 | -23.6611667 | ACS/F814W | 12102 | Postman | 8132 | 2011-08-21 |
| | | | WFC3/F105W | | | 2814 | 2011-09-09 |
| | | | WFC3/F125W | | | 2514 | 2011-09-02 |
| | | | WFC3/F140W | | | 2311 | 2011-09-09 |
| | | | WFC3/F160W | | | 5029 | 2011-08-21 |
| MACS J0326 | 51.708118 | -0.7310381 | ACS/F814W | 11103 | Ebeling | 500 | 2008-11-13 |
| | | | ACS/F606W | | | 500 | 2007-11-17 |
| MACS J1427 | 216.9144704 | -25.3506079 | ACS/F814W | 12884 | Ebeling | 1440 | 2014-07-21 |
| MACS J0417 | 64.3945486 | -11.9088174 | ACS/F606W | 12009 | von der Linden | 7152 | 2011-01-20 |
| | | | ACS/F435W | 14096 | Coe | 2000 | 2017-06-16 |
| MACS J0949 | 147.4659359 | 17.1195712 | ACS/F606W | 14096 | Coe | 1013 | 2015-11-20 |

## 3.3 Observations

### 3.3.1 Photometry

#### Hubble Space Telescope Imaging

I utilize imaging from the *Advanced Camera for Surveys* (*ACS*) onboard *HST* obtained from the Cluster Lensing And Supernova survey with Hubble (CLASH) survey (Postman et al., 2012a) in the F814W, F6606W, and F435W pass-bands for A383 and MS2137 in order to identify multiple images (see Table 3.1 for details). I also use imaging from the Wide Field Camera 3 (WFC3) in the F105W, F125W, F140W, and F160W pass-bands in order to perform source identification. All imaging was obtained from the Mikulski Archive for Space Telescopes (MAST)[1]. Basic

[1]https://archive.stsci.edu/prepds/clash/

data reduction procedures were applied to all imaging using `HSTCAL` and standard calibration files. `Tweakreg` was used to register individual frames to a common *ACS* reference image, after which `Astrodrizzle` was used to co-add the frames together.

The observations of MACS J0326 and MACS J1427 are shallower and consist of fewer bands. F606W and F814W images are available for MACS J0326 and are sourced from the *HST* SNAP programme 11103 (PI: Ebeling). The single F814W image available for MACS J1427 is taken from archival data made available by *HST* SNAP programme 12166 (PI: Ebeling).

I additionally use the F606W bands from the Reionization Lensing Cluster Survey (RELICS, PID: 14096, PI: Coe) for both MACS J0949 and MACS J0417 to obtain photometric measurements of the BCG. I also include the F435W band from the *HST* programme 12009 (PI: von der Linden) for MACS J0417 as an additional check on my F606W measurements. These images were not used for any other purpose in the course of constructing the lens models.

A summary of the observations, exposure times, and bands used for each cluster are listed in Table 3.1. Cluster members for the first three clusters were identified using SExtractor (Bertin & Arnouts 1996b) in dual mode on the F814W and F606W pass-band images. Cluster members for MACS J1427 were identified using MUSE spectroscopy. Cluster members for MACS J0949 and MACS J0417 were taken from their existing lens models, and so I only list the *HST* filters used to perform photometric analysis of the BCG for these two clusters.

### *HST* Catalogues

I create new catalogues of multiple image systems from the *HST* imaging for A383, MS2137, MACS J0326, and MACS J1427. I identify arc systems used for lens modeling within the images based on geometry, color and morphology. Properties of the arcs for these four clusters are given in Tables 3.4-3.7. For A383, MS2137, and MACS J0326, galaxy catalogues for each cluster are built using SExtractor in dual mode, using the F814W and F606W pass-band images, with threshold parameters `DETECT_THRESH` = 1.5, which only considers pixels with a value above this threshold when extracting a source, and `DETECT_MINAREA` = 20, which sets the

minimum number of pixels with a value above the threshold that a source must have in order to be extracted. Detections with error flags or unreliable magnitude measurements (i.e. `MAG_AUTO=-99`) were dropped, and detections with a stellarity measurement greater than 0.5 were removed as they are more likely to be stars rather than galaxies. Only objects that appeared in both pass-bands were kept in the final catalogue. For MACS J1427, I build a galaxy catalogue based on the MUSE detections. For MACS J0417 and MACS J0949, I use the galaxy and arc system catalogues from their existing lens models.

### 3.3.2 Spectroscopy

#### VLT-MUSE Observations

The VLT/MUSE observations for each cluster are summarized in Table 3.8. Each cluster observation consisted of three individual exposures (imaged sequentially) of 970 s each. To minimize the effect of observational systematics, a small dither is applied (0.3 arcsec) between each exposure, and each frame is rotated 90 degrees clockwise relative to the previous frame. Observations were then stacked together to create a single cube with a total exposure of 2910 s. The resulting average seeing and airmass of the stacked cubes are reported in Table 3.8.

Data reduction of the MUSE cubes was performed using the standard procedures of the `esorex` pipeline (MUSE-KIT-2.4.1; Weilbacher et al. 2016), along with additional calibration and cleaning steps (as described in e.g., Richard et al. 2021 or Lagattuta et al. 2022). Bias subtraction and flat fielding were performed with basic calibration files using illumination and twilight exposures with dates closest to that of the source exposure. Flux calibration and telluric correction were performed with the standard star taken closest to the date of the source exposure. After an initial reduction process to align individual exposures, the final calibration step (the "scipost" phase) is re-run to improve flux variation between individual IFU slices. This is achieved using an auto-calibration algorithm included in the MUSE reduction pipeline, but a mask is first applied to eliminate flux from bright cluster members and intra-cluster light that bias the measurement. Finally, the ZURICH

Atmospheric Purge (ZAP; Soto et al. 2016) is applied to the fully reduced final data cube in order to eliminate strong skyline residuals after sky subtraction.

### VLT-MUSE Catalogues

Source extraction is performed for four clusters following the procedure detailed in Lagattuta et al. (2022); I briefly describe the procedure here. The clusters evaluated were A383, MS2137, MACS J0326, and MACS J1427. Spectroscopic redshifts were obtained for objects in the MUSE cubes with a proprietary programme called Source Inspector, developed and hosted by CRAL (Centre de Recherche Astrophysique de Lyon). SExtractor (Bertin & Arnouts, 1996a) was first run on the MUSE data using the `muselet` routine from `mpdaf` (Bacon et al. 2016; Piqueras et al. 2017)[2], which identifies sources with flux above the local continuum level by subtracting the average flux measured around a narrow wavelength range from the average flux within that wavelength range. This process creates a pseudo-narrow-band for each wavelength range, or slice. A narrow-band cube was formed by combining all the slices together, and SExtractor was run on each slice to identify emission peaks. Unique detections in the cube had their spectrum extracted after peaks at different wavelength slices that are spatially 'close' to each other (i.e. within the same seeing disk) were combined into multi-line objects. Distinct individual features, like Ly-$\alpha$ and [OII], were also extracted. The spectra of sources that were identified using bright objects in the existing *HST* imaging were also extracted. A final sky correction was applied by subtracting, from each spectrum, the sum of the 500 nearest blank spaxels (spaxels not associated with any detection in the field) that were located within a 0.4"-4.0" circular annulus centered on the target object.

Each spectrum was then evaluated using Source Inspector, which calculated five possible redshift fits for each spectrum using the tool `Marz` (Hinton, 2016). Redshift fits were visually inspected by three individual users, with each user able to select one of the `Marz` values or manually enter a different value. Each fit was assigned a confidence 'rating' between 0-3, where 3 is a confirmed detection (redshift

[2]https://mpdaf.readthedocs.io/en/latest/muselet.html

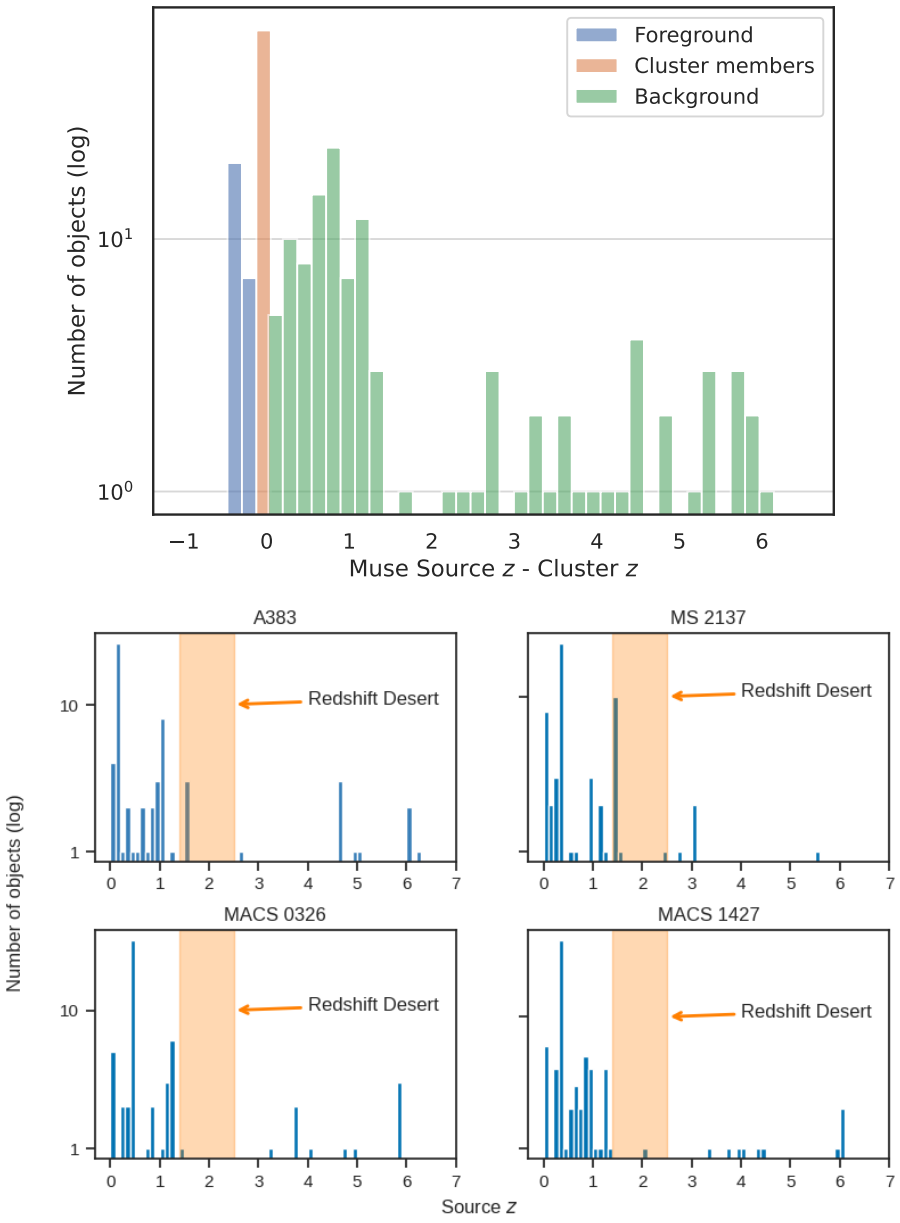


Figure 3.3: *Top:* Relative distribution of MUSE source redshifts for all clusters modeled in this chapter: A383, MS 2137, MACS J0326, and MACS J1427. Redshifts for MACS J0949 and MACS J0417 are not included as I did not perform source inspection for these clusters. All redshifts are plotted relative to 0, where 0 is equivalent to the cluster redshift and thus denotes all the cluster members identified via MUSE. *Bottom:* Exact distributions of redshifts for identified sources in the four clusters. The redshift desert, spanning the range $1.5 \lesssim z \lesssim 2.9$, is marked as the orange shaded region. The tallest bin in each cluster corresponds to the cluster redshift.

identified from multiple features or one unambiguous feature, such as a Ly-$\alpha$ or [OII] doublet), 2 is a probable detection (several lines that are noisy, which boosts the redshift error, or a single feature that is probably known but could also be something else, i.e. a blended [OII] line that could also be a wide [OIII] line or noisy Ly-$\alpha$), 1 is a possible detection (a best guess, though this is very uncertain), and 0 is no detection (no features, just noise). The selections of the three users were then evaluated against each other, and a complete catalogue was created for each cluster based on the agreement between these selections. Redshifts with a confidence rating of 3 were strongly agreed upon by all three users; redshifts with a confidence rating of 2 were tentatively agreed upon by all three users; and redshifts with a confidence rating of 1 were included as a 'best guess'. Confidence 1 redshifts were not included in the final lens models unless they were assigned to lensed galaxies whose positions were supported by the structure of the lens model. Figure 3.3.2 shows the distribution of redshifts found in the four source catalogues created for the galaxy clusters A383, MS2137, MACS J0326, and MACS J1427. Catalogues for MACSJ0949 and MACSJ0417 are not included in this paper as I did not perform source inspections for them; I refer the reader to Jauzac et al. (2019) and Allingham et al. (2023) for details.

Arc systems selected from *HST* photometry were confirmed with the full redshift catalogues for each cluster where possible; these catalogues can be found in Section 3.9.

## 3.4 Mass Modeling

Strong lensing is a powerful tool for modeling the mass distribution of galaxy clusters, but as I have described in previous sections, lensing as a technique cannot differentiate between baryonic and dark matter without ancillary information. This can be partially alleviated by breaking up the overall mass distribution into different 'clumps' of matter, such as cluster member galaxies or galaxy-scale perturbers, and modeling them as separate distributions from the main dark matter halo of the cluster. The BCG is a distinct component of any cluster mass model, and in the

case of radial arcs, it is particularly useful to model it separately to place stricter constraints on the mass potential at the center of the cluster (Newman et al. 2011). There are multiple ways to parameterize the BCG in the model. However, in this thesis, I elect to utilize a combination of kinematic measurements from VLT/MUSE and photometry from *HST* to place physical constraints on the distribution of mass in the BCG, following the example of N13. I describe the parameterization of the cluster mass in this section, and in the following section, I detail the kinematic measurements of the BCG.

### 3.4.1 Cluster Member Galaxies

Cluster member galaxies are selected using the cluster red sequence method (Gladders & Yee, 2000), which classifies galaxies as cluster members if they have colors consistent with the red sequence at the cluster redshift. Two different pass bands are required to perform a red sequence fit. An example red sequence for the galaxy cluster Abell 383 is presented in Figure 3.4. Cluster members are modeled following the description given in Section 2.3.2. I use 124 cluster members for A383, 78 for MS2137, 108 for MACS J0326, and 24 for MACS J1427. The cluster members used in MACS 0417 and MACS 0949 are described in Jauzac et al. (2019) and Allingham et al. (2023), respectively.

### 3.4.2 Multiple Images

The model is constrained using the positions of multiply imaged sources, or arcs, within the image. Arcs are identified through a combination of MUSE spectroscopy, visual identification of sources with matching color and morphology, and, where relevant, referencing previous models constructed for these clusters. The positions for each source with spectroscopy were fixed to the MUSE detections, which was especially relevant for each of the radial arcs, as their exact substructure and shape is obscured by the BCG light. A summary of the MCMC fit values for each cluster can be found in Table 3.2.

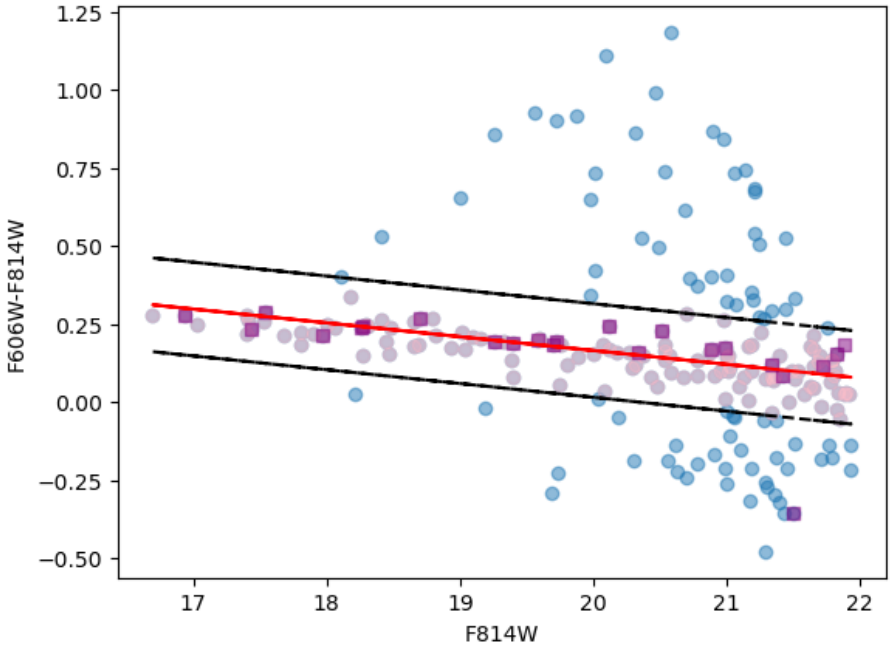


Figure 3.4: Example color magnitude diagram for Abell 383. All sources identified from photometric data are plotted in blue, and sources with spectroscopically confirmed redshifts around the cluster redshift ($z = 0.187$) are over plotted as purple squares. The red line corresponds to the best fit for the red sequence, with a slope of $0.044 \pm 0.015$ and an intercept of $1.05 \pm 0.30$. The boundary (f = 0.15) for cluster member selection is marked by the dashed black lines, and the sources identified as cluster members are marked as light purple circles.

Table 3.2: Statistical values derived from the `Lenstool` MCMC fitting for the models of each cluster presented in Section 3.4. Column 1 shows the likelihood, log $L$. Column 2 shows the rms deviation from the predicted positions of the multiple images from their observed positions in the image plane, $rms$. Column 3 shows the $\chi^2$. Column 4 shows the number of haloes optimized in the model. Column 5 shows the number of arcs used as constraints. Column 6 shows the number of cluster members included in the model.

| Cluster | log $L$ | $rms$ | $\chi^2$ | $N_{\rm halo}$ | $N_{\rm arcs}$ | $N_{\rm gals}$ |
|---|---|---|---|---|---|---|
| A383 | 18.73 | 0.61 | 35.76 | 5 | 29 | 123 |
| MS2137 | 16.01 | 0.70 | 14.22 | 2 | 16 | 59 |
| MACS J0326 | 11.05 | 0.85 | 23.08 | 3 | 12 | 80 |
| MACS J1427 | 7.41 | 0.61 | 0.83 | 2 | 4 | 27 |
| MACSJ0417 | 47.66 | 0.49 | 44.29 | 6 | 56 | 183 |
| MACSJ0949 | 80.17 | 0.41 | 17.58 | 3 | 21 | 177 |

### A383

Abell 383 ($z = 0.187$) was first modeled using `Lenstool` in Sand et al. (2004). It was later remodeled in Sand et al. (2008) in response to criticism leveled against the initial modeling method's assumptions ignoring cluster substructure, and using spherically symmetric mass distributions; the 2008 model used a full 2D strong lensing model to avoid making these assumptions. The cluster was then observed by CLASH (Postman et al. 2012b), and the discovery of a multiply-imaged system at $z = 6.027$ was reported in Richard et al. (2011), while a mass model was presented in Newman et al. (2011) and Newman et al. (2013a). Zitrin et al. (2011) then identified four new multiple image systems and presented an updated model, which was later refined with additional spectroscopy for one system by Zitrin et al. (2015).

A total of nine systems of multiple images are used to constrain the lens model. The properties of the systems are presented in Table 3.4. Systems 1, 2, and 9 are all fixed to the spectroscopic redshift measured and optimized from the MUSE cubes. The redshifts of the remaining systems were solved for by the lens model. Systems 2-9 are used in previous lens models of this cluster (Sand et al., 2008; Zitrin et al., 2011; Newman et al., 2011; Richard et al., 2011; Newman et al., 2013a; Zitrin et al., 2015), while system 1 is a new identification confirmed by MUSE spectroscopy.

### MS2137−223

MS 2137−23 ($z = 0.313$) was first modeled with `Lenstool` in Sand et al. (2004) and then updated in Sand et al. (2008) using a full 2D strong lensing model. Donnarumma et al. (2009) presented a mass profile for the cluster based on strong gravitational lensing and *Chandra X-ray Observatory* imaging. Newman et al. (2013b) later created a mass model with similar imaging and new Keck spectroscopy for seven multiply-imaged sources, and extended stellar velocity dispersions for the BCG. The lack of multiple images in these models caused them to all have slightly different results for the mass profiles. CLASH observations (Postman et al. 2012b) were later carried out on the cluster, and a new model with an additional multiply-imaged system with a confirmed spectroscopic redshift was published in Zitrin et al. (2015). A KMOS study has also recently been performed that includes several galaxies in

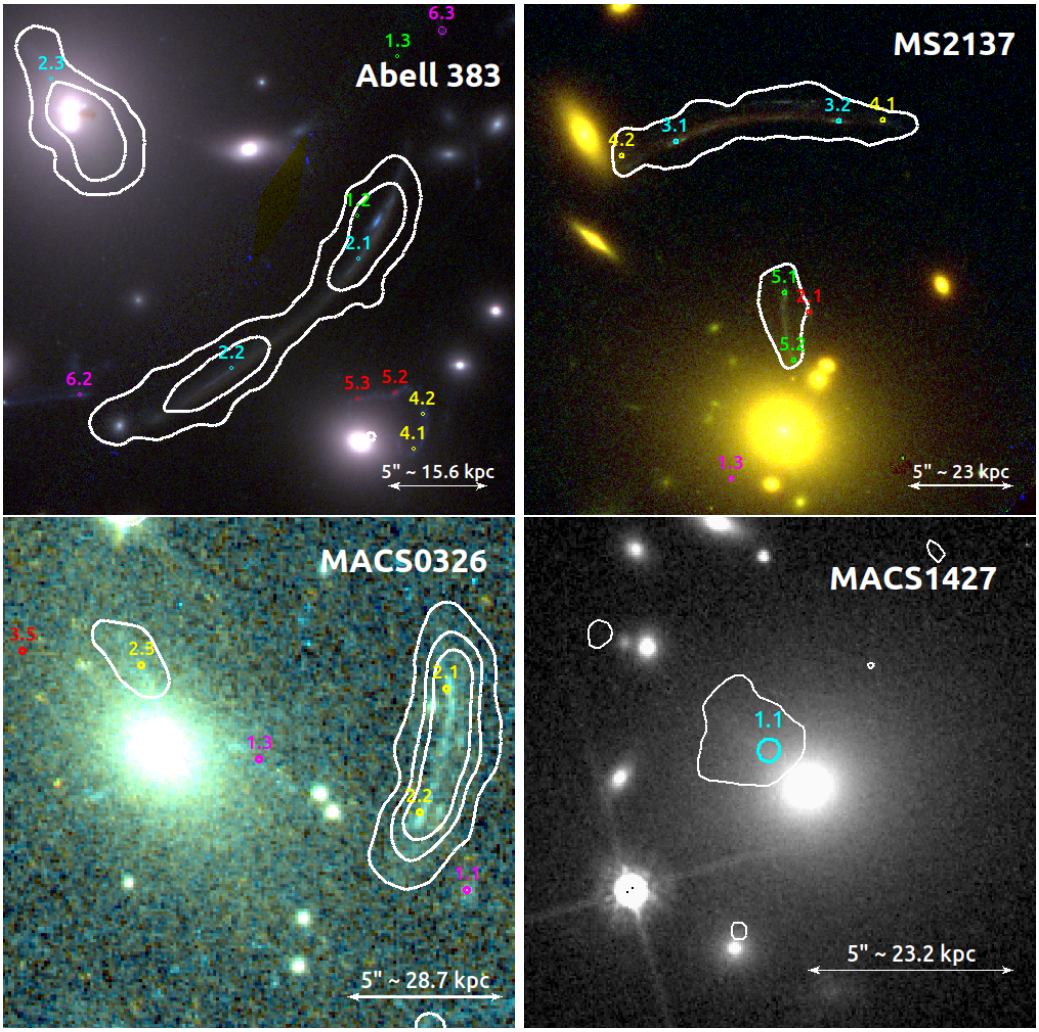


Figure 3.5: Snapshots of the radial arcs in each cluster. All images are oriented North-up, East-left. Each individual arc in a system is labeled as a pair of numbers, i.e. 1.1. In the case where an arc is labeled, for example, 1a.1, the letter corresponds to a sub-division of the same lensed galaxy 1. Each arc 'family' is marked in a different color for clarity. *Top Left*: A383 image of the BCG with MUSE detection contours for the radial arc and its nearby tangential counterpart at 7495 Å overplotted in white. *Caption continued on following page.*

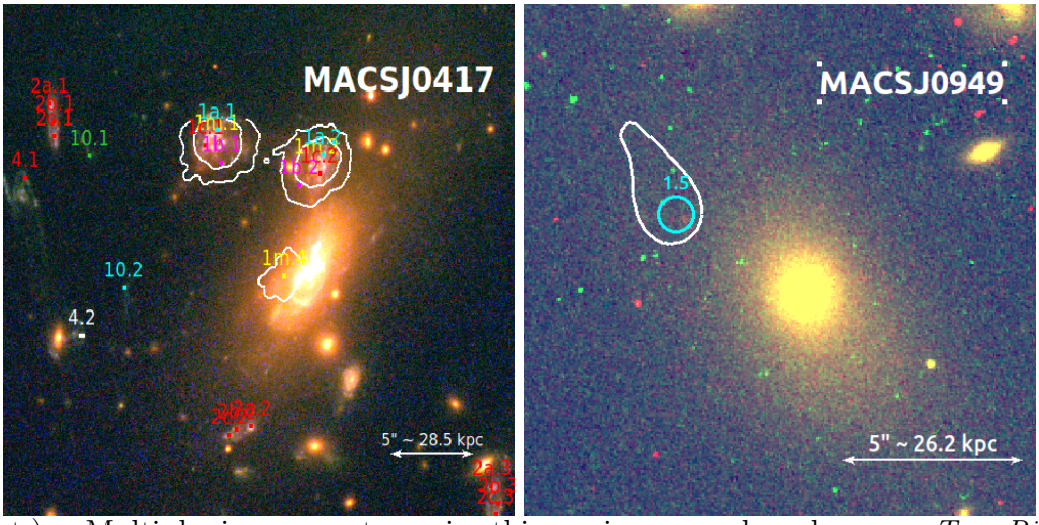


(cont.) Multiple image systems in this region are also shown. *Top Right*: MS 2137 image of the BCG with MUSE detection contours of the radial arcs and the nearby tangential arc at 9300 Å overplotted in white. Multiple image systems in this region are also shown. *Middle Left*: MACS J0326 image of the BCG with MUSE detection contours of the radial arc at 8376 Å overplotted in white. Multiple image systems in this region are also shown. *Middle Right*: MACS J1427 image of the BCG with MUSE detection contours of the radial arc at 7020 Å overplotted in white. Multiple image systems in this region are also shown. *Bottom Left*: MACSJ0417 image of the BCG with MUSE detection contours of the radial arc and its nearby counterpart images at 6975 Å overplotted in white. Multiple image systems in this region are also shown. *Bottom Right*: MACSJ0949 image of the BCG with MUSE detection contours of the radial arc at 7160 Å overplotted in white. Multiple image systems in this region are also shown.

MS 2137 (Tiley et al., 2020). This work created a sample of H$\alpha$ galaxies from the CLASH fields to study the evolution of star-forming galaxies in galaxy clusters, and found that their sample had systematically lower stellar masses than star-forming galaxies in the field, which hints at the role galaxy clusters have played in the formation of the red sequence over the past 10 Gyr.

A total of four systems of multiple images are used to optimize this lens model. The properties of the systems are presented in Table 3.5. All systems have redshifts from MUSE observations. System 1 was first identified in Zitrin et al. (2015), but only with photometric information. I confirm its redshift here with MUSE spectroscopy. The remaining systems are referenced in previous works (Sand et al., 2008; Donnarumma et al., 2009; Newman et al., 2013a; Zitrin et al., 2015). I note that while system 2 is not a new detection, this is the first time this arc has been included in a parametric lens model. I include this arc because the spectroscopic

Table 3.3: Values for the BCG of each cluster extracted from the photometric fitting process. Column 1 is the name of the cluster. Column 2 lists the filter used for the photometric fit of the BCG. Column 3 lists the $b/a$ value, where the ellipticity $e$ is defined as $e = 1 - b/a$. Column 4 lists the position angle $\theta$. Column 5 lists the magnitude of the BCG in the listed filter. Column 6 lists the $r_{\rm core}$ fit value. Column 7 lists the $r_{\rm cut}$ fit value. The errors for $r_{\rm core}$ are extremely small and are thus not listed.

| Cluster | Filter | $b/a$ | $\theta$ | Magnitude | $r_{\rm core}$ [kpc] | $r_{\rm cut}$ [kpc] |
|---|---|---|---|---|---|---|
| A383 | ACS/F606W | 0.87 | 81.77 | 18.82 | 2.26 | 35.5 $\pm$ 1.2 |
| MS2137 | ACS/F625W | 0.86 | 73.56 | 18.40 | 0.76 | 66.2 $\pm$ 12.3 |
| MACS J0326 | ACS/F606W | 0.55 | 46.66 | 19.56 | 1.74 | 77.9 $\pm$ 6.4 |
| MACS J1427 | ACS/F814W | 0.90 | -2.85 | 17.88 | 0.23 | 7.0 $\pm$ 0.31 |
| MACS J0949 | ACS/F606W | 0.52 | 31.12 | 19.96 | 2.81 | 70.6 $\pm$ 4.2 |
| MACS J0417 | ACS/F606W | 0.33 | -34.10 | 19.58 | 6.85 | 101.4 $\pm$ 29 |

redshift from MUSE allows it to be added to the model without introducing unnecessary extra noise; Table 3.5 shows this quite clearly, as the rms for both arcs in system 2 is under 0.3", which indicates that the model is able to reproduce the lensed positions of the multiple images very well. Systems 3 and 4 are parts of the same giant radial arc, and are adopted here as separate constraints in order to refine my lensing model.

### MACSJ 0326.8-0043

MACS J0326 ($z = 0.447$) was first discovered by the MAssive Cluster Survey SNAPshot programs (MACS, PI: Ebeling, Ebeling et al. 2001, Mann & Ebeling 2012), which amassed a sample of the most X-ray luminous galaxy clusters based on X-ray sources detected by the Röntgen Satellit (ROSAT) All-Sky Survey (Voges et al., 1999). These programs were designed to carry out *HST* observations of very X-ray luminous sources to obtain a statistically robust sample of massive distant clusters of galaxies. This is the first published mass model for this cluster.

Three systems are used in this lens model, with all systems having at least one image redshift from MUSE. The properties of the arc systems are presented in Table 3.6. All three arcs are new identifications as this cluster has not previously been modeled. System 2 is a clear tangential arc located North-East of the BCG, and has been split into a northern and southern part for the purposes of this model.

These arcs, 2.1 and 2.2, are MUSE detections, as is 2.3, which is the Northern radial arc shown in Figure 3.5. Image 2.4 is predicted by the model and is located on a similarly-colored source. Systems 1 and 3 are Lyman-$\alpha$ emitters. Images 3.1, 3.2, and 3.3 are MUSE detections, while 3.4 and 3.5 are predicted multiple images from the model. Image 1.2 is a MUSE identification, while images 1.3 and 1.4 are fixed to locations predicted by the model and are confirmed by the presence of similarly-colored sources in the image. Image 1.4 is of particular interest, as it hints at another radial arc next to the BCG. Figure 3.5 seems to indicate the presence of another source in this area, but the shallowness of the *HST* image makes it difficult to confirm. Deeper spectroscopic observations would be needed to confirm the legitimacy of this arc.

#### MACSJ 1427.6−22521

MACS J1427 ($z = 0.318$) was first observed as a part of the MACS programme (Ebeling et al. 2001). This is the first published mass model for this cluster.

Two multiple image systems are used to construct the lens model; the first is the radial arc located near the BCG (1.1), with a spectroscopic redshift of $z = 0.884$, while the second one is another spectroscopic identification at $z = 1.237$ (2.1). The properties of these systems are presented in Table 3.7. The arcs for this cluster are identified solely based upon their spectroscopic redshift and their relative orientation around the cluster in the context of a strong lensing model. The model predicts additional positions for these arcs, but the shallowness of the MUSE data makes it difficult to detect significant emission at these locations. Further, with only a single *HST* band of imaging data, I am unable to use color information to verify if they are lensed images of the same source. The predicted positions are listed in Table 3.7, but should be treated as potential candidates for a lensed arc position rather than a confirmed identification.

### 3.4.3 Additional Clusters with Radial Arcs

The clusters presented thus far represent new, original work. However, they are not the only clusters in the larger Kaleidoscope sample of MUSE cubes that have radial

arcs. In the interest of completeness, I introduce the two remaining clusters in the sample that have been modeled in work outside this chapter. These clusters have both been modeled using `Lenstool` following the methods already described in this chapter, which allows them to be directly incorporated into my broader analysis of the density profiles of galaxy clusters with radial arcs. These two clusters are MACS J0417 and MACS J0949. Both clusters were first observed as a part of MACS (Ebeling et al. 2001; Mann & Ebeling 2012).

MACS J0417 was recently modeled in Mahler et al. 2019 as a part of the Reionization Lensing Cluster Survey (RELICS; Coe et al. 2019), as well as in Jauzac et al. 2019 (J19), which included MUSE spectroscopy. I utilize the fiducial model from J19 in this analysis. The cluster is at a redshift of $z = 0.443$, and is constrained with a total of 17 lensed systems, three of which have spectroscopic redshifts confirmed by MUSE. System 1, a quadruply-lensed galaxy, is of particular interest, as it includes a radial arc whose position is identified from emission lines detected in MUSE, as it is otherwise obscured by the BCG in the available *HST* imaging. Unlike the other five clusters in the sample, MACS J0417 has a fairly elongated cluster core, which can be observed both visually by the separation in projection of the second and third brightest cluster galaxies from the BCG, as well as in the X-ray analysis (see J19), which shows extended emission along the SE-NW axis, as seen in Figure 3.4.3. These factors indicate that the cluster is likely the result of a recent merger, possibly oriented along the line of sight, which makes it the most dynamically complex cluster of the sample.

Finally, I include MACS J0949 in the sample, using the strong lens model recently published in Allingham et al. (2023). The cluster is at a redshift of $z = 0.383$, and X-ray data suggests that it is a post-merger in the process of relaxing. The strong lens model is constrained with a total of 6 lensed systems, two of which have spectroscopic redshifts confirmed by MUSE. Similarly to the other clusters in this paper, its radial arc is also detected by MUSE.

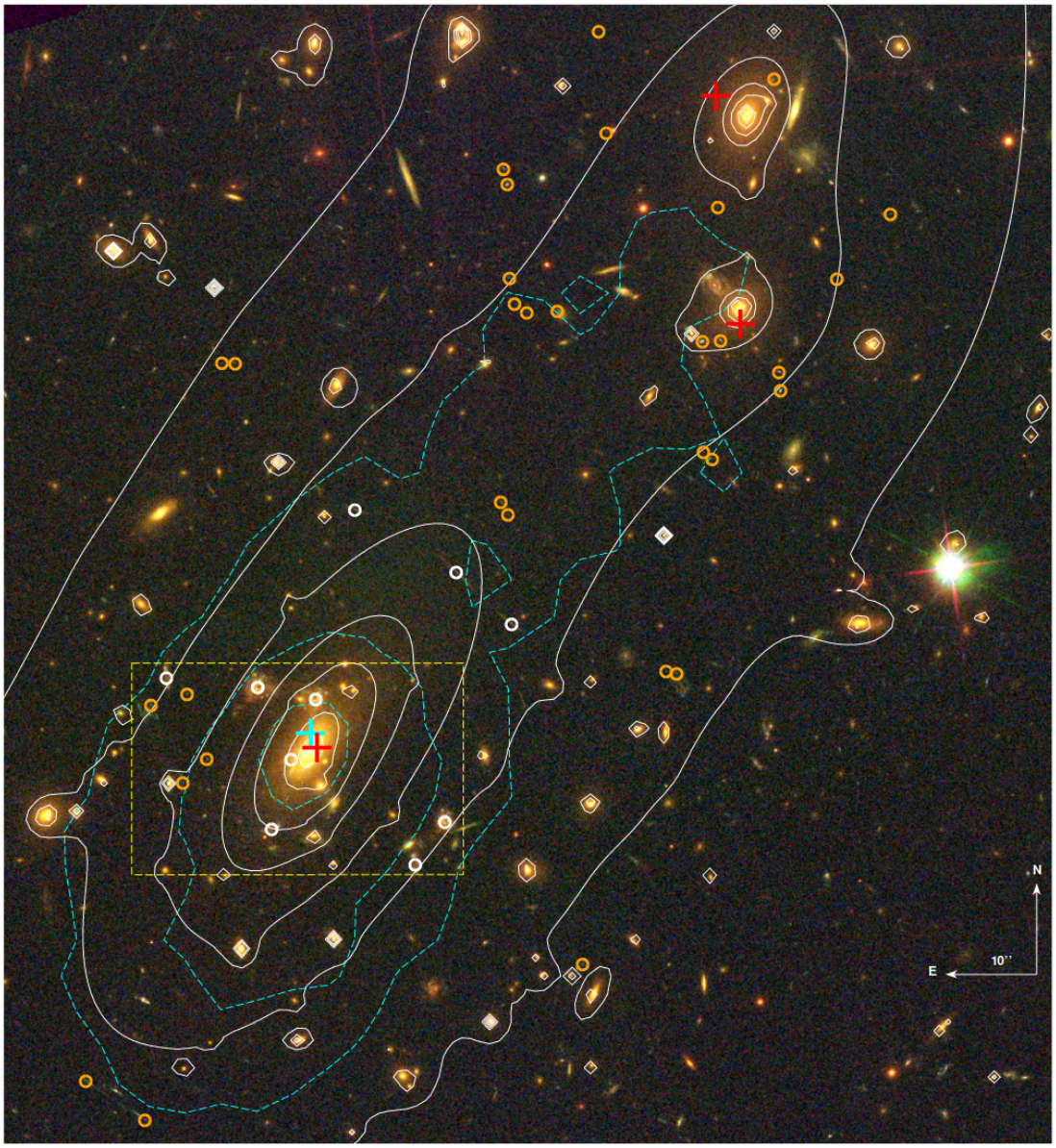


Figure 3.6: False color image of MACS J0417 created from HST/ACS and WFC3/UVIS images in the F814W, F606W, and F435W pass-bands. Orange circles denote the positions of multiple images, white circles denote multiple images with spectroscopic redshifts from MUSE, and the white contours show the mass distribution as reconstructed from the lensing mass model. Red crosses show the positions of dark matter clumps. The cyan cross is placed at the position of the X-ray peak, and the cyan contours show the distribution of gas from *Chandra* observations. J19 find that the main dark-matter halo is well aligned with the light peak of the BCG, but offset with respect to both the peak of the X-ray surface brightness and the peak of the optical line emission from the BCG. Reproduced from J19.

Table 3.4: Properties of the multiple images used as constraints for A383. Column 1 lists the ID of the image. Columns 2 and 3 list the Right Ascension and Declination, given in degrees (J2000). Column 4 lists the redshift value, $z$, where the redshifts for each image are either the spectroscopic value, where the redshift has no error bars, or the lensing model output value, in which case error bars are provided. Column 5 lists the rms for the best fit measured in the image plane for each family of multiple images. Column 6 lists the apparent magnification $\mu$ of each multiple image.

| ID | R.A. | Decl. | $z$ | rms (") | $\mu$ |
|---|---|---|---|---|---|
| 1.1 | 42.0128100 | -3.5257360 | 4.63 | 0.87 | $24.9 \pm 5.3$ |
| 1.2 | 42.0100370 | -3.5306870 | 4.63 | 0.30 | $> 50$ |
| 1.3 | 42.0094730 | -3.5284480 | 4.63 | 0.67 | $12.9 \pm 4.7$ |
| 1.4 | 42.0201622 | -3.5313367 | 4.63 | 0.71 | $4.4 \pm 2.2$ |
| 2.1 | 42.0100213 | -3.5312905 | 1.01 | 0.99 | $> 50$ |
| 2.2 | 42.0118119 | -3.5328386 | 1.01 | 0.95 | $13.8 \pm 1.8$ |
| 2.3 | 42.0143250 | -3.5288310 | 1.01 | 1.52 | $1.8 \pm 0.5$ |
| 3.1 | 42.0124986 | -3.5352872 | 2.55 | 0.56 | $8.1 \pm 0.7$ |
| 3.2 | 42.0095063 | -3.5331842 | 2.55 | 0.39 | $16.6 \pm 4.5$ |
| 3.3 | 42.0100403 | -3.5332656 | 2.55 | 0.74 | $2.6 \pm 1.3$ |
| 3.4 | 42.0159643 | -3.5351566 | 2.55 | 0.62 | $6.2 \pm 5.6$ |
| 4.1 | 42.0092467 | -3.5339770 | 2.55 | 0.09 | $8.2 \pm 3.2$ |
| 4.2 | 42.0091187 | -3.5334797 | 2.55 | 0.41 | $16.9 \pm 4.1$ |
| 4.3 | 42.0117750 | -3.5352866 | 2.55 | 0.42 | $6.7 \pm 2.3$ |
| 5.1 | 42.0136400 | -3.5263550 | 6.03 | 0.87 | $9.5 \pm 3.4$ |
| 5.2 | 42.0191904 | -3.5329396 | 6.03 | 0.71 | $4.8 \pm 4.3$ |
| 6.1 | 42.0177121 | -3.5314173 | $1.55 \pm 0.41$ | 0.56 | $15.3 \pm 8.7$ |
| 6.2 | 42.0139503 | -3.5332126 | $1.55 \pm 0.41$ | 0.36 | $15.2 \pm 7.8$ |
| 6.3 | 42.0088477 | -3.5280946 | $1.55 \pm 0.41$ | 0.20 | $7.7 \pm 3.2$ |
| 6.4 | 42.0153782 | -3.5267347 | $1.55 \pm 0.41$ | 0.40 | $3.1 \pm 1.7$ |
| 7.1 | 42.0170194 | -3.5239029 | $4.15 \pm 0.41$ | 0.87 | $18.3 \pm 9.6$ |
| 7.2 | 42.0148667 | -3.5231278 | $4.15 \pm 0.41$ | 0.96 | $> 50$ |
| 7.3 | 42.0130417 | -3.5229194 | $4.15 \pm 0.41$ | 1.05 | $11.0 \pm 3.6$ |
| 8.1 | 42.0153375 | -3.5235164 | $1.75 \pm 0.41$ | 0.33 | $> 50$ |
| 8.2 | 42.0141083 | -3.5232670 | $1.75 \pm 0.41$ | 0.37 | $> 50$ |
| 9.1 | 42.0165440 | -3.5331830 | $4.27 \pm 0.41$ | 1.12 | $> 50$ |
| 9.2 | 42.0171721 | -3.5326837 | $4.27 \pm 0.41$ | 0.04 | $18.5 \pm 9.6$ |
| 9.3 | 42.0161051 | -3.5264773 | $4.27 \pm 0.41$ | 0.72 | $12.6 \pm 4.6$ |
| 9.4 | 42.0078024 | -3.5279351 | $4.27 \pm 0.41$ | 0.89 | $5.0 \pm 2.2$ |

Table 3.5: Properties of the multiple images used as constraints for MS 2137. The format of each column is the same as the format for Table 3.4.

| ID | R.A. | Decl. | $z$ | rms (") | $\mu$ |
|---|---|---|---|---|---|
| 1.1 | 325.0653010 | -23.6627183 | 3.086 | 0.24 | 3.8 ± 1.5 |
| 1.2 | 325.0573784 | -23.6552507 | 3.086 | 0.97 | 3.2 ± 1.8 |
| 1.3 | 325.0639173 | -23.6617792 | 3.086 | 0.76 | 1.1 ± 0.45 |
| 2.1 | 325.0627881 | -23.6595561 | 1.19 | 0.27 | 31.7 ± 8.0 |
| 2.2 | 325.0660593 | -23.6669070 | 1.19 | 0.16 | 2.8 ± 1.1 |
| 3.1 | 325.0647182 | -23.6572985 | 1.495 | 0.08 | 7.9 ± 2.8 |
| 3.2 | 325.0623619 | -23.6570179 | 1.495 | 0.77 | 50.2 ± 7.1 |
| 3.3 | 325.0667908 | -23.6653782 | 1.495 | 0.68 | 3.9 ± 1.1 |
| 3.4 | 325.0590207 | -23.6614473 | 1.495 | 0.26 | 3.5 ± 1.3 |
| 4.1 | 325.0617177 | -23.6570091 | 1.495 | 2.07 | 17.3 ± 2.4 |
| 4.2 | 325.0654996 | -23.6574819 | 1.495 | 0.43 | 3.5 ± 1.9 |
| 4.3 | 325.0671724 | -23.6648956 | 1.495 | 0.13 | 4.5 ± 1.5 |
| 4.4 | 325.0671724 | -23.6648956 | 1.495 | 0.41 | 2.7 ± 1.1 |
| 5.1 | 325.0631385 | -23.6593017 | 1.496 | 0.40 | 3.8 ± 0.84 |
| 5.2 | 325.0630167 | -23.6601998 | 1.496 | 0.73 | 0.59 ± 1.1 |
| 5.3 | 325.0649681 | -23.6677483 | 1.496 | 1.43 | 2.6 ± 1.6 |

Table 3.6: Properties of the multiple images used as constraints for MACS J0326. The format of each column is the same as the format for Table 3.4.

| ID | R.A. | Decl. | $z$ | rms (") | $\mu$ |
|---|---|---|---|---|---|
| 1.1 | 51.70533 | -0.73235 | 3.755 | 1.57 | 9.2 ± 0.1 |
| 1.2 | 51.7140244 | -0.7348069 | 3.755 | 0.96 | 3.2 ± 2.2 |
| 1.3 | 51.7072192 | -0.7311556 | 3.755 | 0.38 | 6.0 ± 0.16 |
| 2.1 | 51.7055216 | -0.7305184 | 1.248 | 0.48 | 22.7 ± 5.3 |
| 2.2 | 51.7057628 | -0.7316436 | 1.248 | 0.56 | 11.7 ± 3.4 |
| 2.3 | 51.7082900 | -0.7303000 | 1.248 | 0.54 | 4.2 ± 0.6 |
| 2.4 | 51.71047 | -0.73444 | 1.248 | 0.93 | 22.6 ± 4.3 |
| 3.1 | 51.7018015 | -0.7310976 | 5.878 | 0.85 | 4.1 ± 2.3 |
| 3.2 | 51.7067455 | -0.7370053 | 5.878 | 0.65 | 6.7 ± 2.3 |
| 3.3 | 51.7048216 | -0.7359669 | 5.878 | 0.29 | 22.0 ± 10.5 |
| 3.4 | 51.7106978 | -0.7288662 | 5.878 | 0.53 | 7.9 ± 2.3 |
| 3.5 | 51.7093690 | -0.7301727 | 5.878 | 0.59 | 11.3 ± 3.4 |

Table 3.7: Properties of the multiple images used as constraints for MACS J1427. The format of each column is the same as the format for Table 3.4.

| ID | R.A. | Decl. | $z$ | rms (") | $\mu$ |
|---|---|---|---|---|---|
| 1.1 | 216.9148671 | 216.9148671 | 0.8836 | 0.24 | 1.9 ± 1.4 |
| 1.2 | 216.9148671 | 216.9148671 | 0.8836 | 0.24 | 11.2 ± 3.3 |
| 1.3* | 216.9165342 | -25.3486428 | 0.8836 | 0.24 | 3.7 ± 1.9 |
| 2.1 | 216.9106579 | -25.3536281 | 1.23655 | 0.174 | 7.6 ± 2.8 |
| 2.2 | 216.9199276 | -25.3461304 | 1.23655 | 0.174 | 25 ± 5.1 |
| 2.3* | 216.9131520 | -25.3518332 | 1.23655 | 0.174 | 1.2 ± 1.1 |

Table 3.8: Summary of VLT/MUSE observations used. Column 1 is the name of the cluster. Column 2 lists the seeing for the observation. Column 3 lists the airmass. Column 4 lists the P.I. for the observation. Column 5 lists the exposure time. Column 6 lists the observation date. Column 7 lists the ESO Programme ID.

| Cluster | Seeing | Airmass | P.I. | Exp. time [s] | Obs. date | ESO Programme ID |
|---|---|---|---|---|---|---|
| A383 | 1.0" | 1.74 | Edge | 2910 | 2019-11-17 | 0104.A-0801(B) |
| MS2137 | 1.0" | 1.86 | Edge | 2910 | 2019-06-28 | 0103.A-0777(A) |
| MACS J0326 | 0.5" | 1.09-1.11 | Edge | 2910 | 2019-09-21 | 0103.A-0777(A) |
| MACS J1427 | 1.0"-1.5" | 1.01-1.06 | Edge | 2910 | 2018-03-14 | 0100.A-0792(A) |
| MACS J0417 | 1.6" | 1.8 | Edge | 2910 | 2017-12-12 | 0100.A-0792(A) |
| MACS J0949 | 0.71" | 1.4 | Edge | 2910 | 2020-02-20 | 0104.A-0801(A) |

## 3.5 BCG Kinematics

I introduce kinematic constraints into the total density profile of each cluster in order to more closely examine the shape of the mass distribution in the inner 10 kpc of the cluster. Following the methods used in Sand et al. (2004) and Newman et al. (2013b), I include the velocity dispersion of the BCG as an additional constraint for the `Lenstool` model. I incorporate this constraint by measuring observable properties of the BCG through a combination of photometry and spectroscopy. I model the BCG as a separate dPIE mass halo (see Section 2.3.1) within `Lenstool`, with its positional parameters ($x$, $y$, $e$, $\theta$) and two PIEMD parameters ($r_{\rm core}$, $r_{\rm cut}$) fixed to the values obtained from these measurements.

The following subsections discuss the measurements of the observable properties of the BCG that I use to fix the parameters of the BCG mass halo, as well as to constrain the lens model using my kinematic measurements. The combination of kinematics and lensing is discussed more thoroughly in Section 3.6.3.

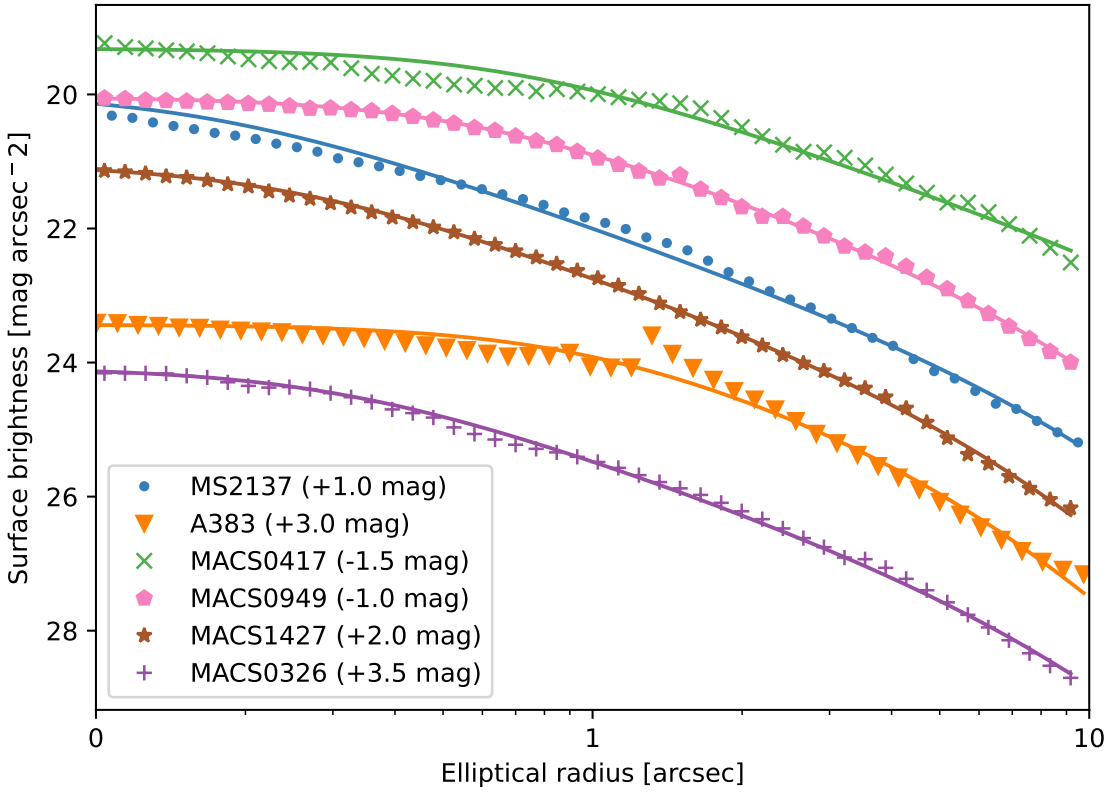


Figure 3.7: Surface brightness profiles of the BCGs for all six clusters, measured using the filters listed in Table 3.3. The dPIE fit for each profile is plotted as the solid line of the same color as each cluster. The magnitudes for each cluster are offset by the listed values to provide visual clarity.

### 3.5.1 BCG Photometry

The surface brightness profile of the BCG in each cluster is measured using *HST* imaging, where preference was given to the *ACS*/F606W filter to more closely align the photometric fit with the wavelengths used in the kinematic fit since these BCGs are largely red and dead. This band was used for A383, MACS J0326, MACS J0949, and MACS J0417, while the *ACS*/F814W filter is used for MACS J1427. However, in MS2137, where this band has a gap in data around the BCG, the F625W filter was used. In MACS J1427, where this band is not available, the F814W filter was used instead. Surrounding objects in the field are masked out using a SExtractor segmentation map, and the PSF is modeled using a field star and a selection of surrounding sky. The BCG light is modeled using the 2-dimensional dPIE profile as described in `Lenstool` (Equation 2.8).

This equation is fitted by using the light profile extracted from isophotal measurements of the BCG. The geometric parameters of ellipticity, position angle, and center coordinates of the central isophote are fixed to the values obtained from fitting a de Vaucouleurs $R^{1/4}$ profile to the 2D data using `GALFIT` (Peng et al. 2002, 2010). The Python Astropy Elliptical Isophote Analysis routine is then used to find the best-fit model for the 2D data out to about 20 kpc, where the light from other objects in the field begins to dominate the light from the BCG, and run the fit in the "bilinear area integration mode". The 1D surface brightness profile is then fit to the dPIE equation, with only the central velocity dispersion, $\sigma_0$, allowed to vary during the fit.

Finally, since the mass of the BCG is used as a constraint in the modeling, a stellar mass-to-light ratio is required to transform the dPIE fit to the light into the mass of the BCG. This value is obtained by performing a SED fit of the combined photometric (see Table 3.1) and spectroscopic (see Table 3.8) data using `pPXF` (Cappellari 2017). I use the Flexible Stellar Population Synthesis (FSPS) models library (Conroy et al. 2009, Conroy & Gunn 2010) generated in Cappellari (2023) as the basis for the fit, which was created using a Salpeter IMF with a mass range between 0.08 and 100 $M_\odot$. These models do not explicitly include the effect of gas or dust, which does not affect the measurements of BCGs in this sample of clusters. The spectra for these Stellar Population Synthesis (SPS) models were created using the MILES stellar library (Sánchez-Blázquez et al. 2006, Falcón-Barroso et al. 2011). The library of these spectra are used to fit the stellar mass-to-light ratio of the BCGs in each cluster.

**Paragraph about radially varying mass to light ratio**

The resulting parameters, surface brightness profiles, and dPIE fits are presented in Table 3.3 and Figure 3.7. This fit enables the simple creation of a separate mass halo for each BCG, whose properties are fixed to these photometric values. I specifically fix the ellipticity, the position angle, and the values of $r_{\rm core}$ and $r_{\rm cut}$. The only free parameter is then the velocity dispersion, $\sigma_0$, which serves as a constraint on the mass profile in the model.

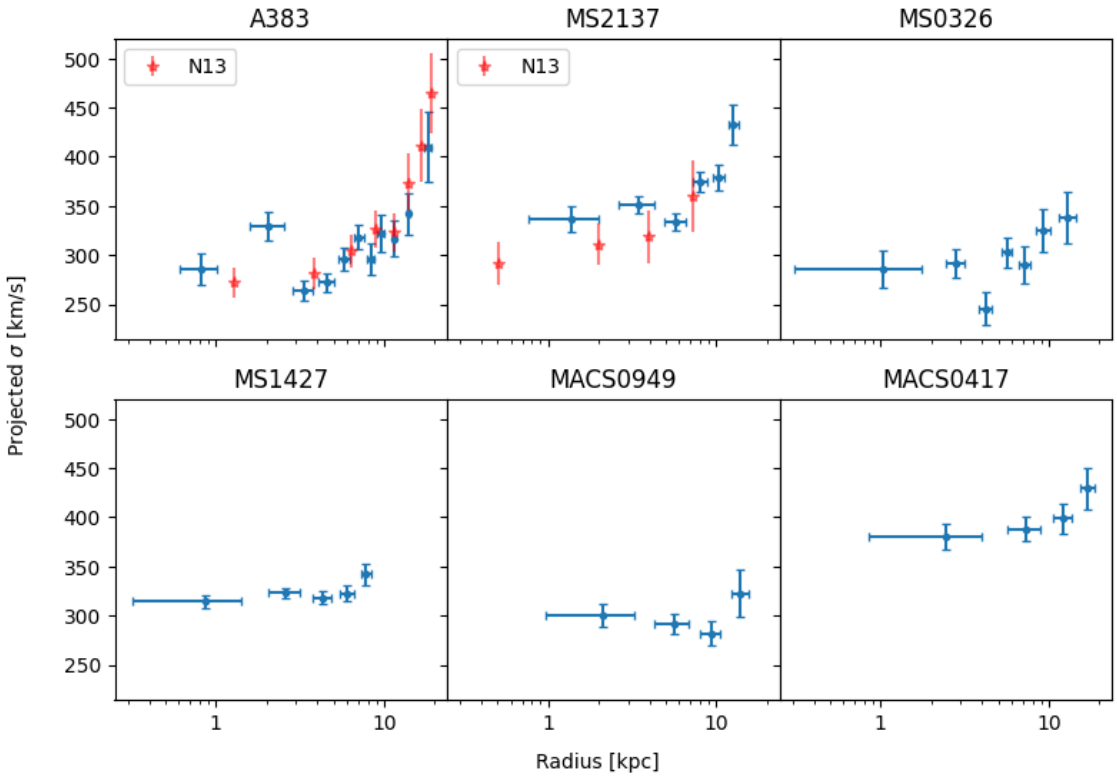


Figure 3.8: BCG stellar velocity dispersion profiles for all six clusters. The error in the velocity dispersion is denoted by the errorbars along the Y axis, while the errorbars on the X axis signify the width of the bin used to make the measurement. The datapoints are centered at the middle of each bin, and each point corresponds to the reported $\sigma$ value in Table 3.9. For the clusters A383 and MS2137, the values reported in N13 are over-plotted as red stars for reference.

### 3.5.2 Velocity Dispersion Profile

BCG kinematics are utilized in tandem with lensing to break down the total mass distribution of the cluster into more clearly defined baryonic and dark matter components. Modeling the BCG mass using stellar dynamics allows for limits to be placed on the contribution of the BCG to the cluster density profile in the very inner region (R <10 kpc), which in turn allows for a more precise examination of the behavior of dark matter in this region.

I model the kinematics of the BCG by creating a profile of the velocity dispersion in different bins, stepping out from the center of the BCG until the S/N ratio dips below a cutoff threshold of 30, which is equivalent to a distance of about ∼20 kpc for each cluster. I choose this S/N cutoff based on the work done in Bergamini et al. (2019), which measured systematic error from `pPXF` measurements of cluster

Table 3.9: Values for the velocity dispersion profile for the BCG of each cluster. The quoted $\sigma$ values are measured at the midpoint of each bin. Column 1 lists the cluster. Column 2 lists the total extent of each bin in arcsec. Column 3 lists the total extent of each bin in kpc. Column 4 lists the measured velocity dispersion in that bin.

| Cluster | Bin [arcsec] | Bin [kpc] | $\sigma$ [km/s] |
|---|---|---|---|
| A383 | 0.0-0.26 | 0.0-0.81 | 285 ± 14 |
| | 0.46-0.66 | 1.44-2.07 | 329 ± 12 |
| | 0.86-1.06 | 2.69-3.32 | 263 ± 10 |
| | 1.26-1.46 | 3.94-4.57 | 272 ± 10 |
| | 1.66-1.86 | 5.19-5.82 | 295 ± 13 |
| | 2.06-2.26 | 6.45-7.07 | 318 ± 15 |
| | 2.46-2.66 | 7.70-8.32 | 296 ± 16 |
| | 2.86-3.06 | 8.95-9.57 | 322 ± 17 |
| | 3.30-3.66 | 10.33-11.45 | 316 ± 20 |
| | 4.46-5.06 | 13.96-15.83 | 341 ± 24 |
| | 5.86-7.26 | 18.34-22.72 | 409 ± 28 |
| MS2137 | 0.0-0.50 | 0.0-2.30 | 337 ± 13 |
| | 0.50-1.0 | 2.30-4.60 | 350 ± 9 |
| | 1.0-1.5 | 4.60-6.90 | 334 ± 8 |
| | 1.5-2.0 | 6.90-9.20 | 374 ± 10 |
| | 2.0-2.5 | 9.20-11.50 | 378 ± 13 |
| | 3.0-3.5 | 13.80-16.09 | 404 ± 19 |
| MACS J0326 | 0.43-0.73 | 2.47-4.19 | 238 ± 15 |
| | 0.73-1.08 | 4.19-6.20 | 276 ± 15 |
| | 1.08-1.66 | 6.20-9.52 | 291 ± 17 |
| MACS J1427 | 0.0-0.38 | 0.0-1.76 | 320 ± 9 |
| | 0.38-0.75 | 1.76-3.48 | 312 ± 9 |
| | 0.75-1.12 | 3.48-5.19 | 297 ± 10 |
| | 1.12-1.5 | 5.19-6.95 | 301 ± 11 |
| | 1.5-1.88 | 6.95-8.71 | 326 ± 16 |
| | 1.88-2.25 | 8.71-10.43 | 344 ± 21 |
| | 2.25-2.62 | 10.43-12.14 | 407 ± 31 |
| MACSJ0949 | 0.0-0.71 | 0.0-3.71 | 300 ± 12 |
| | 0.71-1.42 | 3.71-7.43 | 292 ± 10 |
| | 1.42-2.13 | 7.43-11.14 | 282 ± 12 |
| | 2.13-3.18 | 11.14-16.63 | 323 ± 24 |
| MACSJ0417 | 0.0-0.85 | 0.0-4.85 | 380 ± 13 |
| | 0.85-1.7 | 4.85-9.70 | 388 ± 13 |
| | 1.7-2.55 | 9.70-14.56 | 399 ± 15 |
| | 2.55-3.4 | 14.56-19.40 | 429 ± 22 |

members in MUSE spectroscopic observations and found that an S/N $< 10$ produced unreliable velocity dispersion measurements. I tested this threshold on my own data for the BCG and used the velocity dispersion measurements from N13 for A383 and MS2137 as a reference. I then increased the S/N threshold until I was able to reduce the systematic error of the velocity dispersion to under 20%.

I utilize the MUSE observations from the Kaleidoscope survey to make these measurements of the velocity dispersion. As these observations are all short exposures, the cubes are binned using concentric circular annuli, which maximizes the S/N ratio in each bin and works well for most of the BCGs used in this chapter because they are all nearly circular (see Section 3.5.4 for more details). The width of each annulus is determined by the S/N ratio, where each bin is required to be large enough to obtain a total S/N ratio greater than 30. Each spectrum is fitted over a rest-frame wavelength of 4860-7160 Å, which includes the regions where MUSE sensitivity is the strongest, and excludes regions where sky line residuals are very large.

Nearby bright stars and galaxies are masked out before the fit is performed for each BCG, and bins where these objects interfere strongly with the BCG light are excluded. I choose to mask out surrounding galaxies despite their potential contribution to the velocity dispersion profile because there is no information available that can determine where they are located in the 3D space of the cluster. Additionally, failing to mask these objects distorts the velocity dispersion toward non-physical values. This is particularly relevant for MACS J1427, which has a bright foreground star situated within 5" of the BCG (see Figure 3.5). While masking this star allows for an effective measurement of the velocity dispersion, the fitting is unable to continue past about 10 kpc due to the contamination from the flux of this star and the surrounding cluster galaxies.

The `pPXF` fit for each cluster relies on the use of additive and multiplicative polynomials in order to match the template spectra to the observed VLT/MUSE spectrum. These polynomials are adjusted until the fit in the highest S/N bin of each cluster no longer improves. One first-order multiplicative polynomial is used for every cluster except MS2137, which uses a third-order polynomial, and a fifth-order

additive polynomial is used for every cluster.

These measurements of the velocity dispersion can be compared directly to the results found in Newman et al. (2013a). Figure 3.8 shows the velocity dispersion profiles for all six clusters analyzed in this chapter, and additionally shows how these results compare to those derived in N13 for the clusters A383 and MS2137. The N13 results are based on a Keck/LRIS 23.7 ks exposure with 0.8" seeing for A383, and a Keck/ESI 6.7 ks exposure with 0.7" seeing for MS2137. Relative to the MUSE data, the archival data have a 10x and 3x longer exposure time for A383 and MS2137. Measured seeing conditions were on average 0.2" narrower. However, the advantage of MUSE rests in the ability of IFU observations to capture information about the entire structure of the BCG. In other words, area recovers depth. This is well supported by the measured profiles, because while there is some variation in the innermost bins, the shape of the profile for A383 and MS2137 is generally well reproduced by the measurements. This suggests that this characterization of the BCG profile in the MUSE data is consistent with archival measurements, despite the difference in observing conditions and instrumentation.

### 3.5.3 Extraction Annulus

In this section, I briefly discuss the decision to use a circular annulus to extract the velocity dispersion profile of the BCG, rather than a typical circular aperture. As mentioned briefly in the previous section, the VLT/MUSE data from Kaleidoscope are often shallow and somewhat noisy, which is a consequence of Kaleidoscope's status as a 'filler' programme. In other words, since these observations were classified as non-priority and were made opportunistically to fill a normal observing schedule, the atmospheric conditions were not always ideal. The quality of these observations gave rise to the natural question of whether the intrinsic properties of the MUSE instrument were capable of reproducing an accurate velocity dispersion profile for the BCG.

I tested what effects the shallowness of these observations had on the measured velocity dispersion profile by making use of archival VLT/MUSE data for the galaxy cluster Abell 370 (A370). This data was obtained as a part of the Beyond Ultra-

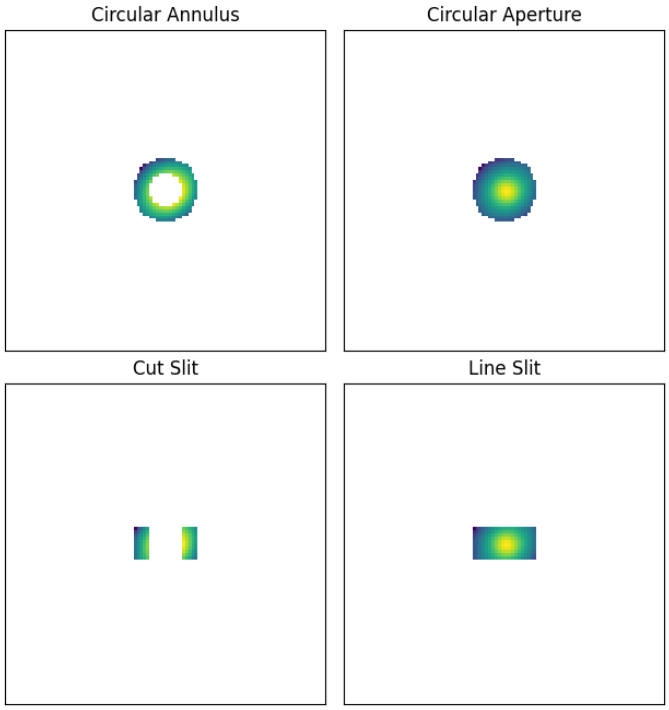


Figure 3.9: Example of the different aperture extractions used to make the velocity dispersion profile measurements. The apertures are positioned over the BCG of A370 and are plotted between 1″ and 2″.

deep Frontier Fields And Legacy Observations (BUFFALO) survey Steinhardt et al. (2020), which sought to expand the existing Hubble Frontier Fields imaging by up to a factor of four times the area of the original pointings. Lagattuta et al. (2019) contains more details about the VLT/MUSE observations for this cluster.

The southernmost BCG for A370 was used to test the effect of depth on MUSE's ability to recapture the velocity dispersion profile of the BCG. The total MUSE observations for A370 had an equivalent depth of 8 hrs of exposure time on the southern BCG. These observations were combined into a single 'deep cube'. This stack was then reduced to have an equivalent exposure time of just one hour, which formed a single 'shallow cube'. I then extracted the velocity dispersion profile using `pPXF` in four different apertures for both the deep and shallow cubes. These apertures were described by a circular aperture, a circular annulus, a line slit, and a 'cut' slit, which described a line slit with the center cut out. An example of these aperture cutouts can be seen in Figure 3.9. The profile was extracted over a series of radial bins, which were selected to have a minimum S/N of 30. The resulting profiles are shown

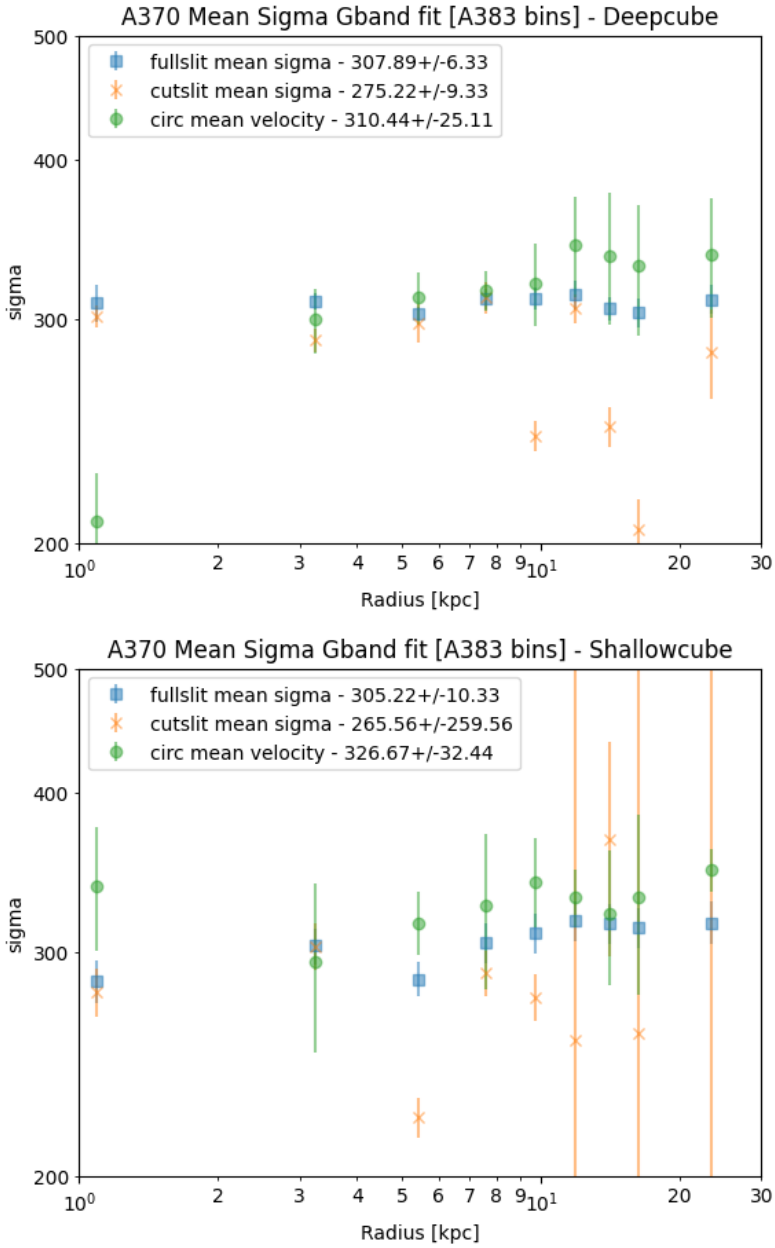


Figure 3.10: BCG stellar velocity dispersion profile for the galaxy cluster A370. The left panel shows the profile as measured from three different aperture extractions in a cube with an effective exposure time of 8 hours, while the right panel shows the same profile measured from the same apertures in a cube with an effective exposure time of 1 hour. The profiles are largely the same despite the difference in depth, which shows that as long as the errors of the velocity dispersion profile can be minimized, the profile can be recovered from shallow data. The minimization of these errors can happen by choosing different apertures for the extraction of the profile.

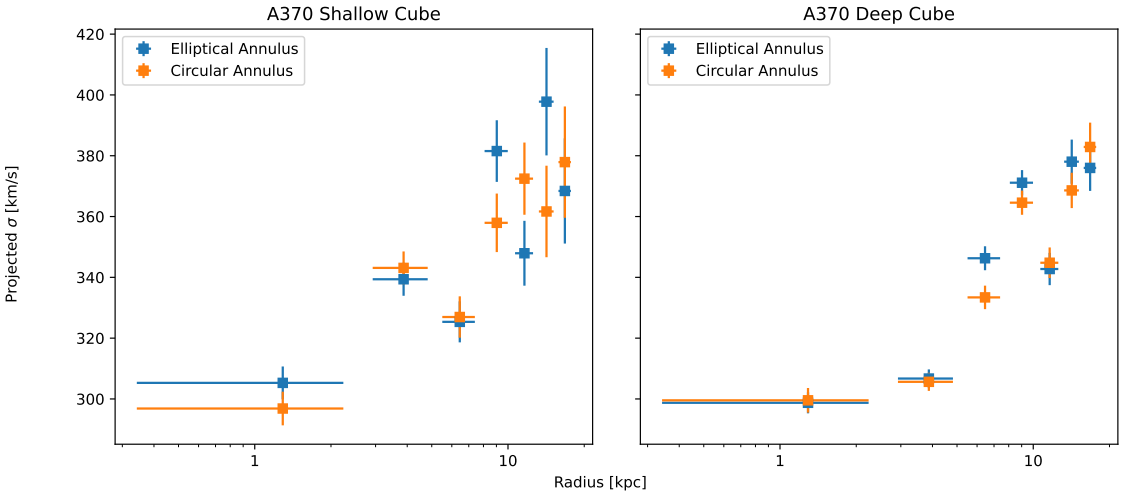


Figure 3.11: BCG stellar velocity dispersion profile for the galaxy cluster A370. The left panel shows the profile as measured from the shallow cube described in Figure 3.10, while the right shows the profile as measured from the deep cube. In both panels, the velocity dispersion profile is shown for an extraction made using a circular annulus originating from the peak of the BCG, and for an extraction made using an elliptical annulus with ellipticity and position angle fixed to the measured light distribution.

in Figure 3.10. The primary test of this deep and shallow cube was to determine if the profiles were dramatically different from each other with different apertures. The result showed that the shallow cube increased errors fairly significantly, but the general shape of the velocity dispersion profile was the same in both the deep and the shallow cube regardless of the aperture used to extract the profile.

I performed an additional test using the datacubes from A370 regarding the difference between calculating the velocity dispersion profile using a circular annulus, as compared to an elliptical annulus. The results of this test are shown in Figure 3.11. The profiles are functionally the same, demonstrating that using a circular annulus is a good measurement of the velocity dispersion profile in both short exposure and longer exposure observations. However, the circular annulus has a higher S/N ratio than the elliptical annulus for the clusters in this sample with nearly circular $b/a$ ratios: A383, MS 2137, and MACS J1427. In these BCGs, I use circular annuli to extract the velocity dispersion profile. For the more oblong BCGs in MACS J0326, MACS J0949, and MACS J0417, I elect to use elliptical annuli.

I then tested the effects of the aperture itself on the profile. I used A383 as

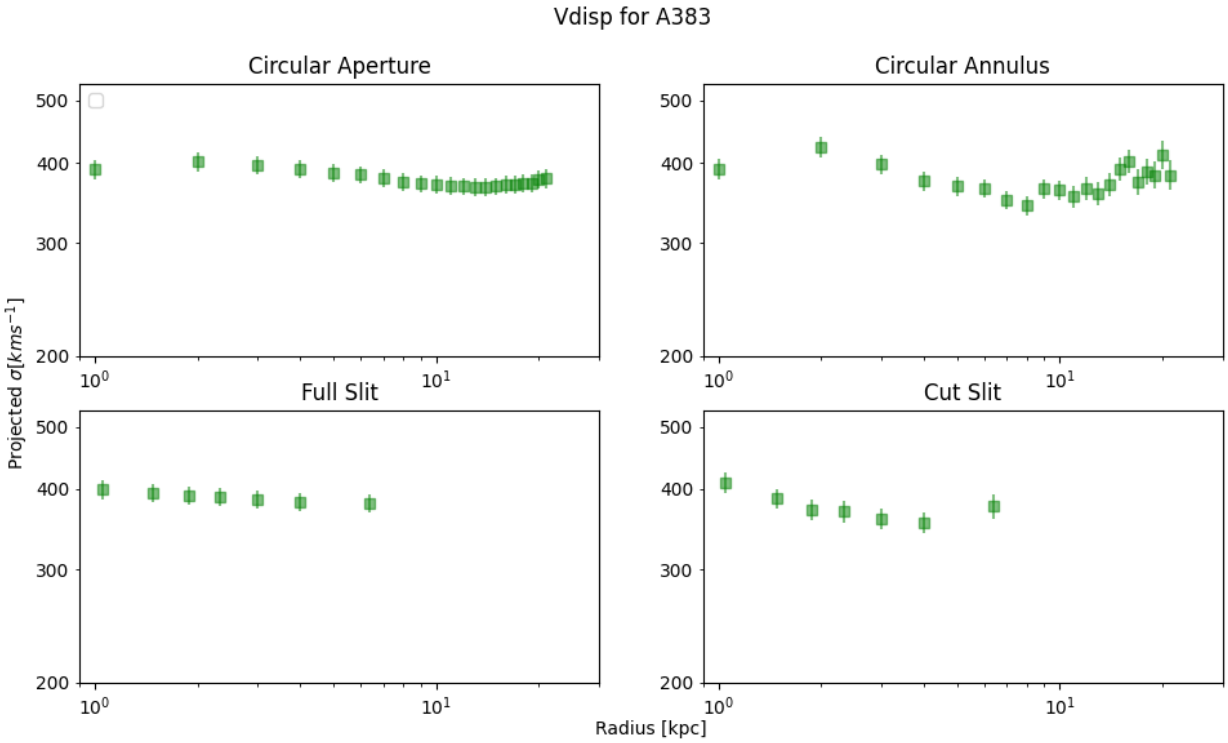


Figure 3.12: BCG stellar velocity dispersion profile for the galaxy cluster A383, as measured with four different aperture selections. The top left panel shows the profile extracted using a circular aperture, the top right panel shows the profile extracted using a circular annulus, the bottom left panel shows a slit, and the bottom right panel shows a 'cut' slit, which is constructed as a slit version of the circular annulus aperture (i.e. a slit with the central region cut out). The circular annulus best reproduces the shape of the velocity dispersion profile.

a reference for this test, since published measurements for the velocity dispersion profile of this cluster exist in literature (see both Sand et al. (2004) and N13). I used four different apertures as a test: a full slit, a cut slit, a circular aperture, and a circular annulus. The results of this test are shown in Figure 3.12. The circular annulus was the aperture most able to reproduce the expected behavior of the velocity dispersion profile of the BCG (i.e. rising with radius because the BCG is embedded in the cluster dark matter halo). This is because an annulus maximizes the S/N of a region by minimizing regions containing potential noise. The top two left panels of Figure 3.8 reinforce the ability of this aperture on the VLT/MUSE IFU cube to reproduce measurements comparable to long-slit exposures made with Keck/LRIS.

### 3.5.4 Rotational Velocity and Anisotropy

In Section 3.6.3, all BCGs are treated as isotropic in the application of the spherical Jeans equation, which is a simplification that warrants some brief additional discussion. While half the BCGs in this sample are nearly circular (b/a $\sim$ 0.85), the other three are more oblate (0.33-0.55), and the noticeably elliptical shape of MACS J0417 makes this assumption harder to justify.

To examine the effects of anisotropy on the BCGs, two different methods are used to evaluate what changes this effect might have on the lensing models. First, the anisotropic Jeans equation is used and the anistropy is fixed to a small, constant value ($\beta = 0.3$) to examine how this affects the results. This value was chosen because BCGs lack significant rotation (see Kronawitter et al. (2000), which studied 21 giant ellipticals and found that the velocity anisotropy was less than $\beta < 0.3$ for the majority of the sample, and Santucci et al. (2023), which measured a similar value for central ellipticals). This sample of BCGs is no exception, as inspection of the velocity maps for each BCG shows no significant rotation. Second, for MACS J0417, I employ the more robust external modeling programme JamPy (Cappellari 2020) in conjunction with MgeFit (Cappellari 2002) to examine the specific effect anistropy might have on this cluster. Introducing a constant anisotropy value shifts the value of the derived velocity dispersion by roughly $\pm$5 km/s in all cases. The more robust examination of anisotropy in MACS J0417 results in around the same changes. Even the most complex BCG is thus still able to be analyzed using this spherical symmetry assumptions.

## 3.6 Results

### 3.6.1 Mass Models

#### Abell 383

The properties of the multiple image systems are given in Table 3.4. One cluster-scale dark matter halo is used to model the cluster, and a total of four galaxy-scale halos are included to separately model the mass distribution of the BCG, as well

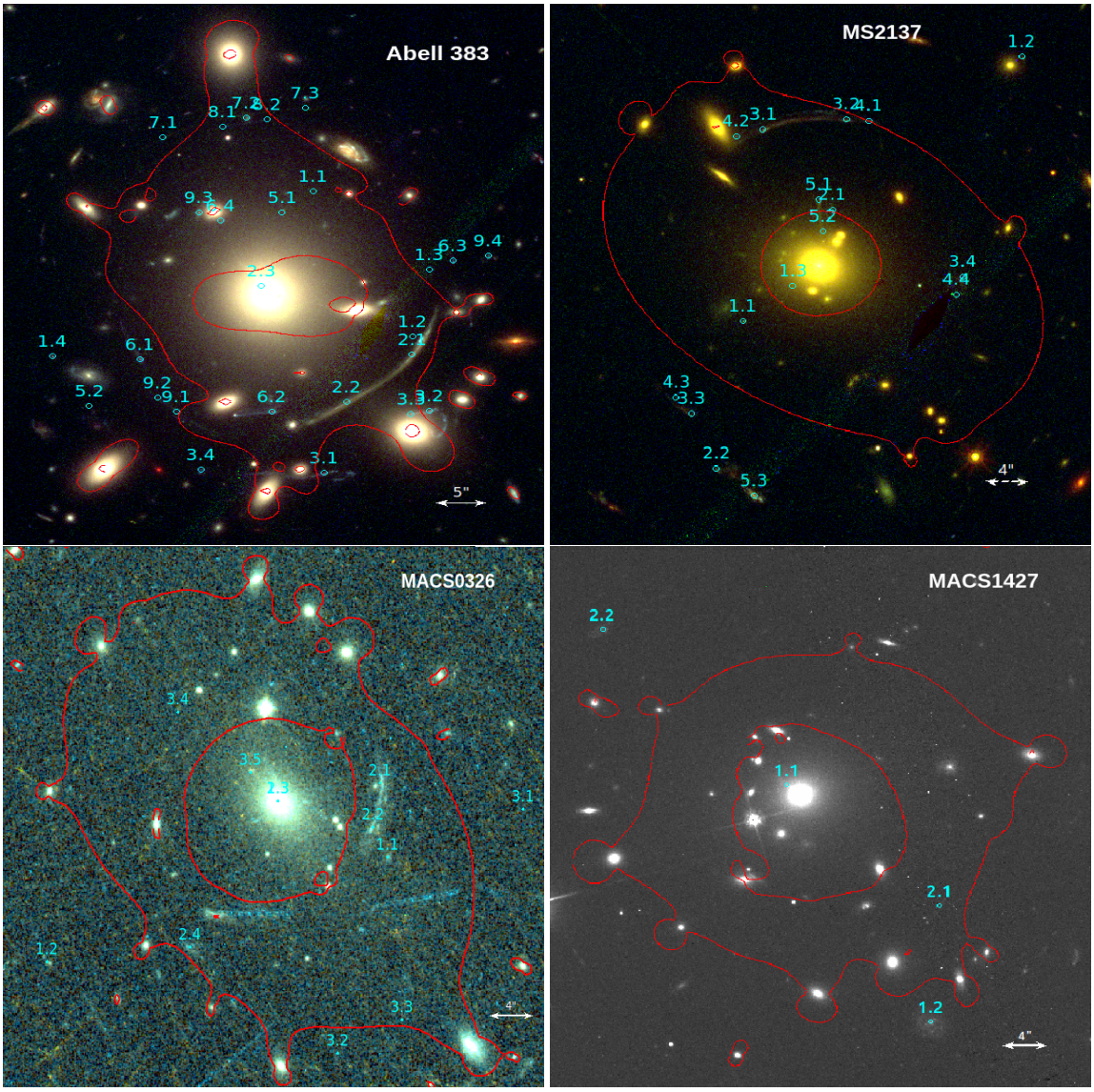


Figure 3.13: Images of the four clusters newly modeled in this chapter. All images are oriented North-up, East-left. *Top Left: HST* composite color image of A383 created using a combination of WFC3/IR imaging in the red (F160W) and ACS imaging in the green (F814W) and blue (F606W). Multiply imaged galaxies are labeled in cyan. The red curve marks the location of the critical curve for a source at $z = 3.0$. *Top Right:* False color image of MS 2137 created using a combination of WFC3/IR imaging in the red (F160W) and ACS imaging in the green (F814W) and blue (F606W). Multiply imaged galaxies are labeled in cyan. The red curve marks the location of the critical curve for a source at $z = 2.5$.*Lower Left:* False color image of MACS J0326 created using a combination of ACS imaging in the green (F814W) and blue (F606W). Multiply imaged galaxies are labeled in cyan. The red curve marks the location of the critical curve for a source at $z = 3.0$. *Lower Right:* F814W image of MACS J1427. Multiply imaged galaxies are labeled in cyan. The red curve marks the location of the critical curve for a source at $z = 1.2$.

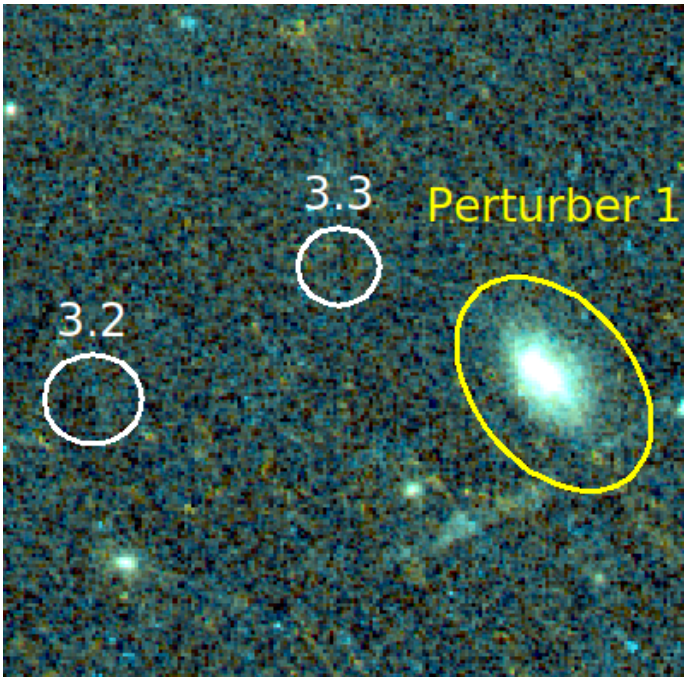


Figure 3.14: Snapshot of the galaxy-scale perturber used for the model of MACS J0326. The location of the galaxy-scale halo is marked in yellow, and the arc locations are shown as white circles.

as three cluster members located near systems 3 and 4. The best fit parameters for these halos are given in Table 3.11. The integrated density profile is presented in Figure 3.16. A snapshot of the radial arc in the south-west portion of the cluster is shown in Figure 3.5. The cluster, multiple images, and critical lines for the model at $z = 3.0$ are shown in Figure 3.13.

**MS 2137−23**

The properties of the multiple image systems are described in Table 3.5. One cluster-scale dark matter halo is used to model the cluster, and two galaxy-scale halos are used to separately model the mass distribution of the BCG and one cluster member located near systems 3 and 4. The parameters for these halos are given in Table 3.12. The integrated density profile is presented in Figure 3.16. A snapshot of the radial arc in the north-east portion of the cluster is presented in Figure 3.5. The cluster, multiple images, and critical lines for the model at $z = 3.0$ are shown in Figure 3.13.

### MACS J0326.8-0043

One cluster-scale dark matter halo is used to model the cluster, one galaxy-scale halo is used to separately model the mass distribution of the BCG, and one additional halo is included for the bright cluster member located near system 3. Figure 3.14 shows a snapshot of this perturber in relation to system 3. The best fit parameters for these halos are given in Table 3.13. The integrated density profile is presented in Figure 3.16. A snapshot of the two radial arcs near the BCG are shown in Figure 3.5, and the properties of the multiple images are listed in Table 3.6. The cluster, multiple images, and critical lines for the model at $z = 3.0$ are shown in Figure 3.13.

### MACS J1427.6−2521

This cluster has not been mass modeled before. One cluster-scale dark matter halo is used to model the cluster and one galaxy-scale halo is used to separately model the mass distribution of the BCG. The best fit parameters for these halos are given in Table 3.14. The integrated density profile is presented in Figure 3.16. A snapshot of the radial arc is shown in Figure 3.5, and the properties of the multiple images are listed in Table 3.7. The cluster, multiple images, and the critical lines for the model at $z = 3.0$ are shown in Figure 3.13.

### MACS J0417.5-1154

I refer the reader to Jauzac et al. (2019) and Mahler et al. (2019) for more details regarding this mass model. The only modification I make to the model described in J19 is the introduction of the parameters listed in Table 3.3 to constrain the mass halo for the BCG. A snapshot of the radial arc is presented in Figure 3.5. The integrated density profile is presented in Figure 3.16.

### MACS J0949.8+1708

I refer the reader to Allingham et al. (2023) for more details regarding this mass model. The only modification I make to the model described in this paper is the

introduction of the parameters listed in Table 3.3 to constrain the mass halo for the BCG. A snapshot of the radial arc is presented in Figure 3.5. The integrated density profile is presented in Figure 3.16.

### 3.6.2 Lensing Model Prior Distributions

The above models each contain different parameters that are optimized over a parameter space that differs slightly between clusters. The given parameter space for each parameter takes the form of a uniform distribution, which is the default distribution for priors in `Lenstool` (Jullo et al. 2007b). This ensures that the full parameter space for each individual parameter is explored without biasing the search toward any particular value. The specific boundaries for each parameter space are provided in Table 3.10, and the corner plots for the key parameters in the fitting procedure are displayed in Figure 3.15. These parameters are the $r_{\rm core}$ parameter for the dark matter halo, and the velocity dispersions for both the dark matter halo and the BCG, which are essentially scaling factors for determining the mass distribution of the primary dPIE cluster-scale dark matter and BCG stellar mass halos within the lens models. There is a strong correlation between the velocity dispersion of the dark matter halo and the measurement for $r_{\rm core}$. Additionally, the lens model parameters are not very well constrained in MACS J1427, which is due to the lack of constraints within the lens model. The models for MACS J0949 and MACS J0417 are unchanged from their published versions, save for the addition of the explicitly constrained BCG, and are included here for completeness.

### 3.6.3 Combining Kinematic Profile with Lensing

Stellar kinematics generally probe the total mass distribution, but in the case of galaxies, where significant amounts of stellar light are concentrated, the mass profile is strongly dominated by baryons. The kinematic measurements of the BCGs of these clusters, which effectively measure the baryonic mass, can thus be combined with strong lensing models, which are sensitive to dark matter, to disentangle the degeneracy between dark and baryonic matter. I employ kinematic measurements of

Table 3.10: Prior distributions for `Lenstool` parameters optimized in the fitting procedure. The priors for $\Delta x$ and $\Delta y$ are given in units of arcseconds relative to the center of the cluster, which is fixed to the position of the BCG. The values in the prior column indicate the lower and upper bounds of the uniform prior assigned to each parameter.

| Parameter | Units | Prior |
|---|---|---|
| Cluster-scale dark matter dPIE halo | | |
| $\Delta x$ | arcseconds | (-5, 5) |
| $\Delta y$ | arcseconds | (-5, 5) |
| $\epsilon$ | .. | (0, 0.8) |
| $\theta$ | deg | (0, 180) |
| $r_{\rm core}$ | kpc | (1, 100) |
| $\sigma_0$ | km s$^{-1}$ | (500, 1000) |
| BCG dPIE Halo | | |
| A383 $\sigma_0$ | km s$^{-1}$ | (220, 420) |
| MS 2137 $\sigma_0$ | km s$^{-1}$ | (120, 500) |
| MACS J0326 $\sigma_0$ | km s$^{-1}$ | (100, 350) |
| MACS J1427 $\sigma_0$ | km s$^{-1}$ | (100, 700) |
| MACS 0949 $\sigma_0$ | km s$^{-1}$ | (250, 450) |
| MACS 0417 $\sigma_0$ | km s$^{-1}$ | (350, 600) |
| Cluster galaxy scaling | | |
| $\sigma_*$ | km s$^{-1}$ | (25, 250) |
| $r_{\rm cut*}$ | kpc | (3, 50) |
| dPIE halos of individually optimized galaxies | | |
| $\epsilon$ | .. | (0, 0.8) |
| $\theta$ | deg | (0, 180) |
| $r_{\rm core}$ | kpc | (0, 1) |
| $r_{\rm cut}$ | kpc | (0,10) |
| $\sigma_0$ | km s$^{-1}$ | (10, 300) |
| Unknown redshifts | | |
| z | .. | (1,7) |

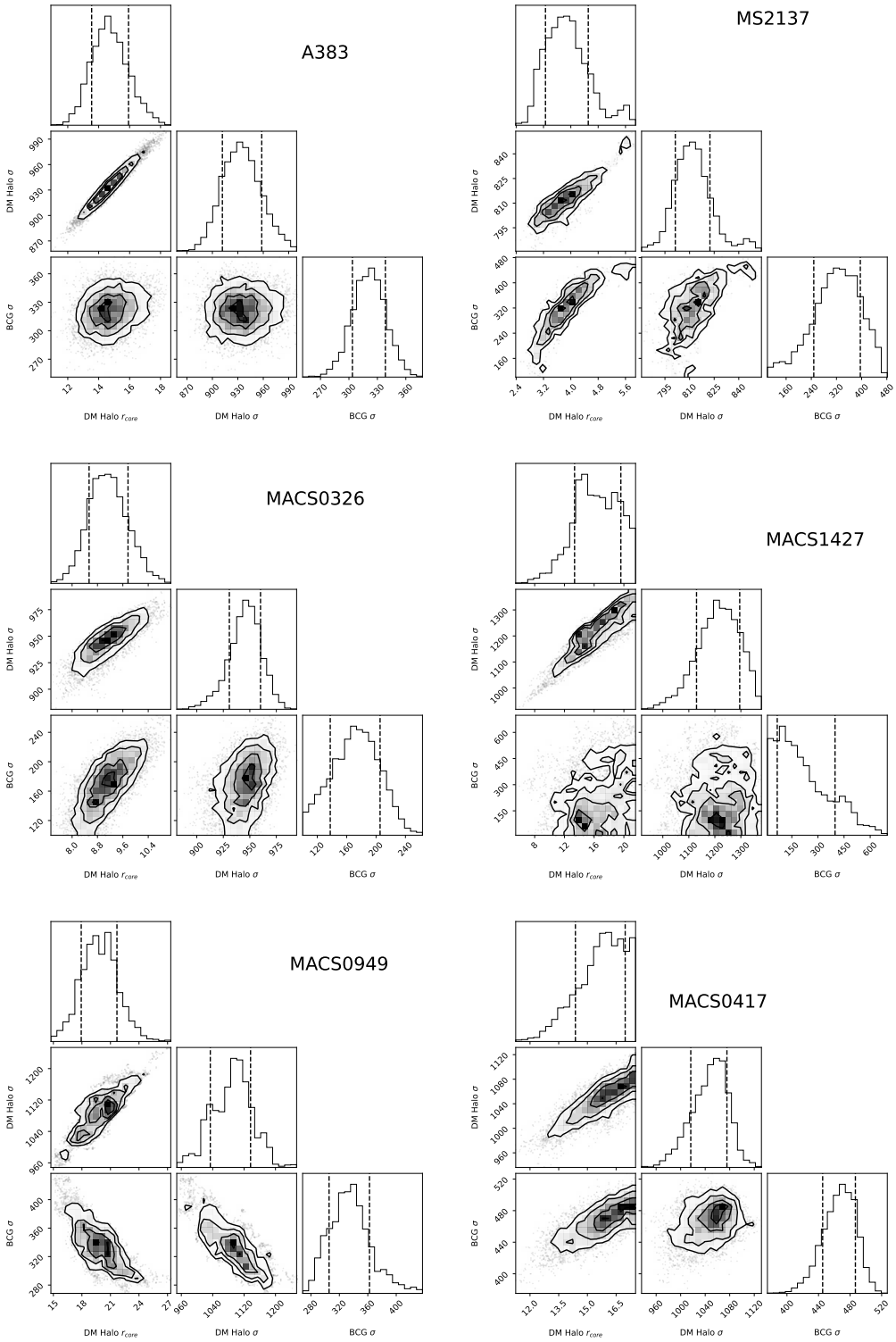


Figure 3.15: Corner plots of the relevant parameters from the `Lenstool` fitting procedure of the six clusters presented in this chapter. The dark matter halo of the cluster is denoted as the 'DM' halo. The vertical lines mark the one-sigma region.

the BCG in my models to more accurately probe the mass distribution at the center of these galaxy clusters. I separately parameterize the BCG using a dPIE profile with `Lenstool`, using parameters derived from photometry. I leave the velocity dispersion as the only free parameter for this profile. The BCG velocity dispersion can then be constrained using the kinematic measurements from MUSE. In this way, physical measurements of the BCG can be used to constrain the lens model.

The velocity dispersion of the BCG is incorporated as a constraint into the model through a-posteriori analysis of the MCMC `Lenstool` model. The original `Lenstool` model is first modified to incorporate photometric information (discussed in Section 3.5.1) for the BCG into the model. This is done by creating a separate mass halo to account for the BCG, with the parameters $r_{\rm core}$ and $r_{\rm cut}$ fixed to the values obtained from the surface brightness profile fit. Ellipticity and position angle are also fixed to the values from the `GALFIT` fitting. The remaining free parameter in the halo, $\sigma_0$, is left free as a proxy for the stellar mass to light ratio (Sand et al. 2004, Sand et al. 2008, Bergamini et al. 2019). This parameter is given a prior that is informed by measurements of the stellar mass to light ratio.

Adding this information to the model allows for the direct calculation of a model version of the velocity dispersion of the BCG based on Jeans fitting. No anisotropy is assumed in the model, an assumption that is validated by the nearly circular BCGs, though I discuss what effect the introduction of anisotropy has on the model values in Section 3.5.4. The form of the spherical Jeans equation is thus as follows:

$$\sigma^2_{\rm los}(R) = \frac{2G}{\sum_*} \int_R^\infty \frac{\nu_*(r) M(r) \sqrt{r^2 - R^2}}{r^2} dr,$$

where $\nu_*$ describes the three-dimensional profile and $\sum_*$ refers to the two-dimensional profile of the stellar component of the BCG. These profiles are drawn directly from the photometric fits to the BCG described in Section 3.5.1. $M(r)$ accounts for the total enclosed mass inside a radius, $r$, and must thus account for both the stellar and DM mass. I draw the value for the enclosed mass directly from the `Lenstool` model at this stage, as the degeneracy between DM and stellar mass makes it difficult to avoid double-counting the mass of the BCG if I add it separately to the `Lenstool` value. The model velocity dispersion for the BCG can then

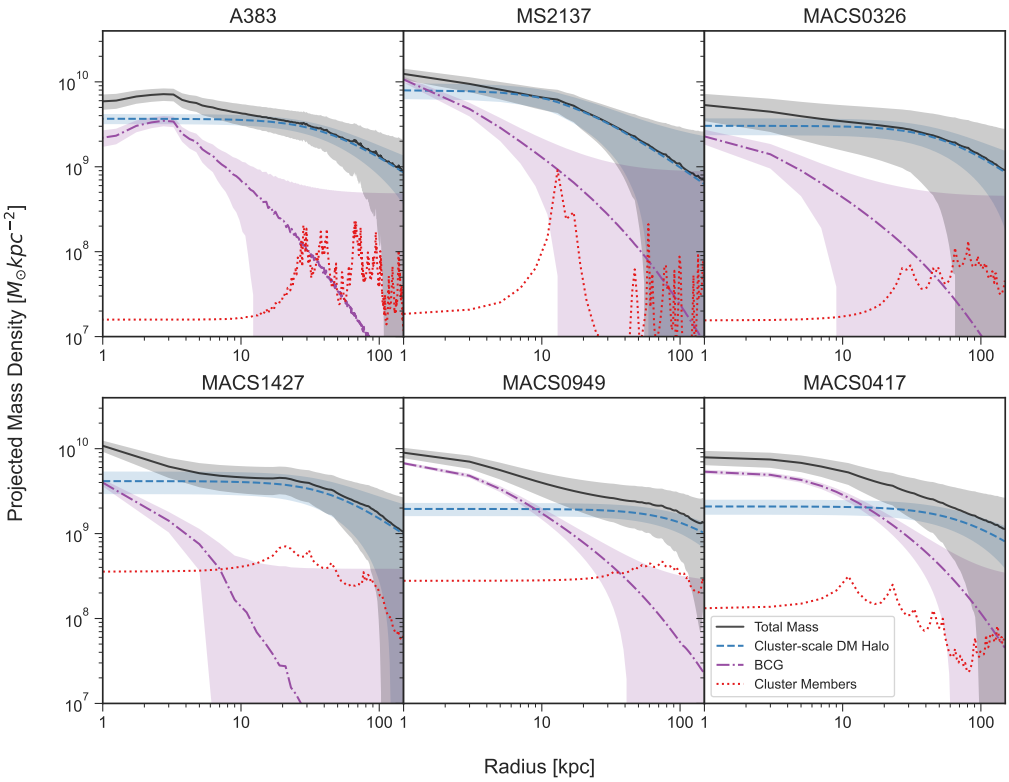


Figure 3.16: Integrated density profiles for all six clusters studied in this chapter. The uncertainty in the measurement is plotted as the shaded region around the line, and only incorporates the uncertainty returned by `Lenstool`; systematic errors are not included. Uncertainty measurements are not included for the mass profile of the cluster member galaxies as they are too large to be meaningful. Density is measured in units of log ($M_\odot$/kpc$^2$).

be calculated at any given radius, $R$. This equation is explicitly written out in Equation 2.21, and the derivation is discussed in Section 2.4.

The optimization of the `Lenstool` model with respect to the stellar kinematics is performed by adding the error from the model to the error of the stellar kinematics,

$$\chi^2_{\rm VD} = \sum_i \frac{\left(\sigma_i - \sigma_i^{obs}\right)^2}{\Delta_i^2},$$

where $\Delta_i$ is the uncertainty in the observed velocity dispersion measurements.

The calculation of the velocity dispersion error is performed after the lensing minimization has been completed, separately from `Lenstool`. As a result, the velocity dispersion and lensing likelihoods can be treated as independent from each other, and the total likelihood is then the product of the velocity dispersion and

lensing likelihoods, where both the lensing and dynamical models are assumed to carry equal weight in the final calculation. The resulting 'best-fit' model is then simply the model that minimizes the total $\chi^2 = \chi^2_{SL} + \chi^2_{VD}$. This treatment of the likelihoods as independent quantities follows previous work done to combine dynamics and lensing models (e.g. Sand et al. 2004, Newman et al. 2013b).

Maximizing the global likelihood function allows for the separation of DM and baryons into distinct profiles, as seen in Figure 3.16. In doing so, the DM and baryon profiles (orange and blue lines, respectively) can be compared to the total mass distribution (black line) to see the relative contributions of each as a function of radius. Each of these profiles possess a core-like structure within the inner 50 kpc. This is perhaps not unexpected, given that all of these clusters have radial arcs, which are preferentially produced in mass distributions with a shallow inner slope (see Section 3.1). However, the agreement between the shape of the profile for each of these clusters is fairly significant, as it shows that the dark matter distribution in the center of the cluster is centrally concentrated.

### 3.6.4 Cluster Density Profile

A dPIE profile is used to construct the density profiles for these clusters. Since I do not use the usual NFW profile, an examination of the properties of the dPIE profile is worth considering.

The obvious test of this profile is to compare it against a 'non-core' model. In Newman et al. (2013a), this comparison between a core and non-core model was performed by using a gNFW profile and a 'cored' NFW profile, with the cored model being ultimately favored. In this case, I choose to use dPIE profiles over NFW because there is no available weak lensing information for the clusters MACS J1427 and MACS J0326. As shown in Limousin et al. (2022), weak lensing is crucial for placing reasonable priors on the scale radius of the NFW profile, and without these priors any attempts to use `Lenstool` to create NFW profiles will result in models that are degenerate with their own parameters. As a result, until weak lensing analyses can be performed for these clusters and priors obtained on their parameters, the information derived from NFW fitting will have a low statistical significance. The

*HST* data for these clusters are too shallow to perform a meaningful fit to the data (e.g. the number density of background sources is too low), which does not allow for weak lensing modeling. Additionally, the lack of multiple bands makes weak lensing analysis difficult to incorporate as the contamination from foreground and cluster objects will be almost impossible to remove (Jauzac et al. 2012; Niemiec et al. 2023). Since only A383 and MS2137 have available weak lensing data, and since both these clusters already have published lens models available (N13), I elect not to repeat this analysis since the available data is the same, and I am not introducing new weak lensing modeling techniques. Additionally, by not using an NFW profile to model the cluster DM profile, I avoid the degeneracy between the scale radius and the asymptotic gNFW profile slope that was demonstrated in He et al. (2020), and do not bias the results toward low slope values as a result of measurement choices in a weak lensing profile. I discuss the exploration of NFW profiles with clusters that have weak lensing modeling available as a constraint in the next chapter.

I have also created 'core' and 'non-core' dPIE models following the approach presented in Limousin et al. (2022). I perform this test by restricting the $r_{\rm core}$ radius to be smaller than 10 kpc to create 'non-cored' models, and comparing the resulting models against the 'cored' dPIE models, where the core radius was left as a free parameter. The results of this experiment are definitive. In each case, the $\chi^2$ value of the 'non-cored' model increased significantly in comparison to the cored model. For instance, the 'cored' model for MACS J0326 has a $\chi^2$ of 23.4, with an rms of 0.37". In comparison, the 'non-cored' model has a $\chi^2$ of 179, with an rms of 3.3", which indicates that the model is unable to reproduce the observational constraints. This discrepancy is consistent across all six clusters, indicating that 'non-cored' models are not favored as a solution.

## 3.7 Discussion

Strong lensing is a powerful tool for examining the inner slope of the dark matter density profile, which can then be used to compare with, and improve upon the information used to build CDM simulations. The clusters modeled in this chapter

all have radial arcs, which are uniquely suited for providing more precise constraints in the inner part of the cluster, i.e. near the BCG.

### 3.7.1 How Rare are Radial Arcs?

Radial arcs are still relatively uncommon among lensed objects, both because the geometric requirements for their appearance are so stringent, and then even when they do appear, they can easily be obscured by the light of surrounding galaxies and the BCG (Bartelmann, 2010). Visual examination of Figure 3.5, for example, would not immediately make the presence of a radial arc obvious; it is only through spectroscopic confirmation that it can be definitively said that an arc is present and can be assigned a redshift, which defines its power as a constraint. As a result, building a large sample of clusters with radial arcs is not trivial. The six clusters selected in this chapter are chosen from a dataset of around 200 MUSE cubes from the Kaleidoscope survey, and are selected from within that dataset specifically for the presence of radial arcs. The ratio of clusters with radial arcs vs clusters without these arcs in the Kaleidoscope sample is around 1%, which easily shows that radial arcs, while a powerful constraint on the inner DM profile, are a unique physical feature and are not universally available in lensing analyses of cluster mass profiles at scale.

An additional, equally important consideration for the robustness of these measurements is that the model and slope profiles presented in this chapter exclusively represent clusters that contain radial arcs. This naturally means that all of these clusters are more core-like, as total density distributions steeper than $\rho \propto r^{-2}$ do not produce radial arcs (see Hattori et al. 1999). As a result, another degree of selection bias is incurred in the results by excluding systems that might be more cuspy. While I do plan to examine this in the future using other clusters in the Kaleidoscope survey, it is useful to mention what potential impact this bias might have by referring to previous work done by Sand et al. (2004) and Newman et al. (2013a) on A383 and MS2137.

In each of these papers, these two clusters were a part of a larger sample, which included clusters that had tangential arcs but did not have radial arcs. The authors

could thus perform a comparison of their results relative to clusters without radial arcs, and the shallowness of the inner DM density profiles for both A383 and MS2137 did not differ significantly from the profiles of clusters with only tangential arcs. These results are encouraging, and I plan to more thoroughly test the robustness of this sample in future work. In this chapter, I present these models as a specific study of density distributions for clusters with radial arcs and shallow IFU spectroscopy, rather than an examination of the general shape of the DM density profile for all clusters. Despite these limitations, however, I obtain measurements for the inner DM slope that are both consistent with previous mass models and are in agreement with other observational measurements from literature, thus demonstrating the strength of using radial arcs as lensing constraints in tandem with MUSE spectroscopy.

### 3.7.2 Comparison With Previous Work

#### Abell 383

A383 has been modeled numerous times, due to its properties and fortuitous magnification of a background $z \sim 6$ galaxy. The most recent model was created using a combination of strong and weak lensing, and was part of a compilation of models built using the complete sample of CLASH clusters (Zitrin et al. 2015; Z15). The multiple image systems used in Z15 correlate to those used in this chapter, with the exception of system 1, which is a new detection. System 1 in Z15 is associated here with my system 2; the remaining systems are numbered in accordance to Z15. I note that the incorporation of VLT/MUSE spectroscopic redshifts allows for the combination of Z15 systems 1 and 2, which are the same object broken into separate systems to allow the lens model to converge, into the system 2 presented in this work.

Systems 1-5 are fixed to spectroscopic redshifts, where systems 1, 2, and 5 are measured from MUSE spectroscopy, and are identical to the values presented in previous literature, including Z15. Systems 3 and 4 are not detected in the MUSE data and are thus fixed to the redshift $z = 2.55$, a spectroscopic measurement obtained by Newman et al. (2011). The remaining redshifts are derived by the

model, and they generally tend to be lower, but within ± 0.5 of the values found by Z15, with one exception. System 8 is a more severe underestimation at $z = 1.746$ compared to $z = 3.1$ from Z15.

Despite the difference in redshift measurements, the mass estimates are generally in agreement. In Z15, the mass enclosed in 100 kpc is $\sim 6 \times 10^{13} M_{\odot}$. In my model, the mass enclosed in the same radius is $\sim 5.5 \pm 0.06 \times 10^{13} M_{\odot}$. The other major model for this cluster that I reference in this chapter is from Newman et al. (2013a), which finds an enclosed mass within 100 kpc of $\sim 6 \times 10^{13} M_{\odot}$. My mass estimate thus matches well with the most recent parametric and light-traces-mass lens models of this cluster.

The error in the mass estimate is larger in the outskirts of the cluster as opposed to the inner regions, consistent with expectations from strong lensing models that are expected to be most accurate in the region enclosed by the critical curve. The total $\chi^2$ error estimate is $\sim 54$, as well, which correlates to the mass profile error, and an rms of 0.53".

The integrated density profile shown in Figure 3.16 is measured by summing the value of all pixels encapsulated within an annulus of width $r(n) - r(n-1)$, where $n$ corresponds to the step number.

### MS 2137−23

MS 2137 has similarly been modeled several times since the work by Sand et al. (2008). The most recent model is again from Zitrin et al. (2015). I break system 5, the large tangential arc, into two different pieces in order to improve the resolution of the model. My systems 3 and 4 correspond to system 1 in Z15. System 2 in Z15 corresponds to my system 5, and system 3 in Z15 corresponds to my system 1. I add one new detection to the model: system 2, which I confirm via MUSE spectroscopy to be at $z \sim 1.19$. This system corresponds to the second radial arc near the BCG, which had been noted before in photometry but lacked a spectroscopic detection both of itself and of a counter image that would make it viable to include in the lens model.

The most direct comparison that can be made between the model presented here

and that of Z15 is the mass estimate. Z15 reports a total 2D integrated mass of $M \sim 4 \times 10^{13} M_{\odot}$ enclosed within 100 kpc. A similar estimate of my mass within the same radius yields a value of $\sim 3.6 \pm 0.1 \times 10^{13} M_{\odot}$

The error in the mass profile is relatively small since my model is well-constrained by the inclusion of five systems with spectroscopic redshifts, with a total $\chi^2$ error estimate of $\sim 40$ and an rms of 0.67".

### MACS J0326.8-0043

This is the first published strong lensing model for MACS J0326, as well as the first mass estimate. Each system used to build the model has a spectroscopic redshift, which contributes to the reduction of overall systematic errors (Johnson et al., 2014). Four multiple images out of the twelve used in the model are predictions made by the model (see Table 3.5). The redshift used for each system is fixed to the spectroscopic redshift of the arc with the highest S/N ratio, and is constrained to four significant figures.

The $\chi^2$ value found for the model is 28.44, while the overall rms in the image plane is 0.77". The largest contributors to the rms are images 1.1 and 2,4, which are predicted images. Because the model is constructed using only two shallow *HST* bands (each band has a short exposure time of 500 s; see Table 3.1), it is somewhat difficult to do the usual color and morphology comparison typically used to identify other strongly-lensed galaxies. As a result, the positions of the predicted images are merely predictions, and are subject to change if deeper spectroscopic or photometric observations are acquired for this cluster.

### MACS J1427.6−2521

This is the first published strong lensing model for MACS J1427, and is also the first examination of this cluster in the visual band. However, it was discussed in Ebeling et al. (2010) as a part of a survey of X-ray bright clusters from the MACS survey using *Chandra* data. The *HST* data used for the cluster is archival, and was observed as part of a SNAP project (PID 12884; PI: Harald Ebeling). Although only one *HST* band makes it difficult to identify multiple images based on the usual

criteria of color and morphology, using it as a spatial reference alongside the MUSE redshifts makes it possible to create a basic lens model for the cluster. I obtain a total $\chi^2$ of $\sim 43$ with an rms of 0.81". Deeper, multi-band imaging will almost certainly change the details of the model, but the current iteration still provides valuable information about the general shape of the mass in the cluster. Because the goal of this work is to present lens models constructed mostly based on MUSE data, it is outside the scope of the current work to perform a thorough comparison of the mass profile against the existing *Chandra* data used in Ebeling et al. (2010) for this cluster. However, deeper *HST* imaging and a subsequently improved lens model would make such a comparison more robust, and is thus left for future work.

**MACS J0417**

The lens model used for this cluster is identical to that presented in J19. There are two BCGs in this cluster, but only the southern one has a radial arc. In J19, both BCGs are separately parameterized with individual dPIE halos. In this work, I fix the parameters of the southern BCG to the properties derived from photometric measurements (see Table 3.3). The second change from the J19 model is the imposition of an additional selection criterion on the best-fit model from MCMC chain through kinematic constraints. The resulting model does not differ strongly from J19 in the overall mass distribution. The reduced $\chi^2$ for the model in this work is $\sim 0.91$, compared to $\sim 0.9$ from J19, and the rms is 0.41", compared to 0.38" from J19. Furthermore, the enclosed mass within 200 kpc is measured to be $1.8 \pm 0.04 \times 10^{14} M_{\odot}$, which is in agreement with the measurement from J19 from $1.78 \times 10^{14} M_{\odot}$. This also indicates that the model is in agreement with Mahler et al. (2019), which has similar values for the mass, rms, and $\chi^2$. The main change is in the value of the inner density slope, which I discuss more in Section 3.7.3. In the lensing only model, this value is $\gamma \sim 0.55$, whereas in the lensing and BCG kinematics model the slope is $\gamma \sim 0.6$. These values still fall within the FWHM of the PDF.

**MACS J0949**

The lens model for this cluster is identical to that presented in Allingham et al. (2023). The authors use a separate parameterization of the BCG as well, so the only change made to the model is to fix these parameters to the properties derived from photometric measurements (see Table 3.3). The enclosed mass within 200 kpc found by Allingham et al. (2023) is $2.0 \times 10^{14} M_{\odot}$, while the model in this chapter finds a value of $2.1 \pm 0.07 \times 10^{14} M_{\odot}$ in the same radius. Allingham et al. (2023) finds a $\chi^2$ of 4.71 with an rms of 0.15", while the kinematic model finds a $\chi^2$ of 8.4 with an rms of 0.3". The model could likely be improved with a finer resolution of bins inside the MUSE cube for the measured velocity dispersions.

### 3.7.3 Inner Density Profile

While strong lensing models measure the total density near the critical curves, lensing alone cannot independently distinguish between the contributions of baryonic and dark matter. Breaking this degeneracy is crucial to understanding the physics occurring at the center of these clusters. To that end, stellar kinematics are introduced into the model to constrain the effect of the baryonic mass of the BCG on the overall density distribution. I restrict the analysis to the kinematics of the BCG exclusively, as this is by far the most dominant stellar component in this region. Following the procedure laid out in Newman et al. (2013b), I measure the inner slope $\gamma = -d \log \rho_{\rm DM} \; / \; d \log r$ over the range $r/r_{200} = 0.003 - 0.03$, which roughly corresponds to a range of 5 - 50 kpc.

I select these boundaries because the profile is strongly dominated by baryonic mass within 5 kpc, so the profile will always increase sharply within this region and is thus not a good indication of the shape of the DM density profile (see Newman et al. 2013b), and outside of 50 kpc, the profile is dominated by dark matter (e.g. Figure 3.16). The intermingling between baryonic and dark matter is thus best probed in the interior of this region. The resulting measurements of the slope of the lens models within this range are shown in two ways in Figure 3.17. The primary results I use in this chapter to compare the inner slope measurements to estimate

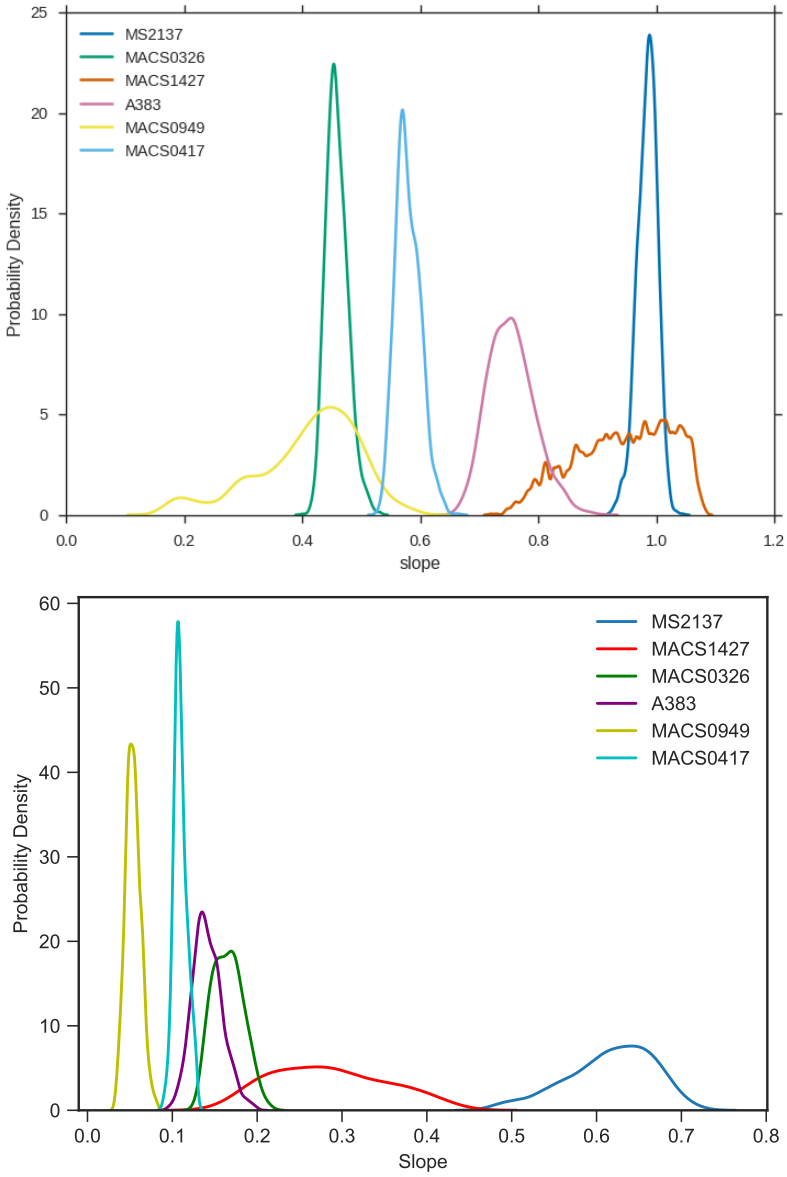


Figure 3.17: *Top*: Density distribution for the slope measurements in all 6 clusters, as calculated from the slope of the total mass density profile with the slope of the BCG subtracted. The probability density is calculated from the MCMC chain run for each model and is based on the derived parameters for the cluster DM halo. *Bottom*: Density distribution the slope of the parameterized dPIE cluster-scale dark matter halo in each cluster.

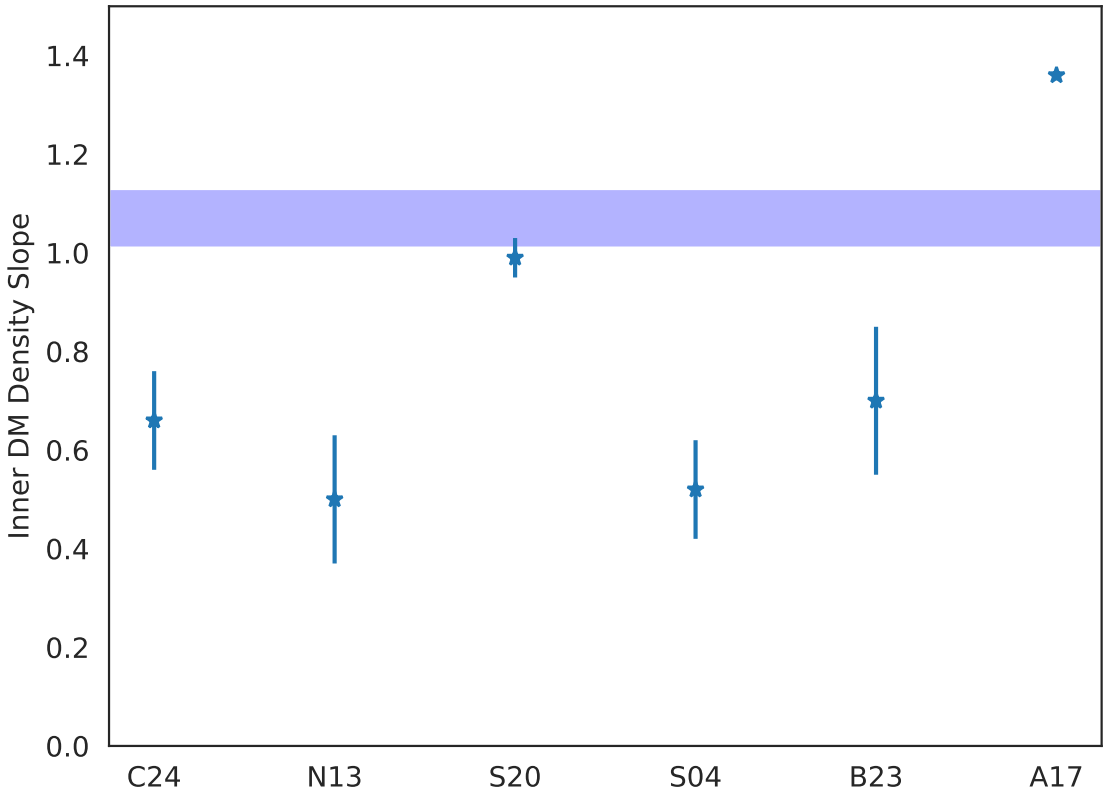


Figure 3.18: The average inner dark matter density slope as measured from five different papers, plotted from left to right as: this work (an average of six clusters), N13 (an average of seven clusters), Sartoris et al. (2020) (Abell 1063), Sand et al. (2004) (an average of four clusters), Biviano et al. (2023) (MACS J1206.2 − 0847), and Annunziatella et al. (2017) (MACS J0416 − 2403). The expected slope measurement from the C-EAGLE simulations as reported in He et al. (2020) is plotted as the blue shaded region.

the slope are shown in the top plot of this figure, which shows the inner slope as measured from the total mass density of the lens model with the stellar component of the BCG subtracted. I elect to use this method to measure the inner slope because directly measuring the slope from the parameterized cluster-scale dPIE halo leads to results that may be misleading. The bottom component of Figure 3.17 shows the same measurement of the inner slope using this halo. The resulting slope values are almost universally cored, which correlates with the results presented in Figure 3.16, which show near-universally flat dPIE halos in all 6 clusters. However, the shape of the dPIE halo does not begin to match the total mass density profile until after roughly 20-30 kpc, which is the cutoff threshold for the region where the BCG stellar mass should dominate. The measurements of the cluster-scale DM halo are thus not necessarily a good reflection of the actual shape of the dark matter in the center of the cluster, especially because other elements may be affecting the shape of the mass profile that are not constrained in the models presented in this chapter, such as intra-cluster light. As a result, rather than assuming that the cluster-scale DM halo represents the 'true' distribution of dark matter in the cluster, I use the total mass obtained from the strong lensing models, which is a good measurement of the mass of the cluster regardless of the state of the individual components that make up that mass distribution, and subtract the mass of the BCG, which I am able to explicitly parametrize using the photometric and kinematic measurements I have described in this chapter, to obtain the inner slope measurements I now report for each of these clusters. The overall results suggest that each of these profiles is very cored, with an average slope measurement of $\gamma \sim 0.66$ for all six clusters. Of all six clusters, MACS J1427 is the most poorly constrained, and could benefit the most from additional observations. However, its probability density is still centered firmly below 1.0, which suggests that it is more likely to be a cored cluster than a cuspy cluster.

These results, when taken in aggregate, demonstrate that clusters with radial arcs clearly present core-like density profiles. This is in-line with our current physical understanding of lensing, which requires the geometric shape of the mass distribution needed to produce radial arcs to be more core-like.

### 3.7.4 Impacts of Assuming Certain BCG Properties

One potential source of additional consideration in this modeling is contained within the estimation of the BCG mass for all the clusters in this chapter. In each of these BCGs, I assume a constant mass-to-light ratio based on a Salpeter IMF to compute the luminosity of the galaxy and fit the surface brightness to a dPIE profile, which then enables me to extract the mass of the BCG through the `Lenstool` optimization procedure. However, this methodology relies on two strict assumptions. First: the stellar initial mass function (IMF) for all the BCGs can be modeled using a Salpeter IMF, rather than a lighter model, such as a Chabrier (Chabrier, 2003) or Kroupa (Kroupa, 2001) IMF. Second, the mass-to-light ratio is constant across the radial expanse of the BCG. While fully addressing these assumptions is outside the scope of this thesis, I will demonstrate below that the main results of 'cored' vs. 'non-cored' slope measurements will not change even if these assumptions are altered.

#### The BCG IMF

The nature of the IMF of early-type galaxies is currently an open question within the community, especially because recent work has shown that the IMF is potentially not a universal constant (Martín-Navarro et al. 2015; Lyubenova et al. 2016; Davis & McDermid 2017). While some studies have reported that the IMF of the most massive early-type galaxies is well-described by an IMF with larger stellar mass-to-light ratios (i.e. a 'heavy' IMF) (La Barbera et al. 2013; Tortora et al. 2013; La Barbera et al. 2015; Rosani et al. 2018), other work has shown stellar IMFs in early-type galaxies and BCGs that are more consistent with that of the Milky Way (Smith et al. 2015; Leier et al. 2016; Smith et al. 2017). In this chapter, I have chosen to use recent work published in Loubser et al. (2020) and Loubser et al. (2021) as a basis for my IMF selection. These two papers examined a sample of 32 BCGs using multi-Gaussian expansion and Jeans anisotropic mass modeling, using weak lensing measurements to constrain the dark matter fraction within each mass measurement. Within this sample, the authors found that the majority of BCGs were described by either a Salpeter or heavier IMF, while only a few individual BCGs could be described by a lighter IMF. The cluster A383 was included in this sample, and the

authors found that it was best described by a Salpeter IMF. In this thesis, I elect to follow the assumption that the majority of BCGs can be described by a Salpeter IMF because the complexity of individually measuring and constraining the IMF of the BCGs in this sample is not justified by the limitations of my models, and is thus outside the scope of this work.

Furthermore, the overall impact of a different IMF on the inner slope measurements is not significant enough to warrant these efforts. A change in the IMF will impact the fit of the BCG surface brightness profile, as it will change the mass-to-light ratio used to convert the luminosity of the BCG to its mass. This will alter the parameters $r_{\rm core}$ and $r_{\rm cut}$ for the BCG dPIE profile used in the `Lenstool` optimization. However, the relevant mass-to-light ratio used in this thesis is the dynamical mass-to-light ratio, which is dependent on the velocity dispersion of the BCG. While I measure the stellar mass-to-light ratio in order to fit the surface brightness profile to a projected dPIE mass profile, I constrain this fit using the velocity dispersion of the BCG at the half-light radius as a prior. This is because the explicit relationship between the projected mass density of the dPIE profile and the observed surface brightness of the BCG is related as $\Sigma = (M_*/L)I$, where $M_*/L$ describes the stellar mass-to-light ratio and I is the surface brightness. In `Lenstool`, the relationship between the mass-to-light ratio and the velocity dispersion of the BCG is described as

$$M_*/L = 1.50\pi\sigma_0^2 r_{\rm cut}/(GL), \tag{3.1}$$

where $L$ represents the total luminosity of the BCG (Sand et al. 2008). The largest impact on the measured mass of the BCG would thus be related to the restrictions on the priors assigned to the velocity dispersion profile, rather than on an explicit optimization of the mass-to-light ratio to a specific IMF. Since these priors are based on the observed kinematic velocity distribution of the BCG (see Section 3.6.2), the parameter space associated with the mass-to-light ratio is allowed to vary. This variance encapsulates much of the difference in the different $r_{\rm core}$ and $r_{\rm cut}$ measurements that can be obtained from using different IMFs, and indeed it preferentially discards models with extreme mass-to-light ratios. To test this, I

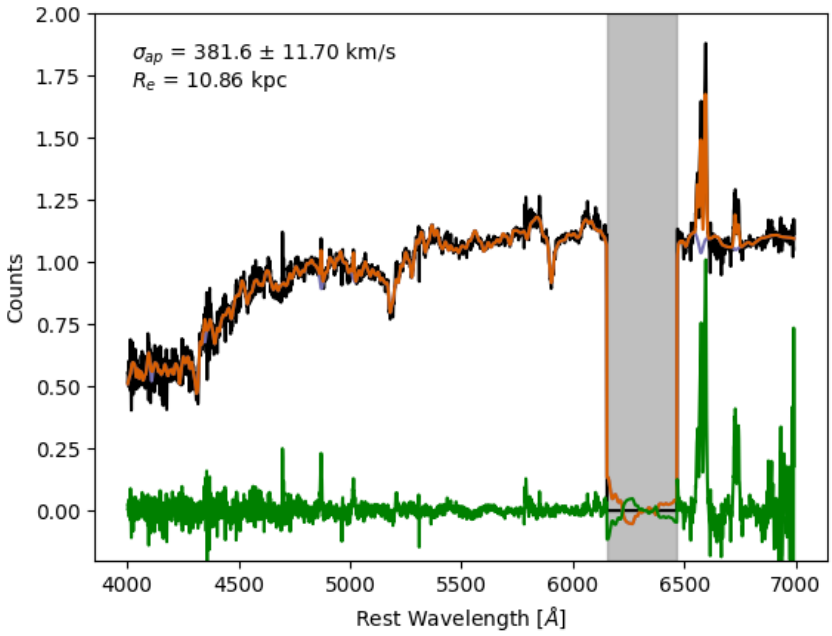


Figure 3.19: `pPXF` fit of the BCG at the half-light radius, denoted as $R_e$ in the figure. The gray bar marks a masked region not present in the templates used to perform the fit. The black line shows the spectrum of the BCG, the orange line shows the `pPXF` fit, and the green line corresponds to the residuals.

varied the mass-to-light ratio that I used to perform the surface brightness profile fit on one cluster, A383. I obtained the fitting values for $r_{\rm core}$ and $r_{\rm cut}$ using the same measurement of the BCG's velocity dispersion at the half-light radius as a prior on the fit ($381.6 \pm 11.7$ km/s). I show the `pPXF` fit for the BCG at this radius in Figure 3.19.

I then vary the stellar mass-to-light ratio to three different values: 2.26, which corresponds with the ratio measured in Newman et al. (2013a) using a Chabrier IMF; 1.5, a value selected as a lower extreme; and 3.0, a value selected as an upper extreme. These different values for the stellar mass-to-light ratio result in $r_{\rm core}$ and $r_{\rm cut}$ values for the BCG mass profile, which I then use to run three different 'test' models, which are otherwise identical to the main model for A383 presented in this chapter. I run these test models in source plane optimization mode as a brief test on the difference that the mass-to-light ratio can have on the measured inner dark matter slope of the cluster. The resulting measurements from each of the three models are shown in Figure 3.20.

The results from this figure indicate that the choice of the mass-to-light ratio

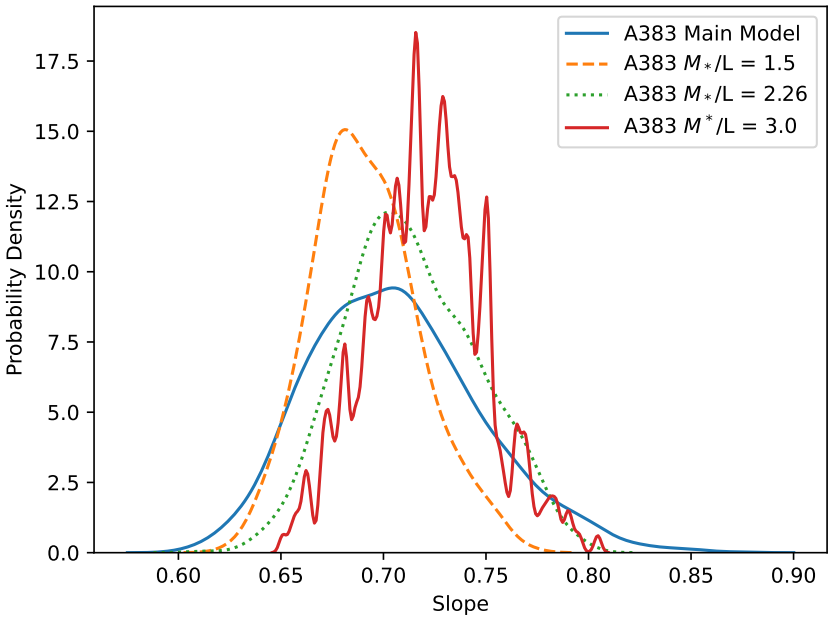


Figure 3.20: Comparison of the slope measurements from A383 using different mass-to-light ratios to extract the $r_{\rm core}$ and $r_{\rm cut}$ values of the dPIE density profile, calculated as the total mass density profile with the mass of the BCG subtracted using the same method as Figure 3.17. The 'main model' presented in the figure here corresponds to a mass-to-light ratio of 2.09 as measured using a Salpeter IMF.

does not have a large effect on the slope of the density profile, in agreement with the assessments made in literature that I have described above. Although there is some variance between the different mass-to-light ratios, the main model slope measurement contains the varying mass-to-light slopes within its error. Of the three mass-to-light ratios I tested in this figure, I note that the slope estimate using the upper extreme value of 3.0 is not well constrained. This indicates that the `Lenstool` model rejects mass-to-light ratio values that constrain the model to non-physical values, i.e. values that do not allow the model to reproduce the fit of the lensing and kinematic constraints.

### A Radially Varying Mass-To-Light Ratio

I now address the second assumption I make in my BCG optimization. Recent work has shown that some early-type galaxies may demonstrate a gradient in the IMF, where areas that are close to the galaxy center are more metal-rich than the outskirts, causing the interior of a galaxy to be described more accurately by, for

instance, a Salpeter IMF, than the outskirts of that same galaxy, which may be less bottom-heavy (Martín-Navarro et al. 2015; Lyubenova et al. 2016; van Dokkum et al. 2017; Parikh et al. 2018). This variance leads, in turn, to a gradient in the mass-to-light ratio, which could plausibly have an effect on the measurement of the dynamical mass. However, Marsden et al. (2022) argues that while variations in the IMF can indeed affect the stellar mass estimates of early-type galaxies and thus warrants consideration in more detailed analyses, ignoring these IMF effects when performing Jeans modeling still accurately reproduces the key observables of a galaxy's velocity dispersion profile. Using a sample of local galaxies from the Sloan Digital Sky Survey (York et al. 2000) MaNGA (Mapping Nearby Galaxies at Apache Point Observatory) Survey (Bundy et al. 2015), Marsden et al. (2022) demonstrates that the aperture-averaged velocity dispersion measurement, $\sigma_{\rm ap}$, is only loosely correlated with the stellar mass-to-light ratio, such that while there is some variance in the measurement, the overall value of $\sigma_{\rm ap}$ does not change by more than $3\sigma$. Loubser et al. (2021) also reports that there are no strong correlations between the stellar mass-to-light ratio and the velocity dispersion of a sample of 32 BCGs, including A383.

Finally, perhaps the most compelling reason to not assume a radially varying mass-to-light ratio in this work is because such a measurement seems to be associated with a varying IMF. The precision needed to constrain IMF measurements requires very high-resolution spectroscopic data across the radial extent of the galaxy in order to accurately measure different line widths. The VLT/MUSE observations presented in this chapter are not of sufficient depth to retrieve line widths with an accuracy that can distinguish between different IMF models, and so using a changing mass-to-light ratio requires making intrinsic underlying assumptions about the structure and composition of the BCGs in this sample that are not supported by current observations. However, this is certainly an area that is worth investigating in future work, and while using a varying mass-to-light ratio should not change the overall 'cored' or 'non-cored' designations of the clusters in this chapter, the exact inner slope measurement may change slightly.

## 3.8 Conclusions and Summary

I select four clusters with radial arcs from a total sample of 150 clusters observed with MUSE, and construct strong lensing models for these clusters, using at least two systems with spectroscopic redshifts from MUSE in each model. The radial arcs impose an additional constraint on the mass distribution near the center of the cluster, enabling a more precise examination of the inner density profiles for these clusters than is typical of strong lensing, as the relative scarcity of radial arcs means that these profiles are usually extrapolated into the inner region of the cluster. I add another two clusters with radial arcs that have already been modeled to the sample, for a total of six clusters with radial arcs. I note that radial arcs are preferentially produced in mass distributions with a shallow inner slope, and each of these clusters has a demonstrably shallow slope measurement regardless of whether photometric and kinematic measurements of the BCG are incorporated into the lensing model; however, including a central kinematic probe reduces systematics of the model.

I additionally utilize stellar kinematics from the BCG to impose further constraints on the inner density profile following the methods used in Newman et al. 2013b. This constrains the contribution of the baryonic mass to the overall cluster density profile. I obtain a mean dark matter slope value of $\gamma \sim 0.66$ for all clusters, which is higher but generally consistent with the measurements from N13 ($\gamma \sim 0.5$). Figure 3.18 places these results into context with several other observational papers, as well as with the results from the C-EAGLE simulations in He et al. (2020). Of the five additional observational papers presented in the figure, N13 and Sand et al. (2004) follow the methods presented in this chapter to obtain their slope measurements. Annunziatella et al. (2017) uses a blend of X-ray, strong lensing, and BCG kinematics to obtain their measurement, although they assume a single power-law mass profile, which may over-estimate the inner slope if the 3D mass profile steepens with radius. Sartoris et al. (2020) and Biviano et al. (2023) exclusively use cluster member kinematics to obtain their slope measurements. These disparate values and techniques clearly show the observational tension currently facing this measurement.

These results were typically obtained with shallow exposure times and in below-average observational conditions, which demonstrates that these techniques can be

used to gain a general understanding of the shape of cluster density profiles without the need for deeper, more observationally constrained *HST* or spectroscopic data. However, I emphasize that these models and results can only improve with the addition of these types of data, and while the overall shape of these profiles should not change drastically, the overall measurements obtained may shift. This can be seen in the difference of the work performed in Sand et al. and N13. In Sand et al., the authors derive a mean slope value of 0.5 for A383 and MS2137 using archival *HST* imaging and spectroscopy from Keck, whereas in N13, which used deeper *HST* images at wavelengths less affected by systematics for kinematic analysis, and deeper spectroscopy from Keck/LRIS, the mean slope value for these two clusters is closer to 0.85. This shift is an example of the sort of change that may occur if these models are ever redone in the future with, in particular, deeper observational data, which will allow for more reliable identification of multiply-imaged systems.

Future work on this subject will make use of the techniques employed in this chapter, applied on other galaxy clusters from the Kaleidoscope survey. Further analysis will include clusters without radial arcs and will exploit the Kaleidoscope sample to fully benefit from the uniform depth and selection of clusters that characterizes the survey. In the next chapter, I discuss the impact of including weak lensing measurements on the measurement of the density profile.

## 3.9 Lens Model Properties and MUSE Catalogue

The following tables are referenced throughout the chapter and are included at the end of the chapter for visual clarity.

Table 3.11: Parameters for the best-fit lens model of A383. Error bars correspond to $1\sigma$ confidence level as inferred from the MCMC optimization. The parameters are provided for the cluster dark matter halo (dPIE DMH), the BCG halo (dPIE BCG), and each of the galaxy-scale perturbers included in the model (Perturber 1-3). $\Delta$R.A. and $\Delta$Decl. are defined in relation to the BCG, located at R.A.=2:48:03.37 and Decl.=-3:31:45.29. Position angles are measured north of west, and the ellipticity $\epsilon$ is defined as $(a^2 - b^2)/(a^2 + b^2)$. $r_{cut}$ is fixed to 1000kpc for the cluster dark matter halo.

| Object | $\Delta$R.A. (") | $\Delta$Decl. (") | $\epsilon$ | $\theta$ (°) | $r_{\rm core}$ (") | $r_{\rm cut}$ (") | $\sigma$ (km $s^{-1}$) |
|---|---|---|---|---|---|---|---|
| dPIE DMH | 0.43 | 2.26 | 0.17 | 106.66 | 50.80 | 1000. | 878.22 |
| dPIE BCG | 0 | 0 | - | - | - | - | 325.59 |
| Perturber 1 | 14.69 | -16.10 | 0.79 | 96.31 | 0.31 | 5.89 | 189.58 |
| Perturber 2 | -0.17 | -23.49 | 0.37 | 139.62 | 0.89 | 5.00 | 139.13 |
| Perturber 3 | 3.27 | -20.82 | 0.77 | 92.84 | 0.81 | 2.00 | 290.66 |

Table 3.12: Parameters for the best-fit lens model of MS 2137. $\Delta$R.A. and $\Delta$Decl. are defined in relation to the center of the BCG, located at R.A.=21:40:15.16 and Decl.=-23:39:40.09. The other table parameters are defined in the same way as Table 3.11.

| Object | $\Delta$R.A. (") | $\Delta$Decl. (") | $\epsilon$ | $\theta$ (°) | $r_{\rm core}$ (") | $r_{\rm cut}$ (") | $\sigma$ (km $s^{-1}$) |
|---|---|---|---|---|---|---|---|
| dPIE DMH | 0.24 | 0.012 | 0.35 | 148.77 | 13.51 | 1000. | 784.81 |
| dPIE BCG | -9.53 | 14.13 | - | - | - | - | 250.3 |

Table 3.13: Parameters for the best-fit lens model of MACS J0326. $\Delta$R.A. and $\Delta$Decl. are defined in relation to the center of the BCG, located at R.A.=3:26:49.96 and Decl.=-0:43:51.47.The other table parameters are defined in the same way as Table 3.11.

| Object | $\Delta$R.A. (") | $\Delta$Decl. (") | $\epsilon$ | $\theta$ (°) | $r_{\rm core}$ (") | $r_{\rm cut}$ (") | $\sigma$ (km $s^{-1}$) |
|---|---|---|---|---|---|---|---|
| dPIE DMH | -0.92 | -0.75 | 0.23 | 134.57 | 42.17 | 1000. | 924.55 |
| dPIE BCG | 17.56 | -20.75 | - | - | - | - | 189.44 |

Table 3.14: Parameters for the best-fit lens model of MACS J1427. $\Delta$R.A. and $\Delta$Decl. are defined in relation to the center of the BCG, located at R.A.=21:40:15.16 and Decl.=-23:39:40.09. The other table parameters are defined in the same way as Table 3.11.

| Object | $\Delta$R.A. (") | $\Delta$Decl. (") | $\epsilon$ | $\theta$ (°) | $r_{\rm core}$ (") | $r_{\rm cut}$ (") | $\sigma$ (km $s^{-1}$) |
|---|---|---|---|---|---|---|---|
| dPIE DMH | 0.24 | 0.012 | 0.35 | 148.77 | 13.51 | 1000. | 784.81 |
| dPIE BCG | 0 | -0.018 | - | - | - | - | 277.92 |
| Perturber 1 | 17.56 | -20.75 | 0.39 | 87.67 | 3.85 | 12.76 | 120.41 |

Table 3.15: Measured redshifts in A383. Column 1 is the ID of the source. Columns 2 and 3 are the R.A. and Decl. in degrees (J2000). Column 4 is the redshift of the source. Column 5 is the quality flag (QF) assigned to the redshift. The QF scales in quality from largest to smallest; a flag value of 3 indicates that a high confidence in the value for the redshift, whereas a flag value of 1 indicates that a low confidence in the value for the redshift.

| ID | R.A. | Decl. | $z$ | QF |
|---|---|---|---|---|
| 1 | 42.01870947 | -3.53513970 | 0.196 | 3 |
| 3 | 42.01413524 | -3.53591378 | 0.195 | 3 |
| 4 | 42.00714291 | -3.53595815 | 0.412 | 3 |
| 7 | 42.00745227 | -3.53755278 | 0.960 | 3 |
| 11 | 42.01410348 | -3.52926656 | 0.188 | 3 |
| 18 | 42.15254730 | -3.53287324 | 1.010 | 3 |
| 50 | 42.02032160 | -3.53682543 | 1.011 | 3 |
| 57 | 42.01432510 | -3.52883110 | 1.011 | 3 |
| 61 | 42.00947290 | -3.52844810 | 4.633 | 3 |
| 70 | 42.01179557 | -3.53284732 | 1.009 | 3 |
| 79 | 42.01001298 | -3.53386725 | 1.505 | 3 |
| 80 | 42.01003680 | -3.53068700 | 4.634 | 3 |
| 83 | 42.01280980 | -3.52573640 | 4.636 | 3 |
| 180 | 42.00583728 | -3.53475354 | 0.928 | 3 |
| 208 | 42.01527605 | -3.53287594 | 0.190 | 3 |
| 242 | 42.00980114 | -3.53086269 | 1.010 | 3 |
| 313 | 42.02047584 | -3.53382125 | 1.092 | 3 |
| 394 | 42.01915633 | -3.53195987 | 0.373 | 3 |
| 410 | 42.01286378 | -3.53353040 | 1.010 | 3 |
| 451 | 42.00810054 | -3.53202013 | 0.186 | 3 |
| 493 | 42.01919295 | -3.53294806 | 6.031 | 3 |
| 501 | 42.01157428 | -3.52974105 | 0.186 | 3 |
| 737 | 42.00958438 | -3.53049744 | 1.010 | 3 |
| 786 | 42.01923866 | -3.52626206 | 0.194 | 3 |
| 1007 | 42.01156363 | -3.52457326 | 0.656 | 3 |
| 1014 | 42.01560756 | -3.52639592 | 0.190 | 3 |
| 1103 | 42.01513734 | -3.52105068 | 0.195 | 3 |
| 1150 | 42.02093902 | -3.52339690 | 0.890 | 3 |
| 1183 | 42.01893922 | -3.52259989 | 0.094 | 3 |
| 1353 | 42.01953604 | -3.52455550 | 0.937 | 3 |
| 1482 | 42.01180784 | -3.52436324 | 0.656 | 3 |
| 1578 | 42.01363994 | -3.52635524 | 6.032 | 3 |
| ⋮ | ⋮ | ⋮ | ⋮ | ⋮ |

| ID | R.A. | Decl. | $z$ | QF |
|---|---|---|---|---|
| ⋮ | ⋮ | ⋮ | ⋮ | ⋮ |
| 1601 | 42.02098120 | -3.52583488 | 0.824 | 3 |
| 1741 | 42.01678438 | -3.52648827 | 0.373 | 3 |
| 17 | 42.01396670 | -3.53270560 | 0.279 | 2 |
| 135 | 42.02019771 | -3.53514563 | 0.137 | 2 |
| 154 | 42.01317449 | -3.53516389 | 0.191 | 2 |
| 329 | 42.00860414 | -3.53278628 | 0.188 | 2 |
| 570 | 42.00709600 | -3.53079003 | 0.764 | 2 |
| 584 | 42.02237334 | -3.53141806 | 0.182 | 2 |
| 1141 | 42.00768973 | -3.52797491 | 1.276 | 2 |
| 1223 | 42.02037639 | -3.52286060 | 0.186 | 2 |
| 1377 | 42.01522849 | -3.52388490 | 0.000 | 2 |
| 1407 | 42.00603086 | -3.52378361 | 4.943 | 2 |
| 1531 | 42.01179860 | -3.52578326 | 0.188 | 2 |
| 1582 | 42.01767138 | -3.52618242 | 0.191 | 2 |
| 1953 | 42.01700107 | -3.52165509 | 0.593 | 2 |
| 5 | 42.01549764 | -3.53712308 | 0.189 | 1 |
| 77 | 42.01967533 | -3.53680155 | 0.187 | 1 |
| 82 | 42.01976480 | -3.52540490 | 6.259 | 1 |
| 110 | 42.01184380 | -3.53511810 | 2.681 | 1 |
| 112 | 42.02161230 | -3.52512230 | 5.033 | 1 |
| 262 | 42.01449268 | -3.53497007 | 0.000 | 1 |
| 270 | 42.01340539 | -3.53364156 | 0.159 | 1 |
| 316 | 42.00696144 | -3.53265637 | 0.185 | 1 |
| 457 | 42.02281348 | -3.53305797 | 0.000 | 1 |
| 746 | 42.00876902 | -3.52981517 | 0.195 | 1 |
| 793 | 42.00807525 | -3.52938858 | 0.183 | 1 |
| 859 | 42.01083523 | -3.52946545 | 0.187 | 1 |
| 914 | 42.00876656 | -3.52927118 | 1.559 | 1 |
| 988 | 42.01139524 | -3.52879504 | 0.187 | 1 |
| 996 | 42.01737083 | -3.52816428 | 1.580 | 1 |
| 1526 | 42.01010281 | -3.52584537 | 0.192 | 1 |
| 1923 | 42.01348284 | -3.52118876 | 0.184 | 1 |

Table 3.16: Measured redshifts in MS 2137. The columns are the same as Table 3.15.

| ID | R.A. | Decl. | $z$ | QF |
|---|---|---|---|---|
| 2 | 325.0612502 | -23.66751981 | 0.163 | 3 |
| 8 | 325.0629407 | -23.65686360 | 1.495 | 3 |
| 51 | 325.0591929 | -23.66169910 | 1.494 | 3 |
| 90 | 325.0650339 | -23.66763583 | 1.496 | 3 |
| 93 | 325.0587208 | -23.66655827 | -4.0E-5 | 3 |
| 143 | 325.0631642 | -23.66114100 | 0.314 | 3 |
| 265 | 325.0658341 | -23.66693218 | 1.191 | 3 |
| 305 | 325.0600151 | -23.66525997 | 0.317 | 3 |
| 432 | 325.0624174 | -23.65700482 | 1.495 | 3 |
| 554 | 325.0717926 | -23.66225558 | 0.539 | 3 |
| 557 | 325.0554316 | -23.65875178 | 0.974 | 3 |
| 564 | 325.0658002 | -23.66232491 | 0.123 | 3 |
| 575 | 325.0652998 | -23.66272321 | 3.086 | 3 |
| 579 | 325.0659165 | -23.65859792 | 0.313 | 3 |
| 594 | 325.0660545 | -23.65719416 | 0.323 | 3 |
| 717 | 325.0626655 | -23.66044969 | 0.313 | 3 |
| 796 | 325.0625407 | -23.66026792 | 0.313 | 3 |
| 804 | 325.0608755 | -23.65919716 | 0.314 | 3 |
| 899 | 325.0603961 | -23.65473848 | 1.265 | 3 |
| 978 | 325.0641418 | -23.65707151 | 1.495 | 3 |
| 982 | 325.0655182 | -23.65546970 | 0.311 | 3 |
| 984 | 325.0577362 | -23.65544930 | 0.313 | 3 |
| 1022 | 325.0573735 | -23.65524711 | 3.086 | 3 |
| 1047 | 325.0631649 | -23.65676262 | 1.495 | 3 |
| 1085 | 325.0646960 | -23.65727918 | 1.495 | 3 |
| 1098 | 325.0681213 | -23.65712822 | 0.317 | 3 |
| 1213 | 325.0627779 | -23.65956801 | 1.191 | 3 |
| 1437 | 325.0607713 | -23.65322025 | 0.317 | 3 |
| 1467 | 325.0555769 | -23.65364726 | 0.281 | 3 |
| 1477 | 325.0710864 | -23.65315590 | 0.315 | 3 |
| ⋮ | ⋮ | ⋮ | ⋮ | ⋮ |

| ID | R.A. | Decl. | $z$ | QF |
|---|---|---|---|---|
| ⋮ | ⋮ | ⋮ | ⋮ | ⋮ |
| 263 | 325.0614965 | -23.66630868 | 0.000 | 2 |
| 290 | 325.0612886 | -23.66452073 | 0.316 | 2 |
| 307 | 325.0596807 | -23.66552547 | 0.314 | 2 |
| 616 | 325.0577885 | -23.66006395 | 0.315 | 2 |
| 689 | 325.0631461 | -23.65977012 | 1.496 | 2 |
| 1129 | 325.0649292 | -23.65706087 | 1.492 | 2 |
| 1 | 325.0557350 | -23.66728671 | 0.999 | 1 |
| 4 | 325.0613087 | -23.66945031 | 0.310 | 1 |
| 63 | 325.0581008 | -23.65941150 | 5.509 | 1 |
| 69 | 325.0639614 | -23.66911864 | 0.000 | 1 |
| 166 | 325.0574263 | -23.66726300 | 0.281 | 1 |
| 221 | 325.0605980 | -23.66653599 | 0.328 | 1 |
| 224 | 325.0592894 | -23.66707065 | 1.543 | 1 |
| 242 | 325.0622637 | -23.66447865 | 0.323 | 1 |
| 269 | 325.0616751 | -23.66637744 | 2.459 | 1 |
| 299 | 325.0544046 | -23.66521798 | 0.222 | 1 |
| 318 | 325.0596921 | -23.66584184 | 0.000 | 1 |
| 431 | 325.0621176 | -23.66431571 | 0.639 | 1 |
| 503 | 325.0536364 | -23.66107318 | 0.316 | 1 |
| 580 | 325.0633467 | -23.66185286 | 0.316 | 1 |
| 644 | 325.0648793 | -23.66182589 | 0.937 | 1 |
| 654 | 325.0642144 | -23.66216598 | 0.000 | 1 |
| 657 | 325.0602975 | -23.66170037 | 0.000 | 1 |
| 805 | 325.0543628 | -23.66046275 | 0.311 | 1 |
| 814 | 325.0653077 | -23.66082818 | 2.744 | 1 |
| 868 | 325.0544333 | -23.66021964 | 0.000 | 1 |
| 869 | 325.0580939 | -23.66019602 | 0.318 | 1 |
| 1128 | 325.0631522 | -23.65935947 | 1.496 | 1 |
| 1261 | 325.0699090 | -23.65869802 | 0.000 | 1 |
| 1389 | 325.0630390 | -23.66044158 | 0.000 | 1 |

Table 3.17: Measured redshifts in MACS J0326. The columns are the same as Table 3.15.

| ID | R.A. | Decl. | $z$ | QF |
|---|---|---|---|---|
| 1 | 51.70806634 | -0.73727226 | 0.440 | 3 |
| 13 | 51.70810324 | -0.73102918 | 0.448 | 3 |
| 15 | 51.71595908 | -0.72429963 | 0.058 | 3 |
| 16 | 51.71636815 | -0.73054060 | 1.431 | 3 |
| 18 | 51.70415754 | -0.72469514 | 0.000 | 3 |
| 20 | 51.71355394 | -0.72488020 | 1.247 | 3 |
| 21 | 51.71485312 | -0.72508425 | 0.449 | 3 |
| 26 | 51.70869202 | -0.72576593 | 0.447 | 3 |
| 29 | 51.70178080 | -0.73721435 | 1.179 | 3 |
| 32 | 51.70734694 | -0.72652196 | 0.443 | 3 |
| 37 | 51.70639179 | -0.72749385 | 0.453 | 3 |
| 42 | 51.71263975 | -0.72735037 | 0.452 | 3 |
| 46 | 51.70401058 | -0.72803930 | 0.438 | 3 |
| 50 | 51.71014411 | -0.72838957 | 0.449 | 3 |
| 52 | 51.70845413 | -0.72881622 | 0.000 | 3 |
| 54 | 51.70380841 | -0.72941315 | 1.248 | 3 |
| 55 | 51.70662959 | -0.72941321 | 0.232 | 3 |
| 57 | 51.71376910 | -0.72767990 | 0.776 | 3 |
| 61 | 51.70590437 | -0.73047397 | 0.446 | 3 |
| 62 | 51.70549223 | -0.73047924 | 1.248 | 3 |
| 68 | 51.71396070 | -0.73078547 | 0.458 | 3 |
| 69 | 51.71124680 | -0.73372370 | 0.494 | 3 |
| 74 | 51.70481740 | -0.73595180 | 5.880 | 3 |
| 76 | 51.71123314 | -0.73155115 | 0.455 | 3 |
| $78_M$ | 51.70655724 | -0.73162210 | 0.000 | 3 |
| $78_P$ | 51.70691830 | -0.72437400 | 4.980 | 3 |
| 81 | 51.71233054 | -0.73199644 | 1.098 | 3 |
| 84 | 51.70674370 | -0.73699870 | 5.879 | 3 |
| 86 | 51.70180090 | -0.73108310 | 5.878 | 3 |
| 88 | 51.71547523 | -0.73306727 | 0.356 | 3 |
| 103 | 51.71046650 | -0.73443810 | 1.248 | 3 |
| 108 | 51.70190169 | -0.73491512 | 0.448 | 3 |
| ⋮ | ⋮ | ⋮ | ⋮ | ⋮ |
| 113 | 51.71150751 | -0.73442642 | 0.446 | 3 |
| 116 | 51.71221832 | -0.73567774 | 0.804 | 3 |
| 121 | 51.7005703 | -0.73653835 | 0.444 | 3 |
| 122 | 51.70323641 | -0.73677771 | 0.325 | 3 |
| 138 | 51.70211192 | -0.73705436 | 1.272 | 3 |
| 139 | 51.71652064 | -0.73709426 | 0.804 | 3 |
| 152 | 51.70378826 | -0.73798640 | 1.181 | 3 |
| 160 | 51.71135863 | -0.72256970 | 0.453 | 3 |
| 161 | 51.71602364 | -0.72303510 | 0.441 | 3 |
| 5 | 51.71293750 | -0.72474400 | 1.145 | 2 |
| 23 | 51.70883990 | -0.73340260 | 0.248 | 2 |
| 34 | 51.70202020 | -0.72244300 | 4.788 | 2 |
| 39 | 51.70925786 | -0.72748144 | 0.455 | 2 |
| 41 | 51.71549023 | -0.72772794 | 0.458 | 2 |
| 44 | 51.71477132 | -0.72779148 | 3.235 | 2 |
| 60 | 51.70565583 | -0.73065953 | 0.453 | 2 |
| 85 | 51.70532607 | -0.73234988 | 3.755 | 2 |
| 94 | 51.70138800 | -0.73333498 | 0.414 | 2 |
| 155 | 51.70649017 | -0.73827485 | 0.450 | 2 |
| 17 | 51.70943969 | -0.72450109 | 0.447 | 1 |
| 35 | 51.71171314 | -0.72674022 | 1.248 | 1 |
| 47 | 51.70971234 | -0.72803052 | 0.452 | 1 |
| 53 | 51.70219623 | -0.72919887 | 0.440 | 1 |
| 62 | 51.70046960 | -0.72423605 | 4.012 | 1 |
| 68 | 51.70504950 | -0.72801140 | 3.755 | 1 |
| 77 | 51.70667121 | -0.73145698 | 0.000 | 1 |
| 86 | 51.70681907 | -0.73258985 | 0.443 | 1 |
| 87 | 51.71079159 | -0.73274959 | 0.434 | 1 |
| 90 | 51.70686528 | -0.73301888 | 0.446 | 1 |
| 105 | 51.70739184 | -0.73472983 | 0.448 | 1 |
| 118 | 51.70982389 | -0.73588872 | 0.436 | 1 |
| 145 | 51.70424116 | -0.73770541 | 0.441 | 1 |

Table 3.18: Measured redshifts in MACS J1427. The columns are the same as Table 3.15.

| ID | R.A. | Decl. | $z$ | QF |
|---|---|---|---|---|
| 25 | 216.91619884 | -25.35766428 | 0.317 | 3 |
| 26 | 216.92217694 | -25.35378681 | 0.000 | 3 |
| 31 | 216.90642465 | -25.35723329 | 1.236 | 3 |
| 32 | 216.91803386 | -25.35737324 | 0.000 | 3 |
| 36 | 216.92494939 | -25.35576190 | 0.232 | 3 |
| 40 | 216.91399381 | -25.35600037 | 0.325 | 3 |
| 41 | 216.91008760 | -25.35561308 | 0.313 | 3 |
| 42 | 216.91088341 | -25.35678064 | 0.883 | 3 |
| 50 | 216.91485845 | -25.35028410 | 0.884 | 3 |
| 54 | 216.91193940 | -25.35514541 | 0.319 | 3 |
| 64 | 216.91063525 | -25.35363405 | 1.236 | 3 |
| 75 | 216.91544327 | -25.34620637 | 0.662 | 3 |
| 84 | 216.91035987 | -25.34988187 | 0.309 | 3 |
| 88 | 216.91447505 | -25.35061860 | 0.318 | 3 |
| 93 | 216.91584053 | -25.35056782 | 0.312 | 3 |
| 94 | 216.91691114 | -25.35060176 | 0.319 | 3 |
| 99 | 216.91571850 | -25.35135379 | 0.000 | 3 |
| 101 | 216.92028056 | -25.35105752 | 0.320 | 3 |
| 108 | 216.91500246 | -25.35168478 | 0.313 | 3 |
| 114 | 216.91434723 | -25.35196763 | 0.207 | 3 |
| 117 | 216.91959666 | -25.35234976 | 0.321 | 3 |
| 118 | 216.91229301 | -25.35263420 | 0.325 | 3 |
| 122 | 216.91602417 | -25.35293113 | 0.322 | 3 |
| 131 | 216.91432235 | -25.35339907 | 0.313 | 3 |
| 132 | 216.91465475 | -25.35352760 | 0.001 | 3 |
| 133 | 216.91264386 | -25.35362011 | 0.883 | 3 |
| 148 | 216.91775549 | -25.35420614 | 0.312 | 3 |
| 156 | 216.90745832 | -25.35435398 | 4.323 | 3 |
| 162 | 216.90934813 | -25.35488005 | 0.324 | 3 |
| 167 | 216.90690018 | -25.35510802 | 0.313 | 3 |
| 180 | 216.90829896 | -25.35540450 | 0.914 | 3 |
| 191 | 216.91571984 | -25.34906701 | 0.317 | 3 |
| 193 | 216.90811293 | -25.34955274 | 0.328 | 3 |
| 195 | 216.91512646 | -25.34888806 | 0.316 | 3 |
| 196 | 216.91563524 | -25.34970724 | 0.316 | 3 |
| 207 | 216.91835520 | -25.34833384 | 0.325 | 3 |
| 217 | 216.92013294 | -25.34813976 | 0.320 | 3 |
| 219 | 216.90701865 | -25.34757320 | 0.695 | 3 |
| 225 | 216.90930004 | -25.34377121 | 0.322 | 3 |
| 226 | 216.91207270 | -25.34651632 | 0.663 | 3 |
| 234 | 216.90966217 | -25.34486568 | 0.856 | 3 |
| ⋮ | ⋮ | ⋮ | ⋮ | ⋮ |

| ID | R.A. | Decl. | $z$ | QF |
|---|---|---|---|---|
| ⋮ | ⋮ | ⋮ | ⋮ | ⋮ |
| 241 | 216.92268855 | -25.34577380 | 0.322 | 3 |
| 251 | 216.91990633 | -25.34613558 | 1.239 | 3 |
| 1 | 216.91549900 | -25.35909370 | 0.232 | 2 |
| 56 | 216.91033590 | -25.35151940 | 0.813 | 2 |
| 68 | 216.91654650 | -25.35620440 | 6.043 | 2 |
| 72 | 216.91702200 | -25.35768770 | 3.961 | 2 |
| 73 | 216.91282910 | -25.34527350 | 6.042 | 2 |
| 81 | 216.92296584 | -25.34974507 | 0.000 | 2 |
| 96 | 216.91911505 | -25.35069157 | 0.780 | 2 |
| 102 | 216.92348540 | -25.35112651 | 0.437 | 2 |
| 103 | 216.90951026 | -25.35120070 | 0.315 | 2 |
| 138 | 216.92258186 | -25.34430751 | 1.119 | 2 |
| 199 | 216.91479272 | -25.34911416 | 0.000 | 2 |
| 218 | 216.90615033 | -25.34387282 | 0.915 | 2 |
| 220 | 216.91306431 | -25.34663774 | 0.315 | 2 |
| 2 | 216.90763630 | -25.35900540 | 0.326 | 1 |
| 22 | 216.91948152 | -25.35840617 | 0.346 | 1 |
| 34 | 216.91844686 | -25.35742171 | 2.055 | 1 |
| 35 | 216.91288324 | -25.35744786 | 0.321 | 1 |
| 53 | 216.92419220 | -25.35758180 | 3.711 | 1 |
| 57 | 216.91773293 | -25.35578650 | 0.347 | 1 |
| 58 | 216.91795080 | -25.34248430 | 5.987 | 1 |
| 74 | 216.92431599 | -25.35543093 | 0.231 | 1 |
| 77 | 216.91119860 | -25.34467890 | 4.474 | 1 |
| 121 | 216.91576496 | -25.35285091 | 1.381 | 1 |
| 140 | 216.90804218 | -25.35371079 | 0.907 | 1 |
| 141 | 216.91940086 | -25.35381755 | 0.309 | 1 |
| 144 | 216.91105772 | -25.35395397 | 0.398 | 1 |
| 164 | 216.92323652 | -25.35479505 | 0.317 | 1 |
| 169 | 216.92067451 | -25.35487997 | 0.575 | 1 |
| 170 | 216.91419559 | -25.34846838 | 4.019 | 1 |
| 172 | 216.90966979 | -25.35508015 | 0.318 | 1 |
| 173 | 216.92047912 | -25.35515232 | 0.575 | 1 |
| 176 | 216.90934137 | -25.35527508 | 0.328 | 1 |
| 185 | 216.90949896 | -25.34656741 | 1.208 | 1 |
| 201 | 216.91901817 | -25.34852172 | 1.040 | 1 |
| 208 | 216.91808783 | -25.34834611 | 3.349 | 1 |
| 213 | 216.90558929 | -25.34828333 | 0.913 | 1 |
| 232 | 216.90673382 | -25.34649694 | 0.783 | 1 |
| 248 | 216.91130553 | -25.34609367 | 0.327 | 1 |
| 254 | 216.91156687 | -25.34619676 | 0.319 | 1 |

# CHAPTER 4

## Variations on Models for the Dark Matter Inner Slope

In this chapter, I review the methodology presented in Chapter 3 to investigate the effects of different mass paramaterizations on the measurement of the inner DM density profile. I specifically review the effects of using the dPIE profile compared to the gNFW profile (see Section 2.3.1 and Section 2.1.2) to model the dark matter component of the cluster. I also examine the effects of choosing different paramaterizations of the BCG mass profile by modeling the BCG with Hernquist, Einasto, Jaffe, and dPIE profiles. The work presented in this chapter is ongoing, and all results should be treated as preliminary.

## 4.1 Cluster Sample

I select two more clusters from the Kaleidoscope survey to examine for this chapter: Abell 2537 (hereafter A2537) and MACS J1423.8+2504 (hereafter MACS J1423). Both clusters are home to radial arcs, making them particularly suited for making precise measurements of the inner profile (as described in Section 3.1). They can also be compared directly to the clusters discussed in Chapter 3. These two clusters also have enough *HST* observations available to reliably distinguish between cluster

member and background galaxies, which allows for weak lensing constraints to be incorporated into the lens model. This, in turn, allows me to describe the dark matter halo of the cluster with a gNFW profile in `Lenstool`, since the addition of weak lensing allows for the scale radius, $r_s$, to be constrained (Limousin et al. 2022). I take the opportunity to investigate the effects of different profile choices on the cluster dark matter halo and the BCG mass profile. However, given the correlation between the inner slope measurement and $r_s$ discussed in Section 2.1.2 and presented in He et al. (2020), I continue to use the dPIE profile to describe the dark matter halo in the main lens models presented in this Chapter.

MACS J1423, located at redshift $z = 0.545$, is a cool-core, relaxed, nearly virialized cluster with minimal substructure (LaRoque et al. 2003; Schmidt & Allen 2007; Ebeling et al. 2007). It was first observed in the MACS survey and is part of the high-redshift MACS subsample, which consists of 12 galaxy clusters at $z > 0.5$. It was also later observed as a part of the CLASH survey and has been modeled several times in previous literature (Limousin et al. 2010; Zitrin et al. 2011, 2015; Merten et al. 2015). Patel et al. (2024) presents the most recent version of its lensing mass model, which includes weak lensing and spectroscopic identifications of cluster members and lensed galaxies drawn from the Kaleidoscope survey. In this chapter, I use this lens model as a basis and only add kinematic and photometric information from the BCG to the model.

A2537, located at redshift $z = 0.296$, by contrast, has a slightly more complex mass distribution than the clusters discussed in Chapter 3, with regular and symmetric X-ray emission located a little more than 10 kpc North of the BCG. This cluster does not show a cool core (Rossetti et al. 2011). It was first modeled as part of the N13 analysis. It is unique in this group due to its extremely low reported $\beta$ value of $0.23^{+0.18}_{-0.16}$, which is comparatively so low that removing this cluster from the sample would cause the average slope measurement to increase by about 40%, from 0.50 to 0.69. This extreme low value marks this cluster as a potentially extreme example of a cored dark matter structure, and remodeling it with new MUSE and *HST* observations is thus of particular interest.

A2537 was observed with *HST* as part of the REionization Lensing Cluster Sur-

vey (RELICS; Coe et al. 2019), a program designed to constrain the galaxy luminosity function at the epoch of reionization by observing lensing and high-mass galaxy clusters in seven different pass-bands (ACS/F435W, F606W, and F814W pass-bands; and WFC3/IR F105W, F125W, F140W, and F160W pass-bands). I take the opportunity in this chapter to revisit the lens model I published in Cerny et al. (2018) as a part of this survey collaboration, and I present a new lens model and a new MUSE catalogue for A2537, which includes the new spectroscopic identification of a gravitationally lensed system. I discuss its special geometry in Section 4.1.1.

### 4.1.1 Hyperbolic Umbilic Configuration

As I showed in Section 3.1, radial arcs form when a source falls on the radial caustic of a lens in the source plane, which causes two images to form that stretch across the critical line of the image plane, and give rise to the characteristic shape of a radial arc. This geometric position of the source on the radial caustic also contains an interesting mathematical implication. Recalling Equation 1.29 for the magnification of an image, if the position of a finite image in the image plane is translated, or mapped, to the source plane, the resulting shape of the image will be a line or a point in the source plane. This transformation from a finite image to a point indicates that the lens mapping for sources lying on caustic or critical lines is 'singular', and the magnification of the source can formally be described as infinite. Of course, in practice, observed sources are small and finite in size, so their magnification is also finite. Still, these locations, also termed 'singularities', are of great interest due to the often complex or unusual shape of the resulting lensing configurations, and they can be classified using catastrophe theory (Poston & Schulman 1978; Berry & Upstill 1980; Blandford & Narayan 1986). Radial arcs belong to a category of lensing configurations called 'stable' singularities, and their position in the source plane can be described by fold and cusp configurations, as shown in Figure 4.1. Stable singularities are not common, as I discussed in Section 3.1, but they are not exceedingly rare.

Of course, the existence of a stable singularity necessarily implies the existence of an *unstable* singularity. These lensing configurations are also known as 'exotic'

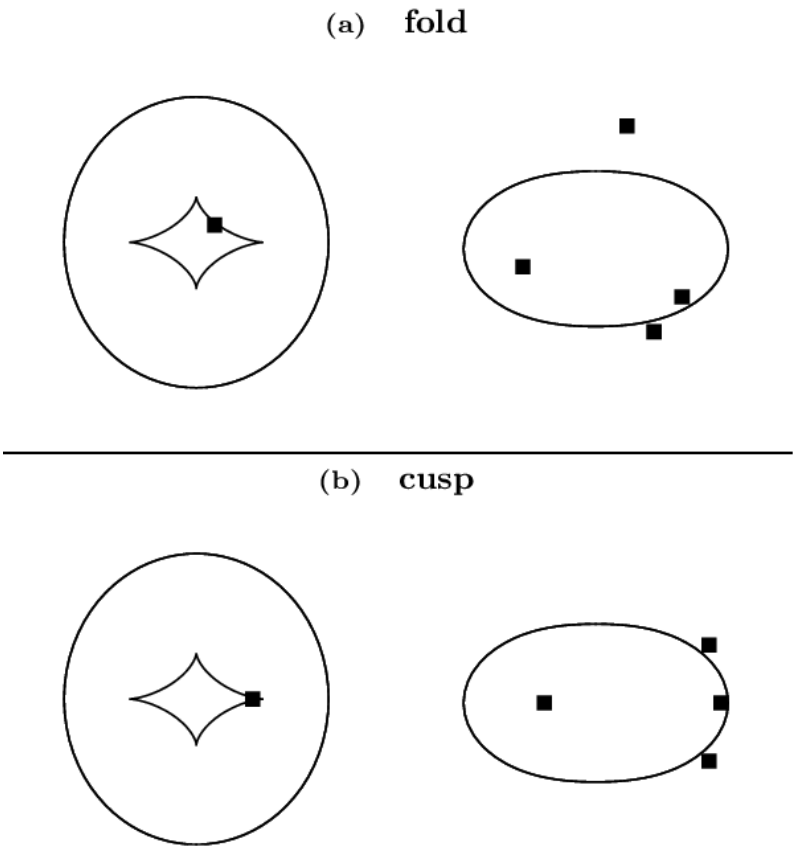


Figure 4.1: Diagram illustrating simple fold and cusp lensing configurations for a singular elliptical isothermal lens. The left-hand image in both panels shows the source plane, and the right-hand image shows the image plane. The source is shown as a black square, and lies on the tangential caustic in the source plane, either on the curved portion (the fold) or the pointed portion (the cusp); hence the origin of the fold/cusp terminology. Adapted from Aazami & Petters (2009).

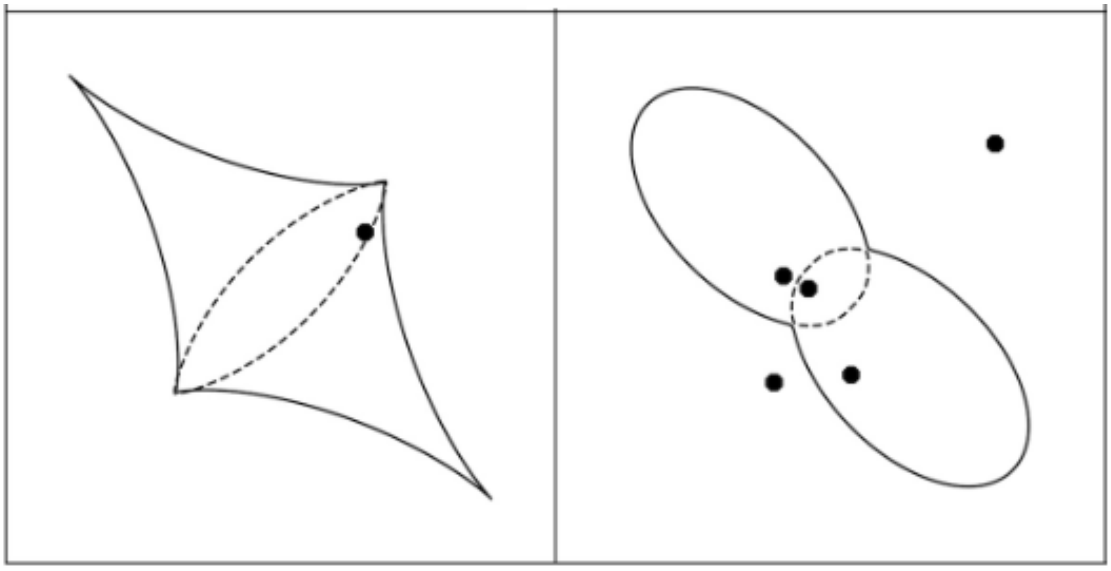

Figure 4.2: Diagram demonstrating the effect of source position on the image formation near a HU singularity for an elliptical lens. The left panel shows the source plane, where the solid line represents the tangential caustic, and the dashed line represents the radial caustic. The source position is marked by the solid black dot. The right panel shows the corresponding image plane configuration, where the solid and dashed lines represent the tangential and radial critical lines, respectively. Image positions are shown by the black dots. This configuration is potentially representative of the two HU systems in Abell 2537. Reproduced from Meena & Singh Bagla (2024).

lens systems (Orban de Xivry & Marshall 2009; Meena & Bagla 2020), and they are particularly interesting because of their high magnification factors ($\mu \geq 100$) and their location, which is always within the innermost region of the image plane. There are several types of exotic lensing configurations (as described in Orban de Xivry & Marshall (2009)), but the most relevant configuration in this chapter is known as the 'Hyperbolic Umbilic' (HU) pattern. HU configurations are formally described by a cusp point in the source plane that is exchanged between two caustic lines (Schneider & Weiss 1992), and this geometry can be seen in Figure 4.2, where the point in the source plane lies between the tangential and radial caustic lines. This configuration is particularly useful for my goal of examining the inner mass profile of clusters since it produces the most multiple images and functions similarly to radial arcs, in that the multiple images are naturally located in the innermost region of the cluster.

However, HU configurations and exotic systems in general have historically been

very difficult to find. The only known system for many years was Abell 1703, which was identified and modeled in Limousin et al. (2008). This is because these multiple images are often not easily visible in broadband imaging, and can be easily masked by the light from cluster member galaxies. Fortunately, observations made with MUSE have recently led to a series of new discoveries of these exotic lensing configurations (Richard et al. 2021; Lagattuta et al. 2023; Meena & Singh Bagla 2024; Ebeling et al. 2024). This is because MUSE's wavelength coverage is particularly adept at detecting emission features from background sources. In this chapter, I identify two new HU system candidates in A2537, which I am able to spectroscopically confirm using MUSE. I discuss these systems more thoroughly in Section 4.4.

## 4.2 Observations

### 4.2.1 Hubble Space Telescope Imaging

I use archival imaging from the RELICS survey (Coe et al. 2019) in the ACS F814W and F606W pass-bands, and the WFC3/IR F160W pass-band, to identify multiple images in A2537. I also use the WFC3/IR F105W pass-band in the construction of the galaxy catalogue for the cluster. These galaxies were identified using SExtractor (Bertin & Arnouts 1996b) in dual mode on the F814W and F105W pass-band images, which straddles the 4000 Å break, with threshold parameters `DETECT_THRESH` = 1.5 and `DETECT_MINAREA` = 20. Detections with error flags or unreliable magnitude measurements (i.e. `MAG_AUTO=-99`) were dropped, and detections with a stellarity measurement greater than 0.5 were removed (unless spectroscopically confirmed to be extra-galactic sources) as they are more likely to be stars rather than galaxies. Only objects that appeared in both pass-bands were kept in the final catalogue. I also identify multiple image systems from the *HST* imaging for A2537 based on geometry, color, and morphology. The properties of the arcs are listed in Table 4.1. All imaging was obtained from MAST[1]. Basic data reduction procedures were applied to all imaging using `HSTCAL` and standard calibration files. `Tweakreg` was

[1]https://archive.stsci.edu/prepds/clash/

Table 4.1: Properties of the multiple images used as constraints for A383. Column 1 lists the ID of the image. Columns 2 and 3 list the Right Ascension and Declination, given in degrees (J2000). Column 4 lists the redshift value, $z$, and all redshifts are fixed to a spectroscopic measurement so no error bars are used. Column 5 lists the rms for the best fit measured in the source plane for each family of multiple images.

| ID | R.A. | Decl. | $z$ | rms (") |
|---|---|---|---|---|
| 1.1 | 347.0893938 | -2.1885798 | 1.97 | 0.35 |
| 1.2 | 347.0967970 | -2.1931717 | 1.97 | 0.46 |
| 1.3 | 347.0878560 | -2.1989489 | 1.97 | 0.52 |
| 1.4 | 347.0962415 | -2.1841333 | 1.97 | 0.29 |
| 1.5 | 347.0925538 | -2.1913284 | 1.97 | 0.34 |
| 12.1 | 347.0896128 | -2.1887695 | 1.97 | 0.13 |
| 12.2 | 347.0971641 | -2.1931830 | 1.97 | 0.44 |
| 12.3 | 347.0882620 | -2.1992306 | 1.97 | 0.51 |
| 12.4 | 347.0968544 | -2.1845748 | 1.97 | 0.21 |
| 12.5 | 347.0925973 | -2.1909716 | 1.97 | 0.26 |
| 2.1 | 347.0978160 | -2.1861945 | 3.61 | 1.10 |
| 2.2 | 347.0907673 | -2.1878363 | 3.61 | 0.88 |
| 2.3 | 347.0925654 | -2.1900782 | 3.61 | 0.10 |
| 2.4 | 347.0988341 | -2.1897756 | 3.61 | 0.11 |
| 2.5 | 347.0876202 | -2.2012870 | 3.61 | 0.51 |
| 3.1 | 347.0827279 | -2.1885369 | 2.79 | 0.92 |
| 3.2 | 347.0818741 | -2.1903123 | 2.79 | 0.72 |
| 3.3 | 347.0879899 | -2.1817137 | 2.79 | 0.17 |
| 31.1 | 347.0826479 | -2.1887931 | 2.79 | 0.77 |
| 31.2 | 347.0819937 | -2.1900864 | 2.79 | 0.78 |
| 31.3 | 347.0885907 | -2.1813703 | 2.79 | 0.32 |
| 4.1 | 347.0859302 | -2.1931026 | 4.99 | 0.00 |
| 4.2 | 347.0860427 | -2.1942949 | 4.99 | 0.00 |
| 4.3 | 347.0930871 | -2.1932384 | 4.99 | 0.73 |
| 4.4 | 347.0939820 | -2.1943938 | 4.99 | 0.10 |
| 4.5 | 347.0967749 | -2.1802956 | 4.99 | 0.43 |

Table 4.2: Summary of *HST* observations used in this chapter. Column 1 is the name of the cluster. Column 2 and 3 are the Right Ascension and Declination, given in degrees (J2000). Column 4 is the pass-band. Column 5 is the PID. Column 6 is the P.I. of the observation. Column 7 is the exposure time. Column 8 is the observation date.

| Name | R.A. | Decl. | Band | PID | P.I. | Exp. time [s] | Obs. date |
|---|---|---|---|---|---|---|---|
| A2537 | 347.09208333 | -2.19222222 | ACS/F606W | 9270 | Allen | 2080 | 2002-10-02 |
| | 347.09098395 | -2.19136208 | ACS/F814W | 14096 | Coe | 2162 | 2016-07-19 |
| | | | WFC3/F105W | | | 756 | 2016-07-19 |
| | | | WFC3/F105W | | | 756 | 2016-08-06 |
| | | | WFC3/F160W | | | 1006 | 2016-07-19 |
| | | | WFC3/F160W | | | 956 | 2016-08-06 |
| MACS J1423 | 215.9497915 | 24.0786826 | ACS/F606W | 12790 | Postman | 1088 | 2013-01-13 |
| | 215.9495000 | 24.0784722 | ACS/F606W | 12790 | Postman | 1032 | 2013-02-05 |

used to register individual frames to a common *ACS* reference image, after which `Astrodrizzle` was used to co-add the frames together.

Since I do not remodel MACS J1423, I refer the reader to Patel et al. (2024) for details on the multiple image identification for this cluster. I use the ACS F606W pass-band to perform photometric measurements of the BCG, which I obtain from archival CLASH images (Postman et al. 2012a). This filter was not otherwise incorporated into the modeling of the cluster.

The *HST* observations, exposure times, and bands used for both clusters are listed in Table 4.2.

### 4.2.2 VLT-MUSE Observations

Since these data also come from the Kaleidoscope survey, the structure of the observations is the same as in Section 3.3.2. A total of three sequential exposures were made in each observation, lasting 970 s each, where a small dither (0.3 arcsec) is applied between each exposure to minimize the effect of observational systematics. Each frame is rotated 90 degrees clockwise relative to the previous frame, and the observations are stacked together to create a single cube with a total exposure time of 2910 s. A summary of the observations and observing conditions for A2537 and MACS J1423 is given in Table 4.3.

I performed data reduction of the MUSE cubes using the standard procedures of the `esorex` pipeline (MUSE-KIT-2.4.1; Weilbacher et al. 2016), along with additional

Table 4.3: Summary of VLT/MUSE observations used. Column 1 is the name of the cluster. Column 2 lists the seeing for the observation. Column 3 lists the airmass. Column 4 lists the P.I. for the observation. Column 5 lists the exposure time. Column 6 lists the observation date. Column 7 lists the ESO Programme ID.

| Cluster | Seeing | Airmass | P.I. | Exp. time [s] | Obs. date | ESO Programme ID |
|---|---|---|---|---|---|---|
| A2537 | 0.79" | 1.96 | Edge | 2910 | 2022-08-23 | 0109.A-0709(A) |
| MACS J1423 | 0.57" | 1.77 | Edge | 2910 | 2019-03-18 | 0102.A-0718(A) |

calibration and cleaning steps (as described in e.g., Richard et al. 2021 or Lagattuta et al. 2022). Using basic calibration files as a reference, I completed bias subtraction and flat fielding using illumination and twilight exposures with dates closest to that of the source exposure. I performed telluric correction and flux calibration with the standard star taken closest to the date of the source exposure. I used the pipeline to complete this initial reduction process to align the three individual exposures in each observation. I subsequently ran the final calibration step (the "scipost" phase) again to improve flux variation between individual IFU slices. A mask is first applied to eliminate flux from intra-cluster light and bright cluster members, as this may bias the measurement. The flux variation is then achieved using an auto-calibration algorithm included in the MUSE reduction pipeline. Finally, I applied the Zurich Atmospheric Purge (ZAP; Soto et al. 2016) algorithm to the fully reduced final data cube in order to eliminate strong skyline residuals after sky subtraction.

I performed source extraction for A2537 only, and used the published catalogue from Patel et al. (2024) for MACS J1423. A full breakdown of this process is given in Section 3.3.2, and I refer the reader to this section for details.

I initialized the source analysis procedure for A2537 by running the Source Extractor pipeline, which identifies individual sources within a datacube by grouping together pixels above a given SNR value. In the case of A2537, I set the SNR cutoff to be higher than 3, which successfully removed isolated individual pixels with a high SNR (i.e. cosmic rays), as well as pixels associated with artifacting at the edge of the datacube, without removing individual sources (i.e. cluster members, stars, foreground galaxies, and background galaxies). A total of 678 sources were extracted by the pipeline.

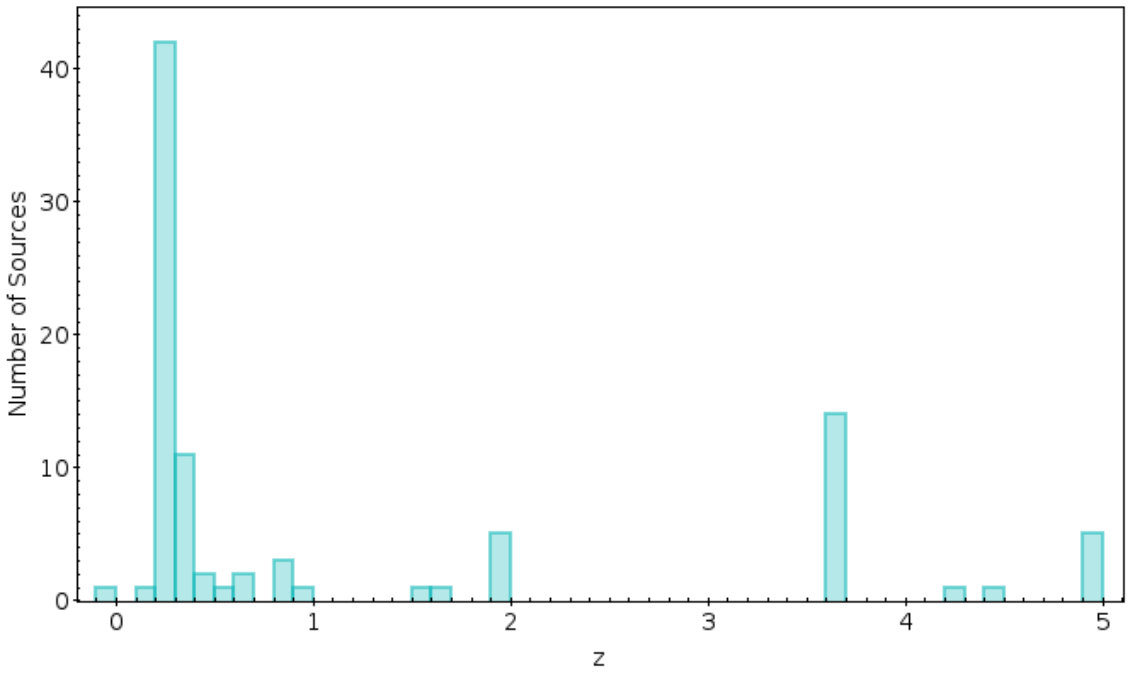


Figure 4.3: MUSE redshift distribution for the galaxy cluster A2537. The largest peak corresponds to the cluster member galaxies at $z$ =0.296, the peak at $z$ =3.6 corresponds to arc system 2, and the peak at $z$ =4.9 corresponds to arc system 4.

I enlisted the assistance of two other users to evaluate each source. Each user independently assigned a redshift and a confidence rating to every extracted source. This confidence rating is set between 0-3, where 3 is a confirmed detection (redshift identified from multiple features or one unambiguous feature, such as a Ly-$\alpha$ or [OII] doublet), 2 is a probable detection (several lines that are noisy, which boosts the redshift error, or a single feature that is probably known but could also be something else, i.e. a blended [OII] line that could also be a wide [OIII] line or noisy Ly-$\alpha$), 1 is a possible detection (a best guess, though this is very uncertain), and 0 is no detection (no features, just noise). Once each user had completed their evaluation, I led a reconciliation session to determine a group ranking for each source based on the agreement between each user's selections. Redshifts with a confidence rating of 3 were strongly agreed upon by all three users; redshifts with a confidence rating of 2 were tentatively agreed upon by all three users; and redshifts with a confidence rating of 1 were included as a 'best guess'. Confidence 1 redshifts were not included in the final lens model unless they were assigned to lensed galaxies whose positions were supported by the structure of the lens model.

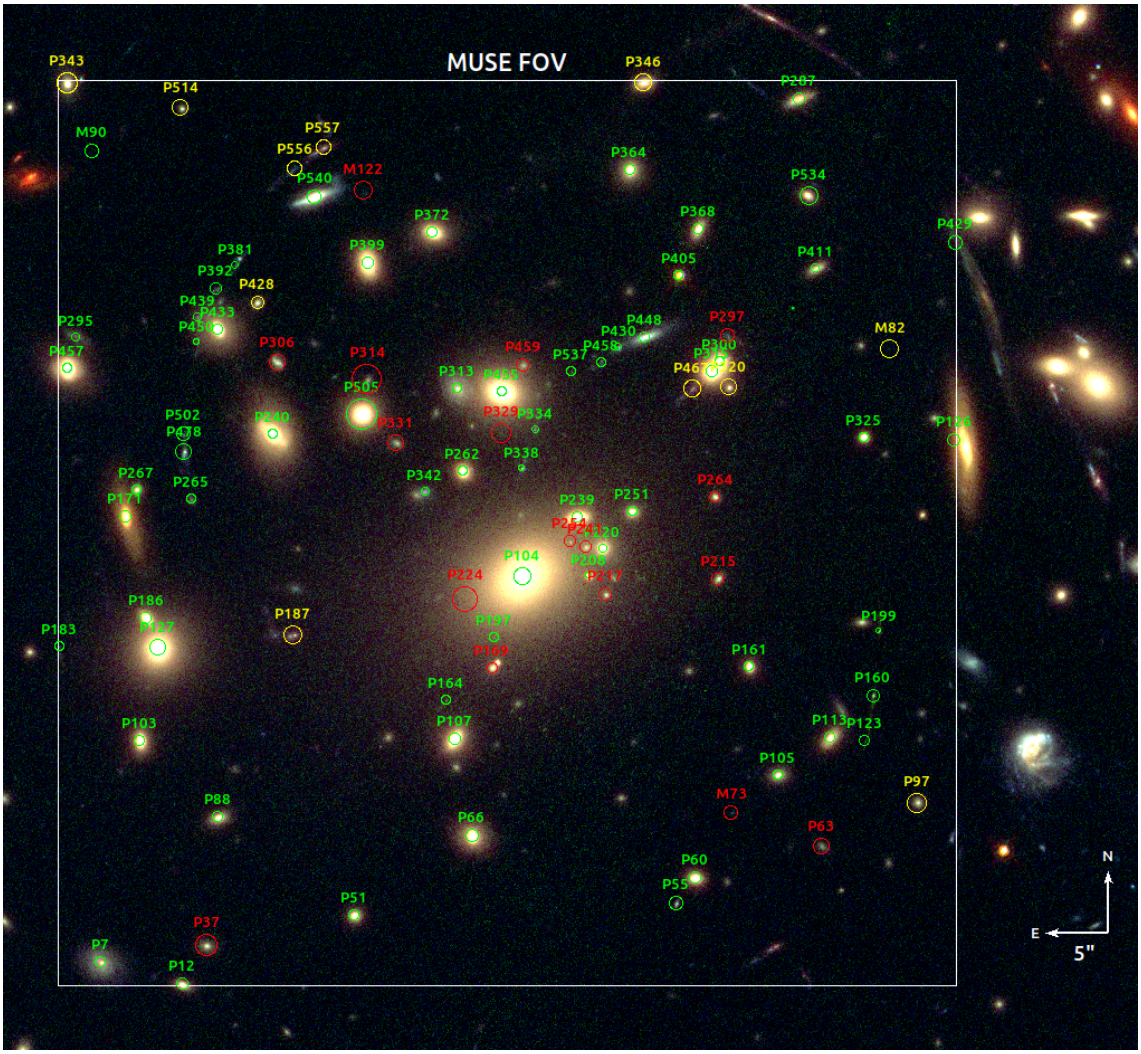


Figure 4.4: *HST* color composite image of A2537 created using a combination of WFC3/IR imaging in the red (F160W pass-band) and ACS imaging in the green (F814W) and blue (F606W) pass-bands. All identified sources from MUSE in the galaxy cluster A2537. The MUSE FOV is shown as a white box, and the image is oriented North-East. Sources with a confidence level of 3 are marked in green, sources with a confidence level of 2 are marked in yellow, and sources with a confidence level of 1 are marked in red. The strength of the identification is measured from 1-3, such that a ranking of 3 corresponds to a highly confident redshift identification, while a ranking of 1 corresponds to a 'guess' at the correct redshift identification.

A total of 92 sources are identified in the A2537 MUSE datacube, of which 50 are cluster members, 2 are foreground sources, and 38 are background sources ($z > 0.33$). Of the four lensing systems in A2537, Systems 1, 12, 2, and 4, each have almost every arc spectroscopically confirmed. System 3 is out of range of the MUSE FOV, and was thus unable to be observed. The distribution of source redshifts in A2537 is shown in Figure 4.2.2, and the spatial location of all identified sources is presented in Figure 4.2.2. I particularly want to highlight P197, P164, P199, P160, and P450, P392, P338, and P458. These identifiers correspond to the two HU systems in the cluster, and all images within the MUSE FOV are independently confirmed with a spectroscopic redshift of confidence 3 (the highest rating), which is strong evidence that these are HU systems. A summary of the redshifts for all identified sources in the MUSE data is given in Table 4.10.

## 4.3 Measured Properties of the BCG

### 4.3.1 BCG Photometry

In order to constrain the stellar mass component of the BCG in the cluster lens models, I fit the surface brightness profile of the BCG to a mass profile, following the conventions introduced in Section 3.5.1. I use the dPIE profile again in the main results for both A2537 and MACS J1423, both because this profile is a good fit to the surface brightness data, and because this particular profile is simple to implement in `Lenstool`.

In both clusters, I use the ACS/F606W band to perform the photometric fit. I use a combination of the `Astropy`, `Photutils`, and `PetroFit` Python packages to build a pipeline to quickly obtain the values presented in this chapter. This pipeline is capable of extracting the shape of the light profile and finding a good fit the isophotal surface brightness profile, but I emphasize that these values are better treated as an initial estimate of the true properties of the BCG. They are valuable for obtaining an understanding of the shape and flux of the BCG, but more testing is needed before I am able to confidently say that this pipeline can completely reproduce results from more robust algorithms like `Galfit`.

Table 4.4: Values for the BCG of each cluster extracted from the photometric fitting process. Column 1 lists the cluster. Column 2 lists the filter used for the photometric fit of the BCG. Column 3 lists the $b/a$ value, where the ellipticity $e$ is equivalent to $e = 1 - b/a$. Column 4 lists the position angle, $\theta$. Column 5 lists the magnitude of the BCG in the listed filter. Columns 6 and 7 list the $r_{\rm core}$ and $r_{\rm cut}$ fit values. The errors for $r_{\rm core}$ are extremely small and are thus not given.

| Cluster | Filter | $b/a$ | $\theta$ | Magnitude | $r_{\rm core}$ [kpc] | $r_{\rm cut}$ [kpc] |
|---|---|---|---|---|---|---|
| A2537 | ACS/F606W | 0.85 | 86.23 | 16.87 | 0.60 | 52.6 $\pm$ 3.7 |
| MACS J1423 | ACS/F606W | 0.62 | 65.83 | 17.92 | 0.25 | 35.1 $\pm$ 9.4 |

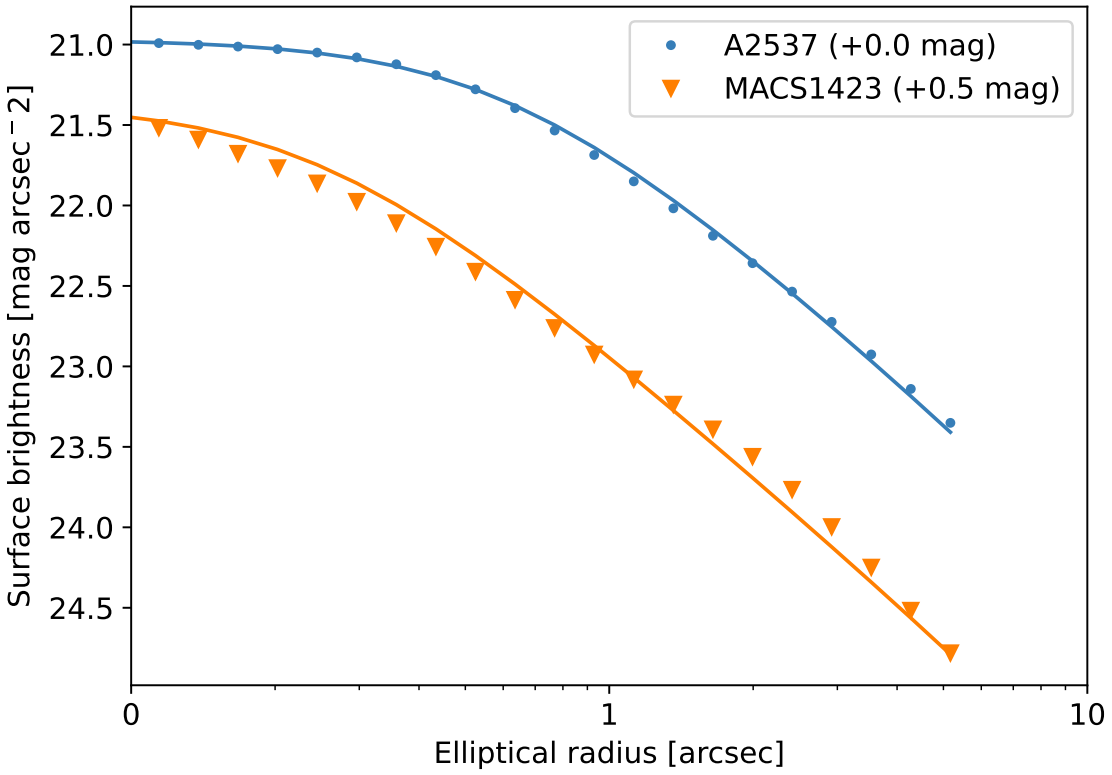


Figure 4.5: Surface brightness profiles of the BCGs for A2537 and MACS J1423, measured using the filters listed in Table 4.4. The dPIE fit for each profile is plotted as the solid line of the same color as each cluster. The magnitudes for each cluster are offset by the listed values to provide visual clarity.

I briefly describe the steps of the pipeline here. First, a 2D cutout of the BCG is made using the relevant *HST* image and the associated error image. This cutout is wide enough to contain the BCG and some of the surrounding sky. I then create a segmentation image of the BCG in order to identify the various sources in the image, where the extent of a source is determined by checking the value of a pixel against some threshold value in the image, which I define here as the standard deviation of the image, as calculated by the `sigma clipped stats` function in the `Astropy` stats package. This segmentation image is then deblended into different sources in order to separate the BCG from any surrounding objects, and a catalog of the deblended sources is constructed. The BCG is selected from the catalog, and all other sources are masked out. The mask is constructed from the deblended segmentation image, which sets the value of individual pixels associated with masked sources to 0. I then use the `Petrofit Source` function to define the BCG as a source and determine initial shape parameters of the light, including the ellipticity and position angle. I then generate a `Petrofit Sersic2D` model using these initial shape parameters. I convolve this `Sersic2D` model with the PSF from the associated *HST* image, which I determine by selecting a 50x50 pixel box around a star within the image. The final step to determining the BCG shape parameters occurs when I use the `Fitting` routine from the `Astropy Modeling` library to fit the masked BCG image to the Sersic model. The error image of the *HST* filter is used as a weight during this fitting process. The final fit is obtained from the `Petrofit fit model` routine. The resulting model reproduces the image data well and leaves minimal residuals, as shown in Figure 4.6, and so I use this fit to report the $b/a$ and $\theta$ values given in Table 4.4.

I obtain the surface brightness profile for the BCG using the fit parameters as a basis for the `Photutils ellipse` routine. I then calculate the magnitude for the BCGs using the flux of the central isophote as a basis. I perform the fit of a dPIE profile to the surface brightness profile using the same methods given in Section 3.5.1. The resulting profiles are shown in Figure 4.5, and the fit parameters are listed in Table 4.4.

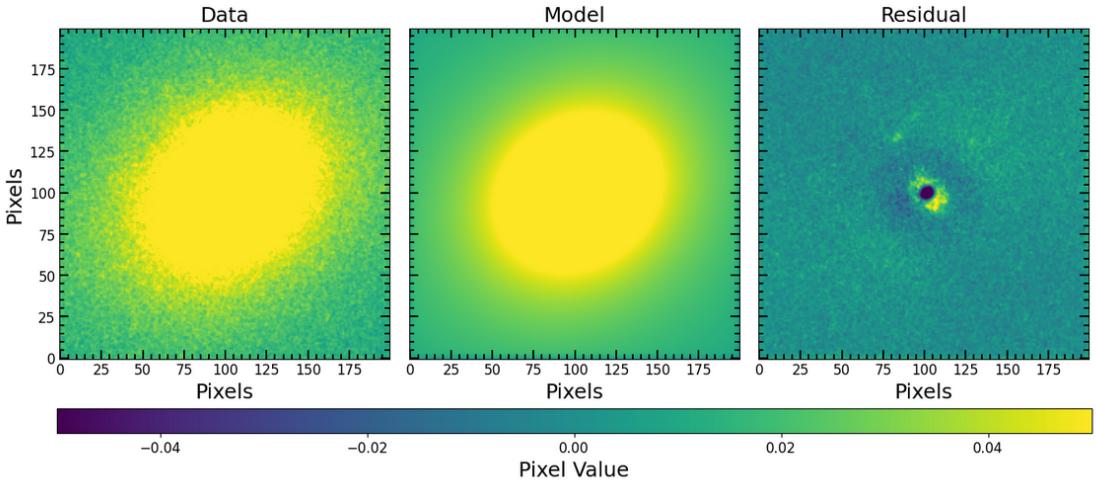


Figure 4.6: Example of the basic pipeline output for BCG photometric modeling described in this section. The left-hand panel shows the cutout of the BCG used for the analysis, the central panel shows the model of the BCG, and the right-hand panel shows the residuals.

### 4.3.2 BCG Velocity Dispersion Profile

I fit the velocity dispersion profiles of the BCGs using the same methods described in Section 3.5.2. However, similarly to Section 4.3.1, I wrap these methods into a new pipeline that can be used to quickly generate a fit to the data. I emphasize that this pipeline works well for simple configurations of light (i.e. a BCG that is not surrounded by many other bright objects), but more care is needed if the data is particularly noisy, or if the BCG light is contaminated by many surrounding objects. Still, this pipeline does fit the data reasonably well (within $1\sigma$ error), and it is useful for the purposes of this chapter to provide an initial estimation of the properties of the BCG velocity dispersion profile. More testing is needed to make the pipeline more robust, however, and the results presented here should be treated as preliminary.

I describe the pipeline briefly here. I define a center for an aperture extraction of the BCG based on the location of the peak of the BCG light as determined in the MUSE imaging. I choose to use the MUSE coordinates because there is a slight offset between the MUSE center and the *HST* center that has the potential to interfere in the measurement of the density profile. I utilize the `MUSE Python Data Analysis Framework (MPDAF)` to handle the MUSE datacubes. I create a

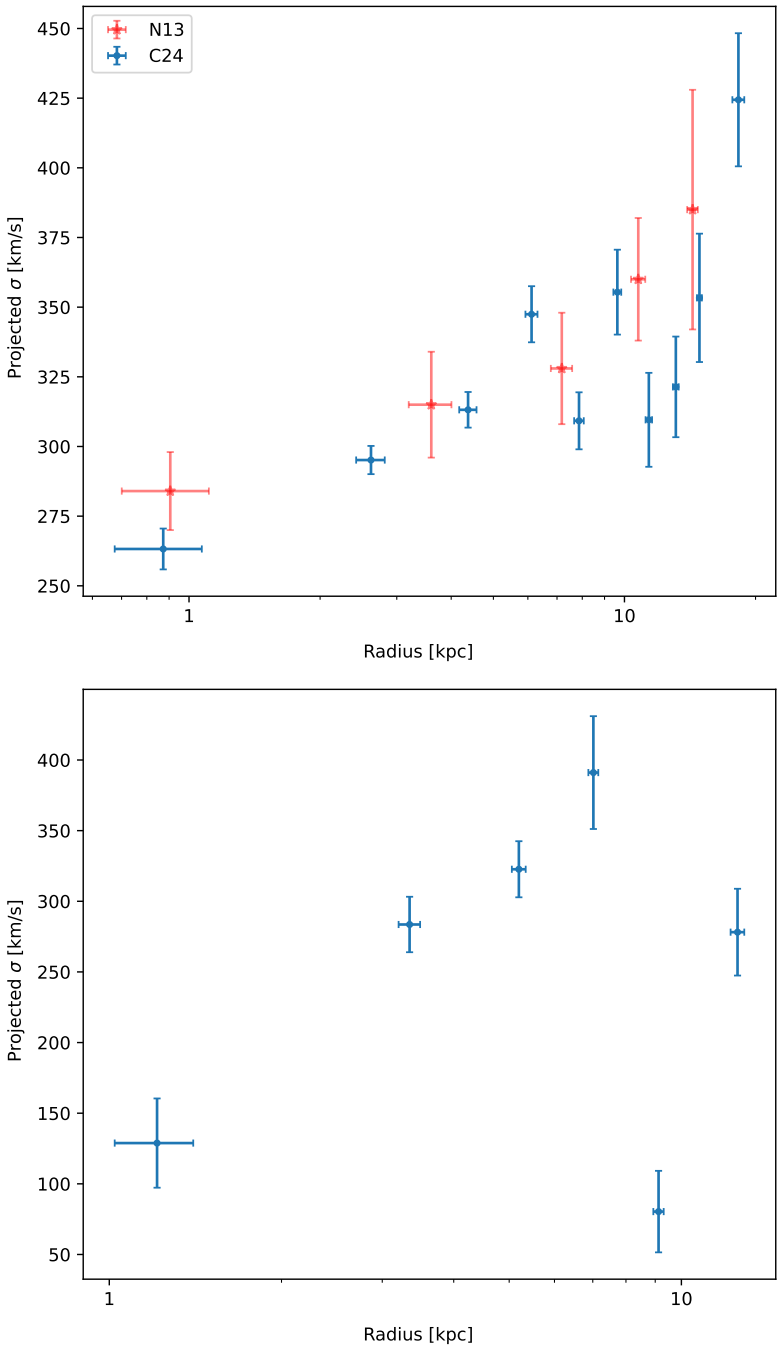


Figure 4.7: *Left:* BCG stellar velocity dispersion profile for the galaxy cluster A2537. The error in the velocity dispersion is denoted by the error bars along the Y axis, while the error bars on the X axis signify the width of the bin used to make the measurement. The data points are centered at the middle of each bin at the values given in Table 4.5. The N13 measurements are plotted as red stars. *Right:* BCG stellar velocity dispersion profile for the galaxy cluster MACS J1423. The formatting is the same as the left plot.

Table 4.5: Values for the velocity dispersion profiles for the BCGs of A2537 and MACS J1423. The quoted $\sigma$ values are measured at the midpoint of each bin. Column 1 lists the cluster. Column 2 lists the total extent of each bin in arcsec. Column 3 lists the total extent of each bin in kpc. Column 4 lists the measured velocity dispersion in that bin.

| Cluster | Bin [arcsec] | Bin [kpc] | $\sigma$ [km/s] |
|---|---|---|---|
| A2537 | 0.0-0.40 | 0.0-1.75 | 294 ± 9 |
| | 0.40-0.79 | 1.75-3.49 | 319 ± 6 |
| | 0.79-1.19 | 3.49-5.26 | 356 ± 8 |
| | 1.19-1.58 | 5.26-6.98 | 386 ± 9 |
| | 1.58-1.98 | 6.98-8.75 | 356 ± 10 |
| | 2.38-2.77 | 8.75-10.51 | 379 ± 12 |
| | 2.77-3.17 | 10.51-12.24 | 338 ± 13 |
| | 3.17-3.56 | 12.24-14.00 | 382 ± 18 |
| | 3.56-4.71 | 14.00-15.73 | 420 ± 23 |
| | 4.46-5.06 | 15.73-20.81 | 392 ± 24 |
| MACS J1423 | 0.0-0.43 | 0.0-2.75 | 473 ± 36 |
| | 0.43-0.71 | 2.75-4.53 | 337 ± 51 |
| | 0.71-0.99 | 4.53-6.32 | 274 ± 25 |
| | 0.99-1.27 | 6.32-8.10 | 354 ± 36 |
| | 1.27-1.70 | 8.10-10.84 | 470 ± 21 |
| | 1.70-2.48 | 10.84-15.82 | 478 ± 25 |

subcube of 20×20 arcseconds around the BCG in order to minimize the size of the objects passed through the code. This subcube contains both the data and the variance of the datacube, which are stored in extension 1 and 2, respectively. I then flatten the cubes into a 2D image, and use the `detect sources` from the `Photutils` library to determine which pixels are associated with the BCG and which belong to interloping objects, where pixels are considered to have signal if they are above a $2\sigma$ threshold, determined by the average value of all pixels in the image. I create a mask on other sources besides the BCG using a circular footprint. I then take the masked image and create a series of circular annuli, as described in Section 3.5.2, out to some radius. I calculate the width of these annuli based on the S/N value of the spectrum between 4860 Å and 7160 Å, adjusted to the redshift of the cluster. I note that in the datacube for MACS J1423, this wavelength range is contaminated by strong skylines, so I restrict the range to 6300 Å and 6900 Å, which fully captures the G band absorption feature at resdshift $z = 0.545$. I require this S/N value to be greater than 20, and adjust the width of the bins so that they are always larger than the seeing. I then take these annuli bins and fit them using the `pPXF` fitting routine, where I use an additive polynomial of 1 and a multiplicative polynomial of value 3 to fit the continuum. The resulting fits are shown in Figure 4.3.2, and the values of the velocity dispersion profiles are given in Table 4.5.

A2537 was included in N13, and as a result I am once again able to compare my values from MUSE to the values from this paper. As shown in the left-hand panel of Figure 4.3.2, these measurements agree well, which demonstrates that the pipeline produces results that agree with other independent measurements. However, the profile for MACS J1423 struggles within the innermost bins, likely due to the skyline contamination. More investigation is needed into the structure of the BCG for this cluster before a finalized velocity dispersion profile can be obtained, and I am currently working on refining the pipeline to handle cases like this with a more robust algorithm.

## 4.4 Strong Lens Models

### A2537

In this section, I present a new strong lensing model for A2537. I updated the model presented in Cerny et al. (2018) (hereafter C18) using spectroscopic redshifts for Systems 1, 2, and 4 as derived from MUSE. Since these spectroscopic redshifts improve the resolution of the model, I remove systems 20 and 32, which were treated as part of systems 2 and 3, respectively, to add precision to the initial model. I remove these systems because they did not improve the model significantly and added more variance to the MCMC fit. I instead add arcs 1.5, 12.5, 2.5, 4.3, 4.4, and 4.5 to the model. Arcs 1.5 and 12.5 were predicted images in the original model that were not included as constraints due to the lack of a spectroscopic redshift for these systems, but since I was able to obtain these redshifts with the MUSE observations, I choose to include these predicted images into the final model, especially because the associated rms is less than 1.0. The location of 1.5 and 12.5 also corresponds to faint features in the *HST* image that do not appear to be associated with the BCG. I include arc 2.5 for the same reason, as it was a predicted image in the original model for which I now have a spectroscopic redshift. The faint feature in the *HST* image near the predicted image location for arc 2.5 could be associated with system 2 based on color, and is thus now included in the model. I include arcs 4.3 and 4.4 due to their spectroscopically confirmed redshift of $z = 4.99$, which matches exactly to the redshifts of 4.1 and 4.2. I also include arc 4.5 as a guess, since there is a feature in the *HST* image at the predicted image location for this system that matches the color and shape of arcs 4.1-4.4. I show snapshots of arcs 1.5, 12.5, 2.5 and 4.5 in context with the other lensed images of their respective systems in Figure 4.8.

In the original model, I used two cluster-scale dark matter haloes to constrain the overall mass of the cluster. In this new model, I use one cluster-scale dark matter dPIE halo in addition to the BCG dPIE mass halo. I also add two galaxy-scale perturbers to the model, located around arcs 2.1 and 2.4, as well as arcs 3.1-3.2 and 31.1-31.2. Finally, I add a smaller third dark matter dPIE halo in the Northern portion of the cluster, which is required to accurately reproduce the lensing

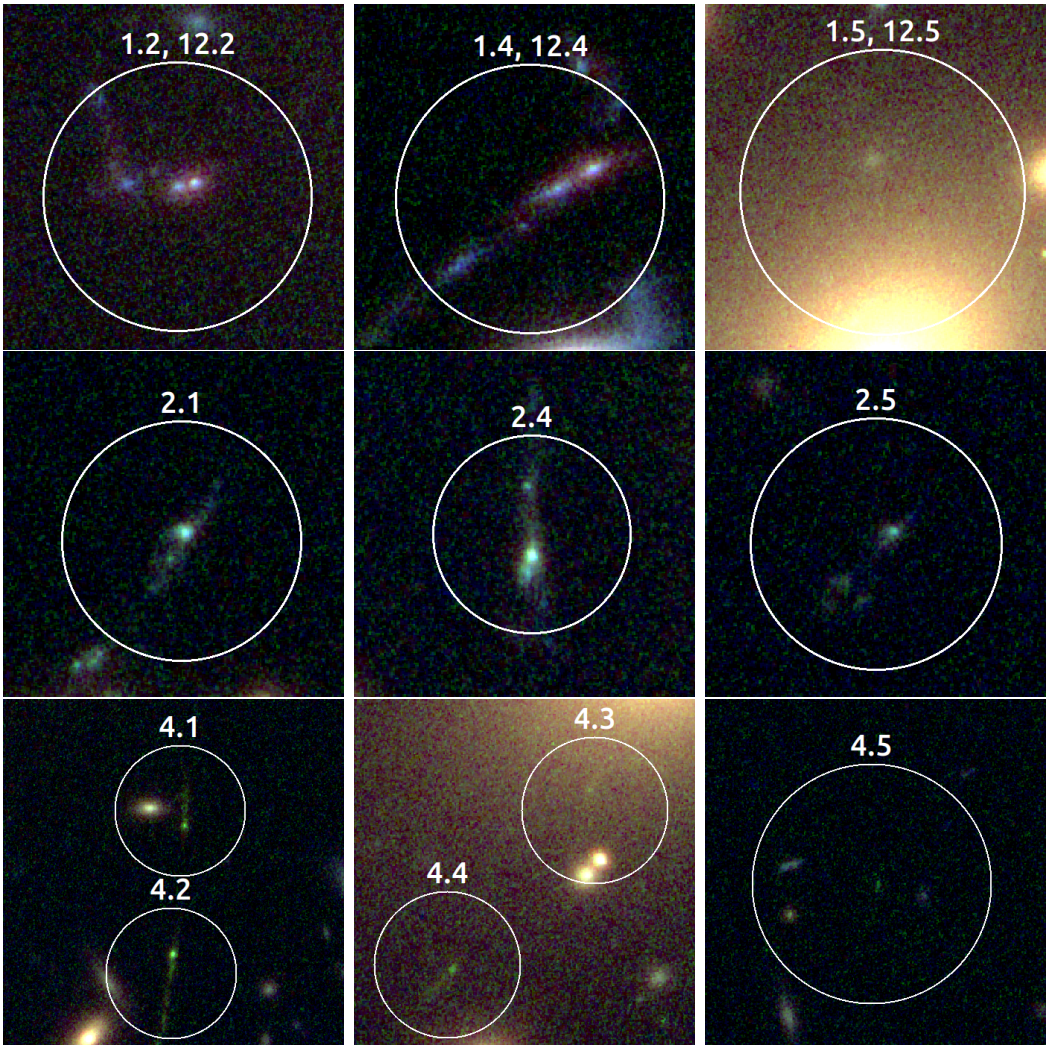


Figure 4.8: *Top row:* Snapshots of arc system 1. Arcs 1.2, 12.2, 1.4, and 12.4 are confirmed with spectroscopic MUSE detections, and arcs 1.5 and 12.5 are included in the model because the predicted fifth image location for this system is within the circle displayed on the top right-hand image, where a faint feature not associated with the BCG can be seen in the *HST* imaging. *Middle row:* Snapshots of arc system 2. Arcs 2.1 and 2.4 are confirmed with spectroscopic MUSE detections, and arc 2.5 is included in the model because its structure is similar and the predicted fifth image location for this system is within the circle displayed on the middle right-hand image. *Bottom row:* Snapshots of arc system 4. Arcs 4.1, 4.2, 4.3, and 4.4 are confirmed with spectroscopic MUSE detections, and arc 4.5 is included in the model because its structure is similar and the predicted fifth image location for this system is within the circle displayed on the bottom right-hand image. All snapshots are made from a *HST* color composite image of A2537 created using a combination of WFC3/IR imaging in the red (F160W) and ACS imaging in the green (F814W) and blue (F606W) pass-bands.

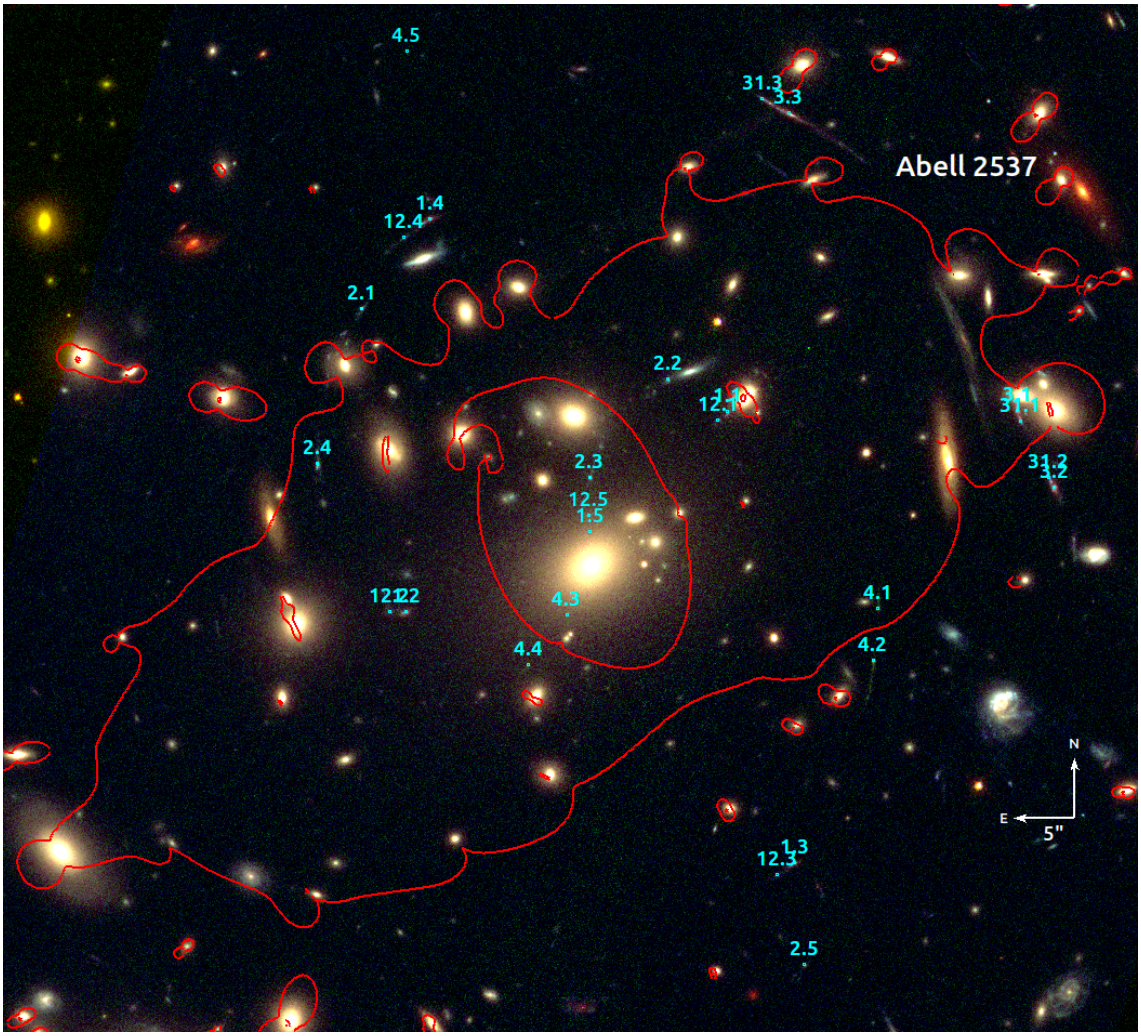


Figure 4.9: *HST* color composite image of A2537 created using a combination of WFC3/IR imaging in the red (F160W) and ACS imaging in the green (F814W) and blue (F606W). Multiply imaged galaxies are labeled in cyan. The red curve marks the location of the critical curve for a source at $z = 4.0$.

configurations there. The current version of this model is shown in Figure 4.9. I am currently investigating the properties of the third halo in order to determine whether it is representative of a potential dark matter subhalo within the cluster. The construction of this model should thus be considered as ongoing, and thus not final.

I now turn to a brief discussion of the two potential HU systems within this cluster. These systems, system 2 and system 4, are highlighted in Figure 4.10. Their configuration is similar to the shape presented in Figure 4.2, and their spectroscopic identifications confirm that each arc is indeed part of its associated system, which seems to be compelling evidence that these systems are indeed exotic. However, they may not be 'critical' HU systems due to the separation between the radial and tangential critical curves, which is somewhat too broad for the ideal form of this configuration. Instead, they may be classified as 'sub-critical' exotic systems. The strongest confirmation that they are true HU systems would come from a spectroscopic confirmation of the redshifts of arcs 2.5 and 4.5, respectively, but as these arcs are out of the field of view of MUSE, the data is too limited to make a true identification. Work is ongoing to determine the exact structure of these systems and to classify them appropriately, but in this chapter, I will continue to treat them both as HU candidates due to the geometry of their lensing configurations.

With this in mind, I note that, if confirmed, A2537 is home to not one, but *three* different unique lensing systems that can be classified as singularities. This also means that there are five different lensing constraints located within $< 20$ kpc of the BCG, which places the most stringent constraints on the inner mass profile of any cluster discussed in this thesis so far. Additionally, the appearance of these potential HU systems may be linked with the shape of the inner dark matter mass profile. The inner slope value of this cluster, which was reported to be $\sim 0.2$ in N13, is potentially extremely cored, which could have interesting implications about the dark matter distribution in clusters that produce HU systems. I discuss this more in Section 4.6.

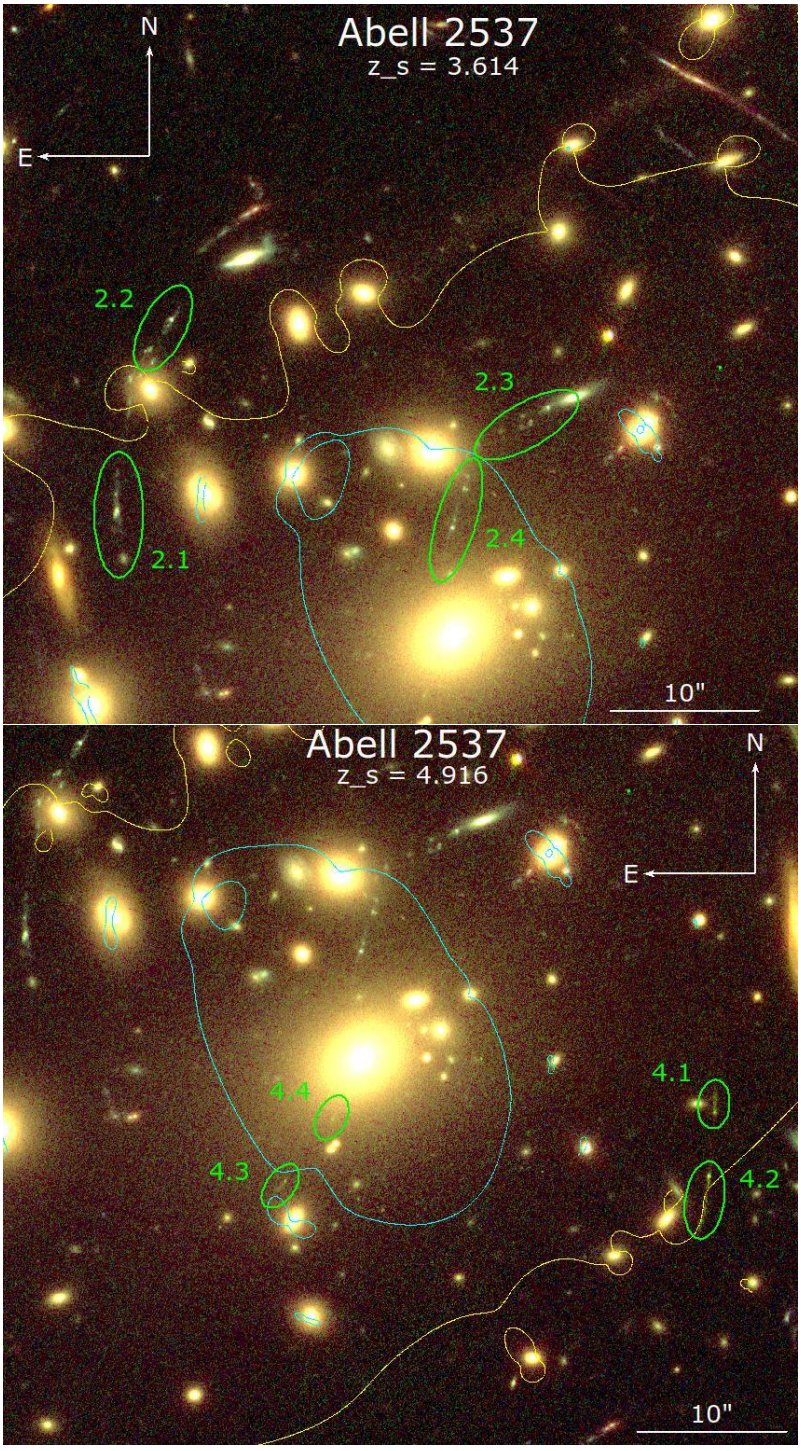


Figure 4.10: *Top:* Snapshot of the geometric configuration of system 2, which is the first HU candidate system. The tangential critical curve at $z = 3.614$ is plotted in yellow, and the corresponding radial critical curve is shown in cyan. *Bottom:* Snapshot of the geometric configuration of system 4, which is the second HU candidate system. The critical curves in this panel are defined in the same way as the top panel, but at a redshift $z = 4.916$. Both snapshots are made from a *HST* color composite image of A2537 created using a combination of WFC3/IR imaging in the red (F160W) and ACS imaging in the green (F814W) and blue (F606W) pass-bands.

**MACS J1423**

I refer the reader to Patel et al. (2024) for more details regarding this mass model. The only modification I make to the model described in this paper is the introduction of the parameters listed in Table 4.4 to constrain the mass halo for the BCG.

## 4.5 Profile Variations

I have now presented the lens model for A2537, which is formulated using the methods I discussed in Chapter 3. However, I am interested in pushing this model further in order to examine the effects of the profile choice on the mass components of the model. I am specifically aiming to review the effects of modeling the cluster dark matter halo with a dPIE profile, which better describes the 2-D mass distribution of the cluster using lensing as a primary constraint. This contrasts with the NFW profile, which is more difficult to observationally constrain, but is the only profile used to model the dark matter of clusters in modern N-body simulations (see the discussion in Section 2.1.2). I am also interested in testing different formulations for the mass profile of the BCG to examine whether the choice of profile has significant effects on the final inner slope measurement. I will discuss some of the work I have done to investigate these questions, but as this project is currently ongoing, I do not yet have all and final results to present. Instead, I will discuss the theory behind these questions, and I will show how I intend to implement these profiles into the mass model.

### 4.5.1 Cluster Dark Matter Halo

When choosing a profile for the dark matter component of a galaxy cluster, modelers must make an assumption about its distribution. Models that use an NFW profile assume that the mass density will follow an intrinsically non-cored shape. On the other hand, dPIE models assume that the mass density remains constant between $r = 0$ and $r_{\rm core}$, then declines with an isothermal profile ($r^{-2}$) between $r_{\rm core}$ and $r_{\rm cut}$, before finally dropping off more steeply ($r^{-4}$) beyond $r_{\rm cut}$. In an ideal scenario, the choice of mass profile will be physically motivated by as much observational

evidence as possible. However, we are limited by our view of the cluster, which is effectively, in lensing, a 2-D, flattened map of the total mass distribution. We are also limited by the reach of our observational data, and the effects of this are felt in several ways: first, in the occasional inclusion into lensing models of a component that applies a uniform "stretching" effect to the model and is physically interpreted either as a proxy for additional, unknown mass components, or as a systematic. This component, which is called external shear, $\gamma_{\rm ext}$, is sometimes required to reproduce the reconstructed lensing configurations (for instance, Lagattuta et al. 2019 reports $\gamma_{\rm ext} = 0.13$ in Abell 370, Bergamini et al. (2019) reports $\gamma_{\rm ext} = 0.12$ in MACS J1206, and Mahler et al. 2018 reports $\gamma_{\rm ext} = 0.17$ for Abell 2744). In this work, I avoid using external shear since it can originate from substructures that are located far from the cluster core (Jauzac et al., 2016; Acebron et al., 2017; Mahler et al., 2018), and are thus outside the field of view of *HST* and MUSE. The reliability of the external shear component is also questioned in Limousin et al. (2022) and Etherington et al. (2024) as a non-physical component that may simply expose the limitations of parametric mass modeling.

Similarly, using a generalized NFW profile to model the cluster relies heavily on the correct determination of the scale radius, $r_s$, and He et al. (2020) showed conclusively that $r_s$ is degenerate with the inner dark matter slope. Placing physically motivated priors on $r_s$ is thus of the highest importance when considering a generalized NFW profile. In the case of lensing, the method to constrain $r_s$ relies on a combination of strong and weak lensing to obtain reasonable measurements. However, what is considered 'reasonable' and what is not, tends to depend uniquely on a given modeler. As an example, the NFW scale radius as determined from lensing measurements is listed in Table 4.6 for three different clusters from three different authors. The variance in values between these different papers is fairly significant (between a 20-140% difference in estimation), but of note is the significant underestimation of this parameter by N13. Biased weak lensing measurements can significantly shift the derived NFW slope (see Figure 2.4), and He et al. (2020) postulated that the measurements made in N13 differed dramatically from the simulated C-EAGLE values because of potentially biased measurements.

With this information in mind, it is important to be as cautious as possible when obtaining weak lensing priors for the scale radius. The key to accurately probing the weak lensing regime is to separate lensed background sources from any sources that lie in the foreground. Contamination by foreground sources can bias average shape estimates by up to $\sim 20\%$ (Heymans et al. 2006). This is because weak lensing is determined through statistical analysis (Medezinski et al. 2010; Jauzac et al. 2012; Umetsu et al. 2014; Medezinski et al. 2016; Umetsu et al. 2016). The best way to eliminate foreground sources is by obtaining their redshifts, either photometrically or spectroscopically, with the latter being the most reliable way to distinguish between foreground and background sources. MUSE IFU spectroscopy is naturally well-suited to perform this task within the field of view of MUSE. However, the scale radius is often much larger than this FOV (for instance, the FOV in MS2137 extends out to $\sim 275$ kpc, but the reported scale radii (with the exception of N13) in Table 4.6 are over twice this distance), and so preference is given to deep *HST* imaging in the furthest regions to accurately determine photometric redshifts and select background sources.

My exploration of the effect of a NFW profile on my cluster models is thus ongoing, as I work to obtain accurate priors on the scale radius to avoid potentially biasing my slope measurements. In Section 4.6, I will discuss the preliminary results of using a NFW profile for MACS J1423 based on the work presented in Patel et al. (2024), which uses a strong lensing only model (SL) and a strong lensing and weak lensing combined model (SL+WL). I will also discuss preliminary results for the NFW profile of A2537. I implement the NFW profile in both models as the cluster-scale dark matter component, and I compare the resulting mass profiles to the profile determined from the strong and weak lensing model that uses a dPIE profile for the cluster-scale DM halo.

### 4.5.2 BCG Stellar Mass Halo

The other major variation that I can apply to my current models is to alter the profile used to fit the BCG, thus obtaining a modified stellar mass estimate at the center of the cluster. The dPIE profile offers many advantages in this regard, as I have

Table 4.6: Different measurements for the scale radius in an NFW profile as reported in three different papers for three different clusters: Abell 383, MS2137, and Abell 611 (A611). The values are listed here for N13, Merten et al. (2015) (M15), and Umetsu et al. (2016) (U16). All values are reported in kiloparsecs and are given for $h = 0.7$. Reproduced from He et al. (2020).

| | MS2137 | A383 | A611 |
|---|---|---|---|
| N13 | $119^{+49}_{-32}$ | $260^{+59}_{-45}$ | $317^{+57}_{-47}$ |
| M15 | $686^{+71}_{-71}$ | $471^{+57}_{-57}$ | $586^{+86}_{-86}$ |
| U16 | $800^{+450}_{-450}$ | $310^{+130}_{-130}$ | $570^{+210}_{-210}$ |

discussed in Section 2.3.1, but it is useful to examine the effects of alternative profile fits to discover what, if any, biases using the dPIE may incur in the acquisition of the mass measurement. There are three alternative profiles that may be useful in this regard. The first is called the Jaffe profile, which was developed from observations of the surface brightness of spherical galaxies (Jaffe 1983). The form of the profile is as follows:

$$\rho_J(r) = \frac{\rho_{s,J}}{4\pi}\left(\frac{r}{r_{s,J}}\right)^{-2}\left(1+\frac{r}{r_{s,J}}\right)^{-2} \tag{4.1}$$

where $\rho_{s,J}$ is the characteristic scale density and $r_{s,J}$ is the characteristic scale radius, and where the subscript $J$ is included to show that these scale parameters are associated with the Jaffe profile. When this profile is projected onto the sky, it reproduces the De Vaucouleurs surface brightness profile. The scale radius is related to the effective radius by the relation $r_{s,J} = R_e/0.76$, and it can thus be obtained by fitting a De Vaucouleurs model to the surface brightness profile of the BCG. The mass of the Jaffe profile can be written as follows:

$$M_j(r) = \frac{M_L r}{r_{s,j}(1+r/r_{s,j})}, \tag{4.2}$$

where $M_L$ corresponds to the total stellar mass of the BCG. The Jaffe profile was used in Sand et al. (2004, 2008); Sartoris et al. (2020), and Biviano et al. (2023) to model the mass of the BCG.

An alternative form of the Jaffe profile, called the Hernquist profile, was later developed, and was proposed as a way to analytically model spherical galaxies (Hern-

quist 1990). The form of the profile is as follows:

$$\rho_H(r) = \frac{\rho_{s,H}}{\left(\frac{r}{r_{s,H}}\right)\left(1+\frac{r}{r_{s,H}}\right)^3}, \tag{4.3}$$

where $\rho_{s,H}$ is the characteristic scale density and $r_{s,H}$ is the characteristic scale radius, and where the subscript $H$ is included to show that these scale parameters are associated with the Hernquist profile. The main difference between this profile and the Jaffe profile is expressed through the exponents used to modify the scale radius. The derivation of the mass and the effective radius is obtained in the same way as the Jaffe profile.

The third profile I intend to consider is a modification of the De Vaucouleurs profile that expresses the surface brightness directly in terms of density. This is known as the Einasto profile (Einasto 1969; Retana-Montenegro et al. 2012), and the form of the profile is as follows:

$$\rho_{\rm EIN}(r) = \rho_{s,\rm EIN}\exp\left\{-d_n\left[\left(\frac{r}{r_{s,\rm EIN}}\right)^{1/n} - 1\right]\right\}, \tag{4.4}$$

where $\rho_{s,\rm EIN}$ is the characteristic scale density, $r_{s,EIN}$ is the characteristic scale radius, $d_n$ is a scaling constant, and where the subscript EIN is included to show that these scale parameters are associated with the Einasto profile. When $n$ is equivalent to 4, this profile is simply the De Vaucouleurs profile expressed in terms of density instead of surface brightness.

This now leads to the question of what possible changes these alternative profiles could have on the modeling of the stellar mass. The answer can be most clearly seen in Figure 4.11. At small radii, the behavior of the Jaffe, Hernquist, and Einasto profiles (here represented as the De Vaucouleurs profile, as these profiles are again identical if the Einasto profile is rewritten in terms of surface brightness) is divergent. Calculations of these profiles using the same parameters result in the Hernquist profile being more cored, the Jaffe profile being more cusp-like, and the Einasto profile lying somewhere in the middle. As a result, testing these different profile types in the modeling of the BCG is worth considering in order to remove potential biases in the measurements of the stellar mass.

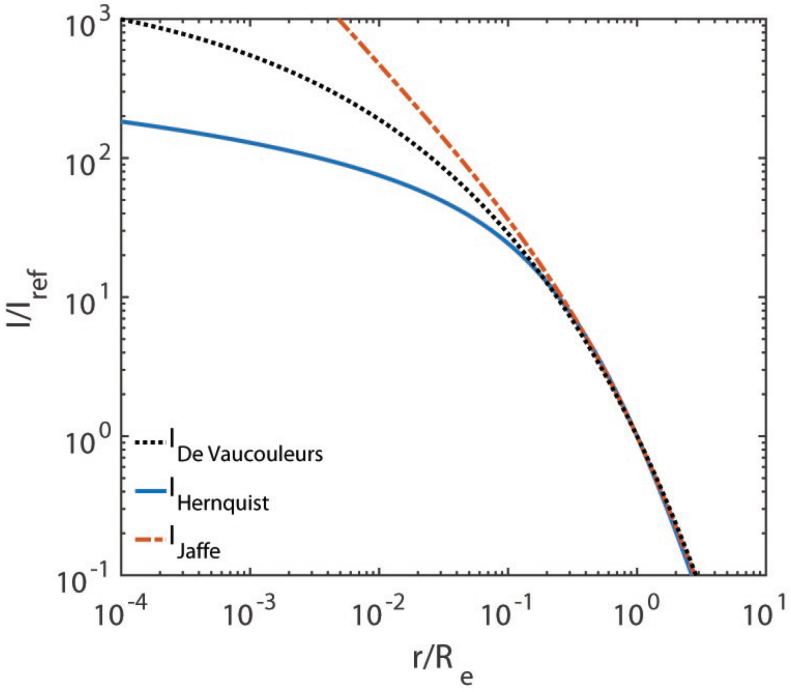


Figure 4.11: Illustration of how the general shapes of the Jaffe, Hernquist, and De Vaucouleurs surface brightness profile change with radius. The De Vaucouleurs profile here is plotted for $n = 4$, and is thus identical to the Einasto profile but is written in terms of surface brightness, which is why it is plotted here. $R_e$ is the half-light radius, and $I/I_{\rm ref}$ is the dimensionless surface brightness. The projected models are produced for a spherically symmetric galaxy. Reproduced from Roncadelli & Galanti (2023).

However, it is worth noting the fractional scale at which the slopes of these profiles differ. In my sample, I do not necessarily have the precision to strictly constrain the profile down to the sub-10 kpc scale needed to see these differences, particularly in the sample from Chapter 3. However, the amount of *HST* data in A2537 and MACS J1423, combined with the velocity dispersion measurements for A2537 in particular, may grant me the ability to distinguish between these profiles. I thus intend to incorporate them into `Lenstool` to investigate any potential differences in the slope. I am currently in the process of creating code to properly include them in the MCMC optimization. I plan to include the results from this experimental modeling of the BCG profile choice in the paper I am writing based on this chapter.

## 4.6 Inner Slope Measurements

Since my exploration of the NFW profile in the models of A2537 and MACS J1423 and its effect on the inner slope measurement is still ongoing, I choose to present initial results for the slope measurement that are created using a dPIE profile in this section. I am also still refining the inclusion of the weak lensing (WL) component in Abell 2537, so I will focus first on the strong lensing (SL) results in this section. In Section 4.7, I will show the progress I have made on creating a new NFW model for this cluster using a blend of strong and weak lensing constraints. Additionally, the lens models I am using in this analysis have not fully converged to their final form. At present, I am optimizing the positions of the multiply-imaged lensing constraints in the (unlensed) source plane only, rather than casting these optimized positions back to the (observed) image plane and comparing with empirical data. The source-plane reconstruction is therefore faster, but typically results in larger parameter uncertainty. Nevertheless, past experience shows that this initial method is a robust and efficient way of reducing the model exploration space needed for the full model optimization (Jullo et al. 2007b; Jullo & Kneib 2009; Richard et al. 2010), and once my initial modeling is complete I will revisit this study using lens-plane techniques I present in Section 2.2.1.

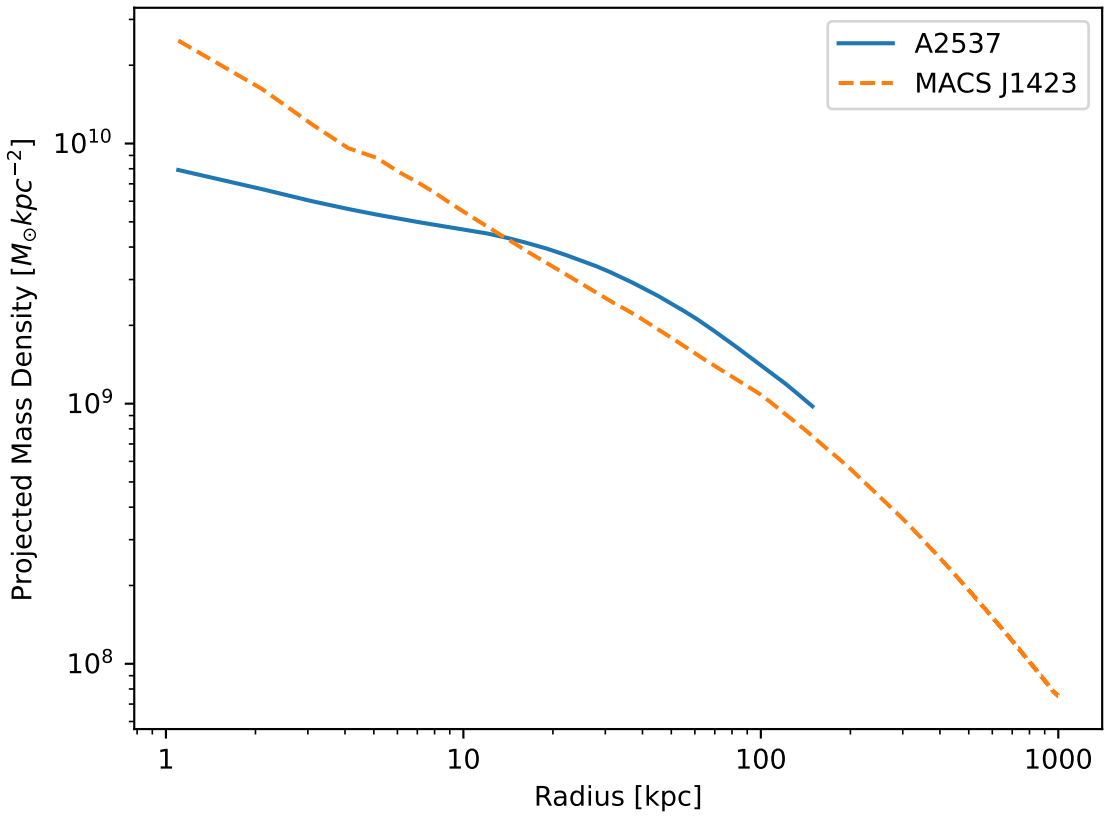


Figure 4.12: Initial measurements of the density profiles for A2537 and MACS J1423. The A2537 model is derived from a SL model only, as the WL model is still under construction. The MACS J1423 model is identical to the SL+WL model presented in Patel et al. (2024). Both the models are modified through the inclusion of the photometric parameters shown in Table 4.4 as constraints for the BCG dPIE profile, and both profiles are calculated using the dPIE realization.

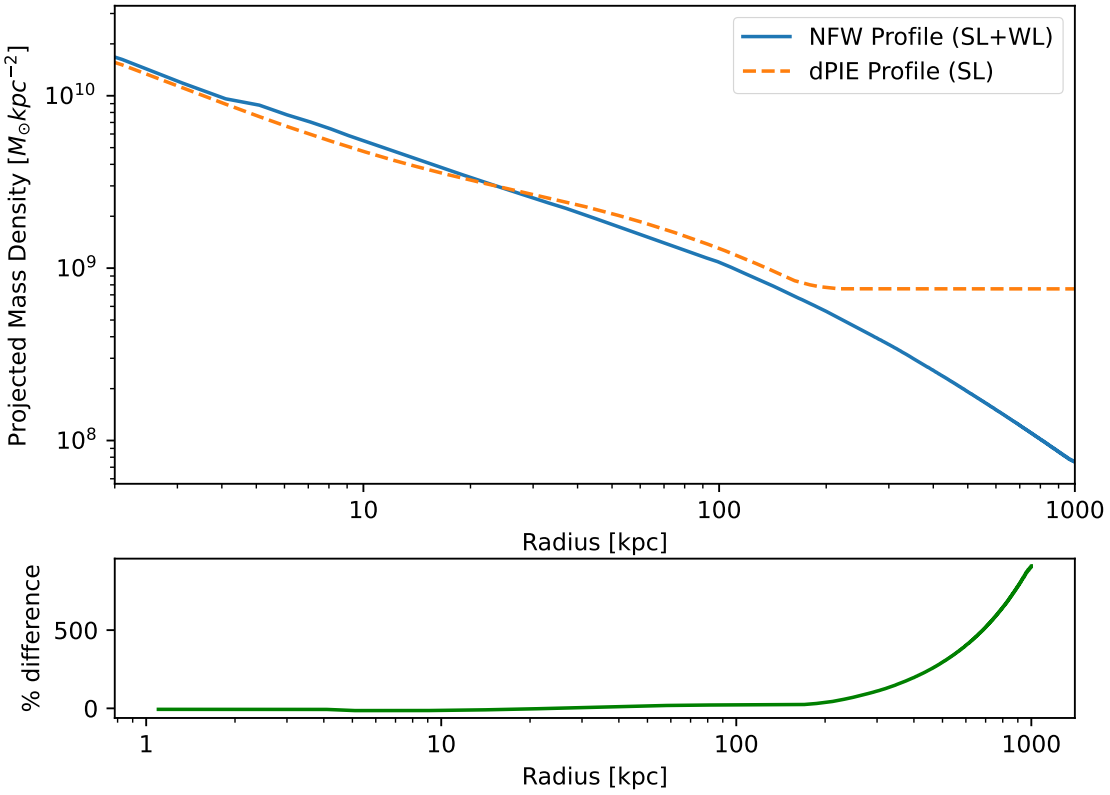


Figure 4.13: Density profile measurement of MACS J1423 using a combined SL+WL model made with an NFW profile to describe the cluster halo, and a SL only model made wtih a dPIE profile to describe the cluster halo. The bottom panel shows the % difference between the models relative to the NFW profile. The models agree remarkably well out to 100 kpc, after which they begin to diverge rapidly since SL is unable to reproduce the mass distribution outside of the SL regime.

Interestingly, an examination of these preliminary models already reveals an exciting difference between the shape of the density profiles in the inner part of the cluster. I use the new SL model I presented in Section 4.4 for A2537, and the SL+WL model of MACS J1423 presented in Patel et al. (2024) updated with photometric constraints shown in Table 4.4 for the BCG, which are included in the model in the same way I described in Chapter 3. Figure 4.12 shows the general shapes of these profiles at the center of the cluster, and it is clear that, while A2537 is obviously more core-like, MACS J1423 actually shows a slope that looks much closer to a NFW profile. These two clusters thus have the potential to be a perfect case study for the core-cusp problem in terms of observational modeling. My initial results for the shape of the central DM density profile for A2537 place the slope at around $0.18 \pm 0.1$, while for the DM slope of MACS J1423, I obtain results of $0.90 \pm 0.08$. Thus, the inner slopes of these two profiles differ by over $3\sigma$.

These measurements, although they are preliminary, are also consistent with results from literature. N13 finds a slope of $0.23^{+0.18}_{-0.16}$ for A2537. Morandi et al. (2010) uses a combined X-ray, weak lensing, and strong lensing method to model MACS J1423, and finds an inner slope of $0.94 \pm 0.09$. The values I obtain are within tolerance for these other studies, and I expect that these findings will stay consistent as I continue to refine the models, though the base value may shift a little. The cored and cusp-like nature of these two clusters suggests again that the inner slope of galaxy clusters varies and cannot necessarily be universally modeled with one single profile.

Finally, one of the major questions I raised in the conclusions of Chapter 3 was regarding whether or not a dPIE profile could accurately reproduce a mass distribution that was intrinsically cuspy. Figure 4.13 shows an initial exploration of this question for MACS J1423. The models I show in this figure are built using the same photometric constraints on the BCG. In the first model, I use the SL+WL model from Patel et al. (2024), and only change the cluster halo to a NFW profile. In the second model, I remove the WL component and only fit the dPIE profile for the SL component. The resulting SL+WL NFW model and the SL only dPIE model agree extremely well within the region constrained by SL, which is in agreement with

the predictions I made in Chapter 3. Although these results are preliminary and are thus not indicative of a final conclusion, these initial findings are a promising sign that the dPIE profile can indeed be used to accurately measure the inner slope with SL and BCG kinematics alone.

## 4.7 A2537 Weak Lensing Measurements

### 4.7.1 Weak Lensing Shear Profile

In this section, I will discuss the steps I have taken to use weak lensing mass measurements for A2537 to constrain the scale radius of an NFW profile and make the inner slope measurement using that profile. Weak lensing relies on statistically averaging over the shapes of all background sources in the field to determine the lensing signal. Identifying these sources requires the creation of a catalogue of background galaxies. In this chapter, the catalogue is created using the *HST* F814W, F606W, and F160W pass-bands. The complete process of generating the catalogue is fully described in Jauzac et al. (2012) and Jauzac et al. (2015), and a summary is also provided in Patel et al. (2024). Essentially, the catalogue is generated using pyRRG (Rhodes et al. 2000; Harvey et al. 2019), a weak lensing shape measurement algorithm that identifies sources within the field based on SExtractor extractions in the *HST*/ACS F814W filter. Sources are then categorized as stars, galaxies, and fake detections, or groups of pixels that are spatially associated with each other that cannot be categorized as a true source (see Richard et al. 2014 and Jauzac et al. 2015 for details). The algorithm uses the stars to construct PSF models that are then used to measure the shapes of all sources within the catalogue. These measurements include the size parameter, $d$, and the ellipticity, which is dependent on two separate components $e1$ and $e2$ such that $e = (e1, e2)$. $e1$ and $e2$ are defined as

$$\begin{aligned} e1 &= \frac{I_{xx} - I_{yy}}{I_{xx} + Iyy} \\ e2 &= \frac{I_{xy}}{I_{xx} + I_{yy}}, \end{aligned} \tag{4.5}$$

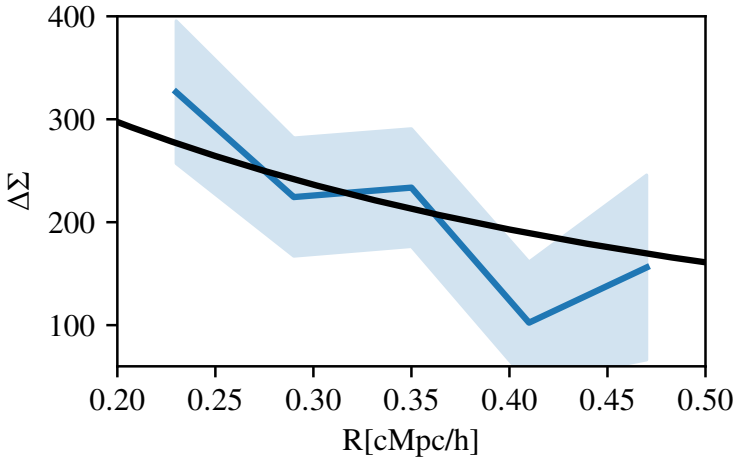


Figure 4.14: The excess surface mass density $\Delta\Sigma$ as a function of radius in comoving units. The shear profile is shown in blue, with the shaded region representing the errors, and the black line shows the fit to an NFW profile.

where $I_{ij}$ are the second-order weighted Gaussian moments, while $d$ is given as

$$d = \sqrt{\frac{I_{xx} + I_{yy}}{2}}. \tag{4.6}$$

The final shape property is the shear estimator, $\tilde{\gamma}$, which is calculated from the ellipticity as

$$\tilde{\gamma} = C\frac{e}{G}, \tag{4.7}$$

where $C$ is the calibration constant, which is fixed to 0.86 for the generation of this catalogue in accordance with Leauthaud et al. (2007), and $G$ is the polarizability, which is calculated using equation 28 from Rhodes et al. (2000).

The source catalogue is then adjusted to only contain background galaxies using a color-color selection to remove foreground and cluster member galaxies in the field. The F606W and F160W pass-bands were used to create this color selection, and a defined polynomial region was used to separate the weakly lensed galaxy population from the foreground and cluster member galaxies, which were in turn identified using photometric and/or spectroscopic redshifts (Jauzac et al. 2015). A final total of 454 galaxies are contained in the weak lensing catalogue after the completion of this step.

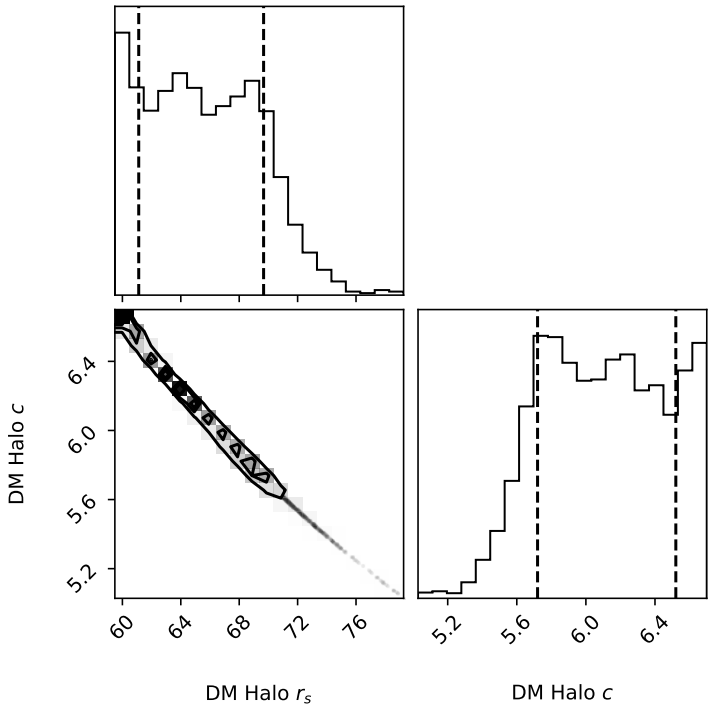


Figure 4.15: Corner plot showing the relationship between $r_s$ and $c$ in the `Lenstool` NFW model.

This catalogue was then used to measure a simple shear profile, which is shown in Figure 4.14. This profile describes the radial dependence of the surface mass density of an NFW lens, where the shear is defined as

$$\gamma_{\rm NFW}(x) = \frac{\bar{\Sigma}_{\rm NFW}(x) - \Sigma_{\rm NFW}(x)}{\Sigma_c}, \tag{4.8}$$

where $c$ is the concentration of the NFW halo, $\Sigma_{\rm NFW}(x)$ is the projected surface mass density inside the dimensionless radius $x$, which is given by

$$\Sigma_{\rm NFW}(x) = \begin{cases} \frac{2r_s\delta_c\rho_c}{(x^2-1)}\left[1 - \frac{2}{\sqrt{1-x^2}}\text{arctanh}\sqrt{\frac{1-x}{1+x}}\right] & x < 1 \\ \frac{2r_s\delta_c\rho_c}{3} & x = 1 \\ \frac{2r_s\delta_c\rho_c}{(x^2-1}\left[1 - \frac{2}{\sqrt{x^2-1}}\arctan\sqrt{\frac{x-1}{1+x}}\right] & x > 1, \end{cases} \tag{4.9}$$

and $\bar{\Sigma}_{\rm NFW}(x)$ is the mean surface mass density inside the dimensionless radius $x$, which is given by

$$\bar{\Sigma}_{\rm NFW}(x) = \frac{2}{x^2}\int_0^x x^{'}\Sigma_{\rm NFW}(x^{'})dx^{'} = \begin{cases} \frac{4}{x^2} r_s \delta_c \rho_c \left[\frac{2}{\sqrt{1-x^2}} \text{arctanh}\sqrt{\frac{1-x}{1+x}} + \ln\left(\frac{x}{2}\right)\right] & x < 1 \\ 4 r_s \delta_c \rho_c \left[1 + \ln\left(\frac{1}{2}\right)\right] & x = 1 \\ \frac{4}{x^2} r_s \delta_c \rho_c \left[\frac{2}{\sqrt{x^2-1}} \arctan\sqrt{\frac{x-1}{1+x}} + \ln\left(\frac{x}{2}\right)\right] & x > 1, \end{cases} \tag{4.10}$$

where $r_s, \delta_c$, and $\rho_c$ are all defined in Section 1.4 (Wright & Brainerd, 2000). From these equations it can be seen that $\Delta\Sigma = \bar{\Sigma}_{\rm NFW} - \Sigma_{\rm NFW}(x) = \gamma_t \times \Sigma_c$, which allows for the use of the the shear profile as a direct constraint on the parameters used to construct the NFW profile. In this chapter, the shear profile is used to directly place priors on the concentration, $c$, which is strongly correlated with the scale radius, as seen in Figure 4.15. Placing priors on the concentration thus constrains the scale radius. The fit to the weak lensing shear profile yields a value for the concentration of $c = 5.490^{1.156}_{-1.058}$. I use this value and these boundaries to create an NFW model for A2537.

### 4.7.2 A2537 NFW Profile

To compute the NFW profile for A2537, I used the dPIE `Lenstool` model I have already presented in this chapter as a basis. The optimization of cluster member galaxies, galaxy-scale perturbers, and the BCG dPIE halo did not change in this model as a result. The priors for these elements are listed in Table 4.7. I added an NFW halo to the model instead of a dPIE halo. An NFW halo is optimized similarly to a dPIE halo in `Lenstool`, save for the use of the parameters $r_s$ and $c$ as the primary 'free' parameters, rather than $r_{\rm core}$ and $\sigma_0$. I also added the weak lensing galaxy catalogue to the model in order to account for the mass outside the strong lensing regime that might be affected by the NFW fit. The weak lensing galaxies are fixed to their shape properties in the catalogue and are not optimized, since this is a strong lensing model. They are only included as a loose constraint on the mass in the outskirts of the cluster.

The resulting model is reasonably well-constrained, though I will perform further iteration on the optimization of the parameters before this work is published. The

Table 4.7: Prior distributions for `Lenstool` parameters optimized in the fitting procedure. The priors for $\Delta x$ and $\Delta y$ are given in units of arcseconds relative to the center of the cluster, which is fixed to the position of the BCG. The values in the prior column indicate the lower and upper bounds of the uniform prior assigned to each parameter.

| Parameter | Units | Prior |
|---|---|---|
| Cluster-scale dark matter NFW halo | | |
| $\Delta x$ | arcseconds | (-5, 5) |
| $\Delta y$ | arcseconds | (-5, 5) |
| $\epsilon$ | .. | (0, 1.0) |
| $\theta$ | deg | (0, 180) |
| $r_s$ | kpc | (20, 300) |
| $c$ | .. | (4.2, 6.7) |
| BCG dPIE Halo | | |
| $\sigma_0$ | km s$^{-1}$ | (350, 700) |
| Cluster galaxy scaling | | |
| $\sigma_*$ | km s$^{-1}$ | (50, 150) |
| $r_{\mathrm{cut}*}$ | kpc | (3, 50) |
| dPIE halos of individually optimized galaxies | | |
| $\epsilon$ | .. | (0, 0.8) |
| $\theta$ | deg | (0, 180) |
| $r_{\mathrm{core}}$ | kpc | (0, 1) |
| $r_{\mathrm{cut}}$ | kpc | (0,10) |
| $\sigma_0$ | km s$^{-1}$ | (10, 300) |
| Unknown redshifts | | |
| z | .. | (1,7) |

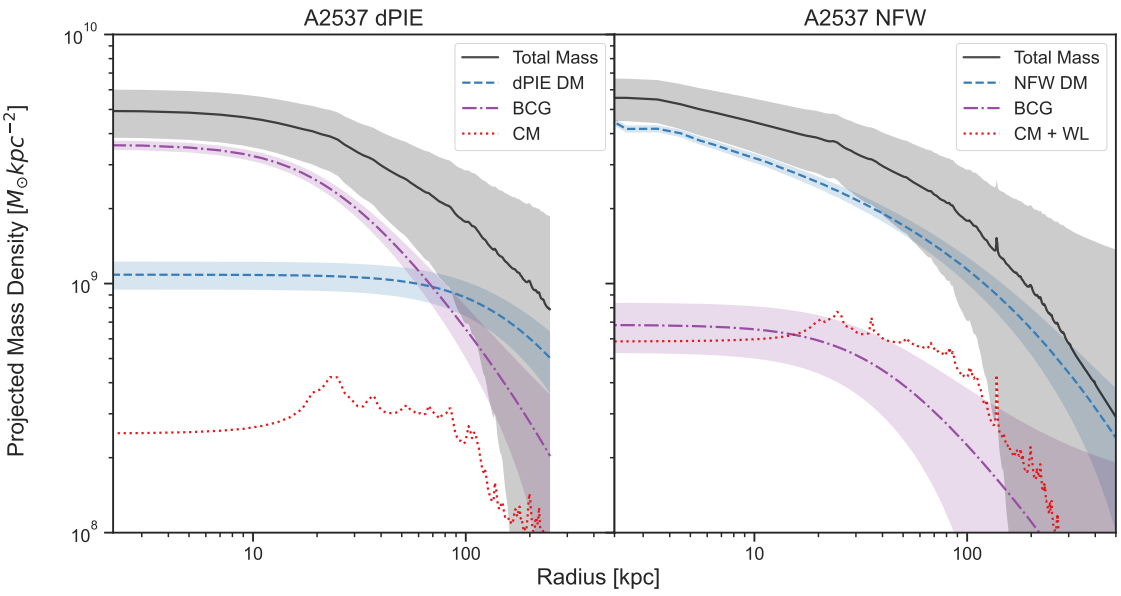


Figure 4.16: Density profile for A2537, constructed using a dPIE profile to describe the cluster-scale dark matter halo on the left, and an NFW profile to describe the cluster-scale dark matter halo on the right. The shaded regions denote the error. The stellar mass of the BCG corresponds to the purple line, and the dotted red line corresponds to cluster member galaxies for the left plot, and to the cluster member galaxies added to the weak lensing galaxy mass catalogue on the right.

rms value for all of the individual systems is 0.314" on average, which confirms that the model is able to physically reproduce the lensing constraints.

The resulting mass density profiles for both the NFW model and the dPIE model presented earlier in this chapter are shown in Figure 4.16. Interestingly, the NFW dark matter halo is a much better tracer of the total mass distribution in the inner 100 kpc than the dPIE halo. However, the discrepancy between the dPIE halo and the mass distribution is, in this case, almost entirely accounted for by the BCG. This indicates that there may be a strong relationship between the scaling parameters of the NFW halo and the central velocity dispersion of the BCG, as the properties of the BCG are consistent between both models. One possible source of the BCG's reduced contribution in the NFW model is the inclusion of the weak lensing catalogue in the outskirts of the cluster. This could indicate that the shape of the BCG stellar mass profile in the NFW profile is being influenced by the presence of additional mass outside of the strong lensing regime. Further investigation is needed to understand how these parameters interact with each other in `Lenstool`.

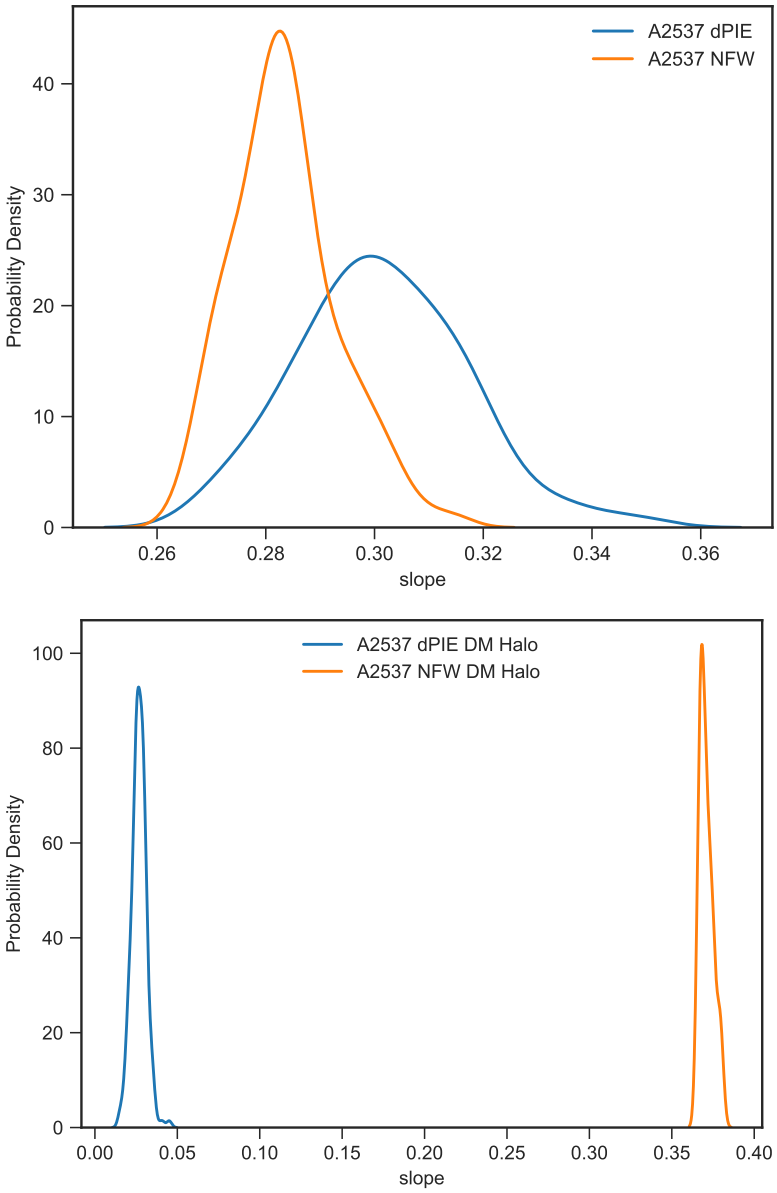


Figure 4.17: *Top*: PDF showing the distribution of the inner slope measurements for A2537 using two different profiles for the dark matter halo, as measured from the total mass density with the stellar mass of the BCG subtracted. The model created using a dPIE dark matter halo is marked in blue, and the model created using an NFW dark matter halo is marked in orange. *Bottom*: PDF showing the distribution of the inner slope measurements for A2537 using two different profiles for the dark matter halo. The model constructed using a dPIE DM halo is shown in blue, and the model constructed using a NFW halo is shown in orange.

Finally, I note that despite this discrepancy in the BCG halo, using the total mass profile as a basis for the dark matter slope fit is still consistent in this cluster. Figure 4.17 shows the distribution of the measurements for the inner slope in this cluster for both the dPIE and NFW halo. Both profiles agree well when the BCG stellar mass is subtracted from the total mass slope, and disagree sharply when only the dark matter halo is modeled. This further supports the conclusion I presented in Chapter 3, in that directly measuring the dark matter contribution from a strong lensing mass model using a dPIE halo to parameterize the dark matter component will not give you a direct measurement of the dark matter inside the interior of the cluster.

## 4.8 Conclusions: Evaluation of Profile Choice

### 4.8.1 `Lenstool` Modeling Efforts

In the course of this work, I have dedicated significant effort toward creating a Python-based module that is capable of interfacing directly with the `Lenstool` MCMC realization in order to perform a joint-fitting procedure for both the BCG kinematic fit and the strong lensing fit. This work is able to be performed with the newest version of `Lenstool`, Version 8.5.1, which was released in early 2023. This version of `Lenstool` incorporates basic support for Python using a wrapper that accesses the underlying C functions that carry out the fitting procedure. It is thus possible to develop Python functions and routines that interface with the C functions without interfering dramatically with the basic C code. However, it is still necessary to understand the implementation of the C code and to make minor adjustments within this code in order for the MCMC fitting routine to successfully optimize a joint-fit.

The steps I have implemented so far are to isolate the functions within the C code that need to be modified to perform the joint fit, and to experiment with the most effective ways to implement 'Cython', a superset of the Python language that allows me to call and adjust C functions. The pain point of this development process is the necessity of modifying many different files that all work together to produce `Lenstool`'s numerous outputs. For example, while I am able to modify

the calculation of the $\chi^2$ function to incorporate kinematic constraints by using the Python code that I have implemented in this thesis, the routines responsible for generating the Bayesian statistical outputs of the fitting procedure are handled in different files and must be isolated and adjusted to accept this modification. The adjustment of the $\chi^2$ function must be applied in both source plane and image plane realizations, with the latter being the more complicated implementation due to the long computational times associated with ray-tracing multiple images back to their origin points through the course of the optimization. An image plane run of `Lenstool` can take anywhere from a few days to a few weeks, and it is thus necessary to fully optimize the integrals I calculate for the Jeans modeling of the BCG (see Section 2.4 for details).

The process of implementing new functions into `Lenstool` is thus non-trivial, and I expect the final adjustment of the code to take an additional several months as I develop the understanding of the over 70 different files involved in the `Lenstool` fitting procedure needed to fully implement the kinematics of the BCG as a separate constraint. Once this code is finalized, it will be released as a separate branch from the 'master' `Lenstool` repository, and will be freely available for download. The expected inputs are the velocity dispersion profile of the BCG and the surface brightness profile of the BCG, as well as a mass-to-light ratio.

### 4.8.2 Future Work

The choice of profile when making observational models is an important question that may affect final results for derivations of sensitive quantities like the inner slope of the dark matter density profile. As a result, it is important to carefully examine the effects of different profiles on observational models. In this chapter, I have introduced some of the work I am currently doing to examine this question. My preliminary results show that the ability of the dPIE profile to accurately model a variety of mass distributions is excellent within the strong lensing regime, as the difference between the dPIE and NFW profile for MACS J1423 is less than 5% in this region, and the dPIE profile appears to not be sensitive or biased toward overly cored distributions. Remaining work on this subject will occur through the

incorporation of the WL component into the A2537 mass model, as well as more examination of the effects of the prior constraints on the scale radius, $r_s$, for the NFW profile in both MACS J1423 and A2537. I will also examine the effects of the BCG profile on these measurements once I have finished creating the code to incorporate the different profiles into `Lenstool`.

I also plan to incorporate additional clusters from the Kaleidoscope survey in the paper currently in preparation that I will publish on this work. The question of variance in inner slopes in galaxy clusters is particularly relevant as systematics and biases in observational models are quantified, and I am interested in completing a statistical assessment of around $\sim 20$ clusters. Constraining the slope for this many clusters will allow me to constrain the uncertainties on the measurement methods I have shown so far to within 5%, which is the fraction required to distinguish between different DM models (Robertson et al. 2019). In this way, I plan to assess whether these measurements of cluster DM densities are indicative of a particular type of DM model, particularly self-interacting dark matter, as lensing studies may support its existence (Robertson et al. 2019; Limousin et al. 2022).

## 4.9 Lens Model Properties and MUSE Catalogue

The following tables are referenced throughout the chapter and are included at the end of the chapter for visual clarity.

Table 4.8: Parameters for the best-fit lens model of A2537. Error bars correspond to $1\sigma$ confidence level as inferred from the MCMC optimization. The parameters are provided for the cluster dark matter halo (dPIE DMH), the BCG halo (dPIE BCG), and each of the galaxy-scale perturbers included in the model (Perturber 1-3). $\Delta$R.A. and $\Delta$Decl. are defined in relation to the BCG, located at R.A.=23:08:22.22 and Decl.=-2:11:31.52. Position angles are measured North of West, and the ellipticity $\epsilon$ is defined as $(a^2 - b^2)/(a^2 + b^2)$. $r_{cut}$ is fixed to 1000 kpc for the cluster dark matter halo.

| Object | $\Delta$R.A. (") | $\Delta$Decl. (") | $\epsilon$ | $\theta$ (°) | $r_{\rm core}$ (kpc) | $r_{\rm cut}$ (kpc) | $\sigma$ (km $s^{-1}$) |
|---|---|---|---|---|---|---|---|
| dPIE DMH | -4.37 | 2.44 | 0.81 | 36.19 | 194.75 | 1000. | 878.22 |
| dPIE BCG | 0 | 0 | - | - | - | - | 390.73 |
| Perturber 1 | -1.47 | 12.34 | 0.70 | 170.00 | 41.73 | 26.12 | 410.47 |
| Perturber 2 | 29.82 | 9.22 | 0.544 | 15.50 | 0.01 | 1.84 | 139.13 |

Table 4.9: Parameters for the best-fit lens model of MACS J1423. Error bars correspond to $1\sigma$ confidence level as inferred from the MCMC optimization. The parameters are provided for the cluster dark matter halo (dPIE DMH) and the BCG halo (dPIE BCG). ΔR.A. and ΔDecl. are defined in relation to the center of the BCG, located at R.A.=-2:11:31.52 and Decl.=24:04:42.440. Position angles are measured North of West, and the ellipticity $\epsilon$ is defined as $(a^2 - b^2)/(a^2 + b^2)$. $r_{cut}$ is fixed to 1000 kpc for the cluster dark matter halo.

| Object | ΔR.A. (") | ΔDecl. (") | $\epsilon$ | $\theta$ (°) | $r_{\rm core}$ (kpc) | $r_{\rm cut}$ (kpc) | $\sigma$ (km $s^{-1}$) |
|---|---|---|---|---|---|---|---|
| dPIE DMH | 0.24 | 0.012 | 0.35 | 148.77 | 13.51 | 1000. | 784.81 |
| dPIE BCG | -9.53 | 14.13 | - | - | - | - | 250.3 |

Table 4.10: Measured redshifts in A2537. Column 1 is the ID of the source. Columns 2 and 3 are the R.A. and Decl. in degrees (J2000). Column 4 is the redshift of the source. Column 5 is the quality flag (QF) assigned to the redshift. The QF scales in quality from largest to smallest; a flag value of 3 indicates that we have high confidence in the value for the redshift, whereas a flag value of 1 indicates that we have low confidence in the value for the redshift.

| ID | R.A. | Decl. | $z$ | QF |
|---|---|---|---|---|
| 90 | 347.10054470 | -2.18417640 | 3.660 | 3 |
| 540 | 347.09642727 | -2.18505537 | 0.163 | 3 |
| 537 | 347.09164325 | -2.18827339 | 3.616 | 3 |
| 534 | 347.08725882 | -2.18501919 | 0.300 | 3 |
| 505 | 347.09553272 | -2.18907761 | 0.288 | 3 |
| 502 | 347.09884177 | -2.18945996 | 3.615 | 3 |
| 478 | 347.09883116 | -2.18977854 | 3.615 | 3 |
| 458 | 347.09109214 | -2.18816110 | 3.616 | 3 |
| 457 | 347.10100649 | -2.18823387 | 0.291 | 3 |
| 455 | 347.09294620 | -2.18866779 | 0.286 | 3 |
| 450 | 347.09859934 | -2.18774704 | 3.614 | 3 |
| 448 | 347.09025138 | -2.18763798 | 0.297 | 3 |
| 439 | 347.09859826 | -2.18726725 | 3.614 | 3 |
| 433 | 347.09821235 | -2.18750097 | 0.289 | 3 |
| 430 | 347.09076636 | -2.18784522 | 3.616 | 3 |
| 429 | 347.08411293 | -2.18684232 | 0.810 | 3 |
| 411 | 347.08709805 | -2.18637510 | 0.298 | 3 |
| 405 | 347.08964174 | -2.18650053 | 0.000 | 3 |
| 399 | 347.09543100 | -2.18627905 | 0.297 | 3 |
| 392 | 347.09822244 | -2.18677645 | 3.614 | 3 |
| 381 | 347.09787299 | -2.18630788 | 3.614 | 3 |
| 372 | 347.09421457 | -2.18570375 | 0.273 | 3 |
| 368 | 347.08928983 | -2.18564474 | 0.294 | 3 |
| 364 | 347.09055860 | -2.18455278 | 0.299 | 3 |
| 342 | 347.09434877 | -2.19051995 | 0.457 | 3 |
| 338 | 347.09255437 | -2.19008719 | 3.611 | 3 |
| 334 | 347.09233183 | -2.18936107 | 3.611 | 3 |
| 325 | 347.08621216 | -2.18950863 | 0.298 | 3 |
| 315 | 347.08903417 | -2.18828420 | 0.300 | 3 |
| 313 | 347.09376609 | -2.18860854 | 0.272 | 3 |
| 300 | 347.08888353 | -2.18810083 | 0.301 | 3 |
| 295 | 347.10082144 | -2.18763527 | 0.641 | 3 |
| 287 | 347.08741393 | -2.18323072 | 0.304 | 3 |
| 267 | 347.09971364 | -2.19047890 | 0.296 | 3 |
| 265 | 347.09870788 | -2.19066473 | 3.615 | 3 |
| 262 | 347.09365597 | -2.19014168 | 0.299 | 3 |
| 251 | 347.09051786 | -2.19089216 | 0.294 | 3 |
| 240 | 347.09719340 | -2.18944011 | 0.305 | 3 |
| 239 | 347.09153223 | -2.19099970 | 0.289 | 3 |
| 220 | 347.09106240 | -2.19156387 | 0.287 | 3 |
| 208 | 347.09132450 | -2.19207724 | 0.291 | 3 |
| 199 | 347.08592834 | -2.19310340 | 4.991 | 3 |
| 197 | 347.09308172 | -2.19323335 | 4.991 | 3 |
| 186 | 347.09954177 | -2.19286101 | 0.294 | 3 |
| 183 | 347.10115951 | -2.19341823 | 0.996 | 3 |
| 171 | 347.09992533 | -2.19098031 | 0.642 | 3 |
| ⋮ | ⋮ | ⋮ | ⋮ | ⋮ |

| ID | R.A. | Decl. | $z$ | QF |
|---|---|---|---|---|
| ⋮ | ⋮ | ⋮ | ⋮ | ⋮ |
| 164 | 347.09397142 | -2.19439292 | 4.992 | 3 |
| 161 | 347.08833587 | -2.19376676 | 0.297 | 3 |
| 160 | 347.08603700 | -2.19430202 | 4.991 | 3 |
| 127 | 347.09932309 | -2.19343484 | 0.289 | 3 |
| 126 | 347.08433344 | -2.18968554 | 0.565 | 3 |
| 123 | 347.08618015 | -2.19514034 | 4.992 | 3 |
| 113 | 347.08682916 | -2.19508744 | 0.295 | 3 |
| 107 | 347.09381277 | -2.19510832 | 0.295 | 3 |
| 105 | 347.08780507 | -2.19577476 | 0.293 | 3 |
| 104 | 347.09254200 | -2.19209864 | 0.294 | 3 |
| 103 | 347.09965114 | -2.19513979 | 0.286 | 3 |
| 88 | 347.09820117 | -2.19657032 | 0.294 | 3 |
| 66 | 347.09348537 | -2.19690985 | 0.295 | 3 |
| 60 | 347.08934674 | -2.19769056 | 0.297 | 3 |
| 55 | 347.08969728 | -2.19816157 | 0.336 | 3 |
| 51 | 347.09567135 | -2.19838434 | 0.300 | 3 |
| 12 | 347.09886486 | -2.19967062 | 0.287 | 3 |
| 7 | 347.10037383 | -2.19926350 | 0.303 | 3 |
| 82 | 347.08571310 | -2.18790950 | 3.629 | 2 |
| 557 | 347.09624155 | -2.18414105 | 1.970 | 2 |
| 556 | 347.09684491 | -2.18457005 | 1.970 | 2 |
| 514 | 347.09887974 | -2.18341102 | 0.295 | 2 |
| 467 | 347.08938367 | -2.18858876 | 1.968 | 2 |
| 428 | 347.09748105 | -2.18701398 | 0.298 | 2 |
| 346 | 347.09029746 | -2.18293159 | 0.274 | 2 |
| 343 | 347.10101365 | -2.18294530 | 0.297 | 2 |
| 320 | 347.08871454 | -2.18858728 | 0.300 | 2 |
| 187 | 347.09678653 | -2.19317895 | 1.969 | 2 |
| 97 | 347.08521347 | -2.19628382 | 0.300 | 2 |
| 122 | 347.09555140 | -2.18492480 | 4.439 | 1 |
| 73 | 347.08869000 | -2.19653920 | 0.899 | 1 |
| 459 | 347.09253721 | -2.18817116 | 0.419 | 1 |
| 331 | 347.09489865 | -2.18962065 | 0.302 | 1 |
| 329 | 347.09292143 | -2.18945410 | 1.632 | 1 |
| 314 | 347.09542835 | -2.18844633 | 1.587 | 1 |
| 306 | 347.09711102 | -2.18811413 | 0.274 | 1 |
| 297 | 347.08873638 | -2.18765208 | 1.960 | 1 |
| 264 | 347.08897552 | -2.19061223 | 0.300 | 1 |
| 254 | 347.09166095 | -2.19145408 | 0.294 | 1 |
| 241 | 347.09137439 | -2.19155276 | 0.287 | 1 |
| 224 | 347.09360543 | -2.19249465 | 4.264 | 1 |
| 217 | 347.09100213 | -2.19243425 | 0.295 | 1 |
| 215 | 347.08891552 | -2.19213443 | 0.290 | 1 |
| 169 | 347.09310846 | -2.19378148 | 0.297 | 1 |
| 63 | 347.08699181 | -2.19710006 | 0.838 | 1 |
| 37 | 347.09842312 | -2.19894512 | 0.302 | 1 |

# CHAPTER 5

## Comparisons and Conclusions

Our current understanding of the Universe is governed by the Λ-CDM paradigm, which breaks up the matter content of the Universe in such a way that the visible matter we observe only constitutes 5% of the total energy density of the Universe. The remaining 95% of the Universe is dark, in the sense that we have so far not been able to directly detect any part of it. Yet this dark part of the Universe is crucial to explaining a number of physical observations, from large-scale structure to gravitational lensing. Of course, since we, so far, lack any concrete evidence about the exact physical nature of dark matter and dark energy, particulate or otherwise, we have a certain amount of freedom in developing models to characterize these dark components of the Universe.

While the Λ-CDM model is currently the most commonly used cosmological model due to its ability to explain many physical observations, it is not by any means a perfect model, and several alternative dark matter candidates have been proposed, including self-interacting dark matter and warm dark matter. Though these models are theoretically compelling, the great challenge for any alternative dark matter model in use today is for it to provide answers where Λ-CDM fails. These points of failure are concentrated in the inability of Λ-CDM to explain various observations,

including, but not limited to, the primary tension discussed in this thesis: the core-cusp problem. This thesis approaches this tension observationally by developing and refining models of galaxy clusters, which are the largest observable structures in the Universe where this problem can be seen. While a true solution to this problem is outside the scope of this work, I offer evidence that the core-cusp problem is likely not a simple issue with observational models, provide more measurements that suggest a scatter in slope values between different clusters, and show that the shape of the central mass distribution in galaxy clusters is not necessarily tied to the lensing configuration used to measure this distribution.

## 5.1 The Inner DM Slope in Galaxy Clusters

Numerically understanding the shape of the central dark matter distribution of clusters relies on accurate modeling of baryonic processes that can potentially affect the formation of the dark matter halo. Perhaps the most important of these processes are adiabatic contraction and feedback. The former can concentrate the dark matter distribution via the cooling of gas at the center of dark matter halos (Gustafsson et al. 2006), and the latter can alter the shape of the distribution in the opposite way through the exchange of energy into the interstellar medium via processes like radiation pressure and stellar winds (Agertz et al. 2013). The relationship between this contraction and loosening of the dark matter density profile is still being explored in theoretical simulations, and no conclusive answer has yet emerged regarding the exact prescription required to model these baryon-DM processes (Bland-Hawthorn et al. 2015; Read et al. 2016; Katz et al. 2018; Bose et al. 2019; Li et al. 2022).

On the observational side, measurements of the inner slope vary depending on both the cluster and the methodology used to constrain the inner slope, which covers X-ray, lensing, and dynamical measurements, and sometimes a combination of all three. However, none of these methods necessarily produce a simple and easy relation to describe the inner slope of galaxy clusters. The scatter in slope measurements shown in Figure 3.18, as well as in the results I present in Figure 3.16, seems to suggest that the inner slope can change quite significantly from cluster to

cluster. This may be due to the difficulty of accurately modeling the baryonic component of clusters, or may point to an underlying variance in the shape of the density profiles for different clusters – possibly originating from their formation history, their evolution, i.e., their dynamical state, or the physical properties of their structures. The lack of easily identifiable trends in this observational measurement points to the need for a more statistical approach, since we cannot easily interpret the underlying physical processes that drive profile shape based on the evidence in less than a dozen clusters. This is especially true given that simulations do not yet sufficiently reproduce the observed shapes of these profiles.

In this thesis, I have presented models of eight different clusters. Of these, three have had slope measurements published previously in literature. However, I have considerably extended the analytical power of both the old and new models by including MUSE IFU spectroscopy from the Kaleidoscope survey, which I use to constrain the baryonic matter distribution of the BCG. The physical property these clusters all have in common is the presence of radial arcs, which provide strong lensing constraints in the inner $\sim$ 50 kpc of the cluster, significantly closer to the BCG than is typically possible in lens modeling. The overall slope measurement I find for all eight of these clusters tends to be cored, but there is some spread in the results I obtain, from the most cored slope in Abell 2537 ($\sim$ 0.2) to the steepest slopes in MS2137 and MACS J1423 ($\sim$ 0.9). This spread is non-trivial, and seems to point toward the idea that cluster dark matter distributions vary between clusters.

I obtained these measurements by using a relatively simple modeling method, relying only on strong lensing and the dynamical mass of the BCG to determine the shape of the dark matter halo. There are two key advantages to performing measurements this way: first, I do not rely on understanding the full dynamical state of the cluster to obtain this measurement, as strong lensing is independent of such considerations. And second, I also do not need to extrapolate my lensing constraints into the center of the cluster due to the presence of radial arcs, which strengthens the ability of the lensing model to reproduce the cluster's true mass distribution in this region. In essence, I am only relying on the constraints that physically exist in the center of the cluster to constrain this central mass slope.

However, this method comes with caveats, in that only relying on these central components may not be the right approach for more dynamically complex clusters. All the clusters studied in this thesis are unimodal, but this approach will not work as simply in bimodal clusters like Abell 1689 (Limousin et al. 2007b) or Abell 1351 (Barrena et al. 2014), which have a more complex mass distribution as a result of their merger history. This method also ignores the potential effects of mass components that are outside the strong lensing region, as these components are only included insofar as they affect the strong lensing mass potential. Explicitly modeling them may lead to better constrained distributions, though quantifying the effect that adding new components to the lensing model may have is a topic outside the scope of this thesis. In this sense, the work I have presented so far is useful for the purposes of statistical analysis of inner slope measurements, as I do not expect the values I have presented to change dramatically with the addition of other mass components to the model (with the exception of additional lensing systems and photometric imaging for MACS J1427, which lacks enough of both to be entirely unambiguous). However, I do intend to add additional mass components to my model in order to restrict the number of potentially 'successful' models (i.e. models that can reproduce physical observables) to the most physically motivated models possible. In this sense, restricting the priors of fitted parameters to reflect real measurements is one of the most effective changes I can make (see Limousin et al. 2022 for a discussion), and so I now turn to the specific modeling techniques I aim to employ in future work.

## 5.2 Future Modeling Methods

### 5.2.1 Strong Lensing, BCG Kinematics, and Weak Lensing

I have already eluded to this work in Section 4.5, but one of the principal questions I would like to answer about my modeling so far is whether or not a 2D dPIE profile can reproduce results consistent with NFW profiles. Of the eight clusters I have modeled, three appear in N13 (A383, MS 2137, and A2537), so in theory, I could make this comparison by using this paper as a basis, as I have done in Section 3.8.

However, given the criticisms in He et al. (2020) about the biased estimation of the inner DM slope in N13, which was theorized to be due to a scale radius measurement that was uniformly about 50% smaller than the true value in each cluster, it is difficult to directly rely on this paper as the only source of comparison for these slope measurements. As a result, I am looking into creating these NFW models myself, using updated weak lensing catalogues, new *HST* imaging, and more lensing constraints from MUSE as a basis. The advantage of using weak lensing is that I can obtain a mass profile of the cluster out to over 1500 kpc, a distance over 10× as great as the area constrained by strong lensing. Crucially, this is the distance described by the scale radius in both the NFW ($r_s$) and dPIE profiles ($r_{\rm cut}$). By fitting a profile to this mass model, it is possible to derive sensible priors for the scale radius that can inform additional runs of the model (Limousin et al. 2022; Niemiec et al. 2023). I aim to perform this fit for the clusters within the Kaleidoscope survey that possess enough high-resolution imaging to effectively distinguish the background source population.

I will then measure the inner dark matter slope derived from this NFW model and compare it to the dPIE model. I will also test the effects of constraining the scale radius on the NFW model, as well as on the dPIE model. In the models presented in this thesis, I fix the cut radius of the dPIE cluster-scale dark matter halo to 1000 kpc, in line with other recent publications (Jauzac et al. 2019; Niemiec et al. 2019; Patel et al. 2024). I will test this assumption at the same time as the NFW model, and I will determine what effect variations on this parameter have on the inner slope. I will evaluate these tests based on how well the resulting models reproduce the lensing observables, both in terms of the strong lensing constraints and the weak lensing profile. An rms of $< 1$" is preferred for parametric models in Limousin et al. (2022), and I will treat this as a threshold value as well.

Finally, I will keep the dynamical mass constraints on the BCG in the model, though as I discuss in Section 4.5, I will examine the effects of different mass profiles for the BCG on the final model. This combination of strong lensing, BCG kinematics, and weak lensing will thus allow me to explicitly test the efficacy of using a dPIE profile to obtain this inner slope measurement, and will also allow me to

test my assumptions against the criticisms presented in He et al. (2020). I plan to do this with both clusters discussed in Chapter 4, as well as well as with at least two more clusters (MACS J0159.0-3412 and RXC J1717.1+2931) that have been observed with the Kaleidoscope survey.

### 5.2.2 Strong Lensing, BCG Kinematics, Weak Lensing, and Cluster Member Kinematics

The final mass component I plan to incorporate into my model is derived from the velocity dispersions of cluster members, which I can obtain through MUSE spectroscopy. The velocity dispersions can be used to constrain the total mass profile of the galaxy cluster, as can be seen in studies by Bergamini et al. (2019); Sartoris et al. (2020); Acebron et al. (2022), and Biviano et al. (2023).

Both Sartoris et al. (2020) and Biviano et al. (2023) utilize the MAMPOSSt code to fit the total mass profile of the galaxy clusters MACS J1206 and Abell 1063 using a combination of the observed BCG velocity dispersion profile and the velocity distribution of cluster member galaxies as constraints. Total mass is determined as

$$M(r) = M_{\rm DM}(r) + M_{\rm BCG}(r) + M_{\rm gal}(r) + M_{\rm ICM}(r), \tag{5.1}$$

where the dark matter mass is characterized by a gNFW model that leaves the inner DM slope and two characteristic radii ($r_s$ and $r_{200}$) as free parameters. In addition, the stellar mass is characterized by a Jaffe model for the BCG, the satellite stellar mass profile is calculated by determining the stellar mass function of the cluster, and the hot intra-cluster gas mass profile is derived from *Chandra* imaging. What emerges is a model of the mass distribution that is made up solely of components derived from direct baryonic detections, which means it can be easily decomposed into its separate components, as seen in Figure 5.2. I am interested in replicating parts of this analysis in the context of lensing, in order to determine what potential benefits lensing could add to this formulation of the mass model, and also to determine how a lensing model made using different constraints (i.e. just strong lensing, strong lensing and weak lensing, strong lensing and BCG dynamical mass,

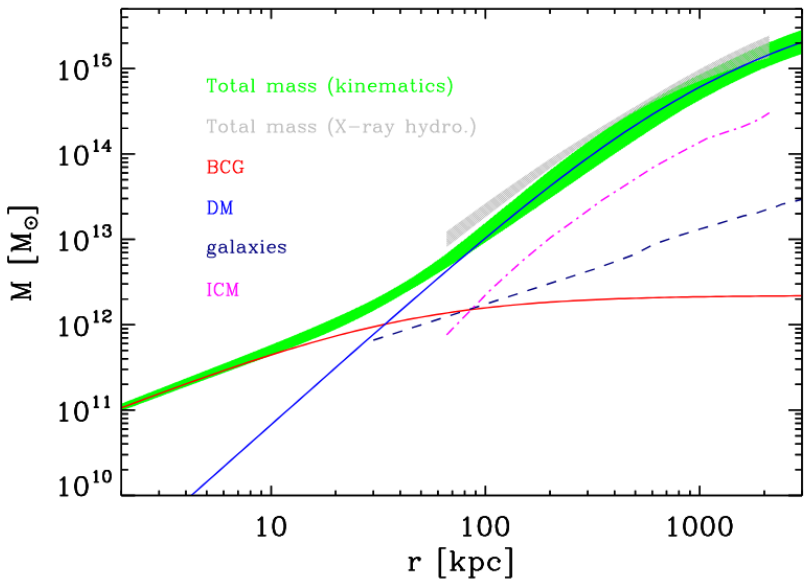


Figure 5.1: Total profile of MACS J1206, reproduced from Biviano et al. (2023). The green and gray shaded regions correspond to the 68% confidence regions for the total mass profile obtained from the dynamical analysis of stellar kinematics and X-ray hydrodynamics, respectively. The blue solid line shows the dark matter profile, and the red solid line shows the BCG stellar mass profile. The navy blue dashed line shows the satellites stellar mass profile, and the magenta dash-dotted line shows the intra-cluster gas mass profile.

etc.) compares to this methodology.

The second application of MUSE spectroscopy to a mass model can be seen in the work by Bergamini et al. (2019) and Acebron et al. (2022). In these papers, the authors use MUSE spectroscopy to constrain the sub-halo mass population generated from cluster member galaxies, where these sub-halos are modeled using dPIE profiles and follow a scaling relation for the central velocity dispersion as

$$\sigma_{LT,i}^{gal} = \sigma_{LT}^{ref} \left( \frac{L_i}{L_0} \right)^{\alpha}, \tag{5.2}$$

and for the truncation radius as

$$r_{cut,i}^{gal} = \sigma_{cut}^{ref} \left( \frac{L_i}{L_0} \right)_{cut}^{\beta}, \tag{5.3}$$

where $L_i$ is the luminosity of the i-th cluster member and $r_{cut,i}^{gal}$ represents the corresponding truncation radius. This scaling relation for the truncation radius is similar

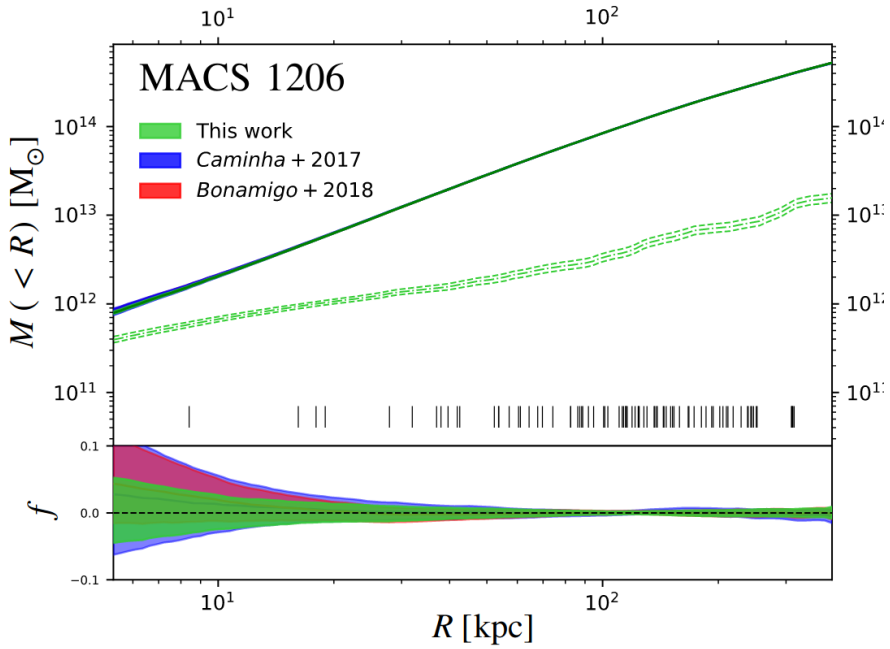


Figure 5.2: Projected cumulative mass profile of MACS J1206, reproduced from Bergamini et al. (2019). The solid green line represents the median mass profile from Bergamini et al. (2019), the blue line represents the median mass profile from Caminha et al. (2017), and the red line represents the median mass profile from Bonamigo et al. (2018). The shaded regions encompass the 16th and 84th percentiles. The dashed green lines correspond to the mass component associated with the cluster members at the 16th, 50th, and 84th percentiles. The vertical black lines mark the positions of the multiple images as measured from the cluster center. The bottom panel shows the relative variation of each of the projected mass models with respect to the reference model in green from Bergamini et al. (2019).

to the $r_{\rm core}$ radius in `Lenstool` , but is treated as a vanishing core radius in this formulation of the scaling relation. $\sigma^{gal}_{LT,i}$ is the `Lenstool` fiducial velocity dispersion of each cluster member. These scaling relations are used in these papers to determine the relationship between $\sigma_{LT}$ and the luminosity $L_i$ of the cluster members, which is measured by fitting for the following relation between 5.2 and 5.3, assuming a fixed scaling between cluster members luminosity $L_i$ and the total mass $M_{tot,i}$, which goes as $M_{tot,i}/L_i \propto L_i^{\gamma}$:

$$\beta_{cut} = \gamma - 2\alpha + 1. \tag{5.4}$$

Directly fitting this $\sigma_{LT} - L$ relation for the cluster members physically constrains the cluster members to observational values, rather than assuming that they

are scaled according to the Faber-Jackson relation (see Section 2.3.2). This reduces the degeneracy between the central velocity dispersion and the truncation radius of the cluster members, which further constrains the model to physical values. Measuring the sub-halo population in this way can help to separate out the mass contribution of cluster members that are located close to the center, and thus provides a more accurate description of the baryonic matter in the cluster, which is crucial for accurately understanding the dark matter density profile slope.

## 5.3 Relation of Lensing Configurations to Inner Dark Matter Slope Measurements

Before I conclude, I will evaluate the potential association between lensing configurations and the slope of the dark matter inside of galaxy clusters. As discussed in Section 3.1, there is an upper limit on the slope of density distributions capable of producing radial arcs, in that if the slope exceeds $\gamma = 2$ then no radial arcs will be produced. However, it is worth restating again that this limit is still well above the simulated prediction for this slope ($\gamma \sim 1$ according to results using C-EAGLE in He et al. 2020). Additionally, the variance in slope measurements demonstrated in this thesis shows that the measurements can range from 0.2 in A2537 to 0.9 in MS2137. This spread indicates that the presence of a radial arc is thus not necessarily a guarantee that the slope of the cluster will be cored.

Of course, A2537 also possesses another special lensing configuration: two hyperbolic-umbilic system candidates, which, while they may not end up being 'critical' HUs, are still definitively classified as exotic lensing configurations. These belong to the same category of lensing singularities as radial arcs, and so a possible conclusion from the fact that A2537 has these two detected HU systems *and* a radial arc is that the presence of HU or exotic systems is a predictor for the inner slope of the cluster to be cored. However, this is still not the case: Limousin et al. (2008) modeled the cluster Abell 1703, which is home to a critical HU system, and found an inner slope measurement of 1.1.

The primary takeaway of these results is thus that the lensing configuration

within a cluster is independent of the dark matter distribution of the cluster, in that a particular configuration cannot necessarily be used as a predictor for the dark matter concentration of the cluster (i.e. a cluster with a radial arc or HU is not guaranteed to have an inner DM slope $< 1$). This is likely due to the fact that lensing relies on all of the projected baryonic and dark matter along the line of sight to function, and it is not trivial to assume that certain concentrations of dark matter will result in certain lensing configurations without also considering the other potential mass components that could be affecting the lensing. However, this also means that the appearance of a radial arc in a cluster is an exciting opportunity to place strong constraints on the mass distributions of both cored and non-cored clusters. Since the presence of a lensing constraint in the center of the cluster improves the reliability of a lensing model within the center of the cluster, the combination of dynamical modeling of the BCG and lensing-based modeling of the cluster-scale dark matter halo and the baryonic cluster member galaxy haloes is a powerful way to directly probe the inner dark matter distribution of different clusters.

## 5.4 Implications for Cluster Physics and Future Work

In this thesis, I have shown that the inner dark matter density slope for eight galaxy clusters can be measured using a combination of strong lensing and BCG kinematic modeling. I have done this measurement while relying on data sourced from the Kaleidoscope survey, which is a large 'filler' program and is often not the highest quality data set available due to its shorter exposures and seeing conditions that were essentially selected at random depending on the weather on the day of the observation. Despite this variability, Kaleidoscope provides good coverage of several strong lensing clusters, eight of which I have discussed in this work. I have also developed an extraction method to obtain the velocity dispersion of the BCGs in these clusters that yields consistent results with previous longslit measurements from Keck/LRIS. While additional data could ultimately change the measured velocity

dispersion results, these changes are not expected to be significant. They are thus reliable in the sense that they can constrain a model built primarily from strong lensing constraints.

These strong lensing constraints, in turn, rely on spectroscopic redshifts from Kaleidoscope, and the survey excels at obtaining these redshifts everywhere except in the redshift desert ($1.5 \lesssim z \lesssim 2.9$). As a result, I am able to add new redshift constraints to every single radial arc system I have studied, and I add new constraints to several models (A383, MACS J0326, MACS J1427, and A2537). The improved lensing models can then be used to disentangle the baryonic and dark matter components of the inner $\sim 50$ kpc of the cluster. The resulting dark matter measurements indicate that these clusters are, on the whole, cored, since the average slope of all eight clusters presented in this thesis is $\sim 0.59$, but the individual measurements are not enough to generalize these results into a statement about the dark matter distributions of clusters with radial arcs. Instead, these measurements can be taken as an indication that there are still tensions that rise with the slope measurement from simulations, and that more work is needed to understand this problem observationally.

One way I am particularly excited to continue this work, in addition to the modeling method tests I described above, is through using deeper observational data to model a galaxy cluster with an exotic lensing configuration. In January, I will return to the model of RXJ0437+00 presented in Lagattuta et al. (2023) with new observational data from the *James Webb Space Telescope (JWST)*. This, in combination with deep MUSE observations, Keck/MOSFIRE near-infrared spectroscopy, and Hubble Space Telescope SNAPshot imaging will allow me to create a high-fidelity mass model of this cluster, since *JWST* will most likely provide a number of new strong lensing constraints in the model. This was the case for the cluster SMACS J0723.3-7323, which was observed by *JWST* in 2023. The resulting updated lens model presented in Mahler et al. (2023) identified a total of *seventeen* new lensing systems from the *JWST* imaging alone, improving on the 4 systems included in the original *HST*-based model, and I hope to see similar results from the observations of RX J0437+00. This opportunity to work with a very well-constrained

strong lensing model will enable me to perform some of the modeling tests I have described in greater detail.

In summary, this thesis has aimed to examine the core-cusp problem in galaxy clusters from an observational perspective, and has found that the problem likely still exists, and that simulations and observations need to continue refining and updating their modeling techniques before reaching agreement. In this exciting new era of observational astronomy, with the launch of telescopes like *JWST* and *Euclid*, as well as the advance of IFU spectroscopy from instruments like MUSE, the future of studying dark matter in this way looks bright.

# Bibliography


Aad G., et al., 2024, Physics Letters B, 848, 138324 1.3

Aazami A. B., Petters A. O., 2009, Journal of Mathematical Physics, 50, 032501 (document), 4.1

Abbott T. M. C., et al., 2018, , 98, 043526 1.2

Acebron A., Jullo E., Limousin M., Tilquin A., Giocoli C., Jauzac M., Mahler G., Richard J., 2017, , 470, 1809 4.5.1

Acebron A., et al., 2022, , 926, 86 5.2.2, 5.2.2

Achúcarro A., et al., 2022, arXiv e-prints, p. arXiv:2203.08128 1.2

Agertz O., Kravtsov A. V., Leitner S. N., Gnedin N. Y., 2013, , 770, 25 5.1

Aghanim N., et al., 2020, Astronomy amp; Astrophysics, 641, A6 1.2.1

Agnello A., Evans N. W., Romanowsky A. J., 2014, , 442, 3284 2.4, 2.4

Allen S. W., Evrard A. E., Mantz A. B., 2011, , 49, 409 1.4

Allingham J. F. V., et al., 2023, , 522, 1118 3.2, 3.3.2, 3.4.1, 3.4.3, 3.6.1, 3.7.2

Alpher R. A., Herman R., 1948, , 162, 774 1.1.1

Annunziatella M., et al., 2017, , 851, 81 (document), 2.1, 2.1.1, 3.18, 3.8

Avila-Reese V., Colín P., Valenzuela O., D'Onghia E., Firmani C., 2001, , 559, 516 1.3.1

Bacon R., Piqueras L., Conseil S., Richard J., Shepherd M., 2016, MPDAF: MUSE Python Data Analysis Framework, Astrophysics Source Code Library, record ascl:1611.003 (ascl:1611.003) 3.3.2

Bahé Y. M., et al., 2017, , 470, 4186 2.1.2

Balkenhol L., et al., 2023, , 108, 023510 1.1.1

Barnes D. J., et al., 2017, , 471, 1088 2.1.2, 2.1.2

Barrena R., Girardi M., Boschin W., De Grandi S., Rossetti M., 2014, , 442, 2216 5.1

Bartelmann M., 2010, Classical and Quantum Gravity, 27, 233001 3.1, 3.7.1

Bartelmann M., Schneider P., 2001, , 340, 291 1.5.2

Bergamini P., et al., 2019, , 631, A130 (document), 3.2, 3.5.2, 3.6.3, 4.5.1, 5.2.2, 5.2.2, 5.2

Berry M. V., Upstill C., 1980, Progess in Optics, 18, 257 4.1.1

Bertin E., Arnouts S., 1996a, , 117, 393 2.3.2, 3.3.2

Bertin E., Arnouts S., 1996b, , 117, 393 3.3.1, 4.2.1

Biviano A., et al., 2023, , 958, 148 (document), 2.1, 2.2, 2.1.1, 3.2, 3.18, 3.8, 4.5.2, 5.2.2, 5.1

Bland-Hawthorn J., Sutherland R., Webster D., 2015, , 807, 154 5.1

Blandford R., Narayan R., 1986, , 310, 568 4.1.1

Bolton A. S., Treu T., Koopmans L. V. E., Gavazzi R., Moustakas L. A., Burles S., Schlegel D. J., Wayth R., 2008, , 684, 248 2.4

Bonamigo M., et al., 2018, , 864, 98 (document), 5.2

Borriello A., Salucci P., Danese L., 2003, , 341, 1109 2.4

Bose S., et al., 2019, , 486, 4790 5.1

Bovy J., 2023, Dynamics and Astrophysics of Galaxies. Princeton University Press, Princeton, New Jersey (document), 1.10, 1.12

Brainerd T. G., Specian M. A., 2003, , 593, L7 2.3.2

Bundy K., et al., 2015, , 798, 7 3.7.4

Caminha G. B., et al., 2017, , 607, A93 (document), 5.2

Cappellari M., 2002, MNRAS, 333, 400 3.5.4

Cappellari M., 2017, , 466, 798 3.5.1

Cappellari M., 2020, MNRAS, 494, 4819 3.5.4

Cappellari M., 2023, , 526, 3273 3.5.1

Cerny C., et al., 2018, , 859, 159 4.1, 4.4

Chabrier G., 2003, , 115, 763 3.7.4

Coe D., et al., 2019, , 884, 85 3.4.3, 4.1, 4.2.1

Cole S., et al., 2005, , 362, 505 1.3.1

Conroy C., Gunn J. E., 2010, , 712, 833 3.5.1

Conroy C., Gunn J. E., White M., 2009, , 699, 486 3.5.1

Cooke L. H., et al., 2022, Monthly Notices of the Royal Astronomical Society, 512, 1012–1031 1.2.1

Copeland E. J., Sami M., Tsujikawa S., 2006, International Journal of Modern Physics D, 15, 1753 1.2.1

Covone G., Kneib J. P., Soucail G., Richard J., Jullo E., Ebeling H., 2006, , 456, 409 2.3.2

Dark Energy Survey Collaboration et al., 2016, , 460, 1270 1.3.2

Davis T. A., McDermid R. M., 2017, , 464, 453 3.7.4

Dehnen W., McLaughlin D. E., Sachania J., 2006, , 369, 1688 (document), 2.5

Del Popolo A., 2009, , 698, 2093 (document), 2.1

Del Popolo A., Le Delliou M., 2022, arXiv e-prints, p. arXiv:2209.14151 (document), 1.4, 1.2.1

Dey A., et al., 2019, , 157, 168 1.3.2

Di Valentino E., et al., 2021, Classical and Quantum Gravity, 38, 153001 1.1.1

Dodelson S., Widrow L. M., 1994, , 72, 17 1.3.1

Donnarumma A., Ettori S., Meneghetti M., Moscardini L., 2009, , 398, 438 3.4.2

Dutta M., Mahapatra S., 2024, European Physical Journal Special Topics, 1.3.1

Ebeling H., Edge A. C., Henry J. P., 2001, , 553, 668 3.4.2, 3.4.2, 3.4.3

Ebeling H., Barrett E., Donovan D., Ma C. J., Edge A. C., van Speybroeck L., 2007, , 661, L33 4.1

Ebeling H., Edge A. C., Mantz A., Barrett E., Henry J. P., Ma C. J., van Speybroeck L., 2010, , 407, 83 3.7.2

Ebeling H., Richard J., Beauchesne B., Basto Q., Edge A. C., Smail I., 2024, arXiv e-prints, p. arXiv:2404.11659 4.1.1

Einasto J., 1969, Astrophysics, 5, 67 4.5.2

Einstein A., 1915a, Sitzungsberichte der Königlich Preussischen Akademie der Wissenschaften, pp 778–786 1.1.2

Einstein A., 1915b, Sitzungsberichte der Königlich Preussischen Akademie der Wissenschaften, pp 844–847 1.1.2

Elíasdóttir Á., et al., 2007, arXiv e-prints, p. arXiv:0710.5636 2.3.1, 2.3.2

Etherington A., et al., 2024, , 531, 3684 4.5.1

Faber S. M., Jackson R. E., 1976, , 204, 668 2.3.2

Falcón-Barroso J., Sánchez-Blázquez P., Vazdekis A., Ricciardelli E., Cardiel N., Cenarro A. J., Gorgas J., Peletier R. F., 2011, , 532, A95 3.5.1

Famaey B., McGaugh S. S., 2012, Living Reviews in Relativity, 15, 10 1.2.1

Friedmann A., 1922, Zeitschrift fur Physik, 10, 377 1.1.1

Gamow G., 1948, , 162, 680 1.1.1

Garrison-Kimmel S., Boylan-Kolchin M., Bullock J. S., Kirby E. N., 2014, , 444, 222 1.2.1

Gerhard O., Kronawitter A., Saglia R. P., Bender R., 2001, , 121, 1936 2.4

Gladders M. D., Yee H. K. C., 2000, , 120, 2148 3.4.1

Gustafsson M., Fairbairn M., Sommer-Larsen J., 2006, , 74, 123522 5.1

Harvey D., Kneib J. P., Jauzac M., 2016, , 458, 660 2.3.2

Harvey D., Tam S.-I., Jauzac M., Massey R., Rhodes J., 2019, arXiv e-prints, p. arXiv:1911.06333 4.7.1

Hashimoto Y., Böhringer H., Umetsu K., 2022, , 511, 2796 1.2.1

Hattori M., Kneib J., Makino N., 1999, Progress of Theoretical Physics Supplement, 133, 1 (document), 3.2, 3.1, 3.7.1

He Q., et al., 2020, , 496, 4717 (document), 2.1, 2.4, 2.1.2, 2.3.1, 3.6.4, 3.18, 3.8, 4.1, 4.5.1, 4.6, 5.2.1, 5.3

Hernquist L., 1990, , 356, 359 4.5.2

Heymans C., White M., Heavens A., Vale C., van Waerbeke L., 2006, , 371, 750 4.5.1

Hinshaw G., et al., 2013, , 208, 19 1.1.1

Hinton S., 2016, MARZ: Redshifting Program (ascl:1605.001) 3.3.2

Hopkins P. F., Kereš D., Oñorbe J., Faucher-Giguère C.-A., Quataert E., Murray N., Bullock J. S., 2014, , 445, 581 1.2.1

Hu W., Barkana R., Gruzinov A., 2000, Phys. Rev. Lett., 85, 1158 1.3.1

Hubble E., 1929, Proceedings of the National Academy of Science, 15, 168 (document), 1.1.1, 1.1

Hui L., Ostriker J. P., Tremaine S., Witten E., 2017, , 95, 043541 1.3.1

Jaffe W., 1983, , 202, 995 4.5.2

Jauzac M., et al., 2012, , 426, 3369 3.6.4, 4.5.1, 4.7.1

Jauzac M., et al., 2015, , 452, 1437 4.7.1, 4.7.1

Jauzac M., et al., 2016, , 463, 3876 4.5.1

Jauzac M., et al., 2019, , 483, 3082 (document), 3.2, 3.3.2, 3.4.1, 3.4.3, 3.6, 3.6.1, 3.7.2, 5.2.1

Johnson T. L., 2018, PhD thesis, University of Michigan, Horace H. Rackham School of Graduate Studies (document), 1.9

Johnson T. L., Sharon K., Bayliss M. B., Gladders M. D., Coe D., Ebeling H., 2014, , 797, 48 3.7.2

Jullo E., Kneib J. P., 2009, , 395, 1319 2.2.1, 4.6

Jullo E., Kneib J. P., Limousin M., Elíasdóttir Á., Marshall P. J., Verdugo T., 2007a, New Journal of Physics, 9, 447 2.2.1

Jullo E., Kneib J. P., Limousin M., Elíasdóttir Á., Marshall P. J., Verdugo T., 2007b, New Journal of Physics, 9, 447 3.6.2, 4.6

Jung M., et al., 2024, , 964, 123 1.2.1

Katz H., Desmond H., Lelli F., McGaugh S., Di Cintio A., Brook C., Schombert J., 2018, , 480, 4287 5.1

Kim S. Y., Peter A. H. G., Hargis J. R., 2018, , 121, 211302 1.3.1

Kneib J. P., Ellis R. S., Smail I., Couch W. J., Sharples R. M., 1996, , 471, 643 2.2.1

Komatsu E., et al., 2011, , 192, 18 1.3.1

Kronawitter A., Saglia R. P., Gerhard O., Bender R., 2000, , 144, 53 3.5.4

Kroupa P., 2001, , 322, 231 3.7.4

La Barbera F., Ferreras I., Vazdekis A., de la Rosa I. G., de Carvalho R. R., Trevisan M., Falcón-Barroso J., Ricciardelli E., 2013, , 433, 3017 3.7.4

La Barbera F., Ferreras I., Vazdekis A., 2015, , 449, L137 3.7.4

LaRoque S. J., et al., 2003, , 583, 559 4.1

Lagattuta D. J., et al., 2019, , 485, 3738 3.5.3, 4.5.1

Lagattuta D. J., et al., 2022, , 514, 497 3.3.2, 3.3.2, 4.2.2

Lagattuta D. J., et al., 2023, , 522, 1091 4.1.1, 5.4

Laureijs R., et al., 2011, arXiv e-prints, p. arXiv:1110.3193 1.3.2

Leauthaud A., et al., 2007, , 172, 219 4.7.1

Leavitt H. S., Pickering E. C., 1912, Harvard College Observatory Circular, 173, 1 1.1.1

Leier D., Ferreras I., Saha P., Charlot S., Bruzual G., La Barbera F., 2016, , 459, 3677 3.7.4

Lemaître G., 1927, Annales de la Société Scientifique de Bruxelles, 47, 49 1.1.1

Li P., McGaugh S. S., Lelli F., Schombert J. M., Pawlowski M. S., 2022, , 665, A143 5.1

Limousin M., Kneib J.-P., Natarajan P., 2005, , 356, 309 2.3.1

Limousin M., Kneib J. P., Bardeau S., Natarajan P., Czoske O., Smail I., Ebeling H., Smith G. P., 2007a, , 461, 881 2.3.2

Limousin M., et al., 2007b, , 668, 643 2.3.2, 5.1

Limousin M., et al., 2008, , 489, 23 4.1.1, 5.3

Limousin M., Sommer-Larsen J., Natarajan P., Milvang-Jensen B., 2009, , 696, 1771 2.3.2

Limousin M., et al., 2010, , 405, 777 4.1

Limousin M., Beauchesne B., Jullo E., 2022, , 664, A90 2.3.1, 3.6.4, 4.1, 4.5.1, 4.8.2, 5.1, 5.2.1

Loubser S. I., Babul A., Hoekstra H., Bahé Y. M., O'Sullivan E., Donahue M., 2020, , 496, 1857 3.7.4

Loubser S. I., Hoekstra H., Babul A., Bahé Y. M., Donahue M., 2021, , 500, 4153 3.7.4, 3.7.4

Lovell M. R., et al., 2012, , 420, 2318 1.3.1

Lovell M. R., Frenk C. S., Eke V. R., Jenkins A., Gao L., Theuns T., 2014, , 439, 300 1.3.1

Lyubenova M., et al., 2016, , 463, 3220 3.7.4, 3.7.4

Mahler G., et al., 2018, , 473, 663 4.5.1

Mahler G., et al., 2019, , 873, 96 3.4.3, 3.6.1, 3.7.2

Mahler G., et al., 2023, , 945, 49 5.4

Mamon G. A., Łokas E. L., 2005, , 363, 705 2.4

Mann A. W., Ebeling H., 2012, , 420, 2120 3.4.2, 3.4.3

Marsden C., Shankar F., Bernardi M., Sheth R. K., Fu H., Lapi A., 2022, , 510, 5639 3.7.4

Martín-Navarro I., La Barbera F., Vazdekis A., Falcón-Barroso J., Ferreras I., 2015, , 447, 1033 3.7.4, 3.7.4

Mateo M. L., 1998, , 36, 435 1.2.1

McCarthy I. G., Schaye J., Bird S., Le Brun A. M. C., 2017, , 465, 2936 2.1.2, 2.1.2

Medezinski E., Broadhurst T., Umetsu K., Oguri M., Rephaeli Y., Benítez N., 2010, , 405, 257 4.5.1

Medezinski E., Umetsu K., Okabe N., Nonino M., Molnar S., Massey R., Dupke R., Merten J., 2016, , 817, 24 4.5.1

Meena A. K., Bagla J. S., 2020, , 492, 3294 4.1.1

Meena A. K., Singh Bagla J., 2024, arXiv e-prints, p. arXiv:2405.16826 (document), 4.2, 4.1.1

Meneghetti M., et al., 2017, , 472, 3177 2.2

Merten J., et al., 2015, , 806, 4 (document), 4.1, 4.6

Moore B., Ghigna S., Governato F., Lake G., Quinn T., Stadel J., Tozzi P., 1999, , 524, L19 1.2.1, 1.3.1

Morandi A., Pedersen K., Limousin M., 2010, , 713, 491 4.6

Müller O., Pawlowski M. S., Revaz Y., Venhola A., Rejkuba M., Hilker M., Lutz K., 2024, , 684, L6 1.2.1

Natarajan P., Kneib J.-P., Smail I., Treu T., Ellis R., Moran S., Limousin M., Czoske O., 2009, , 693, 970 2.3.2

Navarro J. F., Frenk C. S., White S. D. M., 1996, , 462, 563 1.2.1, 1.4

Newman A. B., Treu T., Ellis R. S., Sand D. J., 2011, , 728, L39 (document), 2.6, 3.4, 3.4.2, 3.7.2

Newman A. B., Treu T., Ellis R. S., Sand D. J., Nipoti C., Richard J., Jullo E., 2013a, , 765, 24 (document), 2.1, 2.1.1, 2.1.2, 3.4, 3.4.2, 3.4.2, 3.8, 3.5.2, 3.5.3, 3.6.4, 3.7.1, 3.7.2, 3.18, 3.7.4, 3.8, 4.1, 4.7, 4.3.2, 4.4, 4.5.1, 4.6, 4.6, 5.2.1

Newman A. B., Treu T., Ellis R. S., Sand D. J., 2013b, , 765, 25 3.4.2, 3.5, 3.6.3, 3.7.3, 3.7.3, 3.8

Niemiec A., Jullo E., Giocoli C., Limousin M., Jauzac M., 2019, , 487, 653 2.3.2, 5.2.1

Niemiec A., et al., 2023, , 524, 2883 3.6.4, 5.2.1

Oguri M., 2019, Reports on Progress in Physics, 82, 126901 (document), 1.11

Oh S.-H., et al., 2015, , 149, 180 1.2.1

Orban de Xivry G., Marshall P., 2009, , 399, 2 4.1.1

Pakmor R., et al., 2023a, , 524, 2539 (document), 1.8

Pakmor R., et al., 2023b, , 524, 2539 1.3.2

Parikh T., et al., 2018, , 477, 3954 3.7.4

Patel N. R., et al., 2024, arXiv e-prints, p. arXiv:2405.04577 (document), 4.1, 4.2.1, 4.2.2, 4.4, 4.5.1, 4.12, 4.6, 4.7.1, 5.2.1

Peng C. Y., Ho L. C., Impey C. D., Rix H.-W., 2002, , 124, 266 3.5.1

Peng C. Y., Ho L. C., Impey C. D., Rix H.-W., 2010, , 139, 2097 3.5.1

Penzias A. A., Wilson R. W., 1965, , 142, 419 1.1.1

Perivolaropoulos L., Skara F., 2022, , 95, 101659 1.2.1

Piqueras L., Conseil S., Shepherd M., Bacon R., Leclercq F., Richard J., 2017, arXiv e-prints, p. arXiv:1710.03554 3.3.2

Planck Collaboration et al., 2016, , 594, A1 (document), 1.3, 1.2

Planck Collaboration et al., 2020, , 641, A6 1.1.1, 1.1.1, 1.1.2

Postman M., et al., 2012a, , 199, 25 3.3.1, 4.2.1

Postman M., et al., 2012b, , 199, 25 3.4.2, 3.4.2

Poston T., Schulman L. S., 1978, Physics Today, 31, 11 4.1.1

Poulin V., Smith T. L., Karwal T., Kamionkowski M., 2019, , 122, 221301 1.2.1

Read J. I., Agertz O., Collins M. L. M., 2016, , 459, 2573 5.1

Retana-Montenegro E., van Hese E., Gentile G., Baes M., Frutos-Alfaro F., 2012, , 540, A70 4.5.2

Rhodes J., Refregier A., Groth E. J., 2000, , 536, 79 4.7.1, 4.7.1

Richard J., et al., 2010, , 404, 325 4.6

Richard J., Kneib J.-P., Ebeling H., Stark D. P., Egami E., Fiedler A. K., 2011, , 414, L31 3.4.2

Richard J., et al., 2014, , 444, 268 4.7.1

Richard J., et al., 2021, , 646, A83 3.3.2, 4.1.1, 4.2.2

Riess A. G., et al., 2022a, , 934, L7 1.1.1

Riess A. G., et al., 2022b, The Astrophysical Journal Letters, 934, L7 1.2.1

Riess A. G., et al., 2023, Crowded No More: The Accuracy of the Hubble Constant Tested with High Resolution Observations of Cepheids by JWST (arXiv:2307.15806) 1.2.1

Riess A. G., et al., 2024, , 962, L17 1.1.1

Robertson A., Harvey D., Massey R., Eke V., McCarthy I. G., Jauzac M., Li B., Schaye J., 2019, , 488, 3646 (document), 1.3.1, 2.1.2, 2.3, 4.8.2

Roncadelli M., Galanti G., 2023, Astronomy, 2, 193 (document), 4.11

Rosani G., Pasquali A., La Barbera F., Ferreras I., Vazdekis A., 2018, , 476, 5233 3.7.4

Rossetti M., Eckert D., Cavalleri B. M., Molendi S., Gastaldello F., Ghizzardi S., 2011, , 532, A123 4.1

Rubin V. C., Ford W. K. J., Thonnard N., 1980, , 238, 471 1.3.2

Sales L. V., Wetzel A., Fattahi A., 2022, Nature Astronomy, 6, 897 1.2.1

Sánchez-Blázquez P., et al., 2006, , 371, 703 3.5.1

Sand D. J., Treu T., Smith G. P., Ellis R. S., 2004, , 604, 88 (document), 2.1, 2.1.1, 3.4.2, 3.4.2, 3.5, 3.5.3, 3.6.3, 3.6.3, 3.7.1, 3.18, 3.8, 4.5.2

Sand D. J., Treu T., Ellis R. S., Smith G. P., Kneib J.-P., 2008, , 674, 711 2.1, 2.1.1, 3.4.2, 3.4.2, 3.6.3, 3.7.2, 3.7.4, 3.8, 4.5.2

Santucci G., et al., 2023, , 521, 2671 3.5.4

Sartoris B., et al., 2020, , 637, A34 (document), 2.1, 2.1.1, 2.7, 3.2, 3.18, 3.8, 4.5.2, 5.2.2

Schmidt R. W., Allen S. W., 2007, , 379, 209 4.1

Schneider P., Weiss A., 1992, , 260, 1 4.1.1

Smith G. P., Kneib J., Ebeling H., Czoske O., Smail I., 2001, The Astrophysical Journal, 552, 493–503 2.1.2

Smith R. J., Lucey J. R., Conroy C., 2015, , 449, 3441 3.7.4

Smith R. J., Lucey J. R., Edge A. C., 2017, , 471, 383 3.7.4

Soto K. T., Lilly S. J., Bacon R., Richard J., Conseil S., 2016, , 458, 3210 3.3.2, 4.2.2

Spergel D. N., Steinhardt P. J., 2000, , 84, 3760 1.3.1

Steinhardt C. L., et al., 2020, The Astrophysical Journal Supplement Series, 247, 64 3.5.3

Thomas J., Saglia R. P., Bender R., Thomas D., Gebhardt K., Magorrian J., Corsini E. M., Wegner G., 2007, , 382, 657 2.4

Tiley A. L., et al., 2020, , 496, 649 3.4.2

Tortora C., Romanowsky A. J., Napolitano N. R., 2013, , 765, 8 3.7.4

Treu T., et al., 2016, , 817, 60 2.2

Tulin S., Yu H.-B., 2018, , 730, 1 1.3.1

Umetsu K., et al., 2014, , 795, 163 4.5.1

Umetsu K., Zitrin A., Gruen D., Merten J., Donahue M., Postman M., 2016, , 821, 116 (document), 4.5.1, 4.6

Vogelsberger M., Zavala J., Loeb A., 2012, , 423, 3740 1.3.1

Vogelsberger M., et al., 2014, , 444, 1518 (document), 1.5

Voges W., et al., 1999, , 349, 389 3.4.2

Wald R. M., 1984, General Relativity 1.1.2

Wang L., Dutton A. A., Stinson G. S., Macciò A. V., Penzo C., Kang X., Keller B. W., Wadsley J., 2015, , 454, 83 1.2.1

Weilbacher P. M., Streicher O., Palsa R., 2016, MUSE-DRP: MUSE Data Reduction Pipeline (ascl:1610.004) 3.3.2, 4.2.2

Weinberg D. H., Mortonson M. J., Eisenstein D. J., Hirata C., Riess A. G., Rozo E., 2013, , 530, 87 1.2

Weinberg D. H., Bullock J. S., Governato F., Kuzio de Naray R., Peter A. H. G., 2015, Proceedings of the National Academy of Science, 112, 12249 (document), 1.7

Weinmann S. M., van den Bosch F. C., Yang X., Mo H. J., 2006, , 366, 2 3.1

Wetzel A. R., White M., 2010, , 403, 1072 2.3.2

Williams L. L. R., Navarro J. F., Bartelmann M., 1999, , 527, 535 2.1.2

Wright C. O., Brainerd T. G., 2000, , 534, 34 4.7.1

Wyithe J. S. B., Turner E. L., Spergel D. N., 2001, The Astrophysical Journal, 555, 504–523 2.1.2

York D. G., et al., 2000, , 120, 1579 3.7.4

Zitrin A., et al., 2011, , 742, 117 3.4.2, 4.1

Zitrin A., et al., 2012, , 749, 97 2.1.1

Zitrin A., et al., 2015, , 801, 44 3.4.2, 3.4.2, 3.7.2, 3.7.2, 4.1

van Dokkum P., Conroy C., Villaume A., Brodie J., Romanowsky A. J., 2017, , 841, 68 3.7.4

van Eymeren J., Trachternach C., Koribalski B. S., Dettmar R. J., 2009, , 505, 1 (document), 2.1

van den Bosch F. C., Norberg P., Mo H. J., Yang X., 2004, , 352, 1302 3.1

# APPENDIX A

## The Kaleidoscope Survey: Strong Gravitational Lensing in Galaxy Clusters with Radial Arcs (Cerny+2024)

The following document is a copy of the paper I submitted to MNRAS on 29 May 2024.

# The Kaleidoscope Survey: Strong Gravitational Lensing in Galaxy Clusters with Radial Arcs

Catherine Cerny,[1]★ Mathilde Jauzac,[1,2,3,4] David Lagattuta,[1,2] Anna Niemiec,[5] Guillaume Mahler,[1,2] Alastair Edge[1] and Richard Massey[1,2]

[1]*Centre for Extragalactic Astronomy, Durham University, South Road, Durham DH1 3LE, UK*
[2]*Institute for Computational Cosmology, Durham University, South Road, Durham DH1 3LE, UK*
[3]*Astrophysics Research Centre, University of KwaZulu-Natal, Westville Campus, Durban 4041, South Africa*
[4]*School of Mathematics, Statistics & Computer Science, University of KwaZulu-Natal, Westville Campus, Durban 4041, South Africa*
[5]*LPNHE, CNRS/IN2P3, Sorbonne Université, Université Paris-Cité, Laboratoire de Physique Nucléaire et de Hautes Énergies, 75005 Paris, France*

Accepted XXX. Received YYY; in original form ZZZ

## ABSTRACT

We measure the dark matter density profiles of six galaxy clusters: A383, MS 2137−23, MACS J0326.8-0043, MACS J1427.6−2521, MACS J0417.5-1154, and MACS J0949.8+1708. Each cluster contains at least one radial arc, a unique physical feature that allows for more precise measurements of the inner mass profile ($R < 50$ kpc) from strong lensing. We present the first strong lensing analysis for MACS J0326 and MACS J1427. We use a combination of *HST* imaging and VLT/MUSE observations from the ESO Kaleidoscope Clusters Survey, a large 'filler' program, to identify and measure redshifts for multiply-imaged systems and obtain the 2-D stellar velocity dispersion for each centrally-located brightest cluster galaxy (BCG). The BCG kinematics are used to subtract the baryonic mass component from the inner mass profile. We find total mass density profiles consistent with previous works using a combination of strong lensing and BCG kinematics. The overall shape of these profiles appears core-like, with an average dark matter slope measurement of $\gamma \sim 0.66$. These results demonstrate the ongoing need for the construction of observational models for galaxy clusters, and show how galaxy-scale kinematics can be used to disentangle baryonic and dark matter concentrations in cluster cores.

**Key words:** Galaxies: clusters: general - Galaxies: clusters: individual (Abell 383, MS 2137−23, MS 0326.8−0043, MS 1427.6−2521) - Techniques: imaging, spectroscopy

## 1 INTRODUCTION

Galaxy clusters, which are home to the largest concentrations of mass in our Universe, are the ideal cosmic laboratories for studying the properties of baryonic and dark matter. One way the study of these matter distributions can be accomplished is by utilizing the fact that the high mass density of galaxy clusters distorts and magnifies the light emitted by background sources. This unique process, known as gravitational lensing, occurs when a massive object lying along the line of sight between an observer and a background source bends the path of the light traveling from the background source (for reviews of lensing, see e.g. Massey et al. 2010; Kneib & Natarajan 2011; Hoekstra et al. 2013; Treu & Ellis 2015; Kilbinger 2015; Bartelmann & Maturi 2017). This distortion can result in the appearance of multiple images of a background source around the massive object. Quantifying the amplification and the positions of the lensed images allows the total mass distribution of the cluster to be mapped with high accuracy (e.g. Richard et al. 2014; Jauzac et al. 2014; Johnson et al. 2014; Coe et al. 2015; Caminha et al. 2017; Williams et al. 2018; Diego et al. 2018; Mahler et al. 2018; Lagattuta et al. 2019; Sharon et al. 2020), and modeling the effects of lensing allows for a high-resolution measurement of the dark matter (DM) density profile (Kneib et al. 2004; Broadhurst et al. 2005; Smith et al. 2005; Limousin et al. 2008; Newman et al. 2009; Richard et al. 2010; Jauzac et al. 2016, 2018). As a result, strong gravitational lensing can be an effective tool for studying the distribution of the dark matter mass component in galaxy clusters, although the region that is well constrained by strong lensing is demarcated by the spatial location of lensed images in relation to the center of the cluster ($R \sim 200$ kpc). However, lensing's ability to probe the mass distribution of this inner region is unparalleled, which is useful because the precise shape of the inner dark matter mass profile is not yet well understood.

Numerical collisionless cold dark matter (CDM) simulations, which represent our current physical understanding of the Universe, have generally predicted cluster-scale DM distributions that increase toward the center of the cluster following the shape of the Navarro-Frenk-White (NFW) profile (Navarro et al. 1996), where the DM density, $\rho_{\rm DM}$, increases as $\sim r^{-\gamma}$, where the inner slope, $\gamma$, is equal to 1. Subsequent simulations with higher resolution have suggested that this profile is not necessarily universally applicable, as the inner slope may be slightly shallower (Merritt et al. 2006; Navarro et al. 2010; Gao et al. 2012). Additionally, recent simulations have

★ E-mail: catherine.cerny@durham.ac.uk

shown that adding baryons can also move the inner slope away from $\gamma = 1$, as seen in the steeper slopes obtained in studies performed using BAHAMAS, Hydrangea/ Cluster-EAGLE, and TNG (McCarthy et al. 2017; Bahé et al. 2019; Chan et al. 2015). On a smaller scale, Bose et al. (2019) conducted an analysis of the APOSTLE (Fattahi et al. 2016; Sawala et al. 2016) and AURIGA (Grand et al. 2017) projects of the inner profile of dwarf galaxies and obtained slope measurements between $\gamma \sim 1.3$ and 1.8. These disparate measurements all point to the need for observational data to serve as a point of comparison.

Modeling the density profile of galaxy clusters can be accomplished by placing constraints on the baryonic and DM mass components near the center of the cluster. This is most effectively done by using strong lensing to probe the gravitational potential at the center of the cluster (Zitrin et al. 2012), and can be further constrained by the inclusion of stellar kinematic measurements of the brightest cluster galaxy (BCG) (Kelson et al. 2002), which dominates the baryonic mass budget at the center of the cluster. This combination of lensing and kinematics is uniquely powerful because it allows the distribution of dark and baryonic matter in the center of the cluster to be separated, a crucial STEP for measuring the slope of the inner DM profile. Previous studies using this method have find shallow slope values; each of these papers used long-exposure, long-slit spectroscopy and Hubble Space Telescope (*HST*) imaging for their models, and parameterize the cluster-scale DM halo using the generalized form of the NFW profile. Sand et al. (2004) modeled six clusters and found slope values between $0.52 - 0.57$; Sand et al. (2008) remodeled two of these clusters, Abell 383 and MS2137, using updated methods, and found slope values of around 0.45 for both clusters, with some significant statistical uncertainties in the latter model. Newman et al. (2013a) (hereafter N13), which also remodeled these two clusters as a part of a broader sample of seven clusters, measured an average slope of $0.50 \pm 0.13$. The measurements from N13 were examined in more detail in He et al. (2020), using the Hydrangea/Cluster-EAGLE hydrodynamic simulation suite to investigate the ability of this combination of lensing and kinematics to accurately recapture the inner slope measurement. The results of this paper suggest that there is a strong degeneracy strong degeneracy between the asymptotic generalized NFW slope and the scale radius, $r_s$, which means that incorrectly estimating the scale radius, done using weak lensing in N13, could lead to much shallower measurements of the inner DM profile. However, using the mean inner slope of the dark matter density profile, rather than the asymptotic generalized NFW slope, was shown to be a better metric of comparison between observational models and simulated clusters. This result indicates that as long as the density profile in the center clusters is well constrained by some combination of observational measurements, then the inner slope can be measured accurately.

However, the values for this slope still vary widely. Recent papers by Sartoris et al. (2020) and Biviano et al. (2023) have used stellar kinematic measurements of the BCG in combination with cluster member kinematics, obtained from integral-field unit spectroscopy, as a method to constrain the overall mass profile of the cluster. Sartoris et al. found an inner slope measurement of $0.99 \pm 0.04$ for the cluster Abell S1063, and Biviano et al. found an inner slope of $0.7^{+0.2}_{-0.1}$ for the cluster MACS J1206.2-0847. These divergent measurements indicate that the distribution of DM in galaxy clusters is more diverse than suggested by simulations, which in turn demonstrates the need for more observational models to be made to characterize the potential forms of these distributions.

In this paper, we present the DM inner slope measurements for six different galaxy clusters, using a combination of strong lensing and kinematic measurements of the BCG. We select these clusters from the ESO Kaleidoscope Clusters survey (PID 0104.A-0801; PI A. Edge), a large 'filler' program structured around the identification of bright strong-lensing features in galaxy clusters using new integral-field unit spectroscopy from VLT/MUSE. Each of these clusters has a unique physical feature: a 'radial arc', or a lensed galaxy located within 5 kpc of the BCG. We note that these radial arcs are preferentially produced in clusters with shallow inner slopes. The proximity of this lensed image to the BCG serves as an additional constraint on the inner density profile in the strong lensing model, which cannot normally measure this region without extrapolating the lens model inward as this region is baryon-dominated. We also choose to use a dual pseudo-isothermal elliptical profile to model the cluster-scale DM halos (Elíasdóttir et al. 2007), which avoids the degeneracy between the scale radius and the inner slope measurement pointed out in He et al. (2020).

We present new strong lensing and BCG kinematic velocity dispersion measurements for four clusters: Abell 383 (A383 hereafter), MS 2137−23 (MS2137 hereafter), MACS J0326.8-0043 (MACS J0326 hereafter), and MACS J1427.6−2521(MACS J1427 hereafter). We also include in this paper two more clusters that were observed in the Kaleidoscope survey: MACS J0417.5-1154 (MACS J0417 hereafter), and MACS J0949.8+1708 (MACS J0949 hereafter). We utilize previously published strong lensing models for these two clusters since we have no new strong lensing constraints to add to the existing models, and only add the measurement of the stellar velocity dispersion profile of the BCG to obtain the inner DM slope value. We refer the reader to Jauzac et al. (2019) and Allingham et al. (2023) for more details on the lens models of MACS J0417 and MACS J0949, respectively.

The paper is organized as follows. The data, observations, and the creation of the VLT/MUSE catalogues used for each cluster are presented in Section 2. Section 3 discusses the construction of the mass models, and Section 4 details the kinematic modeling for the BCG. In Section 5, we present our results, and in Section 6, we discuss their implications and describe future work on this problem. We then conclude in Section 7.

We assume a standard ΛCDM cosmology with $\Omega_M$=0.3, $\Omega_\Lambda$=0.7, and $H_0$ =70 km s$^{-1}$ Mpc$^{-1}$. All magnitudes are measured in the AB system unless stated otherwise.

## 2 OBSERVATIONS

### 2.1 Photometry

#### 2.1.1 *Hubble Space Telescope Imaging*

We utilize imaging from the *Advanced Camera for Surveys* (*ACS*) onboard *HST* obtained from the Cluster Lensing And Supernova survey with Hubble (CLASH) survey (Postman et al. 2012a) in the F814W, F6606W, and F435W pass-bands for A383 and MS2137 in order to identify multiple images (see Table 1 for details). We also use imaging from the Wide Field Camera 3 (WFC3) in the F105W, F125W, F140W, and F160W pass-bands in order to perform source identification. All imaging was obtained from MAST[1]. Basic data reduction procedures were applied to all imaging using `HSTCAL` and standard calibration files. `Tweakreg` was used to register individual frames to a common *ACS* reference image, after which `Astrodrizzle` was used to co-add the frames together.

[1] https://archive.stsci.edu/prepds/clash/

**Table 1.** Summary of *HST* observations. The name of the cluster is given in the first column, and the R.A. and Decl. are given in degrees (J2000) in the second and third columns. The band is listed in the fourth column, the PID for each band is given in the fifth column, and the P.I. for the observation is given in the sixth column. Finally, the exposure time is given in the seventh column, and the observation date for the exposure is given in the eigth column.

| Name | R.A. | Decl. | Band | PID | P.I. | Exp. time [s] | Obs. date |
|---|---|---|---|---|---|---|---|
| A383 | 42.0141667 | -3.5291389 | ACS/F435W | 12065 | Postman | 4250 | 2010-12-28 |
| | | | ACS/F606W | | | 4210 | 2011-01-18 |
| | | | ACS/F814W | | | 8486 | 2010-12-08 |
| | | | WFC3/F105W | | | 3620 | 2011-01-18 |
| | | | WFC3/F125W | | | 3320 | 2011-01-05 |
| | | | WFC3/F140W | | | 2411 | 2011-01-18 |
| | | | WFC3/F160W | | | 5935 | 2010-11-19 |
| MS 2137 | 325.0632083 | -23.6611667 | ACS/F435W | 12102 | Postman | 4026 | 2011-09-29 |
| | 325.0916667 | -23.6325000 | ACS/F606W | 10635 | Ziegler | 17920 | 2006-05-16 |
| | 325.0632083 | -23.6611667 | ACS/F814W | 12102 | Postman | 8132 | 2011-08-21 |
| | | | WFC3/F105W | | | 2814 | 2011-09-09 |
| | | | WFC3/F125W | | | 2514 | 2011-09-02 |
| | | | WFC3/F140W | | | 2311 | 2011-09-09 |
| | | | WFC3/F160W | | | 5029 | 2011-08-21 |
| MACS J0326 | 51.708118 | -0.7310381 | ACS/F814W | 11103 | Ebeling | 500 | 2008-11-13 |
| | | | ACS/F606W | | | 500 | 2007-11-17 |
| MACS J1427 | 216.9144704 | -25.3506079 | ACS/F814W | 12884 | Ebeling | 1440 | 2014-07-21 |
| MACS J0417 | 64.3945486 | -11.9088174 | ACS/F606W | 12009 | von der Linden | 7152 | 2011-01-20 |
| | | | ACS/F435W | 14096 | Coe | 2000 | 2017-06-16 |
| MACS J0949 | 147.4659359 | 17.1195712 | ACS/F606W | 14096 | Coe | 1013 | 2015-11-20 |

The observations of MACS J0326 and MACS J1427 are shallower and consist of fewer bands. F606W and F814W images are available for MACS J0326 and are sourced from the *HST* SNAP program 11103 (PI: Ebeling). The single F814W image available for MACS J1427 is taken from archival data made available by *HST* SNAP program 12166 (PI: Ebeling).

We additionally use the F606W bands from the Reionization Lensing Cluster Survey (RELICS, PID: 14096, PI: Coe) for both MACS J0949 and MACS J0417 to obtain photometric measurements of the BCG. We also include the F435W band from the *HST* programme 12009 (PI: von der Linden) for MACS J0417 as an additional check on our F606W measurements. These images were not used for any other purpose in the course of constructing the lens models.

A summary of the observations, exposure times, and bands used for each cluster are listed in Table 1. Sources for the first three clusters were identified using SExtractor (Bertin & Arnouts 1996a) in dual mode on the F814W and F606W pass-band images. Sources for MACS J1427 were identified using MUSE spectroscopy. Sources for MACS J0949 and MACS J0417 were taken from their existing lens models.

### 2.1.2 *HST Catalogues*

We create new catalogues of multiple image systems from the *HST* imaging for A383, MS2137, MACS J0326, and MACS J1427. We identify arc systems used for lens modeling within the images based on geometry, color and morphology. The properties of the arcs for these four clusters are listed in Tables 2-5. For A383, MS2137, and MACS J0326, we build a galaxy catalogue for each cluster using SExtractor in dual mode on the F814W and F606W pass-band images, with threshold parameters `DETECT_THRESH` = 1.5 and `DETECT_MINAREA` = 20. Detections with error flags or unreliable magnitude measurements (i.e. `MAG_AUTO=-99`) were dropped, and detections with a stellarity measurement greater than 0.5 were removed as they are more likely to be stars rather than galaxies. Only objects that appeared in both pass-bands were kept in the final catalogue. Further information on the construction of the galaxy catalogue can be found in Section 3.2. For MACS J1427, we build a galaxy catalogue based on the MUSE detections. For MACS J0417 and MACS J0949, we use the galaxy and arc system catalogues from their existing lens models.

## 2.2 Spectroscopy

### 2.2.1 *VLT-MUSE Observations*

The VLT/MUSE observations for each cluster are summarized in Table 6. Each cluster observation consisted of three individual exposures (imaged sequentially) of 970 s each. To minimize the effect of observational systematics, we apply a small dither (0.3 arcsec) between each exposure, and each frame is rotated 90 degrees clockwise relative to the previous frame. The observations were then stacked together to create a single cube with a total exposure of 2910 s. The resulting average seeing and airmass of the stacked cube are reported in Table 6.

Data reduction of the MUSE cubes was performed using the standard procedures of the `esorex` pipeline (muse-kit-2.4.1; Weilbacher et al. 2016), along with additional calibration and cleaning steps (as described in e.g., Richard et al. 2021 or Lagattuta et al. 2022). Bias subtraction and flat fielding were performed with basic calibration files using illumination and twilight exposures with dates closest to that of the source exposure. Flux calibration and telluric correction were performed with the standard star taken closest to the date of the source exposure. After an initial reduction process to align individual exposures, we re-run the final calibration step (the "scipost" phase) to improve flux variation between individual IFU slices. This is achieved using an auto-calibration algorithm included in the MUSE reduction pipeline, but we first apply a mask to eliminate flux from bright cluster members and intra-cluster light that bias the measurement. Finally, we apply the Zurich Atmospheric Purge (ZAP; Soto et al. 2016) to the fully reduced final data cube in order to eliminate strong skyline residuals after sky subtraction.

**Table 2.** Properties of the multiple images that were used as constraints in the lens model of A383. R.A. and Decl. are given in degrees (J2000). The redshifts for each image are either the spectroscopic value, where the redshift has no error bars, or the lensing model output value, in which case error bars are provided. The rms for the best fit is measured in the image plane for each family of multiple images. The apparent magnification $\mu$ of each multiple image is also listed.

| ID | R.A. | Decl. | $z$ | rms (") | $\mu$ |
|---|---|---|---|---|---|
| 1.1 | 42.0128100 | -3.5257360 | 4.63 | 0.87 | 24.9 ± 5.3 |
| 1.2 | 42.0100370 | -3.5306870 | 4.63 | 0.30 | >50 |
| 1.3 | 42.0094730 | -3.5284480 | 4.63 | 0.67 | 12.9 ± 4.7 |
| 1.4 | 42.0201622 | -3.5313367 | 4.63 | 0.71 | 4.4 ± 2.2 |
| 2.1 | 42.0100213 | -3.5312905 | 1.01 | 0.99 | >50 |
| 2.2 | 42.0118119 | -3.5328386 | 1.01 | 0.95 | 13.8 ± 1.8 |
| 2.3 | 42.0143250 | -3.5288310 | 1.01 | 1.52 | 1.8 ± 0.5 |
| 3.1 | 42.0124986 | -3.5352872 | 2.55 | 0.56 | 8.1 ± 0.7 |
| 3.2 | 42.0095063 | -3.5331842 | 2.55 | 0.39 | 16.6 ± 4.5 |
| 3.3 | 42.0100403 | -3.5332656 | 2.55 | 0.74 | 2.6 ± 1.3 |
| 3.4 | 42.0159643 | -3.5351566 | 2.55 | 0.62 | 6.2 ± 5.6 |
| 4.1 | 42.0092467 | -3.5339770 | 2.55 | 0.09 | 8.2 ± 3.2 |
| 4.2 | 42.0091187 | -3.5334797 | 2.55 | 0.41 | 16.9 ± 4.1 |
| 4.3 | 42.0117750 | -3.5352866 | 2.55 | 0.42 | 6.7 ± 2.3 |
| 5.1 | 42.0136400 | -3.5263550 | 6.03 | 0.87 | 9.5 ± 3.4 |
| 5.2 | 42.0191904 | -3.5329396 | 6.03 | 0.71 | 4.8 ± 4.3 |
| 6.1 | 42.0177121 | -3.5314173 | 1.55 ± 0.28 | 0.56 | 15.3 ± 8.7 |
| 6.2 | 42.0139503 | -3.5332126 | 1.55 ± 0.28 | 0.36 | 15.2 ± 7.8 |
| 6.3 | 42.0088477 | -3.5280946 | 1.55 ± 0.28 | 0.20 | 7.7 ± 3.2 |
| 6.4 | 42.0153782 | -3.5267347 | 1.55 ± 0.28 | 0.40 | 3.1 ± 1.7 |
| 7.1 | 42.0170194 | -3.5239029 | 4.15 ± 0.79 | 0.87 | 18.3 ± 9.6 |
| 7.2 | 42.0148667 | -3.5231278 | 4.15 ± 0.79 | 0.96 | >50 |
| 7.3 | 42.0130417 | -3.5229194 | 4.15 ± 0.79 | 1.05 | 11.0 ± 3.6 |
| 8.1 | 42.0153375 | -3.5235164 | 1.75 ± 0.46 | 0.33 | >50 |
| 8.2 | 42.0141083 | -3.5232670 | 1.75 ± 0.46 | 0.37 | >50 |
| 9.1 | 42.0165440 | -3.5331830 | 4.27 ± 1.37 | 1.12 | >50 |
| 9.2 | 42.0171721 | -3.5326837 | 4.27 ± 1.37 | 0.04 | 18.5 ± 9.6 |
| 9.3 | 42.0161051 | -3.5264773 | 4.27 ± 1.37 | 0.72 | 12.6 ± 4.6 |
| 9.4 | 42.0078024 | -3.5279351 | 4.27 ± 1.37 | 0.89 | 5.0 ± 2.2 |

### 2.2.2 *VLT-MUSE Catalogues*

We performed source extraction for four clusters following the procedure detailed in Lagattuta et al. (2022); we briefly describe the procedure here. The clusters we evaluated were A383, MS2137, MACS J0326, and MACS J1427. Spectroscopic redshifts were obtained for objects in the MUSE cubes with a proprietary program called Source Inspector, developed and hosted by CRAL (Centre de Recherche Astrophysique de Lyon). SExtractor (Bertin & Arnouts 1996b) was first run on the MUSE data using the `muselet` routine from `mpdaf` (Bacon et al. 2016; Piqueras et al. 2017)[2], which identifies sources with flux above the local continuum level by subtracting the average flux measured around a narrow wavelength range from the average flux within that wavelength range. This process creates a pseudo-narrow-band for each wavelength range, or slice. A narrow-band cube was formed by combining all the slices together, and SExtractor was run on each slice to identify emission peaks. Unique detections in the cube had their spectrum extracted after peaks at different wavelength slices that are spatially 'close' to each other (i.e. within the same seeing disk) were combined into multi-line objects. Single-line objects, like Ly-$\alpha$ and [OII], were also extracted. The spectra of sources that were identified using bright objects in the existing *HST* imaging were also extracted. A final sky correction was applied by subtracting, from each spectrum, the sum of the 500 nearest blank spaxels (spaxels not associated with any detection in the field) that were located within a 0.4"-4.0" circular annulus centered on the target object.

Each spectrum was then evaluated using Source Inspector, which calculated five possible redshift fits for each spectrum using the tool `Marz` (Hinton 2016). Redshift fits were visually inspected by three individual users, with each user able to select one of the `Marz` values or manually enter a different value. Each fit was assigned a confidence 'rating' between 0-3, where 3 is a confirmed detection (redshift identified from multiple features or one unambiguous feature, such as a Ly-$\alpha$ or [OII] doublet), 2 is a probable detection (several lines that are noisy, which boosts the redshift error, or a single feature that is probably known but could also be something else (i.e. a blended [OII] line that could also be a wide [OIII] line

[2] https://mpdaf.readthedocs.io/en/latest/muselet.html

**Table 3.** Properties of the multiple images that were used as constraints in the lens model of MS 2137. The format of each column is the same as the format for Table 2.

| ID | R.A. | Decl. | $z$ | rms (") | $\mu$ |
|---|---|---|---|---|---|
| 1.1 | 325.0653010 | -23.6627183 | 3.086 | 0.24 | 3.8 ± 1.5 |
| 1.2 | 325.0573784 | -23.6552507 | 3.086 | 0.97 | 3.2 ± 1.8 |
| 1.3 | 325.0639173 | -23.6617792 | 3.086 | 0.76 | 1.1 ± 0.45 |
| 2.1 | 325.0627881 | -23.6595561 | 1.19 | 0.27 | 31.7 ± 8.0 |
| 2.2 | 325.0660593 | -23.6669070 | 1.19 | 0.16 | 2.8 ± 1.1 |
| 3.1 | 325.0647182 | -23.6572985 | 1.495 | 0.08 | 7.9 ± 2.8 |
| 3.2 | 325.0623619 | -23.6570179 | 1.495 | 0.77 | 50.2 ± 7.1 |
| 3.3 | 325.0667908 | -23.6653782 | 1.495 | 0.68 | 3.9 ± 1.1 |
| 3.4 | 325.0590207 | -23.6614473 | 1.495 | 0.26 | 3.5 ± 1.3 |
| 4.1 | 325.0617177 | -23.6570091 | 1.495 | 2.07 | 17.3 ± 2.4 |
| 4.2 | 325.0654996 | -23.6574819 | 1.495 | 0.43 | 3.5 ± 1.9 |
| 4.3 | 325.0671724 | -23.6648956 | 1.495 | 0.13 | 4.5 ± 1.5 |
| 4.4 | 325.0671724 | -23.6648956 | 1.495 | 0.41 | 2.7 ± 1.1 |
| 5.1 | 325.0631385 | -23.6593017 | 1.496 | 0.40 | 3.8 ± 0.84 |
| 5.2 | 325.0630167 | -23.6601998 | 1.496 | 0.73 | 0.59 ± 1.1 |
| 5.3 | 325.0649681 | -23.6677483 | 1.496 | 1.43 | 2.6 ± 1.6 |

**Table 4.** Properties of the multiple images that were used as constraints in the lens model of MACS J0326. The format of each column is the same as the format for Table 2.

| ID | R.A. | Decl. | $z$ | rms (") | $\mu$ |
|---|---|---|---|---|---|
| 1.1 | 51.70533 | -0.73235 | 3.755 | 1.57 | 9.2 ± 0.1 |
| 1.2 | 51.7140244 | -0.7348069 | 3.755 | 0.96 | 3.2 ± 2.2 |
| 1.3 | 51.7072192 | -0.7311556 | 3.755 | 0.38 | 6.0 ± 0.16 |
| 2.1 | 51.7055216 | -0.7305184 | 1.248 | 0.48 | 22.7 ± 5.3 |
| 2.2 | 51.7057628 | -0.7316436 | 1.248 | 0.56 | 11.7 ± 3.4 |
| 2.3 | 51.7082900 | -0.7303000 | 1.248 | 0.54 | 4.2 ± 0.6 |
| 2.4 | 51.71047 | -0.73444 | 1.248 | 0.93 | 22.6 ± 4.3 |
| 3.1 | 51.7018015 | -0.7310976 | 5.878 | 0.85 | 4.1 ± 2.3 |
| 3.2 | 51.7067455 | -0.7370053 | 5.878 | 0.65 | 6.7 ± 2.3 |
| 3.3 | 51.7048216 | -0.7359669 | 5.878 | 0.29 | 22.0 ± 10.5 |
| 3.4 | 51.7106978 | -0.7288662 | 5.878 | 0.53 | 7.9 ± 2.3 |
| 3.5 | 51.7093690 | -0.7301727 | 5.878 | 0.59 | 11.3 ± 3.4 |

**Table 5.** Properties of the multiple images that were used as constraints in the lens model of MACS J1427. The format of each column is the same as the format for Table 2.

| ID | R.A. | Decl. | $z$ | rms (") | $\mu$ |
|---|---|---|---|---|---|
| 1.1 | 216.9148671 | 216.9148671 | 0.8836 | 0.24 | 1.9 ± 1.4 |
| 1.2 | 216.9148671 | 216.9148671 | 0.8836 | 0.24 | 11.2 ± 3.3 |
| 1.3* | 216.9165342 | -25.3486428 | 0.8836 | 0.24 | 3.7 ± 1.9 |
| 2.1 | 216.9106579 | -25.3536281 | 1.23655 | 0.174 | 7.6 ± 2.8 |
| 2.2 | 216.9199276 | -25.3461304 | 1.23655 | 0.174 | 25 ± 5.1 |
| 2.3* | 216.9131520 | -25.3518332 | 1.23655 | 0.174 | 1.2 ± 1.1 |

**Table 6.** Summary of VLT/MUSE observations used. The name of the cluster is given in the first column, the seeing for the observation is given in the second column, and the airmass for the observation is given in the third column. The P.I. for the observation is given in the fourth column, the exposure time is given in the fifth column, the observation date is given in the sixth column, and the ESO project code is given in the seventh column.

| Cluster | Seeing | Airmass | P.I. | Exp. time [s] | Obs. date | ESO Project Code |
|---|---|---|---|---|---|---|
| A383 | 1.0" | 1.74 | Edge | 2910 | 2019-11-17 | 0104.A-0801(B) |
| MS2137 | 1.0" | 1.86 | Edge | 2910 | 2019-06-28 | 0103.A-0777(A) |
| MACS J0326 | 0.5" | 1.09-1.11 | Edge | 2910 | 2019-09-21 | 0103.A-0777(A) |
| MACS J1427 | 1.0"-1.5" | 1.01-1.06 | Edge | 2910 | 2018-03-14 | 0100.A-0792(A) |
| MACS J0417 | 1.6" | 1.8 | Edge | 2910 | 2017-12-12 | 0100.A-0792(A) |
| MACS J0949 | 0.71" | 1.4 | Edge | 2910 | 2020-02-20 | 0104.A-0801(A) |

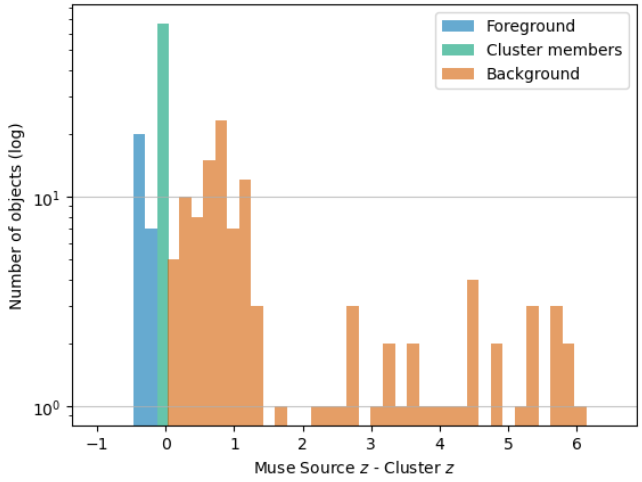


**Figure 1.** Distribution of MUSE source redshifts for all clusters modeled in this paper: A383, MS2137, MACS J0326, and MACS J1427. Redshifts for MACS J0949 and MACS J0417 are not included as we did not perform source inspection for these clusters. All redshifts are plotted relative to 0, where 0 is equivalent to the cluster redshift and thus denotes all the cluster members identified via MUSE.

or noisy Ly-$\alpha$), 1 is a possible detection (a best guess, though this is very uncertain), and 0 is no detection (no features, just noise). The selections of the three users were then evaluated against each other, and a complete catalogue was created for each cluster based on the agreement between these selections. Redshifts with a confidence rating of 3 were strongly agreed upon by all three users; redshifts with a confidence rating of 2 were tentatively agreed upon by all three users; and redshifts with a confidence rating of 1 were included as a 'best guess'. Confidence 1 redshifts were not included in the final lens models unless they were assigned to lensed galaxies whose positions were supported by the structure of the lens model. A full catalogue for the clusters modeled in this paper (A383, MS2137, MACS J0326, and MACS J1427) can be found in the appendix at the end of this paper in Table A6, Table A7, Table A8, and Table A9, respectively. Catalogues for MACSJ0949 and MACSJ0417 are not included in this paper as we did not perform source inspections for these clusters; we refer the reader to Jauzac et al. and Allingham et al. for details. Arc systems selected from *HST* photometry were confirmed with these redshift catalogues where possible.

## 3 MASS MODELING

Strong lensing is a powerful tool for modeling the mass distribution of galaxy clusters, but lensing as a technique cannot differentiate between baryonic and dark matter without ancillary information. This can be partially alleviated by breaking up the overall mass distribution into different 'clumps' of matter, such as cluster member galaxies or galaxy-scale perturbers, and modeling them as separate distributions from the main dark matter halo of the cluster. The BCG is a distinct component of any cluster mass model, and in the case of radial arcs, it is particularly important to model it separately because it affects the lensing potential of the cluster more strongly (Newman et al. 2011). The parameterization of the BCG can be done in a few different ways, but in this paper, we elect to utilize a combination of kinematic measurements from VLT/MUSE and photometry from *HST* imaging to place physical constraints on the distribution of mass in the BCG. This combination of kinematics and lens modeling is a useful technique utilized in many different papers to perform this type of analysis, from N13 to recent papers like Bergamini et al. (2019). We describe the parameterization of the cluster mass in this section, and in the following section, we detail the kinematic measurements of the BCG.

### 3.1 Lenstool

Strong lens models for each cluster in our sample were constructed using the software `Lenstool` (Jullo et al. 2007), an algorithm that models lensing clusters using a parametric approach. One cluster-scale halo and several smaller substructure halos are combined to create the model, where each halo is treated as a pseudo-isothermal ellipsoidal mass distribution (PIEMD; Limousin et al. 2005a). The parameters for each halo are: the $x$ and $y$ positions of the center, the ellipticity, $e$, the position angle, $\theta$, the core radius, $r_{\rm core}$, the effective velocity dispersion, $\sigma$, and the truncation radius of the cluster halo, $r_{\rm cut}$.

Markov Chain Monte Carlo (MCMC) sampling is used to sample the posterior density of the model, which is expressed as a function of the likelihood of the model (as described in Jullo et al. 2007). This function is minimized as

$$\chi^2_{SL} = \sum_i \chi^2_i$$

where the sum is performed over the different families of multiple images in the model, and $\chi^2_i$, the chi-square value for each multiply imaged source, is given as

$$\chi^2_i = \sum_{j=1}^{n_i} \frac{\left(\theta^j_{\rm obs} - \theta^j(\mathbf{p})\right)^2}{\sigma^2_{ij}}.$$

$\theta^j_{\rm obs}$ is the vector position of the observed multiple image $j$, $\theta^j$ is the predicted vector position of the image $j$, $n_i$ is the number of images in system $i$, and $\sigma_{ij}$ is the error of the position of image $j$, which is fixed to 0.5" for multiple images. The model with maximum likelihood thus minimizes the distance between the observed and predicted

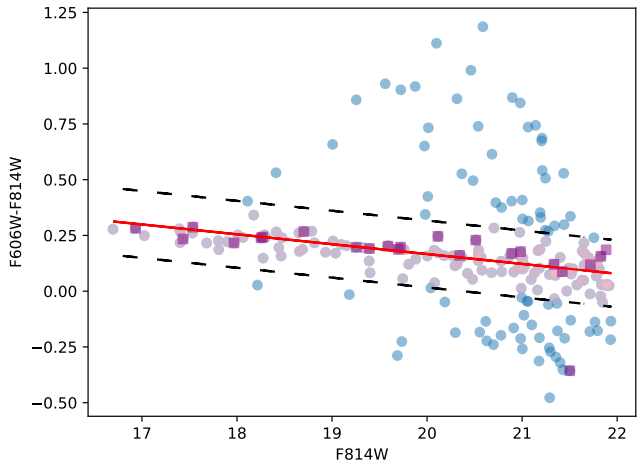


**Figure 2.** Example color magnitude diagram for A383. All sources identified by SExtractor are plotted in blue, and MUSE sources identified around the cluster redshift ($z = 0.187$) are over plotted as purple squares. The red line corresponds to the best fit for the red sequence, with a slope of $-0.044 \pm 0.015$ and an intercept of $1.05 \pm 0.30$. The boundary ($\sigma = 0.15$) for cluster member selection is marked by the dashed black lines, and the sources identified as cluster members are marked as light purple circles.

positions of the multiple images. This distance is referred to as the rms. The optimized model is then used to solve for the best fit set of parameters of each halo.

### 3.2 Cluster Member Galaxies

Cluster member galaxies for all clusters (except MACS J1427) are selected using the cluster red sequence method (Gladders & Yee 2000), which classifies galaxies as cluster members if they have colors consistent with the red sequence at the cluster redshift. An example red sequence for the cluster A383 is shown in Figure 2. In the case of MACS J1427, the archival data available at the necessary resolution to perform red sequence fitting consists of only a single *HST* filter. Red sequence fitting, which requires at minimum two different pass bands, can thus not be performed to isolate cluster members. Instead, we utilize spectroscopic redshifts from MUSE to identify a total of 30 sources at or around the cluster redshift ($0.30 < z < 0.33$), which we define as the cluster member galaxies for this cluster, with the caveat that this selection can be improved with additional observations.

For all clusters, we follow the assumption that luminosity traces mass (refer to the discussion in Harvey et al. 2016) to model each cluster member with galaxy-scale PIEMD halos, where the positional parameters for each halo $(x, y, e, \theta)$ are fixed to the properties of their light distribution as measured with SExtractor (Bertin & Arnouts 1996b). The remaining PIEMD parameters ($\sigma$, $r_{\rm core}$, $r_{\rm cut}$) are then rescaled to match a reference galaxy with luminosity $L^*$ following the Faber & Jackson (1976) relation:

$$\begin{cases} \sigma = \sigma^* \left(\frac{L}{L^*}\right)^{1/4} \\ r_{\rm core} = r^*_{\rm core} \left(\frac{L}{L^*}\right)^{1/2} \\ r_{\rm cut} = r^*_{\rm cut} \left(\frac{L}{L^*}\right)^{1/2} \end{cases}$$

The mass of each halo is then derived with the following relation:

$$M = \frac{\pi}{G} (\sigma^*)^2 r^*_{\rm core} \left(\frac{L}{L^*}\right)$$

where $\sigma^*$, $r^*_{\rm core}$, and $r^*_{\rm cut}$ are the reference velocity dispersion, core radius, and truncation radius, respectively. Previous models have demonstrated that $r^*_{\rm core}$ is small in galaxy-scale halos and has a minimal effect on mass models (e.g. Covone et al. 2006; Limousin et al. 2007b; Elíasdóttir et al. 2007). $r^*_{\rm core}$ is thus fixed to 0.15 kpc for cluster galaxies. The remaining two parameters, velocity dispersion and cut radius, are optimized by the model for a reference galaxy $L^*$ in each cluster. The velocity dispersion is allowed to vary between 27 and 250kms$^{-1}$, and the cut radius between 3 and 50 kpc. The cut radius is constrained to an upper limit in order to account for tidal stripping of galactic dark matter halos (Limousin et al. 2007a, 2009; Natarajan et al. 2009; Wetzel & White 2010; Niemiec et al. 2019). These parametric constraints do not allow any dark matter halos to contain zero mass, which enables the model to reproduce observational constraints. We differentiate between models using $\chi^2$ and rms statistics, where a low rms generally indicates a better model.

### 3.3 Multiple Images

The model is constrained using the positions of multiply imaged sources, or arcs, within the image. Arcs are identified through a combination of MUSE spectroscopy, visual identification of sources with matching color and morphology, and, where relevant, referencing previous models constructed for these clusters. The positions for each source with spectroscopy were fixed to the MUSE detections, which was especially relevant for each of the radial arcs, as their exact substructure and shape is obscured by the BCG light. A summary of the MCMC fit values for each cluster can be found in Table A5.

#### *3.3.1 A383*

Abell 383 ($z = 0.187$) was first modeled using `Lenstool` in Sand et al. (2004). It was later remodeled in Sand et al. (2008) in response to criticism leveled against the initial modeling method's assumptions ignoring cluster substructure, and using spherically symmetric mass distributions; the 2008 model used a full 2D strong lensing model to avoid making these assumptions. The cluster was then observed by CLASH (Postman et al. 2012b), and the discovery of a multiply-imaged system at $z = 6.027$ was reported in Richard et al. (2011), while a mass model was presented in Newman et al. (2011) and Newman et al. (2013a).Zitrin et al. (2011) then identified four new multiple image systems and presented an updated model, which was later refined with additional spectroscopy for one system by Zitrin et al. (2015).

A total of nine systems of multiple images are used to constrain the lens model. The properties of the systems are presented in Table 2. Systems 1, 2, and 9 are all fixed to the spectroscopic redshift measured and optimized from the MUSE cubes. The redshifts of the remaining systems were solved for by the lens model. Systems 2-9 are used in previous lens models of this cluster (Sand et al. 2008; Zitrin et al. 2011; Newman et al. 2011; Richard et al. 2011; Newman et al. 2013a; Zitrin et al. 2015), while system 1 is a new identification confirmed by MUSE spectroscopy. The spectroscopic redshifts for the multiple images are listed in Table A6.

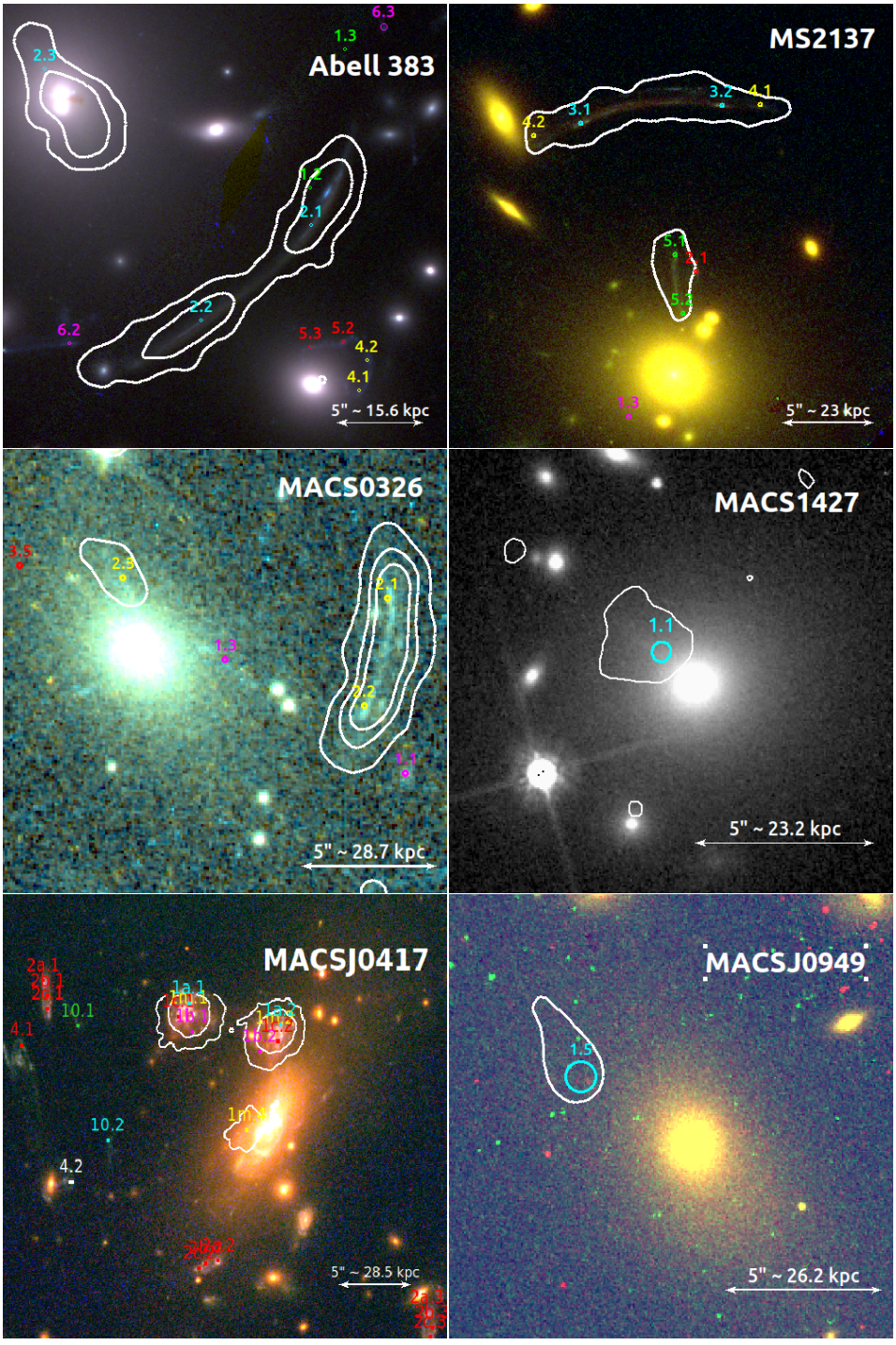


**Figure 3.** Snapshots of the radial arcs in each cluster. All images are oriented North-up, East-left. Each individual arc in a system is labeled as a pair of numbers, i.e. 1.1. In the case where an arc is labeled, for example, 1a.1, the letter corresponds to a sub-division of the same lensed galaxy 1. Each arc 'family' is marked in a different color for clarity. *Top Left*: A383 image of the BCG with MUSE detection contours for the radial arc and its nearby tangential counterpart at 7495 Å overplotted in white. Multiple image systems in this region are also shown. *Top Right*: MS 2137 image of the BCG with MUSE detection contours of the radial arcs and the nearby tangential arc at 9300 Å overplotted in white. Multiple image systems in this region are also shown. *Middle Left*: MACS J0326 image of the BCG with MUSE detection contours of the radial arc at 8376 Å overplotted in white. Multiple image systems in this region are also shown. *Middle Right*: MACS J1427 image of the BCG with MUSE detection contours of the radial arc at 7020 Å overplotted in white. Multiple image systems in this region are also shown. *Bottom Left*: MACSJ0417 image of the BCG with MUSE detection contours of the radial arc and its nearby counterpart images at 6975 Å overplotted in white. Multiple image systems in this region are also shown. *Bottom Right*: MACSJ0949 image of the BCG with MUSE detection contours of the radial arc at 7160 Å overplotted in white. Multiple image systems in this region are also shown.

#### 3.3.2 MS2137−223

MS 2137−23 ($z = 0.313$) was first modeled with `Lenstool` in Sand et al. (2004) and then updated in Sand et al. (2008) using a full 2D strong lensing model. Donnarumma et al. (2009) presented a mass profile for the cluster based on strong gravitational lensing and *Chandra X-ray Observatory* imaging. Newman et al. (2013b) later created a mass model with similar imaging and new Keck spectroscopy for seven multiply-imaged sources, and extended stellar velocity dispersions for the BCG. The lack of multiple images in these models caused them to all have slightly different results for the mass profiles. CLASH observations (Postman et al. 2012b) were later carried out on the cluster, and a new model with an additional multiply-imaged system with a confirmed spectroscopic redshift was published in Zitrin et al. (2015). A KMOS study has also recently been performed that includes several galaxies in MS 2137 (Tiley et al. 2020).

We use a total of four systems of multiple images to optimize this lens model. The properties of the systems are presented in Table 3. All systems have redshifts from MUSE observations. System 1 was first identified in Zitrin et al. (2015), but only with photometric information. We confirm its redshift here with MUSE spectroscopy. The remaining systems are referenced in previous works (Sand et al. 2008; Donnarumma et al. 2009; Newman et al. 2013a; Zitrin et al. 2015). We note that while system 2 is not a new detection, this is the first time this arc has been included in a parametric lens model. We are able to include it because it has a confirmed redshift measurement from MUSE spectroscopy. Systems 3 and 4 are parts of the same giant radial arc, and are adopted here as separate constraints in order to refine our lensing model.

#### 3.3.3 MACSJ 0326.8-0043

MACS J0326 ($z = 0.447$) was first discovered by the MAssive Cluster Survey SNAPshot programs (MACS, PI: Ebeling, Ebeling et al. 2001, Mann & Ebeling 2012), which amassed a sample of the most X-ray luminous galaxy clusters based on X-ray sources detected by the Röntgen Satellit (ROSAT) All-Sky Survey (Voges et al. 1999). These programs were designed to carry out *HST* observations of very X-ray luminous sources to obtain a statistically robust sample of massive distant clusters of galaxies. This is the first published mass model for this cluster.

Three systems are used in this lens model, with all systems having at least one image redshift from MUSE. The properties of the arc systems are presented in Table 4. All three arcs are new identifications as this cluster has not previously been modeled. System 2 is a clear tangential arc located North-East of the BCG, and has been split into a northern and southern part for the purposes of this model. These arcs, 2.1 and 2.2, are MUSE detections, as is 2.3, which is the Northern radial arc shown in Figure 3. Image 2.4 is predicted by the model and is located on a similarly-colored source. Systems 1 and 3 are Lyman-$\alpha$ emitters. Images 3.1, 3.2, and 3.3 are MUSE detections, while 3.4 and 3.5 are predicted multiple images from the model. Image 1.2 is a MUSE identification, while images 1.3 and 1.4 are fixed to locations predicted by the model and are confirmed by the presence of similarly-colored sources in the image. Image 1.4 is of particular interest, as it hints at another radial arc next to the BCG. Figure 3 seems to indicate the presence of another source in this area, but the shallowness of the *HST* image makes it difficult to confirm. Deeper spectroscopic observations would be able to confirm the legitimacy of this arc.

#### 3.3.4 MACSJ 1427.6−22521

MACS J1427 ($z = 0.318$) was first observed in the MACS program (Ebeling et al. 2001). This is the first published mass model for this cluster.

Two multiple image systems are used to construct the lens model; the first is the radial arc located near the BCG (1.1), with a spectroscopic redshift of $z = 0.884$, while the second is another spectroscopic identification at $z = 1.237$ (2.1). The properties of these systems are presented in Table 5. The arcs for this cluster are identified solely based upon their spectroscopic redshift and their relative orientation around the cluster in the context of a strong lensing model. The model predicts additional positions for these arcs, but the shallowness of the MUSE data makes it difficult to detect significant emission at these locations. Further, with only a single *HST* band of imaging data, we are unable to use color information to verify if they are lensed images of the same source. The predicted positions are listed in Table 5, but should be treated as potential candidates for a lensed arc position rather than a confirmed identification.

### 3.4 Additional Clusters with Radial Arcs

The clusters presented thus far represent new, original work. However, they are not the only clusters in the larger Kaleidoscope sample of MUSE cubes that have radial arcs. In the interest of completeness, we introduce the two remaining clusters in the sample that have been modeled in work outside this paper. These clusters have both been modeled using `Lenstool` following the methods already described in this paper, which allows us to directly incorporate them into our broader analysis of the density profiles of galaxy clusters with radial arcs. These two clusters are MACS J0417 and MACS J0949. Both clusters were first observed by the MAssive Cluster Survey (MACS, Ebeling et al. 2001; Mann & Ebeling 2012), which amassed a sample of the most X-ray luminous galaxy clusters based on X-ray sources detected by the Röntgen Satellit (ROSAT) All-Sky Survey (Voges et al. 1999). MACS includes many powerful gravitational lenses, including these two clusters.

MACS J0417 was recently modeled in Mahler et al. 2019 as a part of the Reionization Lensing Cluster Survey (RELICS; Coe et al. 2019), as well as in Jauzac et al. 2019 (J19), which included MUSE spectroscopy. We utilize the fiducial model from J19 in our analysis. The cluster is at a redshift of $z = 0.443$, and is constrained with a total of 17 lensed systems, three of which have spectroscopic redshifts confirmed by MUSE. System 1, a quadruply-lensed galaxy, is of particular interest, as it includes a radial arc whose position is identified from emission lines detected in MUSE, as it is otherwise obscured by the BCG in the available *HST* imaging. Unlike the other five clusters in our sample, MACS J0417 has a fairly elongated cluster core, which can be observed both visually by the separation in projection of the second and third brightest cluster galaxies from the BCG, as well as in the X-ray analysis (see J19), which show extended emission along the SE-NW axis. These factors indicate that the cluster is likely the result of a recent merger, possibly oriented along the line of sight, which makes it the most dynamically complex cluster of our sample.

Finally, we include MACS J0949 in our sample, using the strong lens model recently published in Allingham et al. (2023). The cluster is at a redshift of $z = 0.383$, and X-ray data suggests that it is a post-merger in the process of relaxing. The strong lens model is constrained with a total of 6 lensed systems, two of which have spectroscopic redshifts confirmed by MUSE. Similarly to the other clusters in this paper, its radial arc is also detected by MUSE.

**Table 7.** Values for the BCG of each cluster extracted from the photometric fitting process. The first column lists the cluster, and the second column lists the filter used for the photometric fit of the BCG. The third column lists the $b/a$ value, the fourth column lists the position angle $\theta$, the fifth column lists the magnitude of the BCG in the listed filter, and the sixth and seventh columns list the $r_{\rm core}$ and $r_{\rm cut}$ fit values. The errors for $r_{\rm core}$ are extremely small and are thus not listed.

| Cluster | Filter | $b/a$ | $\theta$ | Magnitude | $r_{\rm core}$ [kpc] | $r_{\rm cut}$ [kpc] |
|---|---|---|---|---|---|---|
| A383 | ACS/F606W | 0.87 | 81.77 | 18.82 | 3.32 | 23.8 ± 5.6 |
| MS2137 | ACS/F625W | 0.86 | 73.56 | 18.40 | 0.76 | 66.2 ± 12.3 |
| MACS J0326 | ACS/F606W | 0.55 | 46.66 | 19.56 | 1.74 | 77.9 ± 6.4 |
| MACS J1427 | ACS/F814W | 0.90 | -2.85 | 17.88 | 0.23 | 7.0 ± 0.31 |
| MACS J0949 | ACS/F606W | 0.52 | 31.12 | 19.96 | 2.81 | 70.6 ± 4.2 |
| MACS J0417 | ACS/F606W | 0.33 | -34.10 | 19.58 | 6.85 | 101.4 ± 29 |

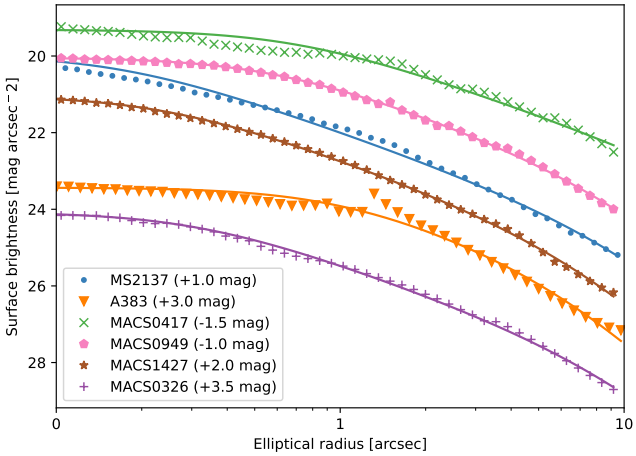


**Figure 4.** Surface brightness profiles of the BCGs for all six clusters, measured using the filters listed in Table 7. The dPIE fit for each profile is plotted as the solid line of the same color as each cluster. The magnitudes for each cluster are offset by the listed values to provide visual clarity.

## 4 BCG KINEMATICS

We introduce kinematic constraints into the total density profile of each cluster in order to more closely examine the shape of the mass distribution in the inner 10 kpc of the cluster. Following the methods used in Sand et al. (2004) and Newman et al. (2013b), we include the velocity dispersion of the BCG as an additional constraint for our `Lenstool` model. We incorporate this constraint by measuring observable properties of the BCG through a combination of photometry and spectroscopy. We model the BCG as a separate dPIE mass halo within `Lenstool`, with its parameters fixed to the values obtained from these measurements. The following subsections discuss the measurements of the observable properties of the BCG that we use to fix the parameters of the BCG mass halo, as well as to constrain the lens model using our kinematic measurements. We discuss the combination of kinematics and lensing more thoroughly in Section 5.2.

### 4.1 BCG Photometry

We measure the surface brightness profile of the BCG in each cluster using *HST* imaging, where preference was given to the *ACS*/F606W filter to more closely align the photometric fit with the wavelengths used in the kinematic fit since these BCGs are largely red and dead. This band was used for A383, MACS J0326, MACS J0949, and MACS J0417, while the *ACS*/F814W filter is used for MACS J1427. However, in MS2137, where this band has a gap in data around the BCG, the F625W filter was used. In MACS J1427, where this band is not available, the F814W filter was used instead. Surrounding objects in the field are masked out using a SExtractor segmentation map, and the PSF is modeled using a field star and a selection of surrounding sky. We model the BCG light using the 2 dimensional dPIE equation, adopting the specific form used in `Lenstool` (Limousin et al. 2005b):

$$\Sigma_{\rm dPIE}(R) = \frac{\sigma_0^2 r_{\rm cut}}{2G(r_{\rm cut} - r_{\rm core})}\left(\frac{1}{\sqrt{r_{\rm core}^2 + R^2}} - \frac{1}{\sqrt{r_{\rm cut}^2 + R^2}}\right),$$

where $r_{\rm core}$ is the core radius, $r_{\rm cut}$ is the cut radius, and $\sigma_0$ is the central velocity dispersion of the BCG. The half-light radius, $r_h$, is related to the cut radius as $r_h \approx r_{\rm cut}$, and in the limit $r_{\rm core}/r_{\rm cut} \ll 1$, the projected effective radius is $R_e \approx (3/4)r_{\rm cut}$.

We fit this equation by using the light profile extracted from isophotal measurements of the BCG. We first fix the geometric parameters of ellipticity, position angle, and center coordinates of the central isophote to the values we obtain from fitting a de Vaucouleurs $R^{1/4}$ profile to the 2D data using `GALFIT` (Peng et al. 2002, 2010). We then use the Python Astropy Elliptical Isophote Analysis routine to find the best-fit model for the 2D data out to about 20 kpc, where the light from other objects in the field begins to dominate the light from the BCG, and run the fit in the bilinear area integration mode. The 1D surface brightness profile is then fit to the dPIE equation, with only $\sigma_0$ allowed to vary during the fit.

Finally, since we use the mass of the BCG as a constraint in our modeling, we require a stellar mass-to-light ratio to transform the dPIE fit to the light into the mass of the BCG. We obtain this value by performing a SED fit of the combined photometric (see Table 1) and spectroscopic (see Table 6) data using `ppxf` (Cappellari 2017). We use the FSPS models library (Conroy et al. 2009, Conroy & Gunn 2010) generated in Cappellari (2023) as the basis for the fit, which was created using a Saltpeter IMF with a mass range between 0.08 and 100 $M_\odot$. These models do not explicitly include the effect of gas or dust. The spectra for these SPS models were created using the MILES stellar library (Sánchez-Blázquez et al. 2006, Falcón-Barroso et al. 2011). We use the library of these spectra to fit the stellar mass-to-light ratio of the BCGs in each cluster.

The resulting parameters, surface brightness profiles, and dPIE fits are presented in Table 7 and Figure 4. This fit allows us to easily create a separate mass halo for each BCG whose properties are fixed to these photometric values. We specifically fix the ellipticity, the position angle, and the values of $r_{\rm core}$ and $r_{\rm cut}$. The only free parameter is then the velocity dispersion, $\sigma_0$, which serves as a constraint on the mass profile in our model.

### 4.2 Velocity Dispersion Profile

We utilize BCG kinematics in tandem with lensing to break down the total mass distribution of the cluster into more clearly defined

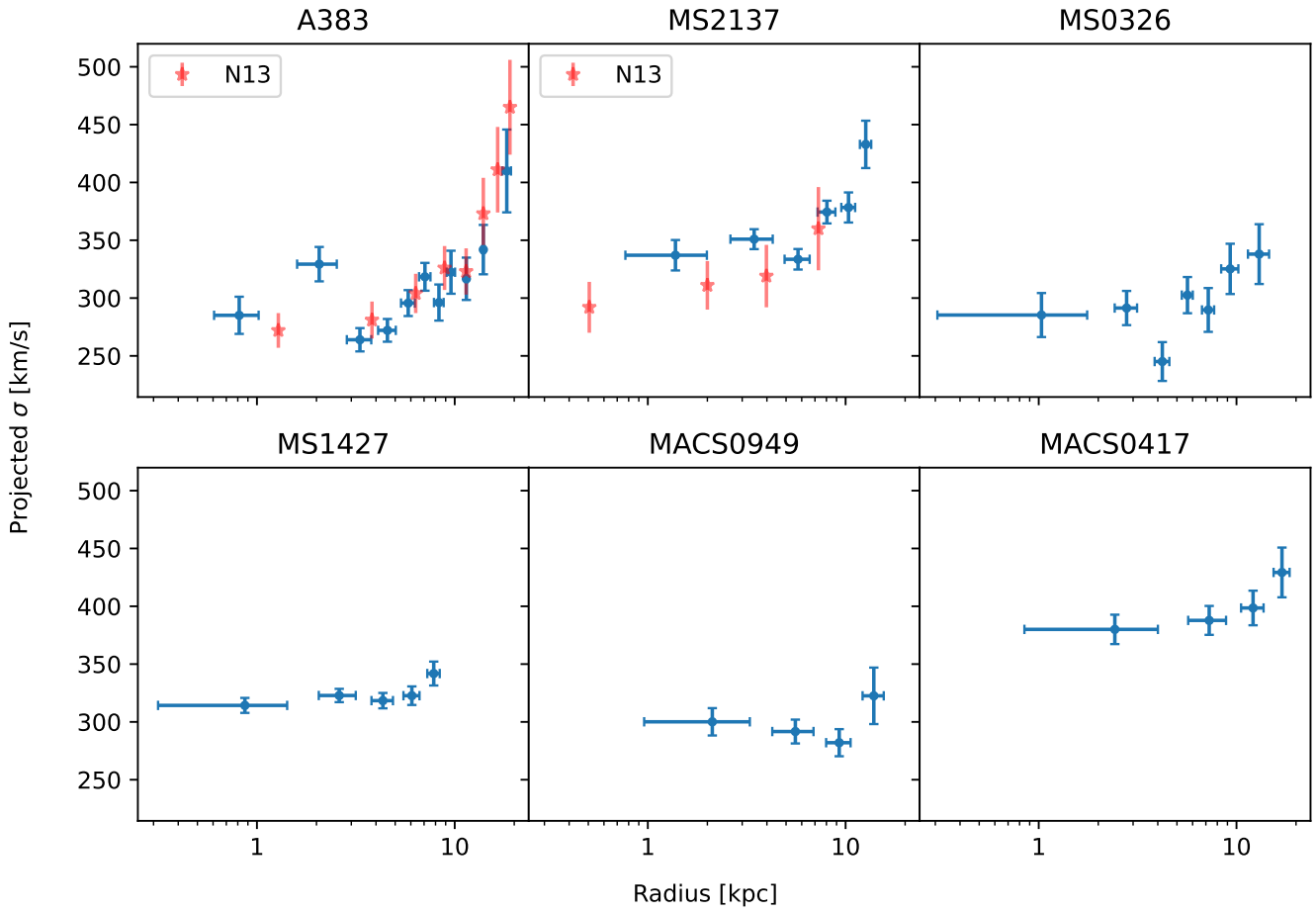


**Figure 5.** BCG stellar velocity dispersion profiles for all six clusters. The error in the velocity dispersion is denoted by the errorbars along the Y axis, while the errorbars on the X axis signify the width of the bin used to make the measurement. The datapoints are centered at the middle of each bin, and each point corresponds to the reported $\sigma$ value in Table 8. For the clusters A383 and MS2137, the values reported in N13 are over-plotted as red stars for reference.

baryonic and dark matter segments. Modeling the BCG mass using stellar dynamics allows us to place limits on the contribution of the BCG to the cluster density profile in the very inner portion of the cluster (<10 kpc), which in turn allows us to more precisely examine the behavior of dark matter in this region.

We elect to model the kinematics of the BCG by creating a profile of the velocity dispersion in different bins, stepping out from the center of the BCG until the S/N ratio dips below a cutoff threshold of 30, which is equivalent to a distance of about ~20 kpc for each cluster. We utilize the MUSE observations from the Kaleidoscope survey to make these measurements of the velocity dispersion. As these observations are all short exposures, we choose to bin the cubes using concentric circular annuli, which maximizes the S/N ratio in each bin and works well for the BCGs used in this paper because they are all nearly circular (see Section 4.3 for more details). The width of each annulus is determined by the S/N ratio, where we require each bin to be large enough to obtain a total S/N ratio greater than 30. We fit each spectrum over a rest-frame wavelength of 4860-7160 Å, which includes the regions where MUSE sensitivity is strongest and excludes regions where sky line residuals are very large.

Nearby bright stars and galaxies are masked out before the fit is performed for each BCG, and bins where these objects interfere strongly with the BCG light are excluded. We choose to mask out surrounding galaxies despite their potential contribution to the velocity dispersion profile because we do not know where they are located in the 3D space of the cluster. Additionally, failing to mask these objects distorts the velocity dispersion toward non-physical values. This is particularly relevant for MACS J1427, which has a bright foreground star situated within 5" of the BCG. While masking this star allows for an effective measurement of the velocity dispersion, we are unable to continue fitting past about 10 kpc due to the contamination from the flux of this star and the surrounding cluster galaxies.

The `pPXF` fit for each cluster relies on the use of additive and multiplicative polynomials in order to match the template spectra to the observed VLT/MUSE spectrum. These polynomials are adjusted until the fit in the highest S/N bin of each cluster no longer improves. One first-order multiplicative polynomial is used for every cluster except MS2137, which uses a third-order polynomial, and a fifth-order additive polynomial is used for every cluster.

We are able to compare our measurements for the velocity dispersion directly to the results found in Newman et al. (2013a). Figure 5 shows the velocity dispersion profiles for all six clusters analyzed in this paper, and additionally shows how our results compare to those derived in N13 for the clusters A383 and MS2137. The N13 results are based on a Keck/LRIS 23.7 ks exposure with 0.8" seeing for A383, and a Keck/ESI 6.7 ks exposure with 0.7" seeing for MS2137.

**Table 8.** Values for the velocity dispersion profile for the BCG of each cluster. The quoted $\sigma$ values are measured at the midpoint of each bin. The first column lists the cluster, the second column lists the total extent of each bin in arcsec, the third column lists the total extent of each bin in kpc, and the fourth column lists the measured velocity dispersion in that bin.

| Cluster | Bin [arcsec] | Bin [kpc] | $\sigma$ [km/s] |
|---|---|---|---|
| A383 | 0.0-0.26 | 0.0-0.81 | 285 ± 14 |
| | 0.46-0.66 | 1.44-2.07 | 329 ± 12 |
| | 0.86-1.06 | 2.69-3.32 | 263 ± 10 |
| | 1.26-1.46 | 3.94-4.57 | 272 ± 10 |
| | 1.66-1.86 | 5.19-5.82 | 295 ± 13 |
| | 2.06-2.26 | 6.45-7.07 | 318 ± 15 |
| | 2.46-2.66 | 7.70-8.32 | 296 ± 16 |
| | 2.86-3.06 | 8.95-9.57 | 322 ± 17 |
| | 3.30-3.66 | 10.33-11.45 | 316 ± 20 |
| | 4.46-5.06 | 13.96-15.83 | 341 ± 24 |
| | 5.86-7.26 | 18.34-22.72 | 409 ± 28 |
| MS2137 | 0.0-0.50 | 0.0-2.30 | 337 ± 13 |
| | 0.50-1.0 | 2.30-4.60 | 350 ± 9 |
| | 1.0-1.5 | 4.60-6.90 | 334 ± 8 |
| | 1.5-2.0 | 6.90-9.20 | 374 ± 10 |
| | 2.0-2.5 | 9.20-11.50 | 378 ± 13 |
| | 3.0-3.5 | 13.80-16.09 | 404 ± 19 |
| MACS J0326 | 0.43-0.73 | 2.47-4.19 | 238 ± 15 |
| | 0.73-1.08 | 4.19-6.20 | 276 ± 15 |
| | 1.08-1.66 | 6.20-9.52 | 291 ± 17 |
| MACS J1427 | 0.0-0.38 | 0.0-1.76 | 320 ± 9 |
| | 0.38-0.75 | 1.76-3.48 | 312 ± 9 |
| | 0.75-1.12 | 3.48-5.19 | 297 ± 10 |
| | 1.12-1.5 | 5.19-6.95 | 301 ± 11 |
| | 1.5-1.88 | 6.95-8.71 | 326 ± 16 |
| | 1.88-2.25 | 8.71-10.43 | 344 ± 21 |
| | 2.25-2.62 | 10.43-12.14 | 407 ± 31 |
| MACSJ0949 | 0.0-0.71 | 0.0-3.71 | 300 ± 12 |
| | 0.71-1.42 | 3.71-7.43 | 292 ± 10 |
| | 1.42-2.13 | 7.43-11.14 | 282 ± 12 |
| | 2.13-3.18 | 11.14-16.63 | 323 ± 24 |
| MACSJ0417 | 0.0-0.85 | 0.0-4.85 | 380 ± 13 |
| | 0.85-1.7 | 4.85-9.70 | 388 ± 13 |
| | 1.7-2.55 | 9.70-14.56 | 399 ± 15 |
| | 2.55-3.4 | 14.56-19.40 | 429 ± 22 |

Relative to the MUSE data, the archival data have a 10x and 3x longer exposure time for A383 and MS2137. Measured seeing conditions were on average 0.2" narrower. However, the advantage of MUSE rests in the ability of IFU observations to capture information about the entire structure of the BCG. In other words, area recovers depth. This is well supported by our measured profiles, because while there is some variation in the innermost bins, the shape of the profile for A383 and MS2137 is generally well reproduced by our measurements. This suggests that our characterization of the BCG profile in the MUSE data is consistent with archival measurements, despite the difference in observing conditions.

### 4.3 Rotational Velocity and Anisotropy

In Section 5.2, we treat all BCGs as isotropic in our application of the spherical Jeans equation, which is a simplification that warrants some brief additional discussion. While half the BCGs in this sample are nearly circular (b/a ~ 0.85), the other three are more oblate (0.33-0.55), and the noticeably elliptical shape of MACS J0417 makes this assumption harder to justify.

To examine the effects of anisotropy on our BCGs, we thus employ two different methods to evaluate what changes this effect might have on our lensing models. First, we use the anisotropic Jeans equation and fix the anistropy to a small, constant value ($\beta = 0.3$) to examine how this affects our results. This value was chosen because BCGs lack significant rotation (see Kronawitter et al. (2000), which studied 21 giant ellipticals and found that the velocity anisotropy was less than $\beta < 0.3$ for the majority of the sample, and Santucci et al. (2023), which measured a similar value for central ellipticals). Our sample of BCGs is no exception, as inspection of the velocity maps for each BCG shows no significant rotation. Second, for MACS J0417, we employ the more robust external modeling program JamPy (Cappellari 2020) in conjunction with MgeFit (Cappellari 2002) to examine the specific effect anistropy might have on this cluster. Introducing a constant anisotropy value shifts the value of the derived velocity dispersion by roughly ±5 km/s in all cases. The more robust examination of anisotropy in MACS J0417 results in around the same changes. Even the most complex BCG is thus still able to be analyzed using our spherical symmetry assumptions.

## 5 RESULTS

### 5.1 Mass Models

#### *5.1.1 Abell 383*

The properties of the multiple image systems are given in Table 2. One cluster-scale dark matter halo is used to model the cluster, and a total of four galaxy-scale halos are included to separately model the mass distribution of the BCG, as well as three cluster members located near systems 3 and 4. The best fit parameters for these halos are given in Table A1. The integrated density profile is presented in Figure 7. A snapshot of the radial arc in the south-west portion of the cluster is shown in Figure 3. The cluster, multiple images, and the critical lines for the model at $z = 3.0$ are shown in Figure 6.

#### *5.1.2 MS 2137−23*

The properties of the multiple image systems are described in Table 3. One cluster-scale dark matter halo is used to model the cluster, and two galaxy-scale halos are used to separately model the mass distribution of the BCG and one cluster member located near systems 3 and 4. The parameters for these halos are given in Table A2. The integrated density profile is presented in Figure 7. A snapshot of the radial arc in the north-east portion of the cluster is presented in Figure 3. The cluster, multiple images, and the critical lines for the model at $z = 3.0$ are shown in Figure 6.

#### *5.1.3 MACS J0326.8-0043*

One cluster-scale dark matter halo is used to model the cluster, one galaxy-scale halo is used to separately model the mass distribution of the BCG, and one additional halo is included for the bright cluster member located near system 3. The best fit parameters for these halos are given in Table A3. The integrated density profile is presented in Figure 7. A snapshot of the two radial arcs near the BCG are shown in Figure 3, and the properties of the multiple images are listed in Table 4. The cluster, multiple images, and the critical lines for the model at $z = 3.0$ are shown in Figure 6.

#### *5.1.4 MACS J1427.6−2521*

This cluster has not been mass modeled before. One cluster-scale dark matter halo is used to model the cluster and one galaxy-scale

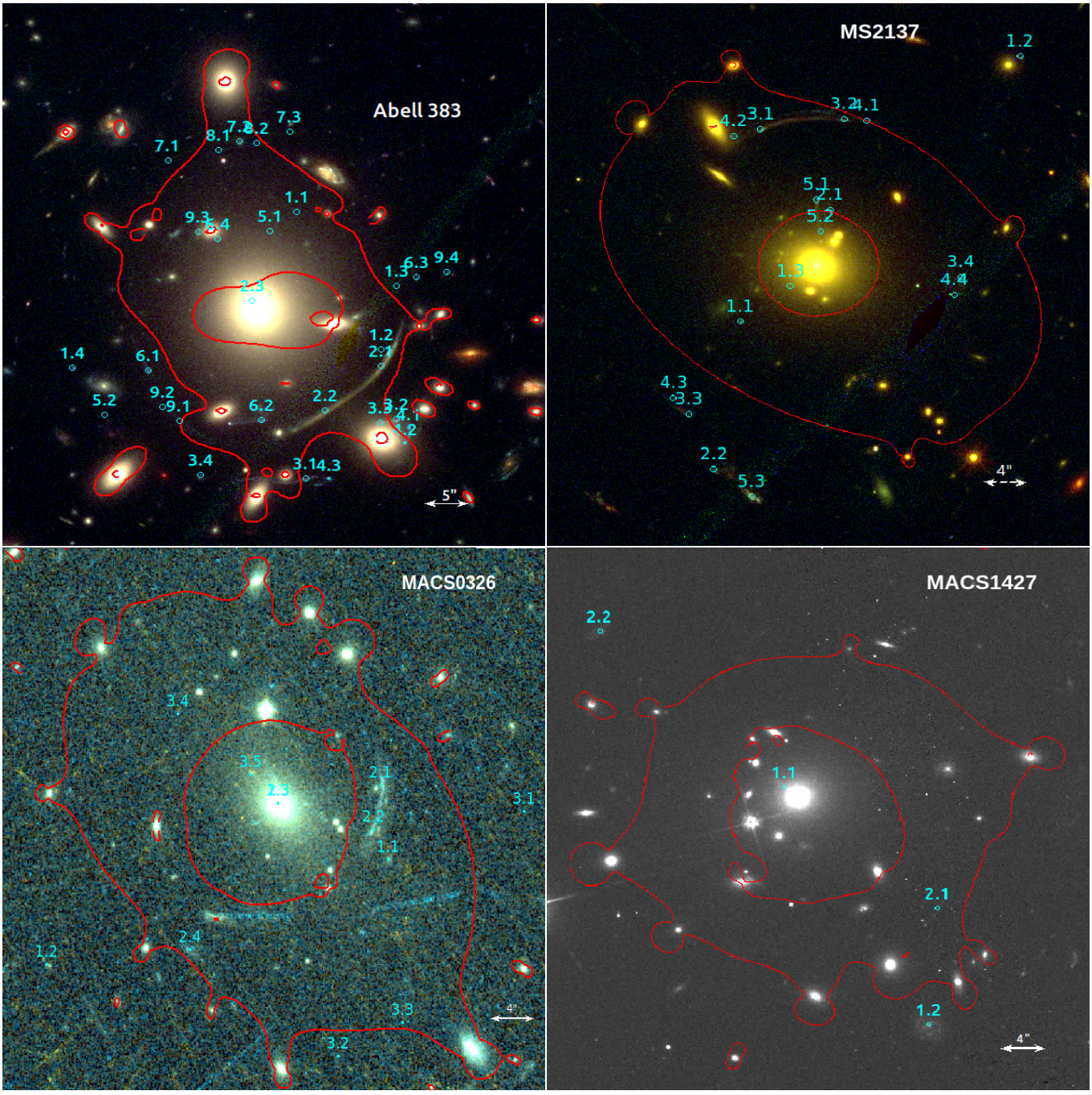


**Figure 6.** Images of the four clusters newly modeled in this paper. All images are oriented North-up, East-left. *Top Left: HST* composite color image of A383 created using a combination of WFC3/IR imaging in the red (F160W) and ACS imaging in the green (F814W) and blue (F606W). Multiply imaged galaxies are labeled in cyan. The red curve marks the location of the critical curve for a source at $z = 3.0$. *Top Right:* False color image of MS 2137 created using a combination of WFC3/IR imaging in the red (F160W) and ACS imaging in the green (F814W) and blue (F606W). Multiply imaged galaxies are labeled in cyan. The red curve marks the location of the critical curve for a source at $z = 2.5$.*Lower Left:* False color image of MACS J0326 created using a combination of ACS imaging in the green (F814W) and blue (F606W). Multiply imaged galaxies are labeled in cyan. The red curve marks the location of the critical curve for a source at $z = 3.0$. *Lower Right:* F814W image of MACS J1427. Multiply imaged galaxies are labeled in cyan. The red curve marks the location of the critical curve for a source at $z = 1.2$.

halo is used to separately model the mass distribution of the BCG. The best fit parameters for these halos are given in Table A4. The integrated density profile is presented in Figure 7. A snapshot of the radial arc is shown in Figure 3, and the properties of the multiple images are listed in Table 5. The cluster, multiple images, and the critical lines for the model at $z = 3.0$ are shown in Figure 6.

#### 5.1.5 MACS J0417.5-1154

We refer the reader to Jauzac et al. (2019) and Mahler et al. (2019) for more details regarding this mass model. The only modification we make to the model described in J19 is the introduction of the parameters listed in Table 7 to constrain the mass halo for the BCG. A snapshot of the radial arc is presented in Figure 3. The integrated density profile is presented in Figure 7.

#### 5.1.6 MACS J0949.8+1708

We refer the reader to Allingham et al. (2023) for more details regarding this mass model. The only modification we make to the model described in this paper is the introduction of the parameters listed in Table 7 to constrain the mass halo for the BCG. A snapshot of the radial arc is presented in Figure 3. The integrated density profile is presented in Figure 7.

### 5.2 Combining Kinematic Profile with Lensing

Stellar kinematics generally probe the total mass distribution, but in the case of galaxies, where significant amounts of stellar light are concentrated, the mass profile is strongly dominated by baryons. We can thus combine the kinematic measurements of the BCGs of these clusters, which effectively measure the baryonic mass, with strong lensing models, which are sensitive to dark matter, to disentangle the degeneracy between dark and baryonic matter. We elect to employ kinematic measurements of the BCG in our models to more accurately probe the mass distribution at the center of these galaxy clusters. We separately parameterize the BCG using a dPIE profile with `Lenstool`, using parameters derived from photometry. We leave the velocity dispersion as the only free parameter for this profile. We can then constrain the BCG velocity dispersion using our real kinematic measurements from MUSE. In this way, we can use physical measurements of the BCG to constrain the lens model.

The velocity dispersion of the BCG is incorporated as a constraint into the model through a-posteriori analysis of the MCMC `Lenstool` model. The original `Lenstool` model is first modified to incorporate photometric information (discussed in Section 4.1) for the BCG into the model. This is done by creating a separate mass halo to account for the BCG, with the parameters $r_{\rm core}$ and $r_{\rm cut}$ fixed to the values obtained from the surface brightness profile fit. Ellipticity and position angle are also fixed to the values from the `GALFIT` fitting. The remaining free parameter in the halo, $\sigma_0$, is left free as a proxy for the stellar mass to light ratio (Sand et al. 2004, Sand et al. 2008, Bergamini et al. 2019). This parameter is given a prior that is informed by measurements of the stellar mass to light ratio.

Adding this information to the model allows us to directly calculate a model version of the velocity dispersion of the BCG based on Jeans fitting. We assume no anisotropy in our model, an assumption that is validated by our nearly circular BCGs, though we discuss what effect the introduction of anisotropy has on our model values in Section 4.3. The form of the spherical Jeans equation is thus as follows:

$$\sigma^2_{\rm los}(R) = \frac{2G}{\sum_*}\int_R^\infty \frac{\nu_*(r)M(r)\sqrt{r^2-R^2}}{r^2}dr,$$

where $\nu_*$ describes the three-dimensional profile and $\sum_*$ refers to the two-dimensional profile of the stellar component of the BCG. These profiles are drawn directly from the photometric fits to the BCG described in Section 4.1. $M(r)$ accounts for the total enclosed mass inside a radius, $r$, and must thus account for both the stellar and DM mass. We draw the value for the enclosed mass directly from the `Lenstool` model at this stage, as the degeneracy between DM and stellar mass makes it difficult to avoid double-counting the mass of the BCG if we add it separately to the `Lenstool` value. We can then calculate a model velocity dispersion for the BCG at any given radius, $R$.

The optimization of the `Lenstool` model with respect to the stellar kinematics is performed by adding the error from the model to the error of the stellar kinematics,

$$\chi^2_{\rm VD} = \sum_i \frac{\left(\sigma_i - \sigma_i^{obs}\right)^2}{\Delta_i^2},$$

where $\Delta_i$ is the uncertainty in the observed velocity dispersion measurements.

The calculation of the velocity dispersion error is performed after the lensing minimization has been completed, separately from `Lenstool`. As a result, the velocity dispersion and lensing likelihoods can be treated as independent from each other, and the total likelihood is then the product of the velocity dispersion and lensing likelihoods, where we assume that both the lensing and dynamical models carry equal weight in the final calculation. The resulting 'best-fit' model is then simply the model that minimizes the total $\chi^2 = \chi^2_{SL} + \chi^2_{VD}$. This treatment of the likelihoods as independent quantities follows previous work done to combine dynamics and lensing models (e.g. Sand et al. 2004, Newman et al. 2013b).

Maximizing the global likelihood function allows us to separate DM and baryons into distinct profiles, as seen in Figure 7. In doing so, we can compare the DM and baryon profiles (yellow and blue lines, respectively) to the total mass distribution (black line) to see the relative contributions of each as a function of radius. Each of these profiles possess a core-like structure within the inner 50 kpc. This is perhaps not unexpected, given that all of these clusters have radial arcs, which are preferentially produced in mass distributions with a shallow inner slope. However, the agreement between the shape of the profile for each of these clusters is fairly significant, as it shows that the dark matter distribution in the center of the cluster is centrally concentrated.

### 5.3 Cluster Density Profile

We use a dPIE profile to construct our density profiles for these clusters. Since we do not use the usual NFW profile, an examination of the properties of the dPIE profile is worth considering.

The obvious test of this profile is to compare it against a 'non-core' model. In Newman et al. (2013a), this comparison between a core and non-core model was performed by using a gNFW profile and a 'cored' NFW profile, with the cored model being ultimately favored. In our case, we choose to use dPIE profiles over NFW because we lack weak lensing information for the clusters MACS J1427 and MACS J0326. As shown in Limousin et al. (2022), weak lensing is crucial for placing reasonable priors on the scale radius of the NFW profile, and without these priors any attempts to use `Lenstool` to create NFW profiles will result in models that are degenerate with their own parameters. As a result, until we are able to perform weak lensing analyses for these clusters and obtain priors on their parameters, the information we derive from NFW fitting will have a low statistical significance. While we can investigate weak lensing modeling, the *HST* data for these clusters are too shallow to perform a meaningful fit to the data (e.g. the number density of background sources is too low). Additionally, the lack of multiple bands makes weak lensing analysis difficult to incorporate as the contamination from foreground and cluster objects will be almost impossible to remove (Jauzac et al.

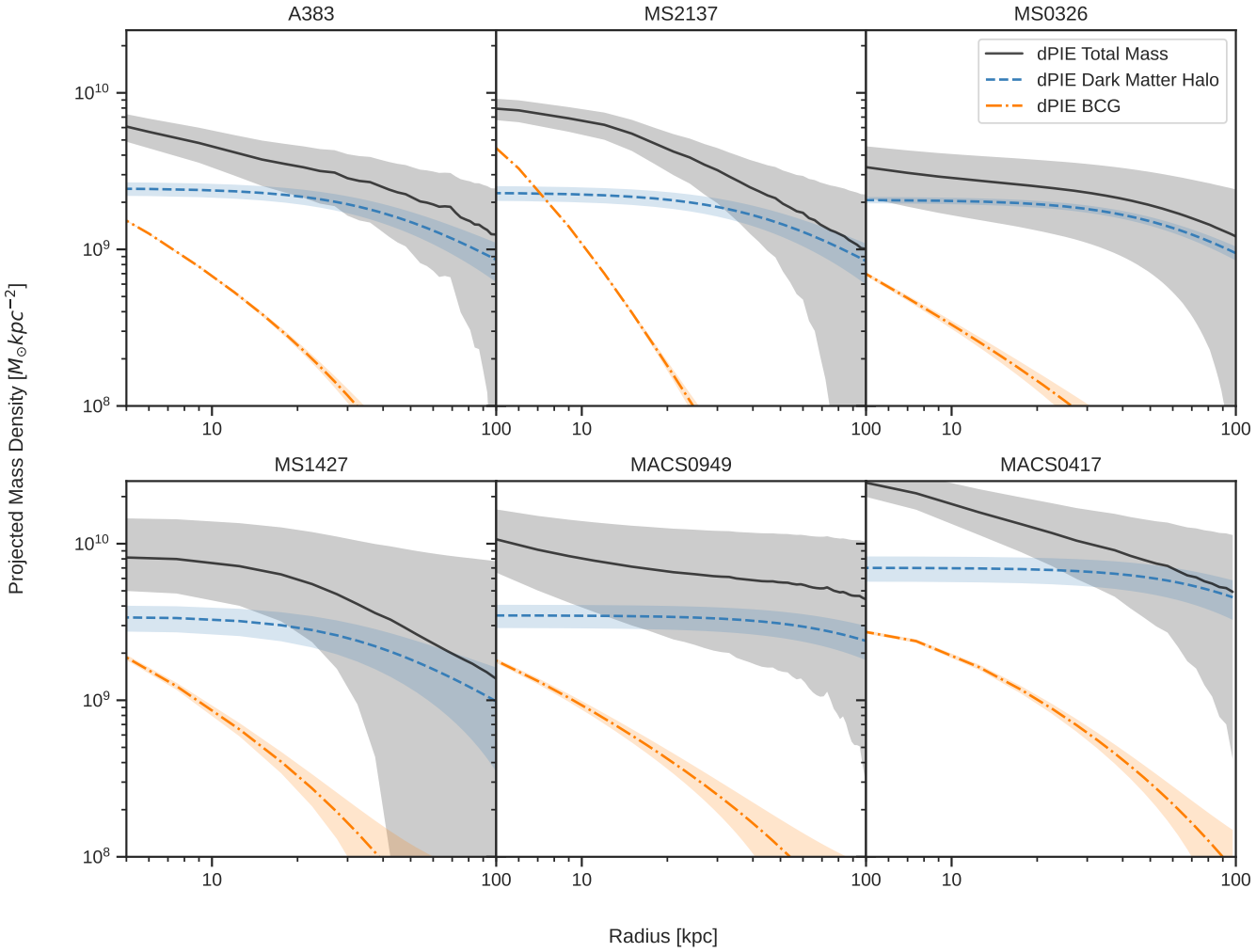


**Figure 7.** The integrated density profiles for all six clusters studied in this work. The uncertainty in the measurement is plotted as the shaded region around the line, and only incorporates the uncertainty returned by `Lenstool`; systematic errors are not included. Density is measured in units of log ($M_\odot$/kpc$^2$), except in the case of MACSJ0417: for this cluster, the mass density is plotted in terms of log (10 $M_\odot$/kpc$^2$) for visual clarity.

2012; Niemiec et al. 2023). Since all clusters covered in this work, besides these two, have published weak lensing models (see Newman et al. 2013b; Jauzac et al. 2019; Allingham et al. 2023), we elect not to repeat this analysis since the available data is the same, and we are not introducing new weak lensing modeling techniques. Additionally, by not using an NFW profile to model the cluster DM profile, we avoid the degeneracy between the scale radius and the asymptotic gNFW profile slope that was demonstrated in He et al. (2020), and do not bias our results toward low slope values as a result of measurement choices in a weak lensing profile. As a result, we leave the potential exploration of NFW profiles to future work.

Instead, we choose to create 'core' and 'non-core' dPIE models following the approach presented in Limousin et al. (2022). We perform this test by restricting the $r_{\rm core}$ radius to be smaller than 10 kpc to create 'non-cored' models, and comparing the resulting models against our 'cored' dPIE models, where the core radius was left as a free parameter. The results of this experiment are definitive. In each case, the $\chi^2$ value of the 'non-cored' model increased significantly in comparison to the cored model. For instance, the 'cored' model for MACS J0326 has a $\chi^2$ of 23.4, with an rms of 0.37". In comparison, the 'non-cored' model has a $\chi^2$ of 179, with an rms of 3.3", which indicates that the model is unable to reproduce the observational constraints. This discrepancy is consistent across all six clusters, indicating that 'non-cored' models are not favored as a solution.

## 6 DISCUSSION

Strong lensing is a powerful tool for examining the inner slope of the dark matter density profile, which can then be used to compare with, and improve upon the information used to build CDM simulations. The clusters modeled in this paper all have radial arcs, which are uniquely suited for providing more precise constraints in the inner part of the cluster, i.e. near the BCG.

### 6.1 How Rare are Radial Arcs?

Radial arcs are still relatively uncommon among lenses, both because the geometric requirements for their appearance are so stringent, and then even when they do appear, they can easily be obscured by the

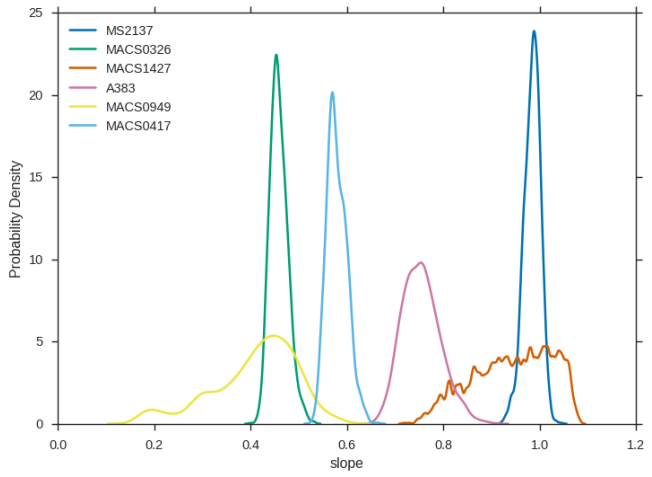


**Figure 8.** Density distribution for the slope measurements in all 6 clusters. The probability density is calculated from the MCMC chain run for each model and is based on the derived parameters for the cluster DM halo.

light of surrounding galaxies and the BCG (Bartelmann 2010). Visual examination of Figure 3, for example, would not immediately make the presence of a radial arc obvious; it is only through spectroscopic confirmation that we can definitively say an arc is present and assign it a redshift, which defines its power as a constraint. As a result, building a large sample of clusters with radial arcs is not trivial. The six clusters selected in this paper are chosen from a dataset of around 150 MUSE cubes (PID 0104.A-0801; PI A. Edge) from the Kaleidoscope survey, a large 'filler' program, and are selected from within that dataset specifically for the presence of radial arcs. The ratio of clusters with radial arcs vs clusters without these arcs in the Kaleidoscope sample is around 1%, which easily shows that radial arcs, while a powerful constraint on the inner DM profile, are a very unique physical feature and cannot be relied upon to appear in lensing analyses of cluster mass profiles at scale.

An additional, equally important consideration for the robustness of our measurements is that the model and slope profiles presented in this work exclusively represent clusters that contain radial arcs. This naturally means that all of these clusters are more core-like, as total density distributions steeper than $\rho \propto r^{-2}$ do not produce radial arcs (see Hattori et al. 1999). As a result, we incur another degree of selection bias in our results by excluding systems that might be more cuspy. While we do plan to examine this in the future using other clusters in the Kaleidoscope survey, it is useful to mention what potential impact this bias might have by referring to previous work done by Sand et al. (2004) and Newman et al. (2013a) on A383 and MS2137.

In each of these papers, these two clusters were a part of a larger sample, which included clusters that had tangential arcs but did not have radial arcs. The authors could thus perform a comparison of their results relative to clusters without radial arcs, and the shallowness of the inner DM density profiles for both A383 and MS2137 did not differ significantly from the profiles of clusters with only tangential arcs. These results are encouraging, and we plan to more thoroughly test the robustness of our own sample in future work. In this paper, we present our models as a specific study of density distributions for clusters with radial arcs and shallow IFU spectroscopy, rather than an examination of the general shape of the DM density profile for all clusters. Despite these limitations, however, we are able to obtain measurements for the inner DM slope that are both consistent with previous mass models and are in agreement with other observational measurements from literature, thus demonstrating the strength of using radial arcs as lensing constraints in tandem with MUSE spectroscopy.

### 6.2 Comparison with previous work

#### *6.2.1 Abell 383*

A383 has been modeled numerous times, due to its properties and fortuitous magnification of a background $z \sim 6$ galaxy. The most recent model was created using a combination of strong and weak lensing, and was part of a compilation of models built using the complete sample of CLASH clusters (Zitrin et al. 2015; Z15). The multiple image systems used in Z15 correlate to those used in this paper, with the exception of our system 1, which is a new detection. System 1 in Z15 is associated here with our system 2; the remaining systems are numbered in accordance to Z15. We note that our system 2 is a combination of Z15 system 1 and system 2, as we treat the tangential arc and the radial arc as the same system based on our MUSE observations.

Systems 1-5 are fixed to spectroscopic redshifts, where systems 1, 2, and 5 are measured from our MUSE spectroscopy, and are identical to the values presented in previous literature, including Z15. Systems 3 and 4 are not detected in our MUSE data. We thus fix these to the redshift $z = 2.55$, a spectroscopic measurement obtained by Newman et al. (2011). The remaining redshifts are derived by our model, and they generally tend to be lower, but within $\pm$ 0.5 of the values found by Z15, with one exception. System 8 is a more severe underestimation at $z = 1.746$ compared to $z = 3.1$ from Z15.

Despite the difference in redshift measurements, our mass estimates are generally in agreement. In Z15, the mass enclosed in 100 kpc is $\sim 6 \times 10^{13} M_{\odot}$. In our model, we find that the mass enclosed in the same radius is $\sim 5.5 \pm 0.06 \times 10^{13} M_{\odot}$. The other major model for this cluster that we reference in this paper is from Newman et al. (2013a), which finds an enclosed mass within 100 kpc of $\sim 6 \times 10^{13} M_{\odot}$. Our mass estimate thus matches well with the most recent parametric and light-traces-mass lens models of this cluster.

The error in the mass estimate is larger in the outskirts of the cluster as opposed to the inner regions, consistent with expectations from strong lensing models that are expected to be most accurate in the region enclosed by the critical curve. The total $\chi^2$ error estimate is $\sim$ 54, as well, which correlates to the mass profile error, and an rms of 0.53".

The integrated density profile shown in Figure 7 is measured by summing the value of all pixels encapsulated within an annulus of width $r(n) - r(n-1)$, where $n$ corresponds to the step number.

#### *6.2.2 MS2137−23*

MS 2137 has similarly been modeled several times since the work by Sand et al. (2008). The most recent model is again from Zitrin et al. (2015). We break system 5, the large tangential arc, into two different pieces in order to improve the resolution of the model. Our systems 3 and 4 correspond to system 1 in Z15. System 2 in Z15 corresponds to our system 5, and system 3 in Z15 corresponds to our system 1. We add one new detection to the model: system 2, which we confirm via MUSE spectroscopy to be at $z \sim 1.19$. This system corresponds to the second radial arc near the BCG, which had been noted before in photometry but lacked a spectroscopic detection both of itself and

of a counter image that would make it viable to include in the lens model.

The most direct comparison we can make between our model and that of Z15 is the mass estimate. Z15 reports a total 2D integrated mass of $M(R < 100 \text{ kpc}) \sim 4 \times 10^{13} M_{\odot}$. A similar estimate of our mass within the same radius yields a value of $\sim 3.6 \pm 0.1 \times 10^{13} M_{\odot}$

The error in the mass profile is relatively small since our model is well-constrained by the inclusion of five systems with spectroscopic redshifts, with a total $\chi^2$ error estimate of $\sim 40$ and an rms of 0.67".

#### 6.2.3 MACS J0326.8-0043

This is the first published strong lensing model for MACS J0326, as well as the first mass estimate. Each system used to build the model has a spectroscopic redshift, which contributes to the reduction of overall systematic errors (Johnson et al. 2014). Four multiple images out of the twelve used in the model are predictions made by the model (see Table 3). The redshift used for each system is fixed to the spectroscopic redshift of the arc with the highest S/N ratio, and is constrained to four significant figures. We report a total integrated mass of $M(R < 100 \text{ kpc}) \sim 6 \times 10^{13} M_{\odot}$. The $\chi^2$ value found for the model is 28.44, while the overall rms in the image plane is 0.77". The largest contributors to the rms are images 1.1 and 2,4, which are predicted images. Because the model is constructed using only two shallow *HST* bands (each band has a short exposure time of 500 s; see Table 1), it is somewhat difficult to do the usual color and morphology comparison typically used to identify other strongly-lensed galaxies. As a result, the positions of the predicted images are merely predictions, and are subject to change if deeper spectroscopic or photometric observations are acquired for this cluster.

#### 6.2.4 MACS J1427.6−2521

This is the first published strong lensing model for MACS J1427, and is also the first examination of this cluster in the visual band. However, it was discussed in Ebeling et al. (2010) as a part of a survey of X-ray bright clusters from the MACS survey using *Chandra* data. The *HST* data used for the cluster is archival, and was observed as part of a SNAP project (PID 12884; PI: Harald Ebeling). Although only one *HST* band makes it difficult to identify multiple images based on the usual criteria of color and morphology, using it as a spatial reference alongside the MUSE redshifts makes it possible to create a basic lens model for the cluster. We report a total integrated mass of $M(R < 100 \text{ kpc}) \sim 8 \times 10^{13} M_{\odot}$. We obtain a total $\chi^2$ of $\sim 43$ with an rms of 0.81". Better quality imaging will almost certainly change the details of the model, but the current iteration still provides valuable information about the general shape of the mass in the cluster. Because the goal of this paper is to present lens models constructed mostly based on MUSE data, it is outside the scope of the current work to perform a thorough comparison of the mass profile against the existing *Chandra* data used in Ebeling et al. (2010) for this cluster. However, deeper *HST* imaging and a subsequently improved lens model would make such a comparison more robust, and is thus left for future work.

#### 6.2.5 MACS J0417

The lens model used for this cluster is identical to that presented in J19. There are two BCGs in this cluster, but only the southern one has a radial arc. In J19, both BCGs are separately parameterized with individual dPIE halos. In this work, we fix the parameters of the southern BCG to the properties we derive from our photometric measurements (see Table 7). The second change we make from the J19 model is to impose an additional selection criterion on the best-fit model from MCMC chain through our kinematic constraints. The resulting model does not differ strongly from J19 in the overall mass distribution. The reduced $\chi^2$ for the model in this paper is $\sim 0.91$, compared to $\sim 0.9$ from J19, and the rms is 0.41", compared to 0.38" from J19. Furthermore, the enclosed mass within 200 kpc is measured to be $1.8 \pm 0.04 \times 10^{14} M_{\odot}$, which is in agreement with the measurement from J19 from $1.78 \times 10^{14} M_{\odot}$. This also indicates that the model is in agreement with Mahler et al. (2019), which has similar values for the mass, rms, and $\chi^2$. The main change is in the value of the inner density slope, which we discuss more in Section 6.3. In the lensing only model, this value is $\gamma \sim 0.55$, whereas in the lensing and BCG kinematics model the slope is $\gamma \sim 0.6$. These values still fall within the FWHM of the PDF, however.

#### 6.2.6 MACS J0949

The lens model for this cluster is identical to that presented in Allingham et al. (2023). The authors use a separate parameterization of the BCG as well, so the only change we make to the model is to fix these parameters to the properties we derive from our photometric measurements (see Table 7). The enclosed mass within 200 kpc found by Allingham et al. is $2.0 \times 10^{14} M_{\odot}$, while the model in this paper finds a value of $2.1 \pm 0.07 \times 10^{14} M_{\odot}$ in the same radius. Allingham et al. finds a $\chi^2$ of 4.71 with an rms of 0.15", while the kinematic model we use finds a $\chi^2$ of 8.4 with an rms of 0.3". The model could likely be improved with a finer resolution of bins inside the MUSE cube for our measured velocity dispersions.

### 6.3 Inner Density Profile

While strong lensing models measure the total density near the critical curves, lensing alone cannot independently distinguish between the contributions of baryonic and dark matter. Breaking this degeneracy is crucial to understanding the physics occurring at the center of these clusters. To that end, we introduce stellar kinematics into the model to constrain the effect of the baryonic mass of the BCG on the overall density distribution. We restrict our analysis to the kinematics of the BCG exclusively, as this is by far the most dominant stellar component in this region. Following the procedure laid out in Newman et al. (2013b), we measure the inner slope $\gamma = -d \log \rho_{\rm DM} \,/\, d \log r$ over the range $r/r_{200} = 0.003 - 0.03$, which roughly corresponds to a range of 5 - 50 kpc.

We select these boundaries because the profile is strongly dominated by baryonic mass within 5 kpc, so the profile will always increase sharply within this region and is thus not a good indication of the shape of the DM density profile (see Newman et al. 2013b), and outside of 50 kpc, the profile is dominated by dark matter (e.g. Figure 7). The intermingling between baryonic and dark matter is thus best probed in the interior of this region. The overall results suggest that each of these profiles is very cored, with an average slope measurement of $\gamma \sim 0.66$ for all six clusters. Of all six clusters, MACS J1427 is the most poorly constrained, and could benefit the most from additional observations. However, its probability density is still centered firmly below 1.0, which suggests that it is more likely to be a cored cluster than a cuspy cluster.

These results, when taken in aggregate, demonstrate that clusters with radial arcs clearly present core-like density profiles. This is in-line with our current physical understanding of lensing, which re-

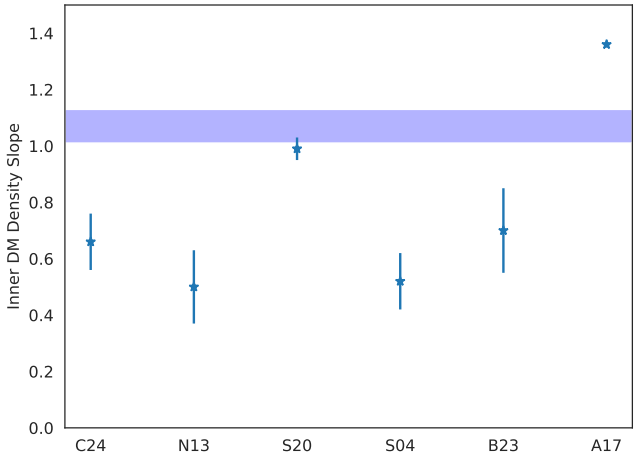


**Figure 9.** The average inner dark matter density slope as measured from five different papers, plotted from left to right as: this work (an average of six clusters), N13 (an average of seven clusters), Sartoris et al. (2020) (Abell 1063), Sand et al. (2004) (an average of four clusters), Biviano et al. (2023) (MACS J1206.2 − 0847), and Annunziatella et al. (2017) (MACS J0416 − 2403). The expected slope measurement from the C-EAGLE simulations as reported in He et al. (2020) is plotted as the blue shaded region.

quires the geometric shape of the mass distribution needed to produce radial arcs to be more centrally concentrated.

## 7 CONCLUSIONS AND SUMMARY

We select four clusters with radial arcs from a total sample of 150 clusters observed with MUSE, and construct strong lensing models for these clusters, using at least two systems with spectroscopic redshifts from MUSE in each model. The radial arcs impose an additional constraint on the mass distribution near the center of the cluster, enabling a more precise examination of the inner density profiles for these clusters than is typical of strong lensing, as the relative scarcity of radial arcs means that these profiles are usually extrapolated into the inner region of the cluster. We add another two clusters with radial arcs that have already been modeled to our sample, for a total of six clusters with radial arcs. We note that radial arcs are preferentially produced in mass distributions with a shallow inner slope, and each of these clusters has a demonstrably shallow slope measurement regardless of whether photometric and kinematic measurements of the BCG are incorporated into the lensing model; however, including a central kinematic probe reduces systematics of the model.

We additionally utilize stellar kinematics from the BCG to impose further constraints on the inner density profile following the methods used in Newman et al. 2013b. This allows us to constrain the contribution of the baryonic mass to the overall cluster density profile. We obtain a mean dark matter slope value of $\gamma \sim 0.66$ for all clusters, which is higher but generally consistent with the measurements from N13 ($\gamma \sim 0.5$). Figure 9 places our results into context with several other observational papers, as well as with the results from the C-EAGLE simulations in He et al. (2020). Of the five additional observational papers presented in the figure, N13 and Sand et al. (2004) follow the methods presented in this paper to obtain their slope measurements. Annunziatella et al. (2017) uses a blend of X-ray, strong lensing, and BCG kinematics to obtain their measurement, although they assume a single power-law mass profile, which may over-estimate the inner slope if the 3D mass profile steepens with radius. Sartoris et al. (2020) and Biviano et al. (2023) exclusively use cluster member kinematics to obtain their slope measurements. These disparate values and techniques clearly show the observational tension currently facing this measurement.

These results were typically obtained with shallow exposure times and in below-average observational conditions, which demonstrates that these techniques can be used to gain a general understanding of the shape of cluster density profiles without the need for deeper, more observationally constrained *HST* or spectroscopic data. However, we emphasize that our models and results can only improve with the addition of these types of data, and while the overall shape of our profiles should not change drastically, the overall measurements we obtain may shift. This can be seen in the difference of the work performed in Sand et al. and N13. In Sand et al., the authors derive a mean slope value of 0.5 for A383 and MS2137 using archival *HST* imaging and spectroscopy from Keck, whereas in N13, which used deeper *HST* images at a better wavelength for kinematic analysis, and deeper spectroscopy from Keck, the mean slope value for these two clusters is closer to 0.85. This shift is an example of the sort of change that we may expect to see if our models are ever redone in the future with, in particular, deeper observational data, which will allow for more reliable identification of multiply-imaged systems.

Future work on this subject will make use of the techniques employed in this paper, applied on other galaxy clusters from the Kaleidoscope survey. Further analysis will include clusters without radial arcs and will exploit the Kaleidoscope sample to fully benefit from the uniform depth and selection of clusters that characterizes the survey.

## ACKNOWLEDGEMENTS

CC, AN, and DJL acknowledge support from the UKRI FLF grant numbers MR/S017216/1 + NR/X006069/1. CC is additionally supported by a Durham Doctoral Studentship (Faculty of Science), awarded in 2020. MJ is supported by the United Kingdom Research and Innovation (UKRI) Future Leaders Fellowship 'Using Cosmic Beasts to uncover the Nature of Dark Matter' (grant numbers MR/S017216/1 + NR/X006069/1). DJL is also supported by the Science and Technology Facilities Council (STFC) grants ST/T000244/1 and ST/W002612/1. This research made use of Photutils, an Astropy package for detection and photometry of astronomical sources (Bradley et al. 2022).

## DATA AVAILABILITY

All *HST* data used for this work are available on the MAST archive. All VLT/MUSE data used for this work are available on the ESO Science Archive. The lensing mass models and other data products will be shared by the authors upon request.

## REFERENCES

Allingham J. F. V., et al., 2023, MNRAS, 522, 1118
Annunziatella M., et al., 2017, ApJ, 851, 81
Bacon R., Piqueras L., Conseil S., Richard J., Shepherd M., 2016, MPDAF: MUSE Python Data Analysis Framework, Astrophysics Source Code Library, record ascl:1611.003 (ascl:1611.003)
Bahé Y. M., et al., 2019, MNRAS, 485, 2287

Bartelmann M., 2010, Classical and Quantum Gravity, 27, 233001
Bartelmann M., Maturi M., 2017, Scholarpedia, 12, 32440
Bergamini P., et al., 2019, A&A, 631, A130
Bertin E., Arnouts S., 1996a, A&AS, 117, 393
Bertin E., Arnouts S., 1996b, A&AS, 117, 393
Biviano A., et al., 2023, ApJ, 958, 148
Bose S., et al., 2019, MNRAS, 486, 4790
Bradley L., et al., 2022, astropy/photutils: 1.6.0, doi:10.5281/zenodo.7419741
Broadhurst T., et al., 2005, ApJ, 621, 53
Caminha G. B., et al., 2017, A&A, 607, A93
Cappellari M., 2002, MNRAS, 333, 400
Cappellari M., 2017, MNRAS, 466, 798
Cappellari M., 2020, MNRAS, 494, 4819
Cappellari M., 2023, MNRAS, 526, 3273
Chan T. K., Kereš D., Oñorbe J., Hopkins P. F., Muratov A. L., Faucher-Giguère C. A., Quataert E., 2015, MNRAS, 454, 2981
Coe D., Bradley L., Zitrin A., 2015, ApJ, 800, 84
Coe D., et al., 2019, ApJ, 884, 85
Conroy C., Gunn J. E., 2010, ApJ, 712, 833
Conroy C., Gunn J. E., White M., 2009, ApJ, 699, 486
Covone G., Kneib J. P., Soucail G., Richard J., Jullo E., Ebeling H., 2006, A&A, 456, 409
Diego J. M., et al., 2018, ApJ, 857, 25
Donnarumma A., Ettori S., Meneghetti M., Moscardini L., 2009, MNRAS, 398, 438
Ebeling H., Edge A. C., Henry J. P., 2001, ApJ, 553, 668
Ebeling H., Edge A. C., Mantz A., Barrett E., Henry J. P., Ma C. J., van Speybroeck L., 2010, MNRAS, 407, 83
Elíasdóttir Á., et al., 2007, arXiv e-prints, p. arXiv:0710.5636
Faber S. M., Jackson R. E., 1976, ApJ, 204, 668
Falcón-Barroso J., Sánchez-Blázquez P., Vazdekis A., Ricciardelli E., Cardiel N., Cenarro A. J., Gorgas J., Peletier R. F., 2011, A&A, 532, A95
Fattahi A., et al., 2016, MNRAS, 457, 844
Gao L., Navarro J. F., Frenk C. S., Jenkins A., Springel V., White S. D. M., 2012, MNRAS, 425, 2169
Gladders M. D., Yee H. K. C., 2000, AJ, 120, 2148
Grand R. J. J., et al., 2017, MNRAS, 467, 179
Harvey D., Kneib J. P., Jauzac M., 2016, MNRAS, 458, 660
Hattori M., Kneib J., Makino N., 1999, Progress of Theoretical Physics Supplement, 133, 1
He Q., et al., 2020, MNRAS, 496, 4717
Hinton S., 2016, MARZ: Redshifting Program (ascl:1605.001)
Hoekstra H., Bartelmann M., Dahle H., Israel H., Limousin M., Meneghetti M., 2013, Space Sci. Rev., 177, 75
Jauzac M., et al., 2012, MNRAS, 426, 3369
Jauzac M., et al., 2014, MNRAS, 443, 1549
Jauzac M., et al., 2016, MNRAS, 463, 3876
Jauzac M., Harvey D., Massey R., 2018, MNRAS, 477, 4046
Jauzac M., et al., 2019, MNRAS, 483, 3082
Johnson T. L., Sharon K., Bayliss M. B., Gladders M. D., Coe D., Ebeling H., 2014, ApJ, 797, 48
Jullo E., Kneib J. P., Limousin M., Elíasdóttir Á., Marshall P. J., Verdugo T., 2007, New Journal of Physics, 9, 447
Kelson D. D., Zabludoff A. I., Williams K. A., Trager S. C., Mulchaey J. S., Bolte M., 2002, ApJ, 576, 720
Kilbinger M., 2015, Reports on Progress in Physics, 78, 086901
Kneib J.-P., Natarajan P., 2011, A&ARv, 19, 47
Kneib J.-P., Ellis R. S., Santos M. R., Richard J., 2004, ApJ, 607, 697
Kronawitter A., Saglia R. P., Gerhard O., Bender R., 2000, A&AS, 144, 53
Lagattuta D. J., et al., 2019, MNRAS, 485, 3738
Lagattuta D. J., et al., 2022, MNRAS, 514, 497
Limousin M., Kneib J.-P., Natarajan P., 2005a, MNRAS, 356, 309
Limousin M., Kneib J.-P., Natarajan P., 2005b, MNRAS, 356, 309
Limousin M., Kneib J. P., Bardeau S., Natarajan P., Czoske O., Smail I., Ebeling H., Smith G. P., 2007a, A&A, 461, 881
Limousin M., et al., 2007b, ApJ, 668, 643
Limousin M., et al., 2008, A&A, 489, 23
Limousin M., Sommer-Larsen J., Natarajan P., Milvang-Jensen B., 2009, ApJ, 696, 1771
Limousin M., Beauchesne B., Jullo E., 2022, A&A, 664, A90
Mahler G., et al., 2018, MNRAS, 473, 663
Mahler G., et al., 2019, ApJ, 873, 96
Mann A. W., Ebeling H., 2012, MNRAS, 420, 2120
Massey R., Kitching T., Richard J., 2010, Reports on Progress in Physics, 73, 086901
McCarthy I. G., Schaye J., Bird S., Le Brun A. M. C., 2017, MNRAS, 465, 2936
Merritt D., Graham A. W., Moore B., Diemand J., Terzić B., 2006, AJ, 132, 2685
Natarajan P., Kneib J.-P., Smail I., Treu T., Ellis R., Moran S., Limousin M., Czoske O., 2009, ApJ, 693, 970
Navarro J. F., Frenk C. S., White S. D. M., 1996, ApJ, 462, 563
Navarro J. F., et al., 2010, MNRAS, 402, 21
Newman A. B., Treu T., Ellis R. S., Sand D. J., Richard J., Marshall P. J., Capak P., Miyazaki S., 2009, ApJ, 706, 1078
Newman A. B., Treu T., Ellis R. S., Sand D. J., 2011, ApJ, 728, L39
Newman A. B., Treu T., Ellis R. S., Sand D. J., Nipoti C., Richard J., Jullo E., 2013a, ApJ, 765, 24
Newman A. B., Treu T., Ellis R. S., Sand D. J., 2013b, ApJ, 765, 25
Niemiec A., Jullo E., Giocoli C., Limousin M., Jauzac M., 2019, MNRAS, 487, 653
Niemiec A., et al., 2023, MNRAS, 524, 2883
Peng C. Y., Ho L. C., Impey C. D., Rix H.-W., 2002, AJ, 124, 266
Peng C. Y., Ho L. C., Impey C. D., Rix H.-W., 2010, AJ, 139, 2097
Piqueras L., Conseil S., Shepherd M., Bacon R., Leclercq F., Richard J., 2017, arXiv e-prints, p. arXiv:1710.03554
Postman M., et al., 2012a, ApJS, 199, 25
Postman M., et al., 2012b, ApJS, 199, 25
Richard J., et al., 2010, MNRAS, 404, 325
Richard J., Kneib J.-P., Ebeling H., Stark D. P., Egami E., Fiedler A. K., 2011, MNRAS, 414, L31
Richard J., et al., 2014, MNRAS, 444, 268
Richard J., et al., 2021, A&A, 646, A83
Sánchez-Blázquez P., et al., 2006, MNRAS, 371, 703
Sand D. J., Treu T., Smith G. P., Ellis R. S., 2004, ApJ, 604, 88
Sand D. J., Treu T., Ellis R. S., Smith G. P., Kneib J.-P., 2008, ApJ, 674, 711
Santucci G., et al., 2023, MNRAS, 521, 2671
Sartoris B., et al., 2020, A&A, 637, A34
Sawala T., et al., 2016, MNRAS, 457, 1931
Sharon K., et al., 2020, ApJS, 247, 12
Smith G. P., Kneib J.-P., Smail I., Mazzotta P., Ebeling H., Czoske O., 2005, MNRAS, 359, 417
Soto K. T., Lilly S. J., Bacon R., Richard J., Conseil S., 2016, MNRAS, 458, 3210
Tiley A. L., et al., 2020, MNRAS, 496, 649
Treu T., Ellis R. S., 2015, Contemporary Physics, 56, 17
Voges W., et al., 1999, A&A, 349, 389
Weilbacher P. M., Streicher O., Palsa R., 2016, MUSE-DRP: MUSE Data Reduction Pipeline (ascl:1610.004)
Wetzel A. R., White M., 2010, MNRAS, 403, 1072
Williams P. R., et al., 2018, MNRAS, 477, L70
Zitrin A., et al., 2011, ApJ, 742, 117
Zitrin A., et al., 2012, ApJ, 749, 97
Zitrin A., et al., 2015, ApJ, 801, 44

## APPENDIX A: LENS MODEL PROPERTIES AND MUSE CATALOGUE

This paper has been typeset from a TEX/LATEX file prepared by the author.

**Table A1.** Parameters for the best-fit lens model of A383. Error bars correspond to $1\sigma$ confidence level as inferred from the MCMC optimization. The parameters are provided for the cluster dark matter halo (dPIE DMH), the BCG halo (dPIE BCG), and each of the galaxy-scale perturbers included in the model (Perturber 1-3). ΔR.A. and ΔDecl. are defined in relation to the BCG, located at R.A.=2:48:03.37 and Decl.=-3:31:45.29. Position angles are measured north of west, and the ellipticity $\epsilon$ is defined as $(a^2 - b^2)/(a^2 + b^2)$. $r_{cut}$ is fixed to 1000kpc for the cluster dark matter halo.

| Object | ΔR.A. (") | ΔDecl. (") | $\epsilon$ | $\theta$ (°) | $r_{\rm core}$ (") | $r_{\rm cut}$ (") | $\sigma$ (km $s^{-1}$) |
|---|---|---|---|---|---|---|---|
| dPIE DMH | 0.43 | 2.26 | 0.17 | 106.66 | 50.80 | 1000. | 878.22 |
| dPIE BCG | 0 | 0 | - | - | - | - | 325.59 |
| Perturber 1 | 14.69 | -16.10 | 0.79 | 96.31 | 0.31 | 5.89 | 189.58 |
| Perturber 2 | -0.17 | -23.49 | 0.37 | 139.62 | 0.89 | 5.00 | 139.13 |
| Perturber 3 | 3.27 | -20.82 | 0.77 | 92.84 | 0.81 | 2.00 | 290.66 |

**Table A2.** Parameters for the best-fit lens model of MS 2137. Error bars correspond to $1\sigma$ confidence level as inferred from the MCMC optimization. The parameters are provided for the cluster dark matter halo (dPIE DMH) and the BCG halo (dPIE BCG). ΔR.A. and ΔDecl. are defined in relation to the center of the BCG, located at R.A.=21:40:15.16 and Decl.=-23:39:40.09. Position angles are measured north of west, and the ellipticity $\epsilon$ is defined as $(a^2 - b^2)/(a^2 + b^2)$. $r_{cut}$ is fixed to 1000kpc for the cluster dark matter halo.

| Object | ΔR.A. (") | ΔDecl. (") | $\epsilon$ | $\theta$ (°) | $r_{\rm core}$ (") | $r_{\rm cut}$ (") | $\sigma$ (km $s^{-1}$) |
|---|---|---|---|---|---|---|---|
| dPIE DMH | 0.24 | 0.012 | 0.35 | 148.77 | 13.51 | 1000. | 784.81 |
| dPIE BCG | -9.53 | 14.13 | - | - | - | - | 250.3 |

**Table A3.** Parameters for the best-fit lens model of MACS J0326. Error bars correspond to $1\sigma$ confidence level as inferred from the MCMC optimization. The parameters are provided for the cluster dark matter halo (dPIE DMH) and the BCG halo (dPIE BCG). ΔR.A. and ΔDecl. are defined in relation to the center of the BCG, located at R.A.=3:26:49.96 and Decl.=-0:43:51.47. Position angles are measured north of west, and the ellipticity $\epsilon$ is defined as $(a^2 - b^2)/(a^2 + b^2)$. $r_{cut}$ is fixed to 1000kpc for the cluster dark matter halo.

| Object | ΔR.A. (") | ΔDecl. (") | $\epsilon$ | $\theta$ (°) | $r_{\rm core}$ (") | $r_{\rm cut}$ (") | $\sigma$ (km $s^{-1}$) |
|---|---|---|---|---|---|---|---|
| dPIE DMH | -0.92 | -0.75 | 0.23 | 134.57 | 42.17 | 1000. | 924.55 |
| dPIE BCG | 17.56 | -20.75 | - | - | - | - | 189.44 |

**Table A4.** Parameters for the best-fit lens model of MACS J1427. Error bars correspond to $1\sigma$ confidence level as inferred from the MCMC optimization. The parameters are provided for the cluster dark matter halo (dPIE DMH) and the BCG halo (dPIE BCG). ΔR.A. and ΔDecl. are defined in relation to the center of the BCG, located at R.A.=21:40:15.16 and Decl.=-23:39:40.09. Position angles are measured north of west, and the ellipticity $\epsilon$ is defined as $(a^2 - b^2)/(a^2 + b^2)$. $r_{cut}$ is fixed to 1000kpc for Halo 1.

| Object | ΔR.A. (") | ΔDecl. (") | $\epsilon$ | $\theta$ (°) | $r_{\rm core}$ (") | $r_{\rm cut}$ (") | $\sigma$ (km $s^{-1}$) |
|---|---|---|---|---|---|---|---|
| dPIE DMH | 0.24 | 0.012 | 0.35 | 148.77 | 13.51 | 1000. | 784.81 |
| dPIE BCG | 0 | -0.018 | - | - | - | - | 277.92 |

**Table A5.** Statistical values derived from the MCMC fitting for the models of each cluster presented in Section 3. The columns show the likelihood, log $L$; the rms deviation from the predicted positions of the multiple images from their observed positions in the image plane, $rms$, and the reduced $\chi^2$.

| Cluster | log $L$ | $rms$ | $\chi^2$ |
|---|---|---|---|
| A383 | 18.73 | 0.61 | 35.76 |
| MS2137 | 16.01 | 0.70 | 14.22 |
| MACS J0326 | 11.05 | 0.85 | 23.08 |
| MACS J1427 | 7.41 | 0.61 | 0.83 |
| MACSJ0417 | 47.66 | 0.49 | 44.29 |
| MACSJ0949 | 80.17 | 0.41 | 17.58 |

**Table A6.** Measured redshifts in A383. Column 1 is the ID of the source. Columns 2 and 3 are the R.A. and Decl. in degrees (J2000). Column 4 is the redshift of the source. Column 5 is the quality flag (QF) assigned to the redshift. The QF scales in quality from largest to smallest; a flag value of 3 indicates that we have high confidence in the value for the redshift, whereas a flag value of 1 indicates that we have low confidence in the value for the redshift.

| ID | R.A. | Decl. | $z$ | QF |
|---|---|---|---|---|
| 1 | 42.01870947 | -3.53513970 | 0.196 | 3 |
| 3 | 42.01413524 | -3.53591378 | 0.195 | 3 |
| 4 | 42.00714291 | -3.53595815 | 0.412 | 3 |
| 7 | 42.00745227 | -3.53755278 | 0.960 | 3 |
| 11 | 42.01410348 | -3.52926656 | 0.188 | 3 |
| 18 | 42.15254730 | -3.53287324 | 1.010 | 3 |
| 50 | 42.02032160 | -3.53682543 | 1.011 | 3 |
| 57 | 42.01432510 | -3.52883110 | 1.011 | 3 |
| 61 | 42.00947290 | -3.52844810 | 4.633 | 3 |
| 70 | 42.01179557 | -3.53284732 | 1.009 | 3 |
| 79 | 42.01001298 | -3.53386725 | 1.505 | 3 |
| 80 | 42.01003680 | -3.53068700 | 4.634 | 3 |
| 83 | 42.01280980 | -3.52573640 | 4.636 | 3 |
| 180 | 42.00583728 | -3.53475354 | 0.928 | 3 |
| 208 | 42.01527605 | -3.53287594 | 0.190 | 3 |
| 242 | 42.00980114 | -3.53086269 | 1.010 | 3 |
| 313 | 42.02047584 | -3.53382125 | 1.092 | 3 |
| 394 | 42.01915633 | -3.53195987 | 0.373 | 3 |
| 410 | 42.01286378 | -3.53353040 | 1.010 | 3 |
| 451 | 42.00810054 | -3.53202013 | 0.186 | 3 |
| 493 | 42.01919295 | -3.53294806 | 6.031 | 3 |
| 501 | 42.01157428 | -3.52974105 | 0.186 | 3 |
| 737 | 42.00958438 | -3.53049744 | 1.010 | 3 |
| 786 | 42.01923866 | -3.52626206 | 0.194 | 3 |
| 1007 | 42.01156363 | -3.52457326 | 0.656 | 3 |
| 1014 | 42.01560756 | -3.52639592 | 0.190 | 3 |
| 1103 | 42.01513734 | -3.52105068 | 0.195 | 3 |
| 1150 | 42.02093902 | -3.52339690 | 0.890 | 3 |
| 1183 | 42.01893922 | -3.52259989 | 0.094 | 3 |
| 1353 | 42.01953604 | -3.52455550 | 0.937 | 3 |
| 1482 | 42.01180784 | -3.52436324 | 0.656 | 3 |
| 1578 | 42.01363994 | -3.52635524 | 6.032 | 3 |
| ⋮ | ⋮ | ⋮ | ⋮ | ⋮ |
| ⋮ | ⋮ | ⋮ | ⋮ | ⋮ |
| 1601 | 42.02098120 | -3.52583488 | 0.824 | 3 |
| 1741 | 42.01678438 | -3.52648827 | 0.373 | 3 |
| 17 | 42.01396670 | -3.53270560 | 0.279 | 2 |
| 135 | 42.02019771 | -3.53514563 | 0.137 | 2 |
| 154 | 42.01317449 | -3.53516389 | 0.191 | 2 |
| 329 | 42.00860414 | -3.53278628 | 0.188 | 2 |
| 570 | 42.00709600 | -3.53079003 | 0.764 | 2 |
| 584 | 42.02237334 | -3.53141806 | 0.182 | 2 |
| 1141 | 42.00768973 | -3.52797491 | 1.276 | 2 |
| 1223 | 42.02037639 | -3.52286060 | 0.186 | 2 |
| 1377 | 42.01522849 | -3.52388490 | 0.000 | 2 |
| 1407 | 42.00603086 | -3.52378361 | 4.943 | 2 |
| 1531 | 42.01179860 | -3.52578326 | 0.188 | 2 |
| 1582 | 42.01767138 | -3.52618242 | 0.191 | 2 |
| 1953 | 42.01700107 | -3.52165509 | 0.593 | 2 |
| 5 | 42.01549764 | -3.53712308 | 0.189 | 1 |
| 77 | 42.01967533 | -3.53680155 | 0.187 | 1 |
| 82 | 42.01976480 | -3.52540490 | 6.259 | 1 |
| 110 | 42.01184380 | -3.53511810 | 2.681 | 1 |
| 112 | 42.02161230 | -3.52512230 | 5.033 | 1 |
| 262 | 42.01449268 | -3.53497007 | 0.000 | 1 |
| 270 | 42.01340539 | -3.53364156 | 0.159 | 1 |
| 316 | 42.00696144 | -3.53265637 | 0.185 | 1 |
| 457 | 42.02281348 | -3.53305797 | 0.000 | 1 |
| 746 | 42.00876902 | -3.52981517 | 0.195 | 1 |
| 793 | 42.00807525 | -3.52938858 | 0.183 | 1 |
| 859 | 42.01083523 | -3.52946545 | 0.187 | 1 |
| 914 | 42.00876656 | -3.52927118 | 1.559 | 1 |
| 988 | 42.01139524 | -3.52879504 | 0.187 | 1 |
| 996 | 42.01737083 | -3.52816428 | 1.580 | 1 |
| 1526 | 42.01010281 | -3.52584537 | 0.192 | 1 |
| 1923 | 42.01348284 | -3.52118876 | 0.184 | 1 |

**Table A7.** Measured redshifts in MS 2137. Column 1 is the ID of the source. Columns 2 and 3 are the R.A. and Decl. in degrees (J2000). Column 4 is the redshift of the source. Column 5 is the quality flag (QF) assigned to the redshift. The QF scales in quality from largest to smallest; a flag value of 3 indicates that we have high confidence in the value for the redshift, whereas a flag value of 1 indicates that we have low confidence in the value for the redshift.

| ID | R.A. | Decl. | $z$ | QF |
|---|---|---|---|---|
| 2 | 325.0612502 | -23.66751981 | 0.163 | 3 |
| 8 | 325.0629407 | -23.65686360 | 1.495 | 3 |
| 51 | 325.0591929 | -23.66169910 | 1.494 | 3 |
| 90 | 325.0650339 | -23.66763583 | 1.496 | 3 |
| 93 | 325.0587208 | -23.66655827 | -4.0E-5 | 3 |
| 143 | 325.0631642 | -23.66114100 | 0.314 | 3 |
| 265 | 325.0658341 | -23.66693218 | 1.191 | 3 |
| 305 | 325.0600151 | -23.66525997 | 0.317 | 3 |
| 432 | 325.0624174 | -23.65700482 | 1.495 | 3 |
| 554 | 325.0717926 | -23.66225558 | 0.539 | 3 |
| 557 | 325.0554316 | -23.65875178 | 0.974 | 3 |
| 564 | 325.0658002 | -23.66232491 | 0.123 | 3 |
| 575 | 325.0652998 | -23.66272321 | 3.086 | 3 |
| 579 | 325.0659165 | -23.65859792 | 0.313 | 3 |
| 594 | 325.0660545 | -23.65719416 | 0.323 | 3 |
| 717 | 325.0626655 | -23.66044969 | 0.313 | 3 |
| 796 | 325.0625407 | -23.66026792 | 0.313 | 3 |
| 804 | 325.0608755 | -23.65919716 | 0.314 | 3 |
| 899 | 325.0603961 | -23.65473848 | 1.265 | 3 |
| 978 | 325.0641418 | -23.65707151 | 1.495 | 3 |
| 982 | 325.0655182 | -23.65546970 | 0.311 | 3 |
| 984 | 325.0577362 | -23.65544930 | 0.313 | 3 |
| 1022 | 325.0573735 | -23.65524711 | 3.086 | 3 |
| 1047 | 325.0631649 | -23.65676262 | 1.495 | 3 |
| 1085 | 325.0646960 | -23.65727918 | 1.495 | 3 |
| 1098 | 325.0681213 | -23.65712822 | 0.317 | 3 |
| 1213 | 325.0627779 | -23.65956801 | 1.191 | 3 |
| 1437 | 325.0607713 | -23.65322025 | 0.317 | 3 |
| 1467 | 325.0555769 | -23.65364726 | 0.281 | 3 |
| 1477 | 325.0710864 | -23.65315590 | 0.315 | 3 |
| ⋮ | ⋮ | ⋮ | ⋮ | ⋮ |

| ID | R.A. | Decl. | $z$ | QF |
|---|---|---|---|---|
| ⋮ | ⋮ | ⋮ | ⋮ | ⋮ |
| 263 | 325.0614965 | -23.66630868 | 0.000 | 2 |
| 290 | 325.0612886 | -23.66452073 | 0.316 | 2 |
| 307 | 325.0596807 | -23.66552547 | 0.314 | 2 |
| 616 | 325.0577885 | -23.66006395 | 0.315 | 2 |
| 689 | 325.0631461 | -23.65977012 | 1.496 | 2 |
| 1129 | 325.0649292 | -23.65706087 | 1.492 | 2 |
| 1 | 325.0557350 | -23.66728671 | 0.999 | 1 |
| 4 | 325.0613087 | -23.66945031 | 0.310 | 1 |
| 63 | 325.0581008 | -23.65941150 | 5.509 | 1 |
| 69 | 325.0639614 | -23.66911864 | 0.000 | 1 |
| 166 | 325.0574263 | -23.66726300 | 0.281 | 1 |
| 221 | 325.0605980 | -23.66653599 | 0.328 | 1 |
| 224 | 325.0592894 | -23.66707065 | 1.543 | 1 |
| 242 | 325.0622637 | -23.66447865 | 0.323 | 1 |
| 269 | 325.0616751 | -23.66637744 | 2.459 | 1 |
| 299 | 325.0544046 | -23.66521798 | 0.222 | 1 |
| 318 | 325.0596921 | -23.66584184 | 0.000 | 1 |
| 431 | 325.0621176 | -23.66431571 | 0.639 | 1 |
| 503 | 325.0536364 | -23.66107318 | 0.316 | 1 |
| 580 | 325.0633467 | -23.66185286 | 0.316 | 1 |
| 644 | 325.0648793 | -23.66182589 | 0.937 | 1 |
| 654 | 325.0642144 | -23.66216598 | 0.000 | 1 |
| 657 | 325.0602975 | -23.66170037 | 0.000 | 1 |
| 805 | 325.0543628 | -23.66046275 | 0.311 | 1 |
| 814 | 325.0653077 | -23.66082818 | 2.744 | 1 |
| 868 | 325.0544333 | -23.66021964 | 0.000 | 1 |
| 869 | 325.0580939 | -23.66019602 | 0.318 | 1 |
| 1128 | 325.0631522 | -23.65935947 | 1.496 | 1 |
| 1261 | 325.0699090 | -23.65869802 | 0.000 | 1 |
| 1389 | 325.0630390 | -23.66044158 | 0.000 | 1 |

**Table A8.** Measured redshifts in MACS J0326. Column 1 is the ID of the source. Columns 2 and 3 are the R.A. and Decl. in degrees (J2000). Column 4 is the redshift of the source. Column 5 is the quality flag (QF) assigned to the redshift. The QF scales in quality from largest to smallest; a flag value of 3 indicates that we have high confidence in the value for the redshift, whereas a flag value of 1 indicates that we have low confidence in the value for the redshift.

| ID | R.A. | Decl. | $z$ | QF |
|---|---|---|---|---|
| 1 | 51.70806634 | -0.73727226 | 0.440 | 3 |
| 13 | 51.70810324 | -0.73102918 | 0.448 | 3 |
| 15 | 51.71595908 | -0.72429963 | 0.058 | 3 |
| 16 | 51.71636815 | -0.73054060 | 1.431 | 3 |
| 18 | 51.70415754 | -0.72469514 | 0.000 | 3 |
| 20 | 51.71355394 | -0.72488020 | 1.247 | 3 |
| 21 | 51.71485312 | -0.72508425 | 0.449 | 3 |
| 26 | 51.70869202 | -0.72576593 | 0.447 | 3 |
| 29 | 51.70178080 | -0.73721435 | 1.179 | 3 |
| 32 | 51.70734694 | -0.72652196 | 0.443 | 3 |
| 37 | 51.70639179 | -0.72749385 | 0.453 | 3 |
| 42 | 51.71263975 | -0.72735037 | 0.452 | 3 |
| 46 | 51.70401058 | -0.72803930 | 0.438 | 3 |
| 50 | 51.71014411 | -0.72838957 | 0.449 | 3 |
| 52 | 51.70845413 | -0.72881622 | 0.000 | 3 |
| 54 | 51.70380841 | -0.72941315 | 1.248 | 3 |
| 55 | 51.70662959 | -0.72941321 | 0.232 | 3 |
| 57 | 51.71376910 | -0.72767990 | 0.776 | 3 |
| 61 | 51.70590437 | -0.73047397 | 0.446 | 3 |
| 62 | 51.70549223 | -0.73047924 | 1.248 | 3 |
| 68 | 51.71396070 | -0.73078547 | 0.458 | 3 |
| 69 | 51.71124680 | -0.73372370 | 0.494 | 3 |
| 74 | 51.70481740 | -0.73595180 | 5.880 | 3 |
| 76 | 51.71123314 | -0.73155115 | 0.455 | 3 |
| $78_M$ | 51.70655724 | -0.73162210 | 0.000 | 3 |
| $78_P$ | 51.70691830 | -0.72437400 | 4.980 | 3 |
| 81 | 51.71233054 | -0.73199644 | 1.098 | 3 |
| 84 | 51.70674370 | -0.73699870 | 5.879 | 3 |
| 86 | 51.70180090 | -0.73108310 | 5.878 | 3 |
| 88 | 51.71547523 | -0.73306727 | 0.356 | 3 |
| 103 | 51.71046650 | -0.73443810 | 1.248 | 3 |
| 108 | 51.70190169 | -0.73491512 | 0.448 | 3 |
| ⋮ | ⋮ | ⋮ | ⋮ | ⋮ |

| ID | R.A. | Decl. | $z$ | QF |
|---|---|---|---|---|
| ⋮ | ⋮ | ⋮ | ⋮ | ⋮ |
| 113 | 51.71150751 | -0.73442642 | 0.446 | 3 |
| 116 | 51.71221832 | -0.73567774 | 0.804 | 3 |
| 121 | 51.7005703 | -0.73653835 | 0.444 | 3 |
| 122 | 51.70323641 | -0.73677771 | 0.325 | 3 |
| 138 | 51.70211192 | -0.73705436 | 1.272 | 3 |
| 139 | 51.71652064 | -0.73709426 | 0.804 | 3 |
| 152 | 51.70378826 | -0.73798640 | 1.181 | 3 |
| 160 | 51.71135863 | -0.72256970 | 0.453 | 3 |
| 161 | 51.71602364 | -0.72303510 | 0.441 | 3 |
| 5 | 51.71293750 | -0.72474400 | 1.145 | 2 |
| 23 | 51.70883990 | -0.73340260 | 0.248 | 2 |
| 34 | 51.70202020 | -0.72244300 | 4.788 | 2 |
| 39 | 51.70925786 | -0.72748144 | 0.455 | 2 |
| 41 | 51.71549023 | -0.72772794 | 0.458 | 2 |
| 44 | 51.71477132 | -0.72779148 | 3.235 | 2 |
| 60 | 51.70565583 | -0.73065953 | 0.453 | 2 |
| 85 | 51.70532607 | -0.73234988 | 3.755 | 2 |
| 94 | 51.70138800 | -0.73333498 | 0.414 | 2 |
| 155 | 51.70649017 | -0.73827485 | 0.450 | 2 |
| 17 | 51.70943969 | -0.72450109 | 0.447 | 1 |
| 35 | 51.71171314 | -0.72674022 | 1.248 | 1 |
| 47 | 51.70971234 | -0.72803052 | 0.452 | 1 |
| 53 | 51.70219623 | -0.72919887 | 0.440 | 1 |
| 62 | 51.70046960 | -0.72423605 | 4.012 | 1 |
| 68 | 51.70504950 | -0.72801140 | 3.755 | 1 |
| 77 | 51.70667121 | -0.73145698 | 0.000 | 1 |
| 86 | 51.70681907 | -0.73258985 | 0.443 | 1 |
| 87 | 51.71079159 | -0.73274959 | 0.434 | 1 |
| 90 | 51.70686528 | -0.73301888 | 0.446 | 1 |
| 105 | 51.70739184 | -0.73472983 | 0.448 | 1 |
| 118 | 51.70982389 | -0.73588872 | 0.436 | 1 |
| 145 | 51.70424116 | -0.73770541 | 0.441 | 1 |

**Table A9.** Measured redshifts in MACS J1427. Column 1 is the ID of the source. Columns 2 and 3 are the R.A. and Decl. in degrees (J2000). Column 4 is the redshift of the source. Column 5 is the quality flag (QF) assigned to the redshift. The QF scales in quality from largest to smallest; a flag value of 3 indicates that we have high confidence in the value for the redshift, whereas a flag value of 1 indicates that we have low confidence in the value for the redshift.

| ID | R.A. | Decl. | $z$ | QF |
|---|---|---|---|---|
| 25 | 216.91619884 | -25.35766428 | 0.317 | 3 |
| 26 | 216.92217694 | -25.35378681 | 0.000 | 3 |
| 31 | 216.90642465 | -25.35723329 | 1.236 | 3 |
| 32 | 216.91803386 | -25.35737324 | 0.000 | 3 |
| 36 | 216.92494939 | -25.35576190 | 0.232 | 3 |
| 40 | 216.91399381 | -25.35600037 | 0.325 | 3 |
| 41 | 216.91008760 | -25.35561308 | 0.313 | 3 |
| 42 | 216.91088341 | -25.35678064 | 0.883 | 3 |
| 50 | 216.91485845 | -25.35028410 | 0.884 | 3 |
| 54 | 216.91193940 | -25.35514541 | 0.319 | 3 |
| 64 | 216.91063525 | -25.35363405 | 1.236 | 3 |
| 75 | 216.91544327 | -25.34620637 | 0.662 | 3 |
| 84 | 216.91035987 | -25.34988187 | 0.309 | 3 |
| 88 | 216.91447505 | -25.35061860 | 0.318 | 3 |
| 93 | 216.91584053 | -25.35056782 | 0.312 | 3 |
| 94 | 216.91691114 | -25.35060176 | 0.319 | 3 |
| 99 | 216.91571850 | -25.35135379 | 0.000 | 3 |
| 101 | 216.92028056 | -25.35105752 | 0.320 | 3 |
| 108 | 216.91500246 | -25.35168478 | 0.313 | 3 |
| 114 | 216.91434723 | -25.35196763 | 0.207 | 3 |
| 117 | 216.91959666 | -25.35234976 | 0.321 | 3 |
| 118 | 216.91229301 | -25.35263420 | 0.325 | 3 |
| 122 | 216.91602417 | -25.35293113 | 0.322 | 3 |
| 131 | 216.91432235 | -25.35339907 | 0.313 | 3 |
| 132 | 216.91465475 | -25.35352760 | 0.001 | 3 |
| 133 | 216.91264386 | -25.35362011 | 0.883 | 3 |
| 148 | 216.91775549 | -25.35420614 | 0.312 | 3 |
| 156 | 216.90745832 | -25.35435398 | 4.323 | 3 |
| 162 | 216.90934813 | -25.35488005 | 0.324 | 3 |
| 167 | 216.90690018 | -25.35510802 | 0.313 | 3 |
| 180 | 216.90829896 | -25.35540450 | 0.914 | 3 |
| 191 | 216.91571984 | -25.34906701 | 0.317 | 3 |
| 193 | 216.90811293 | -25.34955274 | 0.328 | 3 |
| 195 | 216.91512646 | -25.34888806 | 0.316 | 3 |
| 196 | 216.91563524 | -25.34970724 | 0.316 | 3 |
| 207 | 216.91835520 | -25.34833384 | 0.325 | 3 |
| 217 | 216.92013294 | -25.34813976 | 0.320 | 3 |
| 219 | 216.90701865 | -25.34757320 | 0.695 | 3 |
| 225 | 216.90930004 | -25.34377121 | 0.322 | 3 |
| 226 | 216.91207270 | -25.34651632 | 0.663 | 3 |
| 234 | 216.90966217 | -25.34486568 | 0.856 | 3 |
| ⋮ | ⋮ | ⋮ | ⋮ | ⋮ |

| ID | R.A. | Decl. | $z$ | QF |
|---|---|---|---|---|
| ⋮ | ⋮ | ⋮ | ⋮ | ⋮ |
| 241 | 216.92268855 | -25.34577380 | 0.322 | 3 |
| 251 | 216.91990633 | -25.34613558 | 1.239 | 3 |
| 1 | 216.91549900 | -25.35909370 | 0.232 | 2 |
| 56 | 216.91033590 | -25.35151940 | 0.813 | 2 |
| 68 | 216.91654650 | -25.35620440 | 6.043 | 2 |
| 72 | 216.91702200 | -25.35768770 | 3.961 | 2 |
| 73 | 216.91282910 | -25.34527350 | 6.042 | 2 |
| 81 | 216.92296584 | -25.34974507 | 0.000 | 2 |
| 96 | 216.91911505 | -25.35069157 | 0.780 | 2 |
| 102 | 216.92348540 | -25.35112651 | 0.437 | 2 |
| 103 | 216.90951026 | -25.35120070 | 0.315 | 2 |
| 138 | 216.92258186 | -25.34430751 | 1.119 | 2 |
| 199 | 216.91479272 | -25.34911416 | 0.000 | 2 |
| 218 | 216.90615033 | -25.34387282 | 0.915 | 2 |
| 220 | 216.91306431 | -25.34663774 | 0.315 | 2 |
| 2 | 216.90763630 | -25.35900540 | 0.326 | 1 |
| 22 | 216.91948152 | -25.35840617 | 0.346 | 1 |
| 34 | 216.91844686 | -25.35742171 | 2.055 | 1 |
| 35 | 216.91288324 | -25.35744786 | 0.321 | 1 |
| 53 | 216.92419220 | -25.35758180 | 3.711 | 1 |
| 57 | 216.91773293 | -25.35578650 | 0.347 | 1 |
| 58 | 216.91795080 | -25.34248430 | 5.987 | 1 |
| 74 | 216.92431599 | -25.35543093 | 0.231 | 1 |
| 77 | 216.91119860 | -25.34467890 | 4.474 | 1 |
| 121 | 216.91576496 | -25.35285091 | 1.381 | 1 |
| 140 | 216.90804218 | -25.35371079 | 0.907 | 1 |
| 141 | 216.91940086 | -25.35381755 | 0.309 | 1 |
| 144 | 216.91105772 | -25.35395397 | 0.398 | 1 |
| 164 | 216.92323652 | -25.35479505 | 0.317 | 1 |
| 169 | 216.92067451 | -25.35487997 | 0.575 | 1 |
| 170 | 216.91419559 | -25.34846838 | 4.019 | 1 |
| 172 | 216.90966979 | -25.35508015 | 0.318 | 1 |
| 173 | 216.92047912 | -25.35515232 | 0.575 | 1 |
| 176 | 216.90934137 | -25.35527508 | 0.328 | 1 |
| 185 | 216.90949896 | -25.34656741 | 1.208 | 1 |
| 201 | 216.91901817 | -25.34852172 | 1.040 | 1 |
| 208 | 216.91808783 | -25.34834611 | 3.349 | 1 |
| 213 | 216.90558929 | -25.34828333 | 0.913 | 1 |
| 232 | 216.90673382 | -25.34649694 | 0.783 | 1 |
| 248 | 216.91130553 | -25.34609367 | 0.327 | 1 |
| 254 | 216.91156687 | -25.34619676 | 0.319 | 1 |